

FDL-TDR-64-65

✓ DYNAMIC BUCKLING OF SHELL STRUCTURES
SUBJECT TO LONGITUDINAL IMPACT, ✓

TECHNICAL DOCUMENTARY REPORT NO. FDL-TDR-64-65

December 1964
✓

Air Force Flight Dynamics Laboratory
Research and Technology Division
= 22 Air Force Systems Command, ✓
Wright-Patterson Air Force Base, Ohio

Project No. 1467, Task No. 146703

(Prepared under Contract No. AF33(657)-10220 ✓
by General Electric Company
P. O. Box 8555, Philadelphia, Pa. 19101
Authors: A. P. Coppa and W. A. Nash)

FOREWORD

This report was prepared by the Space Sciences Laboratory, Missile and Space Division, General Electric Company under USAF Contract No. AF 33(657)-10220. The work was administered under the direction of the Flight Dynamics Laboratory, Research and Technology Division, Mr. A. Abdessalam, project engineer.

The report covers work performed from January 1963 to March 1964.

The work was performed under the general direction of Dr. F. W. Wendt, Manager, Space Structures Operation, Space Sciences Laboratory. Mr. A. P. Coppa, principal investigator, planned the project and conducted the experimental research. Professor W. A. Nash performed the analytical studies of problems (1) and (2).

The experiments were performed by Messrs. S. A. Cimorelli and G. P. Kernicky, whose dedicated efforts through the program are gratefully acknowledged. In addition, acknowledgement is extended to Messrs. O. A. Winter, S. A. Cimorelli, and T. Coffin for computational work, and to Messrs. F. L. Smith and T. Palandro for photographs.

ABSTRACT


Experimental and theoretical studies of the buckling and collapse of circular cylindrical and conical shells under longitudinal impact are described. Various conditions of loading were investigated such as impact with rigid, fluid, and granular media, and such effects as initial geometrical imperfections, edge support, and loading asymmetry were included. In addition, the effect of axial impact at velocities up to 391 ft/sec on the buckling of thin cylindrical shells was studied experimentally. Finally, three problems, relating to the experiments were studied theoretically: (1) the dynamic buckling of a circular cylindrical shell subject to an axial loading which varies linearly with time, using the nonlinear theory, (2) dynamic buckling of a circular cylindrical shell subject to a constant velocity end displacement, including the effects of plasticity and incorporating extremely large deflections, and (3) the inextensional shortening and collapse modes of conical shells for the complete range of end shortening.

Results are presented which show reasonably good comparison between experiment and theory for Problems (1) and (3) and further for the case of internally pressurized circular cylindrical shells under axial impact (this latter result stems from the previous program). In addition, extensional ("ring") collapse waves were obtained in a thin cylindrical shell impacted axially at a velocity of 392 ft/sec. This is believed to be the first time such a mode has been observed in a thin, unpressurized shell.

PUBLICATION REVIEW

This report has been reviewed and is approved for publication.

FOR THE DIRECTOR:



RICHARD F. HOENER
Acting Chief, Structures Division
AF Flight Dynamics Laboratory

Contrails

TABLE OF CONTENTS

	Page
1. INTRODUCTION	1
2. LITERATURE SURVEY	3
PART I. EXPERIMENTAL PROGRAM	
3. EXPERIMENTAL FACILITIES	9
3.1 Pressurized Shell Impact Tester	9
3.2 Modified Pressurized Shell Impact Tester	9
3.3 Non-Rigid Impact Tester	10
3.4 High Velocity Structural Impact Facility	10
4. INSTRUMENTATION	12
4.1 Accelerometers	12
4.2 Strain Gages	12
4.3 Photography	12
4.4 Recording	12
4.5 Triggering	13
5. PHASE I - RIGID IMPACT	14
5.1 Apparatus	14
5.1.1 Pressurized Shell Mounting Fixtures	14
5.1.2 Strain Gage Attachment Fixture	14
5.1.3 Imperfection Measurement System	14
5.2 Specimens and Instrumentation	16
5.3 Initial Imperfection Measurements	18
5.4 Plots of Imperfection Components	21
5.5 Descriptive Outline of Tests	22
5.6 Results	22
5.6.1 Pressurized Cylindrical Shells	22
5.6.2 Pressurized Conical Shells	27
5.6.3 Oblique Impact	30
5.7 Inextensional Buckling Configurations	31
5.7.1 Prizmoidal Shortening Patterns	35
5.7.2 Total Collapse Configuration	35
5.7.3 Profile Characteristics	36
5.7.4 Construction of Inextensional Patterns and Comparison with Experiment	37

	Page
6. PHASE II - HIGH VELOCITY IMPACT	39
6.1 Apparatus	39
6.2 Specimens and Instrumentation	39
6.3 Results	40
7. PHASE III - NON-RIGID IMPACT	45
7.1 Specimens and Instrumentation	45
7.2 Outline of Tests	45
7.2.1 Sand Impact	45
7.2.2 Water Impact	46
7.3 Results	46
7.3.1 Sand Impact	47
7.3.2 Water Impact	51
PART II. ANALYTICAL INVESTIGATION	55
8. ELASTIC BEHAVIOR OF AXIALLY LOADED CYLINDRICAL SHELLS	55
9. PLASTIC BEHAVIOR OF AXIALLY LOADED CYLINDRICAL SHELLS	67
PART III. COMPARISON OF THEORETICAL PREDICTIONS WITH EXPERIMENTAL RESULTS	72
10. RIGID IMPACT OF PRESSURIZED CYLINDRICAL SHELLS	72
11. NON-RIGID IMPACT	72
12. SUMMARY OF DISCUSSIONS AND CONCLUSIONS	74
12.1 Rigid Impact	74
12.2 High Velocity Impact	75
12.3 Non-Rigid Impact	75
13. REFERENCES	77
APPENDIX	81
FIGURES	

ILLUSTRATIONS

1. Pressurized Shell Impact Apparatus
2. Modified Pressurized Shell Impact Apparatus
3. Non-Rigid Impact Test Apparatus
4. High Velocity Structural Impact Facility
5. Pressurized Shell Mounting Fixture
6. Mounting Arrangement of Pressurized Shell
7. Strain Gage Attachment Fixture
8. Precision Shell Measurement System
9. Mounted Instrumented Cylinder
10. Instrumented Conical Shell
11. Measured Traverses of Spec. G-8
12. Relationship Between Actual, Mean, and Reference Sections
13. Relationship Between the Mean "Cylinder" and Reference Cylinder
14. $\Delta(\theta)_i$ Imperfection Components - Specimen G-8
15. $\Delta(i)_\theta$ Imperfection Components - Specimen G-8
16. Components of the Centroidal Axis of the Mean Cylinder - Specimen G-8
17. Accelerometer Record - Test No. G-1
18. Data Records - Test No. G-2
19. Data Records - Test No. G-3
20. Specimens G-2 and G-3
21. Comparison of Data from Accelerometer and Strain Gages
22. Data Records - Test No. G-4
23. Data Records - Test No. G-6
24. Data Records - Test No. G-7
25. Data Records - Test No. G-8
26. Strain Data Records - Test No. C-3
27. Strain Data Records - Test No. C-4
28. Strain Data Records - Test No. C-6
29. Specimen C-6, Showing Orderly Collapse at end
30. Strain Data Records - Test No. C-1
31. Initial and Postbuckling Strain - Time Pulses
32. Specimens After Oblique Impact - Type A
33. Specimens After Oblique Impact - Type B
34. Inextensional Geometry of a Conical Frustum
35. Layout of an Inextensional Pattern for a Cone in the Plane
36. Prismoidal Inextensional Shortening Configuration
37. Profile Geometry
38. 10% Shortened Inextensional Configuration for a Conical Frustum of $\gamma = 25^\circ$, $n_f = 5$
39. 50% Shortened Inextensional Configuration for a Conical Frustum of $\gamma = 25^\circ$, $n_f = 5$
40. Total Collapse Configuration for a Conical Frustum of $\gamma = 25^\circ$, $n_f = 5$
41. Inside View of the Constructed Total Collapse Pattern, $\gamma = 25^\circ$, $n_f = 5$

Contracts

42. Inside View of Collapsed Conical Frustum, Obtained Experimentally, $V_o = 20$ ft/sec, $\gamma = 25^\circ$, $n_f \approx 5$
43. Outside View of a Collapsed Conical Frustum, Obtained Experimentally, $V_o = 20$ ft/sec, $\gamma = 25^\circ$, $n_f \approx 5$
44. Projectile
45. Initial Alignment of the Specimen and Projectile in the High Velocity Impact Facility
46. Instrumented Cylindrical Shell Shown Mounted on its Carriage
47. Calculated Velocity - Chamber Pressure Characteristic of the High Velocity Impact Facility - 14 lb. Projectile
48. Strain Records - Test No. HV - 4, $V_o = 216$ ft/sec, $h = .016$ in
49. Strain Record - Test No. HV - 4, $V_o = 216$ ft/sec, $h = .016$ in
50. Strain Record - Test No. HV - 5, $V_o = 271$ ft/sec, $h = .016$ in
51. Deceleration Record - Test No. HV - 5, $V_o = 201$ ft/sec, $h = .016$ in
52. Specimen HV - 5 After Impact, $V_o = 201$ ft/sec
53. Strain Record - Test No. HV - 6, $V_o = 225$ ft/sec, $h = .016$ in
54. Strain Record - Test No. HV - 6, $V_o = 225$ ft/sec, $h = .016$ in
55. Deceleration Record - Test No. 6, $V_o = 225$ ft/sec, $h = .016$ in
56. Strain Records - Test No. HV - 7, $V_o = 271$ ft/sec, $h = .016$ in
57. Strain Record - Test No. HV - 7, $V_o = 271$ ft/sec, $h = .016$ in
58. Deceleration Record - Test No. HV - 7, $V_o = 271$ ft/sec, $h = .016$ in
59. Specimen HV - 7 After Impact, $V_o = 271$ ft/sec
60. Specimen HV - 8 After Impact, $V_o = 392$ ft/sec
61. Rigid Body Structure for Non-Rigid Impact Experiments
62. Shell Structure for Non-Rigid Impact Experiments (Showing Some Collapse at Plate A End)
63. Force - Time Curve for the Rigid Body - Impact on Dry Sand, $V_o = 23$ ft/sec - Test No. S-4, Plate B.
64. Force - Time Curves for the Rigid Body - Impact on Dry Sand, $V_o = 23$ ft/sec. - Test No. S-5
65. Force - Time Curves for the Rigid Body - Impact on Dry Sand, $V_o = 23$ ft/sec - Test No. S-6
66. Comparison of Deceleration Measurements of a Rigid Body Impacting on Dry Sand, $V_o = 23$ ft/sec
67. Force - Time Curves for the Rigid Body - Impact on Dry Sand, $V_o = 33$ ft/sec
68. Force - Time Curves for the Rigid Body - Impact on Dry Sand, $V_o = 43$ ft/sec
69. Force - Time Curves for the Shell Structure - Impact on Dry Sand, $V_o = 23$ ft/sec
70. Effect of Shell Buckling on the Deceleration of Plate (B) - Showing a Comparison with the Deceleration of Plates (A) and (B) of the Rigid Body - Vertical Impact into Dry Sand, $V_o = 23$ ft/sec
71. Effect of Shell Buckling on the Deceleration of Plate (A), $V_o = 23$ ft/sec
72. Specimen S-16 After Impact into Dry Sand at 23 ft/sec (.008 in Shell, Impacted End Down)
73. Deceleration Records - Test S-17 ($h = .016$ in, $V_o = 23$ ft/sec)

Contents

74. Deceleration Records - Test S-19 ($h = .008$ in, $V_0 = 33$ ft/sec)
75. Effect of Shell Buckling on the Deceleration of Plate (B) - Showing a Comparison with the Deceleration of Plates (A) and (B) of the Rigid Body - Vertical Impact into Dry Sand, $V_0 = 33$ ft/sec
76. Specimen S-19 After Impact into Dry Sand at 33 ft/sec (.008 in Shell, Impacted End Down)
77. Deceleration Records - Test S-14 ($h = .016$ in, $V_0 = 33$ ft/sec)
78. Specimens S-14 (Left) and S-13 (Right) After Impact into Dry Sand at 33 and 43 ft/sec (.016 in. Shells)
79. Deceleration Records - Test No. S-15 ($h = .008$ in, $V_0 = 43$ ft/sec)
80. Effect of Shell Buckling on the Deceleration of Plate (B) Showing a Comparison with the Deceleration of Plate (B) of the Rigid Body - Vertical Impact into Sand, $V_0 = 43$ ft/sec
81. Specimens S-15 (.008 in) and S-13 (.016 in) After Impact into Dry Sand at 43 ft/sec
82. Deceleration Records - Test No. S-13 ($h = .016$ in, $V_0 = 43$ ft/sec)
83. Inside View of Specimen S-13 Showing Permanent Small Amplitude Ring Buckles over a Portion of its Circumference
84. Deceleration Records - Test No. W-2A for the Rigid Body - Impact into Water, $V_0 = 43$ ft/sec
85. Deceleration Records - Test No. W-7 ($h = .008$ in, $V_0 = 43$ ft/sec)
86. Deceleration Records - Test No. W-8 ($h = .008$ in, $V_0 = 43$ ft/sec)
87. Effect of Shell Buckling on Deceleration of Plate (B), Showing a Comparison with the Deceleration of Plate (B) of Rigid Body - Vertical Impact into Water, $V_0 = 43$ ft/sec, $h = .008$ in
88. Specimens W-7 (.008 in) and W-11 (.016 in) After Impact into Water, $V_0 = 43$ ft/sec
89. Specimen W-8 (.008 in) After Impact into Water, $V_0 = 43$ ft/sec
90. Deceleration Records - Test No. W-9 ($h = .016$ in, $V_0 = 43$ ft/sec)
91. Deceleration Records - Test Nos. W-10 and W-11 ($h = .016$ in, $V_0 = 43$ ft/sec)
92. Effect of Shell Buckling on the Deceleration of Plate (B), Showing a Comparison with the Deceleration of Plate (B) of the Rigid Body - Vertical Impact into Water $V_0 = 43$ ft/sec, $h = .016$ in
93. Specimens W-9 and W-11 (.016 in Shell) After Impact into Water at 43 ft/sec
94. Dimensionless Axial Stress vs. Dimensionless Lateral Deflection for a Circular Cylindrical Shell Subject to an Axial Force which Varies Linearly with Time
95. Dimensionless Axial Stress vs. Dimensionless Lateral Deflection for a Circular Cylindrical Shell Subject to an Axial Force which Varies Linearly with Time
96. Dimensionless Axial Stress vs. Dimensionless Lateral Deflection for a Circular Cylindrical Shell Subject to an Axial Force which Varies Linearly with Time
97. Dimensionless Axial Stress vs. Dimensionless Lateral Deflection for a Circular Cylindrical Shell Subject to an Axial Force which Varies Linearly with Time

Contracts

98. Dimensionless Axial Stress vs. Dimensionless Lateral Deflection for a Circular Cylindrical Shell Subject to an Axial Force which Varies Linearly with Time
99. Dimensionless Axial Stress vs. Dimensionless Lateral Deflection For a Circular Cylindrical Shell Subject to an Axial Force which Varies Linearly with Time
100. Dimensionless Axial Stress vs. Dimensionless Lateral Deflection For a Circular Cylindrical Shell Subject to an Axial Force which Varies Linearly with Time
101. Dimensionless Axial Stress vs. Dimensionless Lateral Deflection For a Circular Cylindrical Shell Subject to an Axial Force which Varies Linearly with Time
102. Dimensionless Axial Stress vs. Dimensionless Lateral Deflection For a Circular Cylindrical Shell Subject to an Axial Force which Varies Linearly with Time
103. Dimensionless Axial Stress vs. Dimensionless Lateral Deflection For a Circular Cylindrical Shell Subject to an Axial Force which Varies Linearly with Time
104. Effect of Internal Pressurization on the Buckling Stress of a Circular Cylindrical Shell Subject to a Constant Velocity of End Shortening ($V_0 = 11.5$ ft/sec, $h = .016$ in, Al)
105. Effect of Internal Pressurization on the Buckling Stress of a Circular Cylindrical Shell Subject to a Constant Velocity of End Shortening ($V_0 = 23$ ft/sec, $h = .016$ in, Al)
106. Effect of Internal Pressurization on the Buckling Stress of a Circular Cylindrical Shell Subject to a Constant Velocity of End Shortening ($V_0 = 11.5$ ft/sec, $h = .016$ in, Al)
107. Effect of Internal Pressurization on the Buckling Stress of a Circular Cylindrical Shell Subject to a Constant Velocity of End Shortening ($V_0 = 23$ ft/sec, $h = .016$ in, Al)

Contrails

TABLES

TABLE	PAGE
1. Description of Phase I Tests	23
2. Pressurized Cylindrical Shell Test Results	27
3. Pressurized Conical Test Results	31
4. Description of High Velocity Impact Tests	41
5. High Velocity Impact Test Results	44
6. Description of Sand Impact Tests	46
7. Description of Water Impact Tests	46
8. Sand Impact Test Results	51
9. Water Impact Test Results	54
10. Comparison of Theoretical and Experimental Results-Phase I	72
11. Comparison of Theoretical and Experimental Results-Phase III	73

Contrails

SYMBOLS

D	Flexural rigidity of shell $D = \frac{Eh^3}{12(1-\nu^2)}$
D, D'	Diameters of conical Sections
E	Young's Modulus
E _{k1} , E _{k2}	Kinetic Energy
e	End shortening
f ₀ , ψ ₀	Initial deflection parameters of shell
f ₁ , ψ ₁ , g ₁	Deflection parameters of shell (time dependent)
h	Thickness of cylindrical shell
K ⁺ , K ⁻	Aspect ratios of the triangular buckles corresponding to the (+) and (-) surfaces respectively
k	Bulk modulus of the shell material
L	Length of cylindrical shell
L _{cr}	Critical length
l _x ⁺ , l _x ⁻	Axial (profile) lengths of the triangular buckles corresponding to the (+) and (-) surfaces respectively
l _y	Circumferential half length of the triangular buckle
M	Mass of impacting object
m	Number of half waves in axial direction of shell
n	Number of half waves in circumferential direction of shell
n _f	Number of full circumferential buckle waves
P	Total axial force acting on shell
q	Internal pressure intensity in shell
R	Radius to middle surface of cylindrical shell
t	Time
t _{cr}	Critical (buckling) time
U _B , U _M	Strain energies
U _P , U _q	Potential energies

Contraails

\bar{U}, \bar{W}	Dimensionless coordinates of the inextensional surface profile
u, v, w	Components of displacement of a point in the middle surface of the shell in the $x, y,$ and z directions respectively
V	Elasto-plastic work per unit volume
V_0	Impact velocity
w_0	Initial imperfection of the shell (a function of x and y)
w_1	Total deflection of the shell (a function of x and y)
w	Net deflection of the shell ($w = w_1 - w_0$)
x_i, y_i	Coordinates of the centroid of section i about the reference vertical axis.
x, y, z	Orthogonal coordinates in the directions along a generator around the circumference, and in the inward radial direction respectively
α, β	Profile angles of the (+) and (-) surfaces respectively (or see definitions following Equation (21))
γ	Semi vertex angle of conical shell, also Equation (55)
δ	Total radial deviation of actual shell from reference shell, also Equation (55)
Δ	Radial difference between actual and mean surfaces
$\Delta(\theta)_i$	Circumferential waviness imperfection
$\Delta(i)_\theta$	Longitudinal waviness imperfection
ϵ	Unit end shortening
ϵ_s	Strain at which yielding occurs in uniaxial tension
ϵ_x, ϵ_y	Normal strains in the middle surface of the shell
ϵ_{xy}	Shearing strain in the middle surface of the shell
ζ	Dimensionless lateral deflection ($\zeta = \frac{f_1 + \psi_1}{2}$)
η	Defined in Equation (53)
θ	Circumferential position coordinate, also angle subtended by one circumferential wave at the center of conical blank

Contraails

$\left. \begin{array}{l} \kappa_1 \\ \kappa_2 \end{array} \right\}$	Curvature, defined in Equation (49)
λ	Central angle, defined in Equation (49a)
μ	Prefix signifying 10^{-6} units
ν	Poisson's ratio
Ξ	Dilatation
ρ	Mass density of shell material
ρ_i	Generalized coordinates
σ	Mean axial stress in shell
σ_{cl}	Classical static buckling stress of an unpressurized cylindrical shell
σ_{cr}	Critical (buckling) stress
σ_p	Static buckling stress of a cylindrical shell pressurized at the test pressure
σ_x, σ_y	Normal stresses in the middle surface of the shell
$\bar{\sigma} = \frac{\sigma R}{Eh}$	Dimensionless axial stress parameter
τ	Twist, defined in equation (49)
τ_{xy}	Shearing stress in the middle surface of the shell
ϕ	Airy function of the membrane stresses in the shell

1. INTRODUCTION

Investigations dealing with the buckling of thin cylindrical and conical shells subject to an axisymmetric axial impact were performed under a previous contract with the Flight Dynamics Laboratory, RTD. These studies consisted of experimental and theoretical efforts directed toward obtaining a qualitative and quantitative understanding of the dynamic buckling behavior of such shells under a variety of conditions. The conditions studied were (1) loading due to impact with a rigid body, (2) loading due to impact with a fluid body (water), and (3) initial internal pressure. In addition, methods of increasing the capability of shells to dissipate energy when subjected to an axial impact were studied. The results of the program are summarized in Reference 18.

The program described in this report was a continuation of the previous one. Its objectives were: (1) to extend the previous experimental and analytical efforts expended on the rigid impact of cylindrical and conical shells in order to obtain a prediction of the behavior from the initiation of impact to the onset of plasticity, (2) to study the behavior of shells subjected to rigid impact velocities high enough to produce plastic waves in the shell and to formulate a mechanism of the loading and the mode of response, and (3) to continue the study of shells subjected to longitudinally non-rigid impact so that prediction, at least semi-empirically, of the response to a given impact medium can be accomplished.

The program was divided into three phases, according to the aforementioned objectives.

Phase I - Rigid Impact

In this phase an examination of the effect of certain often undefined conditions on the buckling behavior was made. The conditions considered were initial geometrical imperfections, end support, and non-uniformly distributed axial loading. Initial imperfections of cylindrical shells were measured using a system specifically designed for this program. A method was found to reduce the measured imperfections to two significant components. The effect of edge conditions was studied experimentally and the end conditions considered were the free edge and a free edge containing an internal circular support which prevented inward lateral displacements in a region near the end. Non-uniformity of the axial loading was achieved by impacting obliquely on the end of the shell with a prescribed angle. In addition to examining the effect of this condition on the buckling behavior it was required to determine the maximum angle of obliquity for which an orderly and repeatable collapse would occur. This latter objective is related to the use of shells as energy dissipation devices in landing vehicles.

The term "rigid impact" as used herein means an impact between the shell and a body in which all deformations are confined to the shell. Similarly the term "non-rigid impact" applies to those impacts in which

Manuscript released by authors August 21, 1964 for publication as an RTD Technical Documentary Report.

Contrails

significant displacements are imparted to the impacted body as well as to the shell.

Phase II - High Velocity Impact

The purpose of this effort was to explore through experimentation the mode of response of cylindrical shells to rigid impacts at velocities of several hundred feet per second. According to the hypothesis of Reference 8, a sufficiently high velocity of impact should produce extensional or "ring" buckling and collapse modes in a shell which, due to its thinness, would respond at lower velocities in the inextensional or "triangular" mode. It was desirable to determine whether this is actually so and whether the energy dissipation capacity is increased due to the higher energy mode of response. Another aim was to determine a mechanism of loading a metal shell structure under a velocity sufficiently high to produce plastic strains in the loading wave.

Phase III - Non-Rigid Impact

For the case of rigid impact, the stresses to which a shell is subjected can be significantly large compared to the static buckling stress even at low impact velocities (for instance, less than 50 feet per second for a shell with $R/h = 250$). Hence, buckling and collapse invariably occur, and all of the axial displacements are confined to the shell. When the impacted medium is deformable, however, lower stresses are introduced into the shell, depending on the resistance offered by the medium as it is penetrated. As a result, buckling may or may not occur.

The purpose of this investigation was to determine what the buckling behavior of the shell is under conditions of impact with deformable media, to measure buckling loads, and to evaluate the effectiveness of the buckling in reducing the forces produced by a rigid body impact with the same medium. It was further required to obtain a prediction of the buckling behavior with respect to a given medium.

Experimental efforts were expended in all three phases of the program and, in addition, related theoretical investigations were performed on the following three problems. Problem (1) was a non-linear dynamic buckling analysis of a circular cylindrical shell with internal pressure subject to an axial loading prescribed as a function of time. Problem (2) was a very large deflection analysis of a cylindrical shell under a constant velocity of end displacement. The aim of this problem was to study the effects of plasticity on the dynamic response. Problem (3) was the study of buckling and collapse modes of conical shell frusta having negligible wall flexural rigidity.

2. LITERATURE SURVEY

During the past three decades enormous progress has been made in the field of elastic instability of thin shells of various shapes. This is particularly true for the case of static loadings of various geometries, such as shallow spherical caps, cylindrical shells, and conical shells. For these problem areas it is now well recognized that it is necessary to employ a finite deformation theory which incorporates a consideration of the initial imperfections present in the shell in order accurately to predict buckling loads in agreement with experimental evidence. Rather complete resumes of finite deflection buckling analyses of statically loaded elastic shells are to be found in the survey papers due to Fung and Sechler (Ref. 1) and Thielemann (Ref. 2).

Interest in the problem of dynamic buckling of thin shells has arisen only during the past few years. Perhaps the first effort in this direction was made by Schmitt (Ref. 3) who conducted an experimental investigation of thin walled unstiffened aluminum shells dynamically collapsed by the axial impact of a rigid mass. The maximum impact velocity achieved was approximately 500 inches per second. On the basis of these tests it was possible to conclude that (a) the energy absorbed in the dynamic buckling is greater than that absorbed in the static case, and (b) the ratio of these energies increases with increasing impact velocity over the range of velocities considered.

Pioneering analytical work in the field of dynamically loaded shells was carried out by Volmir (Refs. 4 and 5). He considered a shallow circular cylindrical panel subjected to a rapidly applied compressive loading along its generators. The panel was assumed to have hinged edges and the ends of the panel were brought together at a constant velocity which was taken to be much less than the velocity of sound in the material. This assumption permitted the neglecting of inertia terms corresponding to displacements in the plane of the middle surface. For the particular geometry considered, it was found that the dynamically loaded panel was able to sustain a load sixty-five per cent greater than the upper critical value corresponding to static analysis. After this load was sustained, there occurred an abrupt drop in load followed by an oscillation of the panel. Actually, at the end of the drop in load for a very short interval of time the load became negative, corresponding to an extension of the panel.

An extension of the work described in Reference 5 to the case of a closed circular cylindrical shell subject to dynamically applied hydrostatic pressure or axial compression is due to Agamirov and Volmir (Ref. 6). The authors apply finite deflection analysis together with a consideration of initial imperfections and solve the governing equations by the Galerkin approximation for the case when the lateral pressure increases linearly with regard to time. Dimensionless deflection-time relations are presented from which the loss of shell stability can be determined. It is

Contrails

however, to be noted that in this study the authors greatly simplified the analysis by taking the values of certain parameters to be the same as given by static analysis. This of course introduces an error of unknown magnitude. For the case of lateral pressure increasing at a rate of 2000 atmospheres per second it was found that the dynamic buckling load was approximately twice the upper critical load found from static analysis. No numerical results were presented for the case of axial compression of the cylindrical shell.

An experimental investigation of buckling of cylindrical shells by dynamically applied hydrostatic pressure has been reported by Volmir and Mineev (Ref. 7). The shells were duraluminum, having a radius-thickness ratio of 112. For the case of lateral pressure increasing at a rate of 2000 atmospheres per second it was found that the dynamic buckling load was 2.66 times the upper critical load found from static analysis. For lateral pressures applied even more rapidly this dynamic overload coefficient increased up to a value of 3.98 when the lateral pressure increased at a rate of 6500 atmospheres per second. Also, the number of waves around the circumference increased as the loading rate increased. It is to be observed that this dynamically applied hydrostatic pressure was applied to the specimen by suddenly opening a valve between a high pressure fluid reservoir and a lower pressure fluid surrounding the cylinder. Inspection of the experimental apparatus reveals that the dynamic pressure along the length of the cylindrical shell cannot be constant and hence an error of some unknown magnitude is present in these tests.

In 1960 Coppa (Ref. 8) presented a phenomenological theory for the buckling of a circular cylindrical shell subject to an axially symmetric impact at one end. According to this theory when a cylindrical shell is struck on one end by a rigid, infinite mass with a velocity V a stress wave travels from the struck end at the dilatational wave velocity c . When the wave front has traveled a distance L_{cr} from the struck end, instability will occur in this region, provided that the velocity V is sufficiently great. This instability configuration may be of two types, either an axisymmetric ring-type buckle, or a triangular configuration depending upon the ratio L_{cr}/D where D is the diameter of the cylinder. Once instability has initiated, the unstable region is unable to transmit the axial force which initiated instability and hence the cylindrical region beyond the critical region remains stable. It was further demonstrated that the postbuckling behavior for triangular buckling can be described by a continuous set of stable inextensional configurations having progressively shorter axial lengths, successively lower axial resistances, and the same number of circumferential waves as the critical configuration.

An analytical solution of the problem of a long circular cylindrical shell subject to a suddenly applied radial load which immediately begins to decrease in accordance with a negative exponential relationship has

been offered by Slepov (Ref. 9). The solution is formulated in terms of an assumed Fourier series expansion for stresses and deformations but no numerical data are presented. The problem of stability of a long cylindrical shell submerged in a liquid and suddenly subjected to an increase in lateral pressure has been examined on an energy basis by Pertsev and Kadashevich (Ref. 10). A simplified analysis based upon linearized small deflection theory for the case of a thin cylindrical shell with hinged ends when one end is given a constant velocity and the other end is immovable has been presented by Blokhina (Ref. 11). The shell is assumed to have initial imperfections in the form of ring-type corrugations symmetric around the circumference and only axisymmetric deformations are considered. The analysis based upon these conditions led the author to conclude that the greater the velocity of loading, the smaller will be the amplitude of lateral deflection. Another study based upon linearized small deflection theory is due to Yao (Ref. 12). It treats the stability of a long cylinder under radial pressure of short duration. The equations of motion are reduced to a mass-spring system having a single degree of freedom. It is shown that if the magnitude of the pressure is greater than the static buckling pressure, the displacement will increase monotonically as loading duration becomes long. It is also found that the cylinder can withstand an impulsive loading greater than the static buckling pressure if the loading duration is very short compared to the free vibration period of the cylinder in its first mode.

A refinement of the analysis presented in Reference 6 has been offered by Kadashevich and Pertsev (Ref. 13). In this work the authors again consider the effect of a uniformly distributed transverse dynamic load on a cylindrical shell. However, in contrast to reference 6 here not only is the inertia of the formation of buckling waves taken into account but also the inertia of axisymmetric compression of the shell. This permits the authors to obtain the equations of motion of the shell for the case of more rapid application of the load than is admissible in the system of equations given in Reference 6. Lagrange's equations are employed to obtain the differential equations of motion and these are solved by digital computer techniques.

The problem of impulsive pressure acting on a long elastic cylindrical shell presumed to be in a state of plane strain has been considered by Goodier and McIvor (Ref. 14). The pressure is assumed to impart a uniform initial radial velocity to all elements of the shell thereby producing a purely radial motion in a "breathing" mode. However, this mode can be unstable with respect to small departures from uniformity and the energy of the breathing mode can be quickly transferred almost wholly into the one or two flexural modes whose frequencies are closest to the half-frequency of the breathing mode. Such a frequency implies a relatively high flexural mode. The authors also consider the case of an impulsive pressure sufficiently great to cause inelastic inward flow.

Contrails

Plastic strain hardening and visco-plastic laws are considered. The motions found in all cases have one interesting common characteristic, i. e. a series of wrinkles may develop around the entire circumference. A theory has been postulated by Abrahamson and Goodier (Ref. 15) to explain this wrinkling which has also been observed experimentally.

The stability of a thin cylindrical shell with a constant axial pre-load and subject to dynamic lateral pressure has been investigated by Koval and O'Neill (Ref. 16). The study investigates the coupling between an axisymmetric ring type mode and the asymmetric mode into which the shell will initially buckle. It is demonstrated that under certain conditions when the ring mode is dynamically excited it may be possible to induce buckling at a dynamic critical pressure that is smaller than the static buckling pressure for shells having radius-thickness ratios less than 200. The authors also reported an experimental investigation in which an electrostatic loading system was applied to coated mylar cylinders for the purpose of producing high rates of lateral loading. The coating consisted of an aluminum film that was vacuum deposited on the inside of the mylar specimen. Another recent study is due to Roth and Klosner (Ref. 17) who have refined the analysis appearing in Reference 6 to include more free parameters.

Finally, a recent report by Coppa and Nash (Ref. 18) presents an experimental as well as analytical approach to the problem of buckling of thin elastic cylindrical shells due to axial impact. The experiments indicated that buckling of a cylindrical shell is initiated during the first passage of the axial compression stress wave due to the initial impact when the impact velocity is sufficiently high. Another significant experimental result obtained is that the asymmetrical form of shell buckling occurs as a result of smooth transition from the symmetrical or ring form of buckling in some thin cylindrical shells subjected to an axially symmetric axial impact. The analytical phase of this study consisted of an extension and refinement of the finite deflection analysis due to Volmir. It indicated that both the upper critical stress and the number of circumferential waves increase and the time to initiate buckling decreases with increasing velocity of impact. These trends are in agreement with the phenomenological theory due to Coppa (Ref. 8).

The past few years have also seen several interesting contributions to the problem of dynamically loaded shallow spherical shells. The first of these, due to Suhara (Ref. 19), treated such a shell subject to a suddenly applied uniform pressure of infinite time duration. Non-linear strain-displacement relations were employed and only the inertial term corresponding to the direction normal to the shell middle surface was retained. A buckling configuration geometrically similar to that found in the case of static loading was employed and a solution to the dynamics equations was obtained by a variational method with the equations being solved on an analog computer. The study was of a rather qualitative nature since the

author concluded that a more accurate deflection function should have been employed.

In 1962 Humphreys and Bodner (Ref. 20) employed a nonlinear analysis of this same problem and formulated the critical condition of the dynamic system through an energy method. Although the behavior of the dynamic response was not obtained by this method, the general relation between the geometric shape and critical impulses as well as critical deflections was obtained rather simply. In that same year Budiansky and Roth (Ref. 21) examined the behavior of a shallow spherical shell subject to an impulsive loading uniform over the surface but of various time durations. Nonlinear finite deflection analysis was employed and the authors integrated a five degree of freedom dynamic system numerically to obtain the buckling condition.

The problem of transient response of a shallow spherical shell subject to dynamic loads with arbitrary time history has been investigated by Koval and Bhuta (Ref. 22). These authors employed nonlinear finite deflection theory and approached the problem from the standpoint of expansion of deflections in terms of eigenfunctions of the shell. A digital computer program was presented which gives dynamic response for such shells with a variety of boundary conditions and also with a consideration of small damping.

More recently the problem of dynamic buckling of a clamped edge shallow spherical shell subject to impulsive uniform normal pressure has been examined by Ho and Nash (Ref. 23) and Ho (Ref. 24). These studies were based upon use of nonlinear finite deflection relations, and sought a transitional point for an originally stable system after which the system would be unstable. This of course represents the critical condition for the structure. The dynamic characteristics of the system were considered and it was shown that the study of the stability of the dynamic system is essentially equivalent to the condition that the system moves on the separatrix in the phase plane. Loss of stability as employed here has the same nature as the usual dynamic buckling criteria, i. e. the characteristic deformation undergoes a severe change. This criteria is readily extended to multiple degree-of-freedom systems. Specific cases of a clamped edge shallow spherical shell subject to (a) suddenly applied pressure which is constant with respect to time, or (b) uniform pressure linearly increasing with respect to time were treated on the basis of this criteria.

A problem area closely associated with the dynamic buckling treatments mentioned above is that of instability corresponding to autoparametric excitation in nonlinear oscillations. In this type of problem the objective is to construct a range of parameters which characterizes the impulse imparted to the thin shell and in the presence of which snap-through buckling of the shell does not occur. For example, a long cylindrical shell (if assumed to be in a state of plane strain) when subjected to a pressure

loading of sufficient magnitude buckles statically into an oval shape. If the loading is dynamic, sinusoidally varying pressure for example the shell may still buckle in the sense that the character of the motion may substantially alter as time increases. If the frequencies involved are sufficiently high the dynamic terms must be included and this constitutes a problem in forced vibrations. The term dynamic stability is often employed to characterize this autoparametric phenomena but it should be understood that the significance of the term is somewhat different than the sense in which it has been previously employed in this discussion.

Linearized small deflection problems involving autoparametric oscillations are treated rather completely in a book by Bolotin (Ref. 25). The impulses considered there are usually of a harmonic type superposed on a constant load. The geometries treated include plates, panels, cylindrical and spherical shells. The finite deflection problem of a cylindrical panel subject to a normal impulse which decays exponentially has been investigated by Bolotin et. al. (Ref. 26). Autoparametric oscillations of this same structure when subjected to a pulsating longitudinal pressure producing finite deflections have been investigated by Mishenkov (Refs. 27 and 28). Damping was considered in these treatments. Pulsating radial pressure applied to a circular cylindrical shell undergoing finite deflections creates parametric oscillations which have been investigated by Gnumi (Ref. 29). This same author has also considered parametric oscillations of anisotropic shells (Ref. 30). The problem of autoparametric oscillations of a circular cylindrical shell loaded by pulsating longitudinal pressure has been treated by Bolotin and Boychenko (Ref. 31). One of the very few experimental investigations of this phenomena has been reported (Ref. 32) for the case of cylindrical shells subjected to pulsating lateral pressure. A treatment of dynamic stability for cylindrical shells subject to axial or radial loads for the case of small deflections has been presented by Yao (Ref. 33). The regions of instability and stability are established directly in terms of the shell geometry, the load intensity, and frequency. The results indicate that a cylinder designed according to the static buckling load can withstand an additional periodic load. It was found that the ratio of additional periodic load to the static buckling load was greater for a thin cylinder than for thicker cylinder of the same radius. It was also found that the resistance of a cylinder to loads in excess of the static buckling load increases with increasing frequency of loading.

PART I. EXPERIMENTAL PROGRAM

3. EXPERIMENTAL FACILITIES

3.1 Pressurized Shell Impact Tester

The apparatus on which experiments with pressurized shells under rigid impact are performed was described in Reference 18 and for completeness a description is included herein. Referring to Figure 1 a cross beam assembly is guided vertically along a one inch vertical shaft which is held under tension via two spherical bearing seats. A carriage containing two low friction ball bushings connects the cross beam to the shaft thereby providing accurate, tight positioning and an extremely low friction guidance. An electromagnet which can be raised and lowered by means of a winch operated cable system, provides the force for lifting the cross beam assembly and for quickly releasing it. At one end of the cross beam, the impact head is mounted via a special release pin and at the other end, a counterweight is similarly attached. A mechanical release mechanism, one at each end of the cross beam releases the impact head and counterweight together from the crossbeam. Mounted centrally with the vertical shaft is a shock absorbing system the upper end of whose shaft contains a plastic foam buffer. After release, the crossbeam assembly containing the impact head and counterweight falls freely along the shaft while restrained from rotation by a guide wire. Prior to impacting on the foam buffer, the release mechanism is actuated, the point of release being held as close as practicable to the impact end of the cylinder. Prior to striking the specimen, the impact head impinges against three pivoted rods either of which triggers the oscilloscope traces. Once released, the impact head is unrestrained and therefore free to undergo rotations. By careful adjustment, however, the impact head can be controlled to be coplanar with the specimen end to an acceptable degree at the initiation of impact.

The maximum velocity obtainable at impact is 43.5 ft/sec. and the allowable weight of the impact head, limited by the present magnet, is approximately fifty pounds.

3.2 Modified Pressurized Shell Impact Tester

A simpler modified version of the above described apparatus shown in Figure 2 results in a number of advantages, although the specimen size is limited to eight inches diameter. The advantages are (1) the impact head is restrained from rotating before and after impact, (2) the impact head is retained on the apparatus (3) the maximum allowable weight of the impact head is increased to 100 pounds, (4) the test set up is considerably simpler and (5) the impact velocity is increased to 46 ft/sec. The impact head assembly was designed with a center of gravity that is offset from the vertical guide by a distance of 4 inches. The specimen to be tested is

mounted so that its central axis passes through the center of gravity of the head. Upon impact, the resultant of the head inertia forces is in equal opposition to and aligned with the resistance force of the impacted shell. Consequently, the moment transmitted to the guide shaft is negligible, as long as the alignment is good.

3.3 Non-Rigid Impact Tester

With this apparatus (shown in Figure 3) which is a modification of the described above, shell structures may be impacted into deformable media such as fluids, soils, or any other natural or simulated penetrable media. For fluid tests, a tank, 4 feet in diameter and 50 inches in length, is placed centrally beneath one of the release points. The specimen together with its mounting fixtures is mounted on the cross beam and is made to impact into the tank in the same manner as previously described for the impact head. The tank contains a large window of 1/2 inch thickness Plexiglass, through which high speed pictures of the specimen can be taken during impact.

For tests with solid media, the tank may also be used, but it was found preferable to use a plywood box container in order to prevent abrasion of the Plexiglass window by solid particles.

The maximum velocity and allowable specimen assembly weights are approximately the same as for the pressurized shell impact tester.

3.4 High Velocity Structural Impact Facility

This facility was designed to test structures of appreciable model size under the action of high velocity, heavy mass impact. The kinetic energy available at impact is nominally 55,000 lb. ft. with growth potential up to 150,000 lb. ft. The velocities obtainable depend on the mass which is propelled. As an example, a 14-pound projectile can be given a nominal velocity of 500 ft/sec. The apparatus is shown partly disassembled in Figure 4. The driving element is a pneumatic cylinder which suddenly discharges a volume of high pressure gas when a diaphragm is ruptured. The expanding gas accelerates the projectile through an accurately honed tube whose length and bore diameter are 18 feet and 7.09 inches respectively.

The specimen to be tested is mounted on a housing which is mounted on rollers and thereby is free to move along the direction of impact. On the end of the housing facing the impact is a buffer section whose purpose is to eliminate projectile rebound during the final process of arresting the projectile. The specimen, which may be as large as 6 inches in diameter and several feet in length, protrudes through the buffer section and is exposed to the impact of the projectile. During the test, the specimen retracts into the protection of the buffer housing and is thereby protected against any further damage. The energy stored in the system after the completion of the test is absorbed by a hydraulic shock absorber.

Contrails

This apparatus features accuracy of alignment of the specimen and projectile at impact, a section for taking high speed motion pictures, and a completely enclosed design which allows safe operation in the laboratory.

4. INSTRUMENTATION

The principal quantities that were required to be measured were the axial resistance of the shell to the impact head, the critical buckling stress and time, and the postbuckling load history. It was further desired to obtain visual records of the overall surface of the shell as it responded to the impact. A brief description of the instrumentation that was used to obtain and record the required measurements follows:

4.1 Accelerometers

Accelerometers were used to measure the total axial resistance of the shell as it varied with time. This was done by mounting the accelerometer rigidly within the impact head and measuring the acceleration of the head during impact. The acceleration is due to the sum of the axial resistance of the shell and the force of gravity. The accelerometers that were used were (1) Gulston AA-25 - Oil damped piezoelectric crystal accelerometer with a usable frequency up to 13.6 KC, a damping factor of .65 critical, and a sensitivity of .12 mv/g. (2) Endevco 2225 - Piezoelectric crystal accelerometer with a resonant frequency of 80 KC and a sensitivity of .5 mv/g.

4.2 Strain Gages

The buckling stress and the time at which buckling is initiated was measured by strain gages mounted to the shell wall in opposite pairs so as to cancel bending. The measurement of the buckling stress was considered to be valid when three pairs, equally spaced about the circumference and located sufficiently distant from the region of buckling, showed reasonably similar stress-time records. The buckling stress-time curve was taken as the average of the three records. The strain gages also yielded the postbuckling stress history.

The gages used were Budd Metalfilm types C12-1X1-32A (1/32 in. gage length) and C12-111 (1/16 in. gage length). The bonding material was Eastman 910 cement.

4.3 Photography

A Fastax motion picture camera having a maximum framing rate of 16,000 frames per second was used to obtain a visual record of the overall deformational behavior of the shell during the impact.

4.4 Recording

All acceleration and strain data were recorded with oscilloscopes (Tektronix model nos. 531 and 535) equipped with single sweeps and Polaroid cameras.

4.5 Triggering

Oscilloscope sweeps were initiated by a variety of trigger systems, depending on the type of test. In each case, the impacting body made electrical contact with one or several pivoting trigger rods which were set at a specified distance from the impacted body. In this manner, the initial sweep of the scope was at a zero value of the quantity to be measured.

5. PHASE 1 - RIGID IMPACT

5.1 Apparatus

5.1.1 Pressurized Shell Mounting Fixtures

One of the fixtures that were used for mounting the shells for testing is shown in Figure 5. It has three mounting surfaces, an outer one for mounting 12° semi-vertex angle cones, a middle one for mounting 5° semi-vertex angle cones and inner one for mounting cylinders. On the inner most ring, the Mylar pressure membrane is clamped. Sets of four segmented clamps are used to fix the shells securely to the fixture at their bases. The central hole at the middle leads to a set of six one inch diameter holes that run radially out through the sides of the fixture, thereby providing for venting of the interior of the shell.

At the center bottom of the fixture, a bracket for mounting the membrane support chain is located. This is shown in Figure 6 together with a shell and membrane as they appear in the pressurized configuration.

5.1.2 Strain Gage Attachment Fixture

In order to mount strain gages accurately in any part of the shells used in this program, it became apparent in the previous program that some kind of fixture was necessary. As a result a fixture was built which has since proven its value many times. The fixture is shown in Figure 7. It consists essentially of two parallel arms having an open end and made in one rigid piece. Near the open end, each arm has a hole which is aligned accurately with the other. Through each hole is a circular plug that is restrained from rotation but free to translate in the hole. A cam mechanism actuates the translation of one plug and a micrometer head the other. The arm assembly fits in a slot and is perpendicular to a circular plate and can be positioned with respect to the plate by a clamping nut. In using the fixture, the circular plugs are removed from the arms and strain gages are attached to them with a material like soft wax which will not adhere strongly to the gages. The gages are positioned on the plugs with the aid of scribed cross marks that indicate the axial and circumferential directions. Strain gages adhesive is now placed on the shell at the required location and the entire assembly less the plugs is placed on the shell, via the arms straddling the shell wall. The assembly is attached to the shell when the end of the shell fits on the shoulder of the circular plate. The arm assembly is finally positioned by sliding the arm assembly in the circular plate and locking it. At this point, the plugs with strain gages attached are inserted in their respective holes and the cam turned until the gage makes contact with the inner wall surface with light pressure. Then the micrometer head which is always used outside the shell is screwed in until the gage makes contact with the outer

Contrails

surface of the wall and slips on via its torque limiting ratchet. The contact pressure is now a firm 1-2 pounds, the value recommended by the strain gage manufacturer for proper attachment. The plugs are then moved outward, the fixture removed, and the installation of an opposite pair of gages is completed.

By this means a back to back gage assembly can be installed to within several thousandths of an inch deep in the interior of the shell with additional savings of time, tedious labor, and scrappage.

5.1.3 Imperfection Measurement System

The system for measuring the initial imperfections of shells consists of three parts: (1) the measurement table, (2) the low pressure gage and stand and (3) an oscillograph. Figure 8 shows the system less the oscillograph in a set up for measuring cylindrical shells. The principle of operation is simply to rotate the shell about a fixed central axis which passes through the center of the shell at its base and is perpendicular to a surface plate. A gage mounted on a straight post which is also perpendicular to the surface plate is positioned a certain distance R , from the axis of rotation. If a perfect right circular cylinder having a radius R is mounted centrally and made to rotate about this axis, the gage will not deflect. If the cylinder has any deviations from a perfect one, the gage will deflect when these deviated regions pass it. This applies to non-circular right cylinders as well. If the gage is such that it gives an electrical output that is proportional to a linear deflection, deviations can be recorded automatically on a recorder. If in addition, the speed of rotation is constant, then the record is directly readable in terms of the deviation at all circumferential positions.

In order for this system to work, it is essential that the wobble of the central axis of rotation be negligibly small or else have a known constant value. This was achieved in the system being described merely by supporting the measurement table rotating plate, shown at the bottom of Figure 8 on a thin film of oil. The rotating plate and all subsequent plates that are mounted on the rotating plate are ground or machined flat to within several tenths of a thousandth of an inch and all surfaces for mounting shells are made circular and concentric with the axis of rotation to within very small tolerances.

The rotating table is driven by an electric gear motor at a constant speed of 3 rpm, thereby achieving automatic correlation between the measured deviation and its location along the circumference.

The gage is a Schaevitz linear variable differential transformer type with a pivoting arm which produces a low contact pressure of about 2-4 grams. This is more than adequate for avoiding objectionable deflec-

tions of thin cylindrical shells having a radius to thickness ratio of 700 or less while measurements are being made. The tip deflection of the gage in its linear range is .060 inch.

The cylinder to be measured is mounted on the mounting fixture in its final testing assembly, complete with pressure bag and instrumentation. Prior to tightening the base clamps, an accurate circular plug is inserted at the top end of the shell. The base clamps are then tightened and the plug removed. Continuous transverses of the circumference are then made at as many cross sectional stations as desired. This is done merely by moving the gage bracket to the appropriate positions along the height stand.

The cylinders are measured also under internal pressure by inflating their membranes with air supplied through a long flexible tube connected to the mounting fixture. This tube allows rotation of the assembly while at the same time inserting air to make up for unavoidable leakage through the membranes.

Complete mapping of twenty cross sections can be measured and recorded in about one half hour.

5.2 Specimens and Instrumentation

The cylindrical and conical shells used in Phase 1 were made from 5052H-38 aluminum alloy sheet material. The cylindrical shells had the following dimensions: inner diameter 5.705 in., length 22.80 in., and wall thicknesses of .008 and .016 inch. They were fabricated by rolling an accurately cut rectangular sheet metal blank and carefully butting the edges. The seam was made by bonding a narrow longitudinal strip having a thickness of one half the wall thickness on each side of the butted edges, using an epoxy adhesive. The surface of the .016 in. wall thickness shell had maximum radial deviations of less than .016 in., or one wall thickness with one end held circular and the opposite end free. The deviations of the .008 in. wall thickness shell ranged up to two wall thicknesses.

A grid of axial and circumferential lines was put on the outside surface of the shells. The lines were .010 in. thick and were spaced 1/4 in. apart in both directions. The spacing accuracy was within .002 in/in. The purposes of the grid were (1) to serve as a reference system for making imperfection measurements and reading the high speed motion pictures, (2) to render buckling deformations more visible both in the motion pictures and in the final specimen, and (3) to show large membrane strains to an approximate degree.

The conical shells had an axial length of 22.8 in., a major diameter of 7.68 in., a minor diameter of 3.84 in., and a wall thickness of .008 in. They were fabricated by first cutting a conical blank on a reference tem-

Contrails

plate, rolling and forming a simple lap joint along a generatrix with adhesive bonding materials. Two adhesives were used; both made by the Minnesota Mining and Manufacturing Company. They were no. EC-2216 B/A, a room temperature curing epoxy paste type adhesive and Scotch-weld brand film type adhesive no. AF42, having a film thickness of .004 in. Each required a preparation of the aluminum metal surface as follows: alkaline degrease wash, rinse, and etch for 10 minutes at 150°F in a solution consisting of 30 parts distilled water, 10 parts concentrated sulfuric acid, and one part sodium dichromate. The curing cycle used was 150°F with no clamping pressure for 2 hours for the EC-2216 B/A and 350°F with 50 psi clamping pressure for one hour for the AF-42 adhesive. The EC-2216 B/A adhesive has the advantage of a low temperature cure but has relatively low peel strength and is messy to use. The AF42 adhesive has excellent peel strength and is very convenient to apply, but the 350°F 60 minutes curing requirement must be tolerable to the material being bonded.

The standard instrumentation of the cylindrical shells consisted of an accelerometer mounted centrally in the impact head and strain gages bonded to the shell wall. Strain gages were mounted in opposite pairs in almost all instances and so wired as to cancel the flexural components. The gages were located as follows: three axial pairs equally spaced at mid-length to measure the dynamic buckling and postbuckling loads and times; one axial pair 2 inches behind the impacted end to measure the stress-time character of the dynamic loading as initially introduced into the shell; one circumferential pair to measure the static hoop stress due to internal pressurization for the purpose of verifying the effectiveness of the membrane pressurization method and to measure the dynamic circumferential stress near the impacted end in specific instances. Strain gages were mounted at other positions whenever it became necessary.

An instrumented cylinder mounted in the test fixture is shown in Figure 9 in a ready condition for testing. This particular specimen had an internal circular plate mounted at the impact end, the purpose of which was to test the effect of supporting the end against inward displacement of the shell wall. The plate was not attached to the wall but rather fitted snugly when first introduced into the shell. Upon pressurization the shell wall was free to displace radially and hence was not subject to initial deformations due to pressure. The plate was supported against the axial pressure load by a chain which was attached centrally to the plate at the upper end and to the center of the mounting fixture at the bottom. The pressure bag was mounted to the inside of the plate and to the mounting fixture in a manner similar to that described in Reference 18.

The instrumentation of the conical shells consisted also of an accelerometer mounted in the impact head and strain gages bonded in opposite pairs. The location of the strain gages varied to a certain extent. An example of an instrumented conical shell is shown in Figure 10, which

Contrails

shows a set of three axial pairs equally spaced around the circumference at a station 2 inches behind the impact end, and a set of three (including one of the above) axial gages aligned along a generatrix of the cone and near both ends and at the mid-length position. Other conical specimens had three pairs equally spaced about the circumference at the mid-length station and another set along a generatrix at several axial positions.

5.3 Initial Imperfection Measurements

The zero reference for the imperfection measurements that were made with the previously described system is the cylindrical surface which is formed by a right circular cylinder whose base coincides with the base of the actual cylinder and whose axis coincides with the central axis of the rotating table. Errors due to wobble of the axis of rotation about the reference cylinder axis are accounted for by applying correction factors to the various axial stations. Since the specimen is measured in its test fixture, mounting inaccuracies become part of the effective imperfections that are pertinent to the buckling behavior. Care, however, was taken in mounting the shell so that mounting "imperfections" would not be larger than those resulting from the amount of nonperpendicularity of the base section.

Prior to mounting the shell, a traverse was made of the mounting circle to establish a straight reference line on the oscillograph. The specimen was then mounted, and a traverse made of the outer diameter surface at the base of the shell. This line was slightly wavy due to the difference between the inner diameter of the shell and the diameter of the mounting circle. The radial displacement in this waviness was a maximum of .003 in. (including the seam). Traverses were made of twenty axial stations one inch apart along the cylinder in addition to the base. This was done for zero pressure, half test pressure, and full test pressure for most of the cylinders without disturbing the mounting. Typical traverses are shown in Figures 11(a), (b) in which measurements at axial position 9 of specimen G-8 are compared at two values of internal pressurization, 0 and 17 psig. The circumference of all traversed stations was also measured in later specimens when it was found that their variation was not negligible.

The traverses in themselves are not very meaningful since they merely tell how the actual surface deviates radially from a perfect right circular cylindrical surface whose base section coincides with it. In order for these measurements to be useful for comparing experimental values with theoretical predictions, they must be reduced to meaningful components of deviations which are related to the coordinates of the shell.

The traverses were integrated to determine the position of the centroid of the actual cross sections with respect to the reference base section. Referring to Figure 12 the centroidal position of the section at station i is shown at O' displaced from the center O of the reference base

Contrails

circle by the distance $\bar{\delta}_i$. The line segment OO' is shown oriented by the angle θ_0 from the line OP . The point P specifies the rotational position on the shell at the start of measurements. The point Q is at the point of measurement and the measurement is directed along the line OQ which is located from OP by the angle θ . The circle with center at O' (with radius R_i) and having a circumference equal to that of the actual cross section at station i represents the mean circular position of the actual section. The radius R_i is assumed to be somewhat different in magnitude from radius R , the difference being on the order of δ .

The surface made up of all the mean circular cross sections properly aligned is a circular "cylindrical" surface having a crooked axis and is illustrated in Figure 13.

The radial difference between the actual and mean surfaces, Δ is determined with the aid of Figure 12.

$$\Delta = \delta - [\bar{\delta} \cos(\theta - \theta_0) + R_i \cos \lambda - R]$$

where $\lambda = \sin^{-1} [\bar{\delta} / R_i \sin(\theta - \theta_0)]$. $\Delta(\theta)_i$ defines a waviness type of imperfection about the circumference of the mean circle at station i . A plot of values of Δ at all axial stations for a fixed value of θ , designated by $\Delta(i)_\theta$, gives the waviness about the crooked longitudinal of the mean "cylinder." $\Delta(\theta)_i$ and $\Delta(i)_\theta$, therefore, are the imperfection components and together with \bar{x}_i and \bar{y}_i , the components of the centroids of the sections, completely describe the imperfections of the shell.

This system of imperfection components is related to the manufacture of shells. The $\Delta(\theta)_i$ and $\Delta(i)_\theta$ are due largely to waviness in the sheet material from which many shells are formed. Such waviness occurs as a result of the sheet rolling operation and is usually uncorrectable. Another source is the longitudinal seam which shells formed from sheet material possess. Local distortions in the vicinity of the seam and other joints due to welding are a common form of such imperfections. The \bar{x}_i and \bar{y}_i types of imperfection, on the other hand, are due to inaccuracies in fabrication. If the shell is made from sheet material and the rectangular blank does not have equal and parallel opposite sides, or if in positioning the seam for the joining operation the seam edges are not parallel, the centroids of the shell will be disturbed and result in the x_i and y_i type. Overall shrinkage of welded seams can also contribute to this type of imperfection.

In reducing the measured traverses the following assumptions were made: (a) the radial deviations δ are very small compared with the average radius of the cylinder and (b) the area of the mean circular cross section at station i is equal to the area of the actual cross section at i .

Contrails

Taking as the x axis the line passing between the center of the reference base circle (the center of rotation) and the point on the shell at which measurements start, the cartesian coordinates of the centroid of the actual cross section are (refer to Figure 12):

$$\bar{x}_i = \frac{1}{\pi R_i^2} \int_0^{2\pi} \int_0^{R + \delta(\theta)_i} \rho^2 \cos \theta \, d\rho \, d\theta$$

$$\bar{y}_i = \frac{1}{\pi R_i^2} \int_0^{2\pi} \int_0^{R + \delta(\theta)_i} \rho^2 \sin \theta \, d\rho \, d\theta$$

considering the expression for \bar{x}_i

$$\begin{aligned} \bar{x}_i &= \frac{1}{3\pi R_i^2} \int_0^{2\pi} [R + \delta(\theta)_i]^3 \cos \theta \, d\theta \\ &= \frac{1}{3\pi R_i^2} \int [R^3 + 3R^2\delta + 3R\delta^2 + \delta^3] \cos \theta \, d\theta \end{aligned}$$

The integral of the first term is equal to zero.

$$\bar{x}_i = \frac{1}{\pi} \int_0^{2\pi} \left[\left(\frac{R}{R_i}\right)^2 + \left(\frac{R}{R_i}\right)\left(\frac{\delta}{R_i}\right) + \frac{1}{3} \left(\frac{\delta}{R_i}\right)^2 \right] \delta(\theta)_i \cos \theta \, d\theta$$

Examining the terms and noting that $R \approx R_i$ and $\delta/R_i \ll 1$, it is evident that the second two terms may be neglected in comparison with the first. Hence

$$\bar{x}_i = \frac{1}{\pi} \left(\frac{R}{R_i}\right)^2 \int_0^{2\pi} \delta(\theta)_i \cos \theta \, d\theta$$

and similarly

$$\bar{y}_i = \frac{1}{\pi} \left(\frac{R}{R_i}\right)^2 \int_0^{2\pi} \delta(\theta)_i \sin \theta \, d\theta$$

From these, the \bar{x}_i and \bar{y}_i can be determined easily and therefore $\bar{\delta}_i$ and θ_{o_i} obtained:

$$\bar{\delta}_i = \sqrt{\bar{x}_i^2 + \bar{y}_i^2}$$

$$\theta_{o_i} = \tan^{-1} \frac{\bar{y}_i}{\bar{x}_i}$$

5.4 Plots of Imperfection Components

Plots of the $\Delta(\theta)_i$ imperfections of Specimen G-8 are shown in figure 14 for axial positions 21.6 (Base), 18, 15, 12, 9, 6, 3, and 0, and for internal pressures of 0 and 17 psig. The position numbers refer to the distance in inches of the section from the top or impact end of the shell. The values are plotted about the straightened-out circumference of the local section of the unpressurized shell and hence should be distributed about this reference such that negative and positive areas under the particular $\Delta(\theta)_i$ curve sum to zero. This is in keeping with the assumption that the imperfections leave the cross-sectional area unchanged. This condition is met to a satisfactory degree with discrepancies being less than .003 inch at the top section and considerably less at most other sections. In all the sections represented, it is clear that the internal pressure accomplishes a reduction of the waviness imperfections, both with regard to form and magnitude. Comparing the shapes of the curves at a given section, the correspondence of form between the pressurized and unpressurized cases is evident, showing a reasonable trend in the form from the unpressurized to the pressurized cases. This fact demonstrates the resolution capability of the measurement system.

The deviations throughout the major portion of the shell are within .007 in except in the region between the circumferential positions 12-17, the region about the seam. Deviations in this region are particularly large as high as .020 in. and show that the seam, the center of which is located near position 16 is the major cause of imperfections in the shells used in this program. In addition they show that the disturbance due to the seam extends far beyond its width of 1/4 in. The internal pressure has the particularly beneficial effect of diminishing the magnitudes of the seam disturbances almost throughout this entire shell.

A similar beneficial effect of the pressure on the imperfections is shown in the plots of values of $\Delta(i)_\theta$ corresponding to six circumferential positions of Specimen G-8 is given in Figure 15. The overall effect of reducing imperfections is evident. The base line about which the $\Delta(i)_\theta$ are plotted is the straightened-out longitudinal of the mean imperfect shell which corresponds to the same circumferential location.

In Figure 16 plots of the x_i and y_i components of the centroids of Specimen G-8 about the axis of the reference perfect cylinder (axis of rotation) are shown. The plots indicate an overall lean of the shell from the top to the bottom. The effect of greater internal pressurization is not evident and in fact the centroidal displacement for the pressurized shell (.0055 in.) is greater than that of the unpressurized shell (.0038 in.). This fact is not unreasonable, however, when one considers that the method of pressurization employed is such that essentially no axial force is introduced into the shell wall by the pressure.

5.5 Descriptive Outline of Tests

The tests that were conducted under Phase I are described in Table 1.

5.6 Results

5.6.1 Pressurized Cylindrical Shells

The accelerometer record obtained from this test is shown in Figure 17. The first and second peaks of deceleration which characterize the response are 80 and 58 g's, if the mean of the oscillations is taken. Equating the deceleration force to the resistance of the shell, the average axial stresses corresponding to these are 26,300 and 19,100 psi respectively, the duration of the peaks are 400 and 800 seconds, respectively. The gradual rise in deceleration at the beginning of the trace and prior to impact on the shell is due to the effect of the pressure bag which protrudes above the shell end.

Test No. G-2

The axial strain records obtained from the three pairs of equally spaced gages located at the mid-length of the cylinder were remarkably alike during the initial rise and fall of the first peak. These are shown in Figure 18. The average peak axial compression stress and average time to reach the peak were 26,700 psi and 560 μ sec. Subsequent to attaining the peak, the strain rapidly falls to a tension strain of 9300 psi at a time of 850 μ sec. Thereafter, the strain fluctuates at a mean value of approximately 20% of the peak value.

A record of the deceleration history was not obtained due to a cable failure. The value of deceleration deduced from the average peak strain is 162 g's.

Test No. G-3

The strain records obtained from this test are shown on Figures 19 (a) - (c). As in the previous test results the strain records from the

TABLE I - DESCRIPTION OF PHASE I TESTS

Test No.	Shell Type	V_o ft/sec	q psig	Impact Condition	End Conditions
G-1	Cylindrical - .008 in. wall thickness ↓	11.5	8.5	Vertical ↓	Impacted end: free; Opposite end: clamped ↓
G-2		11.5	17		
G-3		11.5	34		
G-4		23	17		
G-5		23	17		
G-6		23	17		
G-7		23	34		
G-8		11.5	17		Impacted end: free-supported Opposite end: clamped
O-1	Cylindrical - .008 in. wall thickness 14 in. length ↓ Cylindrical - .008 in. wall thickness 14 in. length ↓	16.7 ↓	0 ↓	Vertical	Impacted end: supported; Opposite end: clamped ↓
O-2				Oblique(A) 4°	
O-3			8°		
O-4		16.7 ↓	0 ↓	Oblique(A) 12°	Impacted end: supported; Opposite end: clamped ↓
O-5				16°	
O-6				Oblique(B) 8°	
O-7				12°	
O-8		16°			
C-3	Conical - .008 in. Wall thickness ↓	23	8.5	Vertical ↓	Impacted end: free Opposite end: clamped ↓
C-4		23	8.5		
C-6		23	17		
C-1		46	8.5		

three pairs of gages are much alike. This fact is an indication of the uniformity of the impact around the circumference of the struck end. Again considering the average of the three records, the peak axial compression stress and the time to the start of the rapid decrease in stress are 28,600 psi and 570 μ sec. This stress is 7% higher than that of Test No. G-2 for which the internal pressure was half that used in this test. Similar to Test No. G-2, the strain fluctuates after the initial peak falls through zero and has an average value approximately of 27% the peak value. Photographs of Specimens G-2 and -3 are shown in Figure 20.

The accelerometer trace obtained in this test is shown in Figure 21. It has a peculiar appearance, with a number of smooth horizontal lines that are separated by sharp rises in deceleration. It was determined that this erratic behavior was due to a faulty cable connector which produced intermittent short circuits. The deceleration history was deduced from the average of the three strain records and this was superimposed on the measured deceleration history. This comparison is shown in Figure 21, where the overall agreement between them is evident.

Test No. G-4

The strain records obtained from this test are shown in Figures 22 (a) - (d). As is evident, the magnitudes of strain are much smaller than those of the previous tests. Study of the high speed motion pictures obtained during this test showed that the head impacted the shell unevenly. Buckling initiated locally at the place first struck by the impact head. The axial strains are considerably smaller than those for the symmetrically impacted shells even though they were struck at one half the velocity of this test. This is due apparently to the "fanning out" of the stress from the region initially struck, thereby diminishing in magnitude. During the subsequent time over which substantial crushing of the shell takes place, the strain does not rise to the levels of the previous tests. This may indicate that asymmetrical impact on a shell may not result in the high initial resistance which is typical of symmetrical impact.

Test No. G-6

This test was a rerun of Test No. G-4 which suffered an uneven impact. The axial strain records for three equally spaced pairs of gages located at mid-length are shown in Figures 23 (a)-(d). The initial peak stress and the time just after the peak is attained are 24,700 psi and 260 μ sec., respectively. The stress is somewhat lower than that of Test No. G-2, which had the same value of internal pressure but one half the impact velocity. The time at which the stress begins to fall, however, is slightly less than half that of Test No. G-2. In a generally similar way to the previous tests, the stress rapidly falls from the initial peak, through zero and into a relatively low value of tension and thereafter (at least for

Figure 23 (a) and (c)) fluctuates. In the record of Figure 23 (b), however, two very high peaks are present the first and second of them showing strains of 4700 (at .00112 sec) and 4500 μ in/in (at .00168 sec.) respectively or an average of 1.92 times the initial peak. The reason for this behavior may be that the shell burst apart after initial buckling occurred. The rupture extended over the entire length of the shell, following the seam. The bonded seam was intact, however, and the metal appeared to have ripped apart following an initial tensile rupture. It is not thought at this time that these peaks are significant as far as the buckling behavior per se.

This conclusion is strengthened by the deceleration record obtained during this test, shown in Figure 23 (d). At the time at which the peaks occur there is no indication of an increase in axial resistance. On the other hand the deceleration trace agrees well with the strain data. This shows an initial peak occurring at 260 μ sec, agreeing exactly with the peak strain (average of three records). In addition the time at which the peak positive acceleration, 540 μ sec, agrees exactly with the time at which the peak tensile strain occurs. The time of occurrence of the second peak also checks well from the two types of records.

Test No. G-7

This test was a rerun of Test No. G-5 (not reported) in which the instrumented was triggered prematurely. The strain records are shown in Figures 24 (a), (b), (c), and (d). The average values, taken from three circumferential pairs of strain gages, for the initial peak stress and corresponding time are 21,900 psi and 250 μ sec respectively. The stress is 11% lower than that of test No. G-6, despite the fact that the internal pressure in test No. G-7 was twice as high (34 psig) as in test No. G-6 (17 psig). The record of the deceleration, shown in Figure 24d, is in agreement with the strain records.

Test No. G-8, Effect of End Constraint

Due to the fact that under axial impact loading the shell buckles at the ends, principally the impacted end, it was advisable to study the effect of supporting the impacted edge on the shell response. All of the experimental investigations performed during this program had utilized a free edge condition at the impacted end of the shell. The only constraint imposed on the edge was the friction between the shell and the impact head. This condition had been chosen because it was desirable to permit the shell to deform under the impact in its most natural manner without forcing it into a particular mode of deformation. Measures were taken to maintain this condition even for initially pressurized shells, and especially so in this case, since it was desirable to prevent the initial deformations which an end cap attached to the shell would produce. The chain supported pressure bag technique was developed, therefore, to accomplish this.

In order to determine the effect of end constraint, without getting involved with a large experimental scatter, it was decided to utilize an internally pressurized shell. Since it was desirable here also to avoid initial deflection due to the presence of an attached end plate, the shell specimen was set up with a closely fitting circular end plate. To this plate a pressure bag was attached and the plate was supported by the centrally mounted chain. When the shell was in the pressurized condition the plate was flush with the top of the shell, as shown

Contrails

in Figure 9. The effect of the plate, was to restrict inward lateral deformations of the shell at the impact end. The shell, however, was free to expand and/or deflect outwardly.

The test was arranged so that the results could readily be compared with those previously obtained from Test No. G-2. The impact velocity was, 11.5 ft/sec and the internal pressure 17 psig. The shell, .016 inch in thickness, was instrumented with axial and circumferential strain gages, all of which were mounted in back-to-back pairs. They were mounted at two axial stations, one within two inches of the impacted end and another eleven inches behind the impacted end. At this latter station were three gage pairs equally spaced about the circumference and two other pairs, one circumferential and the other axial, mounted as close as possible to each other.

The results showed that the end restraint is very important and greatly increases the resistance to buckling. This conclusion is presented via the test data.

The axial strains measured at three mid-length positions and one forward position are shown in Figures 25 a, b, c, and d respectively. The mid-length strains have peak values of 3340, 3060, and 2340 μ in/in and the peaks are attained simultaneously at 600 μ sec. The discrepancy between the three peak values may be due to a non-flat impact condition. The average value is 2906 μ in/in. The corresponding values obtained from test No. G-2 are 2520 μ in/in and 560 μ sec. The strain shows an increase of 15%.

The strain measured at the forward gage position (Figure 25d) rises to a peak value of 3760 μ in/in at 600 μ sec and then abruptly decreases to a low level. This behavior is similar to that obtained from the mid-length gages. A measure of the effect of the end constraint on the shell response may be obtained by comparing Figures 25d and 24e, the latter being a record of a forward axial gage from Test G-7. In this, the strain rises rapidly to a peak of about the same magnitude as those obtained from the mid-length gages of Test No. G-7 (see Figure 24). The strain then falls to a low value at about 200 μ sec whereas the mid-length strains do not fall to similar values until 400 μ sec. This rapid reduction of strain in the forward end of the shell is due most probably to local collapse of the edge. A similar behavior is evident in Figure 22d, obtained from Test No. G-4.

Specimen G-8 is not available because it burst apart along its longitudinal joint during the latter stages of the impact. Examination of the deformations at the impacted edge show that, restrained by the end plate, the shell must collapse by bending outward and then inward, whereas without the plate, the edge merely bends inward. This supports the conclusions drawn from the strain data.

Summary of Results

The results of the pressurized cylinder impact tests are summarized in Table 2.

The tests performed at the lower velocity of 11.5 ft/sec in which strain gage instrumentation was the main measurement device, were very satisfactory both with regard to the quality and interpretability of the records. The beneficial effect of internal pressure on the shell instability stress is observed. The measured 7% increase in the buckling stress of specimen G-3 (34 psig) over that of G-2

Contrails

TABLE 2 - PRESSURIZED CYLINDRICAL SHELL TEST RESULTS

Test No.	V_o ft/sec	q psig	h in.	σ_{cr} psi	$\bar{\sigma}_{cr}$	$\frac{\sigma_{cr}}{\sigma_{cl}}$	$\frac{\sigma_p^{(1)}}{\sigma_{cl}}$	t_{cr} μ sec	n_f
G-1	11.5	8.5	.008	19,100	.643	1.067	.530	---	6
G-2	11.5	17	.016	26,700	.450	.745	.461	560	5
G-3	11.5	34	.016	28,600	.482	.799	.530	570	5
G-4	23	17	.016	---	---	---	---	---	5
G-6	23	17	.016	24,700	.417	.690	.461	260	---
G-7	23	34	.016	21,900	.370	.612	.530	250	---
G-8	11.5	17	.016	39,800	.672	1.11	.461	600	---
G-8	11.5	17	.016	30,800	.520	.860	.461	600	---

(1) Reference 2

(17 psig) is low compared to the 15% increase predicted by Thielemann (Ref. 2) for statically compressed shells of equivalent pressurization (see column headed σ_p/σ_{cl}) but considering experimental scatter, the observation was significant.

More significantly, the ratios of σ_{cr}/σ_{cl} are consistently greater than the ratios of σ_p/σ_{cl} , thereby indicating that the gain in buckling stress due to the effect of impact loading can be considerable.

5.6.2 Pressurized Conical Shells

Test No. C-3

The shell was instrumented with three axially oriented opposite strain gage pairs equally spaced around the circumference at a section 11 inches from the impacted end. Mounted along the same generatrix as one of these were another two pairs of axial gages, one located 2 inches and another 20 inches from the impacted end. The shell was pressurized to a pressure of 8.5 psig and impacted at 23 ft/sec. The strain records obtained are shown in Figures 26 (a) to (e). The initial response of the mid-length gages (Figures 26 (b), (d), (e), 11 inches from the impacted end) show an initial rise of 467, 490, and 449 μ in/in followed by an abrupt rise at 868, 915, and 826 μ in/in respectively. These values indicate a fairly good symmetry of the initial impact. Shown in Figures 26 (a), (b), (c) are the strains corresponding to the three axially aligned gages for the forward, middle, and rear gages respectively. The average of the forward portions of these curves (from initiation to the time at which the strain falls to or oscillates about zero) show the following values: (a) 355, (b) 271, (c) 177 μ in/in. These values are the average of the portion of the faired deceleration trace between the initiation of impact and the time at which the faired curve attains a

zero value. The faired curves are similar to those shown in Figure 31 and discussed later. The average values represent the average loading sustained by the shell during the first stage of buckling and collapse. It was desirable to see whether ratios of these values corresponded to the ratios of the appropriate radii of the respective sections. These radii and their ratios were found to be:

$$R_F = 2.09 \text{ in.}, \quad R_M = 2.84 \text{ in.}, \quad R_B = 3.60 \text{ in.}$$

where R_F , R_M , and R_B are the radii of the forward, middle, and rear gage location sections

$$\frac{R_M}{R_F} = 1.36, \quad \frac{R_B}{R_F} = 1.72, \quad \frac{R_B}{R_M} = 1.26$$

The strain ratios are:

$$\frac{\epsilon_F}{\epsilon_M} = 1.31, \quad \frac{\epsilon_F}{\epsilon_B} = 2.00$$

Under static load, $\epsilon_F/\epsilon_M = R_M/R_F$ and $\epsilon_F/\epsilon_B = R_B/R_F$. It is seen that although ϵ_F and ϵ_M approach this closely, the values of ϵ_F and ϵ_B do not.

The regularly oscillatory character of the strain records is evident. These are thought to be due to longitudinal vibrations perhaps caused by the snapping action of buckling formation. From high speed motion pictures this action is seen to be quite violent.

The specimen ruptured after collapsing about eleven inches in a very orderly manner. The rupture was due to seam failure. The collapse pattern consisted of sixteen axial waves and 5-6 full circumferential waves.

Test No. C-4

Specimen C-4, tested under the same conditions as the previous case, contained three axial pairs of gages equally spaced about the forward section ($R = 2.09$ in.) with two other pairs axially aligned with one of them. The records are shown in Figure 27 (a) to (e). The initial peaks of the forward strains (Figures 27 (a), (d), and (e)) are 825, 993, and 1156 μ in/in indicating only a fair loading symmetry. Despite this, the specimen collapse pattern was very orderly. The middle section strain (Figure 27 (b)) has an initial peak of 540 μ in/in followed by an abrupt increase to 854 μ in/in. As in the previous test, the time of occurrence of this second increase is about equal to the time required by the first strain wave reflected from the rear end of the shell to reach the middle gage position.

A comparison of the records of the three axially aligned gages is shown in Figure 27 (a), (b) and (c). The general similarity with the corresponding set from test no. C-3 is evident. Taking the average of the first portions of these records as was done for the previous test, the following values are obtained: (a) 423, (b) 318, and (c) 276 μ in/in. The strain ratios are:

$$\frac{\epsilon_F}{\epsilon_M} = 1.33, \quad \frac{\epsilon_F}{\epsilon_B} = 1.53$$

Here again the values of ϵ_F and ϵ_M are close to the proportion required by a static loading condition but not that of ϵ_B .

Specimen C-4 also ruptured during the impact but as usual, the rupture occurred well after the effective test interval. The collapsed portion displayed an orderly pattern of 5-6 full circumferential waves.

Test No. C-6

Specimen C-6 was tested at an impact velocity of 23 ft/sec and under an initial internal pressure of 17 psig and was instrumented essentially in the same manner as specimen C-4. The strain records are shown in Figures 28 (a) to (d). The initial peaks of the forward strains (Figures 28 (a), (b), and (c)) are 1132, 1213, and 1253 μ in/in and indicate a fairly good loading symmetry, provided that the unexplained excessive peak of Figure 28 (a) is neglected. Of greatest interest are Figures 28 (a) and (b) which show well defined peaks and troughs. Their relationship to the buckling mechanism will be discussed later. These peaks are substantially higher in strain than any of the values obtained in the previous tests and are a result of the higher pressurization of this test.

Specimen C-6 also burst due to a seam failure and its failure time is indicated on several of the strain traces. The collapse pattern definitely showed the effectiveness of the internal pressure in both its orderliness and higher number of waves, $n_f = 6-7$, as opposed to 5-6 of the lower pressurized shells. The collapse pattern of specimen C-6 is shown in Figure 29.

Test No. C-1

Specimen C-1 was instrumented in the same manner as C-3 and was subjected to impact at a velocity of 46 ft/sec with an initial internal pressure of 8.5 psig. The three records of the gages located at the mid-length positions (Figures 30 (b), (c), and (d)) have initial peaks of 902, 864, and 875 μ in/in which represent a good loading symmetry. The initial peak of the forward strain gage trace, Figure 30 (a) has a value of 1509 μ in/in which is higher than all other previous corresponding values except for one of the forward gages of test No. C-6 (Figure 28 (a)). In addition, the broad, well defined peaks of Figures 30 (a) are interestingly high, the higher being 1257 μ in/in.

The specimen collapsed in a very orderly manner and had from 5-6 full circumferential waves.

Critical and Postbuckling Stresses

Study of the strain records and the collapsed specimens from the standpoint of attempting to understand the mechanism of buckling and collapse produced fruitful results. At first, it was not evident what the significance of the initial peak was in relation to other portions of the strain records. The distinct peaks and troughs of some of the strain records stimulated study of their significance. It was asked whether these could be the successive stages of buckling and collapse that were described originally in Reference 8 and which have been seen many times in high speed motion pictures of shells buckling under impact. It was found that the length of the collapse waves in the actual specimen corresponded to the distance traversed by the impact head moving at the test velocity. For example, in Specimen C-3, there were sixteen complete axial waves or stages comprising

the collapsed region, these extending through 11 inches of the initial cone. Hence the average length of these waves along the slant direction is .69 inch. At $V_0 = 23$ ft/sec, the time taken by the head to move through this distance is about .0025 sec. Accounting for the thickness of the shell and the radius with which the actual collapse waves bend over on themselves, the actual distance through which the head moves in collapsing one full wave is .59 inch and the time .0021 sec. In Figure 31 strain traces corresponding to forward gages and representing all the tests are shown replotted. Minor oscillations have been smoothed out in order to detect the basic form of the strain variations. In all cases, the initial peak has been retained because it represents the first loading wave that enters the shell and is significant for initiating buckling.

In Figure 31 (a) and (b), tests (Nos. C-3 and -4) performed under the same conditions, the curves are very similar except for magnitude. In both cases, after the initial peak, the strain rises slowly to another peak and decreases to zero or tension. These are followed by another similar peak. The duration of these pulses is .002 sec. The higher pressure test (No. C-6) is represented by two different forward traces, in Figures 31 (c) and (d). In each curve the pulses follow one another and are shorter in duration than those of Test No. C-3 and -4. This is in accordance with the fact that the number of waves in Specimen C-6 is 6-7 and therefore the collapse length is correspondingly smaller. A further verification of validity of this interpretation is given in Figure 31 (e) which corresponds to Test No. C-1 performed at 46 ft/sec. The pulse times are close to .001 sec, half the times of those for Test Nos. C-3 and -4 which were conducted for the same internal pressure but half the velocity.

From this, the strain trace can be explained completely. The initial pulse causes a buckling failure at the free edge in a very short time. This is the initial response of the shell to the impact. Thereafter, the triangular buckling mode begins as the impact head bottoms on the relatively undeformed portion of the shell. This occurs during the rise of the long pulse. As the buckling deformation increases, the stage progresses into collapse thereby causing a reduction in the strain. This process proceeds for each buckling stage. As the impact proceeds further and further along the cone, the peak values of successively later stages of buckling can be expected to change, probably to increase, as the involved section increases in diameter. The initial and postbuckling strains and loads as obtained from the forward strain gages are given in Table 3. The buckling loads, P , are determined from the strains by means of the relation

$$P = \frac{2\pi R_F E h}{\cos \gamma} \epsilon .$$

5.6.3 Oblique Impact

A series of tests were performed to evaluate the behavior of cylindrical shells under oblique impact. Two series of tests were made: Series A - the shell was dropped vertically on to a horizontal surface with its central axis initially constrained in a non-vertical attitude; Series B - the shell was dropped vertically, with its axis initially constrained in a vertical attitude, onto an inclined surface. In each case, the rear end of the shell was clamped to a circular plate and the front end was supported by a circular plate. The specimens had a diameter of 5.716 in., a length of 14 in, a thickness of .008 in, and were made of 5052 H-38 Aluminum alloy. The unsupported length

TABLE 3 - PRESSURIZED CONICAL SHELL TEST RESULTS.

Test No.	Initial		First Stage		Postbuckling Second Stage		Third Stage	
	ϵ in/in	P lb.	ϵ in/in	P lb.	ϵ in/in	P lb.	ϵ in/in	P lb.
C-3	818	915	448	501	448	501	---	---
C-4	975	1090	737	824	863	965	---	---
C-6	1250	1400	1120	1250	1280	1430	1760	1970
C-6			1090	1220	1320	1475	2070	2300
C-1	1550	1730	1153	1290	1073	1200	1340	1500

of the shell was 13 in. The weight which the shells had to decelerate was 47.2 lb and was dropped through a mean height of 52 in. Four shells, comprising series A are shown in Figure 32 after impact at an axis tilt angle of 4° , 8° , 12° and 16° . Similarly, the three shells of series B are shown in Figure 33 after impact with surface whose plane was oriented from the horizontal by 8° , 12° and 16° (left to right). On the left of these is a cylinder vertically impacted in the same apparatus. In all cases the shells had zero differential pressure at the beginning of impact but contained no venting provisions.

In general the collapse modes of the shells were orderly. The shells of series A tended to undergo the buckling on their opposite end by virtue of bending under the impact moment about the upper clamping plate. This tendency increased with the angle of obliquity. At the impacted end the collapse was confined very locally to the region of collapse. The very opposite was true for the shells of series B.

At least with regard to the orderliness of the collapse, which used up about 40% of the shell, the cylindrical shell appears to have an acceptably wide tolerance to oblique impact.

5.7 Inextensional Buckling Configurations

For inextensional buckling under axial compression it is required that the axial shortening of the shell be produced by a bending of the surface about straight lines in such a way that extensional strain in the middle surface is zero everywhere. We consider first the overall inextensional buckling configuration for the conical shell and show in Figures 34a and b the horizontal and vertical views respectively of the initial and buckled configurations. The conical frustum has a semi-vertex angle of γ and upper and lower bases A_0 and C_0 respectively which are assumed to be free of lateral restraint. The buckled configuration is represented by n_f circumferential waves and one axial wave, although any number of axial waves may be considered as well. As a result of buckling, circular sections like A, B, and C become regular plane polygons of unchanged perimeter. Several vertices of these polygons are shown at j, k, l, and m for circle A and at n, o, and p for circle B, in which the straight line segments between adjacent

vertices are equal in length to their corresponding arcs. The polygons having the same perimeters as A, B and C are shown at stations a, b, and c respectively. The positions of the original circles on the buckled surface are shown by the curved dashed lines in Figure 34b. Plane triangles are formed by connecting adjacent vertices and hence the entire buckled surface consists entirely of plane triangles. A buckle wave is defined as a set of two adjacent triangles whose common edge is a side of the cross sectional polygon. These common edges form the inner folds of the pattern (i. e., they occur at concave intersections) and are indicated by the dashed straight lines. The other common edges, indicated by solid lines, form the outer folds. From Figure 34 it is evident that some triangular surfaces slope in the direction of the conical slope γ (those labeled +) while others slope contrary to γ (those labeled -).

In Figure 35, a layout of the buckle pattern on the conical blank is shown. Here the circular arcs are the layout of the line of intersection of cross sectional planes A, B, and C with the conical surface, and have a common center at the apex of the cone. The radial distances r and r' correspond to cross sections A and B respectively. The radius r_0 is that of an arc which is tangent to the sides of the polygon corresponding to section A; this establishes the position of section A_0 shown in Figure 34.

For inextensionality, l_x^+ and l_x^- must remain unchanged in the initial and buckled configurations, and in addition, $l_y = \pi D / 2n_f$ ($n_f = 2, 3, 4, \dots$). Referring to Figure 34b, the unit axial shortening, ϵ , due to the buckling of a half wave length region adjacent to the end of the cone is

$$\begin{aligned} \epsilon &= \frac{l_x^+ \cos \gamma - l_x^+ \cos (\gamma + \alpha)}{l_x^+ \cos \gamma} \\ &= 1 - \frac{\cos (\gamma + \alpha)}{\cos \gamma} \end{aligned} \tag{1}$$

From Figures 34a and b

$$\cos (\gamma + \alpha) = \sqrt{1 - \left[\frac{1}{l_x^+} \left(\delta_i + \delta'_o + \frac{D' - D}{2} \right) \right]^2} \tag{2}$$

where

$$\begin{aligned} \delta_i &= \frac{D}{2} \left(1 - \frac{\pi}{n_f} \cot \frac{\pi}{n_f} \right) \\ \delta'_o &= \frac{D'}{2} \left(\frac{\pi}{n_f} \frac{1}{\sin \frac{\pi}{h}} - 1 \right) \end{aligned} \tag{3}$$

and D, D' are diameters of sections A and B respectively.

Contrails

Substituting Equations 2 and 3 in Equation 1 yields,

$$\epsilon = 1 - \frac{1}{\cos \gamma} \sqrt{1 - \left[K^+ \frac{1}{\sin \frac{\pi}{n_f}} \left(\frac{D'}{D} - \cos \frac{\pi}{n} \right) \right]^2} \quad (4)$$

where $K^+ = l_y / l_x^+$, the aspect ratio of the (+) surfaces. The diameter ratio D'/D may be determined with the aid of Figure 35. It is readily seen that

$$l_x^+ = r' - r + g + h' \quad (5)$$

where

$$g = \frac{D}{2} \left(\frac{1}{\sin \gamma} - \frac{\pi}{n_f} \cot \frac{\theta}{2} \right)$$

$$h' = \frac{D'}{2} \left(\frac{\pi}{n_f} \frac{1}{\sin \frac{\theta}{2}} - \frac{1}{\sin \gamma} \right)$$

$$\frac{\theta}{2} = \frac{\pi}{n_f} \sin \gamma \quad (6)$$

$$r = \frac{D}{2} \frac{1}{\sin \gamma}$$

$$r' = \frac{D'}{2} \frac{1}{\sin \gamma}$$

Substituting Equation 6 in Equation 5 and rearranging,

$$l_x^+ = \frac{\pi D}{2n_f} \frac{1}{\sin \frac{\theta}{2}} \left(\frac{D'}{D} - \cos \frac{\theta}{2} \right)$$

from which

$$\frac{D'}{D} = \frac{1}{K^+} \sin \frac{\theta}{2} + \cos \frac{\theta}{2} \quad (7)$$

The relation for ϵ in terms of the K^+ , n and γ is obtained by inserting Equation (7) in Equation (4):

$$\epsilon = 1 - \frac{1}{\cos \gamma} \sqrt{1 - \frac{1}{\sin^2 \frac{\pi}{n_f}} \left[\sin \frac{\theta}{2} + K^+ \left(\cos \frac{\theta}{2} - \cos \frac{\pi}{n} \right) \right]^2} \quad (8)$$

If $\gamma = 0$ (cylindrical shell),

$$\begin{aligned} \epsilon &= 1 - \sqrt{1 - \left[K^+ \frac{\left(1 - \cos \frac{\pi}{n_f}\right)}{\sin \frac{\pi}{n_f}} \right]^2} \\ &= 1 - \sqrt{1 - K^2 \tan^2 \frac{\pi}{2n_f}} \end{aligned} \tag{8a}$$

where $K^+ = K^- = K$, the single aspect ratio of the cylindrical shell. Equation (8a) agrees with the relation given in Reference 8.

The aspect ratio of the (-) surfaces, $K^- = \ell_y^+ / \ell_x^-$ may be obtained with the aid of Figure 35.

$$\ell_x^- = \ell_x^+ - (g + g' + h + h') \tag{9}$$

where

$$\begin{aligned} g' &= \frac{D'}{2} \left(\frac{1}{\sin \gamma} - \frac{\pi}{n_f} \cot \frac{\theta}{2} \right) \\ h &= \frac{D}{2} \left(\frac{\pi}{n_f} \frac{1}{\sin \frac{\theta}{2}} - \frac{1}{\sin \gamma} \right) \end{aligned} \tag{10}$$

Substituting Equation 10 and the first two parts of Equation 6 into Equation 9, yields

$$\ell_x^- = \ell_x^+ - \frac{\pi D}{2n_f} \left(1 + \frac{D'}{D} \right) \frac{1}{\sin \frac{\theta}{2}} \left(1 - \cos \frac{\theta}{2} \right)$$

or

$$\frac{\ell_x^-}{\ell_x^+} = 1 - K^+ \left(1 + \frac{D'}{D} \right) \frac{1}{\sin \frac{\theta}{2}} \left(1 - \cos \frac{\theta}{2} \right) \tag{11}$$

By inserting Equation 7 into Equation 11 the following result is obtained:

$$\frac{\ell_x^-}{\ell_x^+} = \cos \frac{\theta}{2} - K^+ \sin \frac{\theta}{2} = \frac{K^+}{K^-} \frac{D'}{D}$$

or

$$K^- = \left(\frac{D'}{D} \right) \frac{K^+}{\cos \frac{\theta}{2} - K^+ \sin \frac{\theta}{2}} \quad (12)$$

K^+ is determined from Equation (4) in terms of ϵ , n , and γ .

$$K^+ = \frac{\sin \frac{\pi}{n_f} \sqrt{1 - [(1 - \epsilon) \cos \gamma]^2} - \sin \frac{\theta}{2}}{\cos \frac{\theta}{2} - \cos \frac{\pi}{n_f}} \quad (13)$$

5.7.1 Prismoidal Shortening Patterns

For the cylindrical shell (referring to Equation 8a), if $K = 0$, $\epsilon = 0$ for all values of n . This is not the case for the conical shell, for if the value $K^+ = 0$ is inserted in Equation 8,

$$\epsilon = 1 - \frac{1}{\cos \gamma} \sqrt{1 - \left(\frac{\sin \frac{\theta}{2}}{\sin \frac{\pi}{n_f}} \right)^2} \quad (14)$$

The corresponding value of K^- as obtained from Equations 7 and 12 is

$$K^- = \tan \frac{\theta}{2} \quad (15)$$

and it is noted that the corresponding diameter ratio

$$\frac{D'}{D} \rightarrow \infty \text{ as } K^+ \rightarrow 0$$

The pattern for $K^+ = 0$ is shown in Figure 36a as it would appear for a fixed value of ℓ_y . The fact, previously noted, however, that the diameter ratio $D'/D \rightarrow \infty$ for this case, means that $\ell_y = 0$ for any finite value of ℓ_y . The pattern for $K^+ = 0$ hence transforms the initial conical shell into a regular conical prismoid. In this configuration, shown in Figure 36b, all (+) surfaces have vanished, leaving only (-) surfaces whose sides are formed by the radial lines which divide the plane blank of the cone into n sides. The prismoid is formed merely by folding along these lines.

5.7.2 Total Collapse Configuration

The aspect ratio for the total collapse pattern ($\epsilon = 1$) is:

$$K^+ = \frac{\sin \frac{\pi}{n_f} - \sin \frac{\theta}{2}}{\cos \frac{\theta}{2} - \cos \frac{\pi}{n_f}} \quad (16)$$

For $\gamma = \frac{\pi}{2}$,

$$K^+ = \cot \frac{\pi}{n_f} \tag{17}$$

The aspect ratio K^- for the total collapse pattern is obtained from Equations 12 and 14:

$$K^- = \left(\frac{D'}{D}\right) \frac{\sin \frac{\pi}{n_f} - \sin \frac{\theta}{2}}{1 - \cos \left(\frac{\theta}{2} - \frac{\pi}{n_f}\right)} \tag{18}$$

The ratio of the two aspect ratios is:

$$\frac{K^+}{K^-} = \left(\frac{D}{D'}\right) \frac{1 - \cos \left(\frac{\theta}{2} - \frac{\pi}{n_f}\right)}{\cos \frac{\theta}{2} - \cos \frac{\pi}{n_f}} \tag{19}$$

The ratio K^+/K^- ranges with γ as follows:

$$\begin{aligned} \frac{K^+}{K^-} &= 1, \text{ for } \gamma = 0 \text{ (cylinder)} \\ &= 0, \text{ for } \gamma = \frac{\pi}{2} \text{ (flat plate)} \end{aligned}$$

Since K^+ (for $\gamma = \pi/2$) $\neq 0$, therefore $K^- \rightarrow \infty$ as the cone angle increases. Thus, with increasing cone angle the portion of the buckle wave of the (-) surface becomes increasingly smaller with respect to that of the (+) surface.

5.7.3 Profile Characteristics

The characteristics of the patterns may further be defined by considering the profiles of (+) and (-) planes with respect to the generatrix of the cone. Referring to Figure 37a the (+) plane IBJ and the (-) plane KBL intersect the generatrix GG' about which they are symmetrical at points E and F respectively. The centerlines $AB = \ell_x^+$ containing point E and $BC = \ell_x^-$ containing point F of (+) and (-) planes respectively lie in the plane containing the generatrix and the cone axis, due to symmetry. Since the line segment IAJ lies in the same plane as the conical cross section S_1 , the extension of the radial line OA passes through point D on the generatrix. The development is similar for point H. The profile view in the radial plane OO'GG' is shown in Figure 37b. The angles between the generatrix and each of the lines AB and BC are α and β respectively. Point P, at the foot of the perpendicular from point A to the generatrix is the origin of coordinate axes U and V respectively along and perpendicular to GG'. Taking the points M and N as the feet of perpendiculars to GG' dropped from points B and C respectively, let $W_0 = PA$, $W_1 = MB$, $W_2 = NC$, and $U(o) = PE$. The

equation of the centerline AB of the profile of the (+) plane is simply (the barred terms are divided by D):

$$\bar{W} = \bar{U} \tan \alpha - \bar{\delta}_i \cos \gamma \quad 0 \leq \bar{U} \leq \bar{U}_1$$

and of the axially adjacent (-) plane

$$\bar{W} = \bar{W}_1 - \bar{U} \tan \beta$$

where α is obtained from

$$\sin(\gamma + \alpha) = \sin \frac{\theta}{2} + K^+ \frac{\left(\cos \frac{\theta}{2} - \cos \frac{\pi}{n_f} \right)}{\sin \frac{\pi}{n_f}}$$

and β from

$$\sin(\gamma - \beta) = \frac{\left(\frac{D'}{D} \cos \frac{\pi}{n_f} - 1 \right)}{\sin \frac{\pi}{n_f} \left(\frac{\cos \frac{\theta}{2}}{K^+} - \sin \frac{\theta}{2} \right)}$$

In Appendix A values of \bar{W}_1 , \bar{W}_2 , $\bar{U}(0)$, α , β , K^+ and K^- are given for various cone angles, wave numbers, and end shortenings. From these quantities, the asymmetry of inextensional patterns can be found by plotting on a graph. The precise definition of these patterns for cones has not been known heretofore and it is hoped that this can contribute to the formulation of more accurate deflection functions in analyses of buckling conical shells. As pointed out later these patterns, especially the total collapse patterns, are physically realistic.

5.7.4 Construction of Inextensional Patterns and Comparison with Experiment

The exact inextensional buckling pattern for a conical shell having any vertex angle and wave number and corresponding to any degree of end shortening may be constructed easily by first laying out the conical blank similar to Figure 35. The total angle at the vertex of the plane pattern is equal to $n_f \theta = 2\pi \sin \gamma$. Taking D as the diameter of the upper (smaller) circle of the conical frustum, the upper arc is drawn about the vertex with a radius $r = (D/2) (1/\sin \gamma)$ and divided into n_f equal segments. Radial lines are drawn from the vertex to the points of division of the arc and the quantity "h" laid in. Straight lines joining the extremities of "h" form the lengths $2\ell_y$, which are then bisected, and radial lines from the vertex are drawn through the points of bisection. The length $\ell_x^+ = \ell_y/K^+$, where K^+ is obtained from Equation 13, is layed out along the lines bisecting $2\ell_y$ according to Figure 35. The extremities of the $2\ell_y$ segments are connected to the extremities of the ℓ_x^+ segments, thereby forming the first row of (+) triangles. The (-) triangles in the first row are obtained merely by connecting the extremities of the ℓ_x^+ lengths with straight lines. These latter lines are equal in length to $2\ell_y'$ which can be checked by computing the ratio D'/D

Contraails

from Equation (7) and determining $l_{y'} = (D'/D)l_y$. The value of l_x^{+1} is then found by applying the relation $l_x^{+1} = l_{y'}/K^+$ and the second row of the triangles is obtained, and so on. When the pattern has been completely laid out in the plane, folds are made along all diagonal lines in the same direction and folds in the opposite direction made along the $2l_y$, $2l_{y'}$, etc., line segments. The construction is complete when the ends of the conical blank close on each other.

Several constructions developed from a conical frustum having $\gamma = 25^\circ$ are shown in Figures 38 to 41 for $n_f = 5$ and various values of unit end shortenings. The end shortenings are $1/10$, $1/2$, and 1 for Figures 38, 39, and 40, respectively. Figure 38 is so oriented as to show the profiles of the planes at the left and right sides of the figure. Going from top to bottom, down the extreme left hand edge are planes (+), (-), (+), and (-) while down along the right-hand edge are planes (-), (+), (-), and (+), all in profile. The greater aspect ratio of the pattern shown in Figure 39 over that in Figure 38 is evident. This is due to the greater value of end shortening. The total collapse pattern of these configurations shown in Figure 40 is presently the most interesting. The blurry lines across the photograph is the edge of a shell of Plexiglass that was used to hold the pattern flat during the picture taking and should be ignored. The total conical surface that was initially above the plane of the pattern is contained in the plane of the collapse pattern. The pattern consists of triangles whose aspect ratios are substantially greater than those in Figure 39. A view of this pattern as it appears on the inside of the shell is shown in Figure 41, in which the array of fold lines is particularly well indicated.

That this process is evident in nature was shown by the results of several experiments in which thin conical shells of aluminum alloy were impacted in a drop testing machine at an initial velocity of approximately 20 ft/sec. The shells, which had the same size and shape as that used for the construction ($\gamma = 25^\circ$), were held circular at both ends and were mounted in the machine with no provision for venting the internally contained ambient air. Inside and outside views of the collapsed portion of one of the shells is shown in Figures 42 and 43. The remarkable degree of similarity between these patterns with the theoretical patterns, especially when viewed from the inside is evident.

This evidence would tend to support the theory that the buckling and collapse process of thin shells having zero Gaussian curvature follows an essentially inextensional path, at least in the later stages of large unit end shortening.

6. PHASE II - HIGH VELOCITY IMPACT

6.1 Apparatus

The projectile, the body that is accelerated in the gun barrel and finally impacts against the shell specimen, consists of two essential parts, the impact head and the carriage. The projectile is shown in Figure 44 with the impact end facing forward. The impact head is a steel ring having the dimensions: 6-3/4 in. OD, 4-3/4 in. ID, 1-1/2 in. length. It was cut from standard steel mechanical tubing and its end faces machined flat. At its rear end, it is attached to the carriage by six screws. The carriage is a one piece aluminum sand casting in a high impact strength grade (220T-4). It is essentially a hollow cylinder having a closed forward end and three bearing rings on which the projectile rides through the barrel. The rings are machined to have a diametral clearance of .003 in. with respect to the barrel bore.

The projectile was carefully designed for superior muzzle exit stability. This property is essential if careful alignment between projectile and specimen is to be achieved at impact. These design features are: (a) three ring design gives the projectile support on two rings until the projectile is out of the muzzle by two-thirds of its length. (b) 40% of the driving pressure is exerted against the forward closure plate, whereas most of the friction forces acting on the projectile are at the rear.

Other provisions that were made to assure good impact alignment were adjustments on the gun barrel and specimen mounting assembly. This permits alignment before each test. The alignment is finally checked by inserting the projectile in the muzzle of the gun (at right) such that it rests on its rear two bearing rings, thereby protruding out a distance of 4 inches. The specimen is extended from the mounting assembly (at left) a maximum amount until it makes contact with the projectile. This is shown in Figure 45, with the gridded shell clearly well aligned with the projectile. In the normal testing position, the end of the specimen is at the extreme left of the picture.

Another factor which contributes to accurate alignment is a low exit gas pressure. This is accomplished by a long barrel, which is itself required to extract a maximum amount of available energy from the propelling gas. The exit pressure, for instance, is only 4 psig. for a firing pressure of 300 psig.

The specimen is mounted to a solid aluminum base which is seven inches in diameter and eight inches long. The base contains a set of six rollers which allow the specimen assembly to translate in its housing with a friction force of only several ounces. The weight of the mount (or carriage) assembly is 43 lb.

6.2 Specimens and Instrumentation

The shells used in this phase were the same as those described in section 5.2. In Figure 46 an instrumented shell is shown mounted to its carriage. It is clamped at its rear end to the carriage by four segments of a ring (not shown) and at the impacted end is open. The edge condition at the impacted end is free.

The shells were instrumented with pairs of strain gages so wired as to cancel the bending strain components. Three pairs of gages were mounted

axially, equally spaced about the mid-length position. Another pair, in line with one of the former was mounted 2 inches behind the impacted end. This instrumentation scheme was used on all specimens except HV-7 which had one pair of gages at the mid-length section and another pair 2 inches behind the impacted end.

In addition, a Statham Model A5-200-350 accelerometer was mounted in the rear end of the aluminum specimen carriage mainly for the purpose of determining the rigid body motion of the shell-carriage assembly.

The shells were unpressurized and were tested without provision for venting of the internal air. This latter condition was acceptable, since during the more interesting part of the measurement time, the static increase in pressure due to decrease of the internal volume is negligible.

A simple and reusable device was employed to secure a measurement of the velocity of the projectile immediately prior to impact and also to trigger the instrumentation. This consisted of two pivoting rod units that were mounted on a wooden block about 6 inches apart. The assembly was mounted in the impact apparatus such that the 6 inch dimension was parallel to the direction of the projectile motion and the tips of the rods were in the path of the projectile. Mounted in the wooden block were two piano wire sections, one near each of the pivoting rods, just beyond the path of the projectile. When the projectile swept by the trigger assembly, the rods were caused to rotate one after the other, thereby making contact with their respective wire sections. The rods and wire sections were connected in an electrical circuit together with an electronic counter, such that the first to be struck by the projectile would initiate the counter and the second would stop it. The second unit would also simultaneously trigger all the instrumentation. With the exact distance between the two contact points known and the time required to traverse the distance, the average velocity of the projectile at a point three inches in front of the impact end of the specimen could be easily determined. The device functioned very well and proved to be both reliable and convenient.

6.3 Results

A total of eight tests were performed during Phase 2, two of which were preliminary in nature, being necessary to check out the operation of the facility and instrumentation. In the first fully instrumented test, (HV-3) data were not obtained due to a failure of the instrumentation trigger device. From the fourth to the next to the last test, the system performed well. In the last test, conducted at a velocity considerably higher than the previous test, data were not obtained although the oscilloscopes triggered apparently as planned and the velocity measurement was obtained. This test, however, yielded a highly significant and long awaited result. A list of the tests performed in which velocity measurements were obtained is given in Table 4.

TABLE 4 — DESCRIPTION OF HIGH VELOCITY IMPACT TESTS

Test No.	Chamber Pressure psig	V _o ft/sec	h in.
HV-3	100	224	.016
HV-4	100	216	.016
HV-5	100	201	.016
HV-6	100	225	.016
HV-7	110	271	.016
HV-8	225	392	.016

The facility performed according to expectations. In addition to producing very symmetrical impacts and reproducibility in observed and measured specimen behavior, it accomplished the deceleration of the projectile each time as anticipated, with no damage to the apparatus. Damage to the expendable projectiles, moreover was held to a minimum and when the cause of the damage was determined, the projectiles were recovered in practically reusable form. The calculated muzzle velocity-chamber pressure characteristic of the facility is shown in Figure 47 for a projectile weighing 14 pounds.

The shell specimens were essentially similar after all the tests, except that obtained from Test No. HV-8. All specimens were recovered essentially intact within the buffer cylinder although some damage occurred due to a restriction in the buffer cylinder which hindered somewhat the motion of the collapsed portion of the shell as it entered the buffer. In all cases, however, whatever damage that did occur was slight and did not hinder the study of the specimen after the test.

All of the specimens collapsed at both ends, a behavior practically always observed in shells of similar radius/thickness ratios, but in the present cases, the collapse at the rear end was considerable. For example, one shell showed collapse at the impacted and opposite ends over distances of 11-1/2 and 7 inch respectively. In all cases, one or several uniform ring buckles were present at the impacted end but none at the opposite end. Collapse elsewhere was in the triangular mode with usually six full circumferential waves present except in the region adjacent to the ring buckles in which the number was substantially higher but difficult to count. Efforts were made to expand the shell in order to obtain a count of the wave number, but this has proven to be quite difficult. A presentation of the data now follows.

Test No. HV-4

The strain records obtained from this test are shown in Figures 48 and 49. Figures 48(a) and (b) apply to the forward and mid-length strain gage positions. The strains at both locations are seen to rise abruptly to a value of 3650 μ in/in and rapidly fall into tension at 104 μ sec after initiation of the response. The strain pulse clearly reaches the mid-length gage after the forward gage as

can be seen from a comparison of their zero traces. The time delay was measured at 40μ sec which corresponds almost exactly to the time required by elastic waves to traverse the distance of nine inches between gage positions. After the initial peak, subsequent strain maxima do not exceed it.

The axial half length of the ring collapse waves present at the impacted end of the specimen was measured and found to be .15 inch. The time of 104μ sec previously noted, corresponds to a projectile displacement of .270 in beyond the initial impact position, which is almost twice the half length of the collapse wave. Hence it is established that the first strain pulse shown in Figure 49 corresponds to the initiation of instability of shell in the ring mode and further to the progression to total collapse in the ring mode of the initial instability. Furthermore, it is clearly seen that the instability occurs at a time close to 24μ sec. after impact which is about one fifth the time required for an elastic stress wave to arrive at the rear end of the shell. These data strongly substantiate the mechanism of buckling described in Reference 8.

The time duration of several adjacent strain pulses in Figure 49 is the same as that of the initial pulse. This suggests the formation of additional ring buckles adjacent to the initial one. This is fairly well evidenced in the specimen.

The initial peak strain value of 3650μ in/in is the highest obtained during these studies. The highest previous strain value of 2140μ in/in was obtained in an aluminum shell of similar dimensions but of half the present wall thickness, impacted at the 46 ft/sec.

Referring to Figure 49, which shows the strain at another mid-length gage position on a 500μ sec/div. time scale, it is seen that the character of the strain variation is changing by about the time of 750μ sec. (Figure 48(b) shows this time to be about 500μ sec.) Prior to this time the strain is maintained at relatively high values but at 700μ sec it falls abruptly to relatively low values of compression for about 500μ sec and then falls to a similar value of tension. Thereafter the strain rises and falls in intervals ranging from 500 to 700μ sec. It is thought that this different character of the strain corresponds to the occurrence of triangular modes of buckling and collapse.

Test No. HV-5

A plot of a faint strain trace obtained from the forward gage position is shown in Figure 50. A much higher peak value of strain was obtained in this test than in the previous one, a value of 6100μ in/in. Although the reason for the difference is not presently understood, it is noted that the strain otherwise behaves essentially as in the previous test. It decreases to 20% of the peak value in 100μ sec, thereby also agreeing with the time to collapse fully a ring buckle.

It is interesting that the acceleration of the shell-mounting carriage assembly as a rigid body, as shown in Figure 51, in no way reflects the severity of the impact even after the substantial time of .0045 sec.

Specimen No. HV-5 is shown in Figure 52 after the impact with the impacted end upward. At this end, two ring collapse modes are evident, these followed by triangular collapse stages.

Test No. HV-6

Strains records obtained from test No. HV-6 show essentially the same data as found in the previous tests. In Figure 53 the strains from two mid-length positions have identical initial peak values of $3140 \mu\text{in/in}$. This is lower than the value of $3650 \mu\text{in/in}$ obtained from test No. HV-4 for a similar location. The time at which these strains decrease to zero are in one case the same as and in the other about ten percent greater than those of test No. HV-4. The strain measured at the forward gage position (Figure 54) goes off scale and is estimated at $7400 \mu\text{in/in}$. The deceleration record (Figure 55) is quite similar to that of the previous test.

Test No. HV-7

The data obtained from test No. HV-7 display much the same values and overall behavior. The mid-length initial peak strains shown in Figure 56 are identical at two different gage positions with a value of $2700 \mu\text{in/in}$. This is still lower than the previous tests, despite the higher velocity. The initial pulse in each case decreases to zero in about the same time as noted previously. The initial response at the forward gage position (Figure 57) goes off scale but its value is at least $6500 \mu\text{in/in}$. Similarly, the deceleration trace (Figure 58) is quite familiar in appearance.

Specimen HV-7 is shown in Figure 59 after impact. Its greater amount of shortening is not necessarily indicative of the higher velocity. The specimen was fully extended from the buffer cylinder in this case, whereas in all previous tests, the specimens were only extended about eight inches beyond the buffer cylinder. Here again two rows of ring collapse patterns are visible. Also noteworthy are the well formed triangular collapse patterns with $n_f = 6$.

Test No. HV-8

In this test no data besides the velocity measurement were obtained. The result, however, was very significant. It was anticipated in Reference 8 that when the impact velocity is sufficiently high, the natural form of buckle and collapse will be in the form of rings rather than triangles. This mode of buckling and collapse, though a higher energy mode than the triangular mode, will occur simply because it can occur in a shorter time than any other mode of collapse. Up to the time of this test, however, the only observed ring collapse modes in thin shells having a free impacted edge occurred largely as a consequence of the inevitable friction between the shell edge and the impacting body. This conclusion was reached principally because such ring modes were confined to one or two (even at 271 ft/sec) waves adjacent to the impacted end. The specimen obtained from this test, performed at 392 ft/sec , however is substantially different and is shown in Figure 60. At the impacted end there are at least six and perhaps twelve complete ring collapse waves. The waviness out of their plane that they exhibit is easily explainable as the effort of the collapsed ring configuration to rid itself of the high extensional circumferential strains intrinsic in such a configuration. Buckling out of their planes is the only path the rings can take, once adjacent rings have formed, since the latter have enormous in-plane rigidity. The occurrence of the rings so far removed from the impacted end cannot be explained by friction. Neither should it be due to the effect of internal pressure which can build up as the volume of the shell collapses in the absence of an air vent. This is because the rings form at the start of the

impact process and therefore during the formation of even a number of them, the volume decrease is not sufficient to produce an internal pressure large enough to cause them by itself.

The results of Phase 2 experiments are summarized in Table 5.

TABLE 5 — HIGH VELOCITY IMPACT TEST RESULTS

Test No.	V_o ft/sec	ϵ_{cr} μ in/in	ϵ_{max} μ in/in	t_{cr} μ sec	Principal Collapse Mode
HV-4	216	3650	3650	24	Triangular
HV-5	201	--	6100	--	Triangular
HV-6	225	3140	7400	55	Triangular
HV-7	271	2700	>6500	32	Triangular
HV-8	392	--	--	--	Ring

In the above table, ϵ_{cr} refers to the strain as measured from the mid-length position, at which abrupt descent from the first peak initiates; t_{cr} is the corresponding time. The mid-length position is taken instead of the forward position because this is considered more pertinent to the question of the overall load carrying ability of the shell structure.

7. PHASE III - NON-RIGID IMPACT

Prior to conducting instrumented tests of shell structures impacting into non-rigid media, tests were performed using a relatively rigid body to determine the impact forces for the case in which the impacting body does not undergo significant changes in length. This was done to establish a reference of loading, in which all the variables due to the apparatus and instrumentation would participate, and against which the subsequent measured loadings for shell structures could be compared.

7.1 Specimens and Instrumentation

The rigid body structure, shown in Figure 61, consisted of three major parts: (1) a flat bottomed circular disc made of aluminum alloy, designated as plate A, had an outside diameter of 7-3/8 inches and was mounted at the impact end of the structure; a piezoelectric crystal accelerometer was mounted at the inside center of the plate; (2) a circular fixture, labelled plate B, to which an accelerometer was also mounted centrally, contained a contoured pin used for holding the structure to the release mechanism of the drop carriage; (3) a thick walled aluminum pipe (1/2 inch thickness) having accurately machined ends. The three parts were clamped together by means of three equally spaced 1/4 inch diameter through bolts. The entire weight of the rigid body structure, including instrumentation, was 12.21 lb.

The flat disc configuration was chosen in order to obtain impact forces that were sufficiently high to produce buckling of the shell specimen. This conclusion was dependent on the maximum impact velocity obtainable from the drop test apparatus. Results previously obtained from high speed motion pictures showed that with the drop test apparatus, very flat impacts between the disc and the initial water surface were obtained. Instrumented tests performed during this contract, however, showed that a considerable amount of variation could not be predetermined. A better configuration, which would provide sufficiently high impact forces, would be a spherical segment of large radius.

The shell specimen was mounted in the same end plates A and B as used in the rigid body structure. The shell was clamped at both ends to these plates by means of circular ring segments as shown in Figure 62. Endevco Model 2225 piezoelectric accelerometers were mounted centrally to both plates A and B and in some tests, a Gulon Model AA 25 accelerometer was mounted to plate A.

The weights of the shell structure were 15.42 lb including a .016 in. thickness shell and 15.09 lb including a .008 in. thickness shell, both with accelerometers. The complete weights of plates A and B were 5.32 and 9.45 lb respectively.

7.2 Outline of Tests

7.2.1 Sand Impact

The impact tests in sand are summarized in Table 6. The sand utilized in all tests was dry Wedron silica sand grade 7020 having a grain fineness (AFS) of 84.42%

TABLE 6 - DESCRIPTION OF SAND IMPACT TESTS

<u>Test No.</u>	<u>Specimen</u>	<u>Impact Velocity ft/sec</u>
S-4	Rigid Body	23
S-5	Rigid Body	23
S-6	Rigid Body	23
S-10	Rigid Body	33
S-11	Rigid Body	33
S-12	Rigid Body	33
S-7	Rigid Body	43
S-8	Rigid Body	43
S-9	Rigid Body	43
S-16	.008 in. shell	23
S-17	.016 in. shell	23
S-19	.008 in. shell	33
S-14	.016 in. shell	33
S-15	.008 in. shell	43
S-13	.016 in. shell	43

7.2.2 Water Impact

The water impact tests are summarized in Table 7 below.

TABLE 7 - DESCRIPTION OF WATER IMPACT TESTS

<u>Test No.</u>	<u>Specimen</u>	<u>Impact Velocity ft/sec</u>
WPI-8	Rigid Body	23
W-1	Rigid Body	43
W-2	Rigid Body	43
W-2A	Rigid Body	43
W-3	Rigid Body	43
W-6	Rigid Body	43
W-7	.008 in. shell	43
W-8	.008 in. shell	43
W-9	.016 in. shell	43
W-10	.016 in. shell	43
W-11	.016 in. shell	43

7.3 Results

In general, the clarity of the measured data was considerably better at the lower than at the higher impact velocities. This is not surprising due to the fact that the rate of force input associated with higher impact velocities excites higher frequency components of vibration in the structure and instrumentation. By first studying the data obtained at the lowest velocity used in the program, 23 ft/sec, the shape of the rigid body impact force curve was clearly established. This served as a guide in estimating the rigid body force curves corresponding to the higher velocities.

Contrails

In most cases of both the sand and water impact tests, but especially in the latter, the deceleration record of plate A showed considerably greater vibratory response than that of plate B, a phenomenon to be expected due to the proximity of accelerometer A to the plane of application of the impact forces. The greater response in the case of water impact can be explained by the initial elastic behavior of the water.

The data obtained from accelerometer B were generally clearer, especially in the tests conducted with shells, thereby permitting a ready evaluation of the buckling load.

7.3.1 Sand Impact

a) Rigid Body Tests - The force-time records obtained from the rigid body impacts at 23 ft/sec velocity are shown in Figures 63 to 65, which represent three tests, namely, S-4, S-5, and S-6, respectively. These are shown to indicate the reproducibility of the measurements and to illustrate certain differences as well. Referring to Figure 65 the correspondence between the A and B records is evident. In addition the clarity and smoothness of the trace is striking. The basic shape of the rigid body impact curve can be described in terms of a rapid initial rise to a rounded peak, followed by a gradual decay. The decay portion consists of a linear part followed by an exponentially decreasing part. In contrast to the relative smoothness of the records shown in Figure 65, the traces obtained from another rigid body impact at 23 ft/sec velocity (Figure 63) contain regions of high frequency, high amplitude, vibrations. These appear to be spurious vibrations, perhaps due to ringing of the accelerometer, which oscillate about the mean rigid body curve. Although their cause is not known, it may be noted from the similarity in the times at which they occur in both the A and B records of Test No. S-5 and the similarity between the B records of Tests Nos. S-4 and S-5, that they have some detailed significance in the sand impact loading mechanism. These vibrations, however, were not considered important to the problem under study. The curve obtained by passing through the mean of the extremes of the oscillations represents the force history of a perfectly rigid body. The curves obtained in this manner from Figures 63 and 64 are remarkably similar to the relatively smooth curves obtained from Test No. S-6.

A comparison of the mean faired curves obtained from Tests Nos. S-4, S-5, and S-6 is shown in Figure 66. The curves for plates A and B for each of tests S-5 and S-6 compare very closely although comparison between the two tests shows some variation both with respect to magnitude of the peak value and the time at which the peak is attained. The mean B curve of test no. S-4 agreed almost identically with that of S-5.

The average of the peak deceleration values was found to be 327 g's and the corresponding time 972 μ seconds.

Another set of A and B records, this obtained from Test No. S-12 run at an impact velocity of 33 ft/sec, is shown in Figure 67. These curves are characterized by well defined oscillations of large amplitude. The mean curve traced through these oscillations has a shape which is similar to the ones previously obtained from the lower velocity tests. The peak deceleration value obtained from the mean curve was close to 950 g's and occurring at a time 250 μ seconds.

Contrails

The corresponding set of deceleration traces obtained from Test No. S-9 run at a velocity of 43 ft/sec is shown in Figure 68. These traces, in comparison with the previous ones, manifest a considerably greater degree of oscillation, particularly the A trace. The main curve is, however, readily obtained from the B trace, and displays a shape similar to the previous ones. The peak value of the deceleration obtained from this curve was 1700 g's occurring at a time of 200 μ seconds.

Summarizing the rigid body tests, the trend with increasing impact velocity is for the peak amplitude of deceleration to increase and the time to attain the peak to decrease.

The impact by the rigid as well as the shell structure produced a crater in the sand which was well formed and symmetrical about the axis of the structure. The crater surface rose to form a rounded lip about the crater center. The diameter of the lip was close to 14 inches, or twice the diameter of the front plate.

b) Shell Impact Tests - It was anticipated that when the shell structure specimen impacted the non-rigid medium the deceleration of plates A and B would follow, in the mean, the rigid body deceleration curve prior to the initiation of buckling. During this time it was expected that the longitudinal vibrations of the shell would play a major role in altering the deceleration curve from that of the rigid body curve. With the occurrence of buckling, it was expected that the deceleration of the plate A would abruptly increase due to the reduced rigidity of the buckling shell behind it. Similarly, the deceleration of plate B was expected to reduce abruptly due to the sudden decrease in axial force transmitted to it through the buckling shell. Thus, the time of initiation of buckling would be detected from the traces of accelerometers A and B. In addition the value of the buckling load could be obtained from the acceleration of plate B by observing the value of deceleration beyond which the mean curve rapidly reduced. This expectation was fulfilled in all of the shell tests.

Test No. S-16 (.008 in. shell, $V_0 = 23$ ft/sec)

The acceleration traces obtained from this test were rather faint and had to be scrutinized with a magnifying glass under suitable illumination. They are nevertheless presented in Figure 69 for the record. The results are shown in Figure 70 against a background of the envelope of the rigid body curves obtained from tests S-4, S-5, and S-6. The dashed curve applies to the .008 in. wall thickness shell and can be seen to rise rapidly to a peak of 170 g's at a time of 375 μ seconds and abruptly decreases thereafter. At about .002 seconds the trace shows a sustained deceleration beginning with a value of 47 g's and thereafter reducing to a value of 25 g's which is sustained beyond .006 seconds. This latter section of the curve may correspond to the average force that can be sustained by the shell in its postbuckled state. The behavior of plate A on the other hand is shown in Figure 71 in which it is seen that the deceleration increases rapidly after an initially slow rise. Thereafter it rapidly descends well within the rigid body envelope. Thus the behavior of both plates A and B agreed with expectations. The buckling load deduced from the record is: $P = 170(9.61) = 1632$ lb. and the buckling stress: $\sigma = 11,330$ psi. which corresponds to a value of $\bar{\sigma} = \sigma R/Eh = .394$.

Contrails

The specimen shown in Figure 72 collapsed at the impacted A end in a pattern of 5 or 6 full waves and was permanently shortened by 18 inches. At the B end there were many small permanent buckles having very small lateral deflections. The number of full waves was 16 and the pattern extended around one half the circumference. The buckling at this end was confined to a region within one inch of the end clamps.

Test No. S-17 (.016 in., $V_0 = 23$ ft/sec)

This test was really the third test conducted on this particular specimen, all at 23 ft/sec. As a result of the first impact, no buckling was present in the shell, at least none that could be detected by the unaided eye. After the second impact, some permanent buckling of low amplitude was present, indicating that some permanent deformations had resulted from the first impact. On the third drop test, data were obtained and are shown in Figure 73. Since this applies to a shell initially containing buckles, the value of the peak deceleration transmitted to plate B by the shell was expected to be smaller than that for an initially underformed shell. The greatly differing gross characters of the A and B records is evident. The faired curve of record B is shown compared to the rigid body deceleration envelope in Figure 70. The peak deceleration value is 475 g's and occurs at 510 μ seconds. The corresponding maximum load is $475(9.77) = 4640$ and the stress $\sigma = 16,100$ psi. This corresponds to a dimensionless stress, $\bar{\sigma}$ of .271. The maximum rigid body force shown in Figure 70 is equal to $357(12.21) = 4360\#$ which is somewhat lower than the maximum force sustained by the shell. This discrepancy reflects the fact that the rigid body deceleration envelope, based as it was on three tests, does not cover the maximum range of variations in the impact deceleration of a flat bottomed object.

Test No. S-19 (.008 in., $V_0 = 33$ ft/sec)

Deceleration records for plates A and B are shown in Figure 74. Here again the great difference in the initial responses of the two plates is evident. Whereas the deceleration of plate A clearly rises to a value of 3,000 g's and remains near this value until about 80 μ sec., the deceleration of plate B attains a peak of 378 g's at 200 μ sec. Thereafter, it abruptly decreases and oscillates about the base line until 460 μ sec. after impact. The faired B curve is shown (Figure 75) together with the rigid body curves obtained from Test S-12. The peak deceleration is 320 g's and occurs at 200 μ sec. The buckling load, therefore is $P = 320(9.61) = 3080$ lb. The corresponding buckling stress and the dimensionless stress are respectively $\sigma = 21,400$ psi and $\bar{\sigma} = .728$.

Specimen S-19 is shown in Figure 76 as it appeared after the test with the impacted end down. At the impacted end is a fully collapsed region of the inextensional type consisting of rows of five full circumferential waves. Adjacent to this is a region of triangular buckles having 10 full circumferential waves, which can be seen in the figure. At the opposite or B end, immediately adjacent to the clamped section, is a row of triangular buckles having about 12 full circumferential waves. In the shell away from the ends, there is no sign of buckling or other permanent deformation. The overall shortening of the shell is 3.51 inches most of which is accounted for on the collapsed region at the impacted end.

Contrails

Test S-14 (.016 in., 33 ft/sec)

Records obtained from this test are shown in Figure 77. The previously noted great difference between the decelerations of plates A and B is again clearly evident. A sharp and well defined decrease in the deceleration of plate B is shown at 400 μ sec after impact. This decrease is taken as the indication of buckling of the shell. The peak value attained prior to the sudden decrease is 1015 g's, which is the highest value of any consequence in trace B. On the other hand, a significantly large peak of 4,400 g's occurs near the beginning of impact in the case of plate A. The smoothed version of the B trace is compared with the rigid body curve in Figure 75. The peak value of the deceleration of plate B is seen to be 800 g's which is comfortably below the rigid body peak value. After the peak is attained, at a time of 290 μ sec., the deceleration abruptly drops and becomes zero at 410 μ sec. The peak force, or buckling load is 7810 lb and the stress is 27,100 psi. The dimensionless stress, $\bar{\sigma}$ is .446.

The specimen shown at the left of Figure 78 shows buckling at both ends with a transition extensional stage at the impacted end in the early stages of formation of a triangular buckle pattern of 6 full circumferential buckles in a fairly advanced stage of collapse. The specimen is shorter than the initial length by .36 inch.

Test No. S-15 (.008 in., $V_0 = 43$ ft/sec)

The enormous difference between the responses of accelerometers A and B as shown in Figure 79 is evident. The peak of the deceleration of plate B, 585 g's, occurs at 190 μ sec., and thereafter abruptly falls to below zero. A smoothed curve of the above record is shown in Figure 80 together with the rigid body curve. This shows the peak deceleration to be 330 g's which corresponds to a force (buckling load) of 3170 lb. The buckling stress is then $\sigma = 22,000$ psi and $\bar{\sigma} = .741$.

The specimen displays a shortening of 4.68 inches, essentially all of this being due to the orderly collapse of the impacted end. This is shown at the left in Figure 81. The collapsed region consists of fourteen rows of triangular buckles having 5 full circumferential waves. There are very minor deformations in the region adjacent to the clamping station on plate B, but the shell is otherwise undamaged.

Test S-13 (.016 in., $V_0 = 43$ ft/sec)

Deceleration records for plates A and B are shown in Figure 82, that of plate B clearly showing the effect of shell buckling. The maximum peak sustained by plate B is seen to be about 1590 g's whereas the deceleration trace for plate A shows very much larger values, such as the 3800 and 6600 g peaks near the beginning of the trace. The smoothed version of the initial part of the B trace is shown in Figure 80 together with the rigid body curve. The peak value of the force transmitted to plate B is 810 g's or a force of 7910 lb. The buckling stress is therefore 27,400 psi and the dimensionless value $\bar{\sigma} = .462$.

The specimen, shown at the right of Figure 81 displays a number of interesting features. At the impacted end there is a region of collapse in the form of triangular buckles of seven circumferential waves and at the opposite end a

partially collapsed region adjacent to the clamping station. This latter region is in a less advanced stage of collapse than that of specimen S-14 but at the impacted end, specimen S-13 is considerably more collapsed than specimen S-14. At the opposite end of specimen S-14 the partial collapse is in the form of a transition configuration between an initially extensional pattern and a triangular pattern which appears would have eight full circumferential waves when more fully developed. At the center length of the shell is an array of triangular buckles in a diagonal configuration. The full circumferential wave number of these buckles is ten. By far the most interesting feature of this specimen can only be seen by observing the inside polished surface of the shell with grazing incidence light. This reveals that the circumferential region at which the diagonally arrayed buckles are positioned and extending practically over the entire length of the shell are extremely uniform extensional ("ring") buckles permanently present. These are indistinguishable to the touch. The axial wave length of these buckles is .65 inch as compared with .74 from the infinitesimal deflection theory. These ring buckles most probably are the first configuration of deformation other than simple compression-expansion in the evolutionary chain of deformational patterns which ultimately ends in total collapse. The diagonally arrayed triangular buckles clearly result from further shortening of the ring configuration beyond the state present in specimen S-13 and in fact have an axial wave length of about .70 inch. This is very evident in Figure 83 which shows a properly illuminated view of the inside surface of the shell.

The shell was shortened by .72 inch as a result of the impact.

A summary of the results obtained from the sand impact tests is given in Table 8.

TABLE 8 - SAND IMPACT TEST RESULTS

Test No.	V_0 ft/sec	h in.	p lb.	σ psi	$\bar{\sigma}$	n_f	Δl in.
S-16	23	.008	1632	11,330	.394	5-6	1.8
S-17	23	.016	4640	16,100	.271	---	---
S-19	33	.008	3080	21,400	.728	5 10	3.51
S-14	33	.016	7810	27,100	.446	6	.36
S-15	43	.008	3170	22,000	.741	5	4.68
S-13	43	.016	7910	27,400	.462	10 7	.72

7.3.2 Water Impact

As previously noted, the accelerometer response to water impact contained many high frequency oscillations which made difficult the problem of finding the rigid body response. Several approaches to this problem were used. An R-C low pass filter with a 10KC cutoff was employed at first, and although it was found to be useful in clarifying the response in the lower velocity impacts, such as 23 ft/sec, it was inadequate in the higher velocity tests. The

Contrails

difficulty seemed to be that significant information present in the form of oscillations higher than 10KC was not passed through the filter. Another approach was to use a high frequency oil damped accelerometer, but the presence of high frequency components in the input caused considerable oscillation despite the damping quality; in addition a large zero shift due to the accelerometer was unacceptable. The best approach found was to use very high frequency piezoelectric crystal accelerometers for both plates A and B, and Endevco Model 2225 units were found satisfactory. Notwithstanding, there remains considerable room for improvement in force measuring instrumentation for structural impact.

The rigid body reference deceleration curve was obtained from Test No. W2A. The records for plates A and B are shown in Figure 84. The rigid body curve was estimated from the B record and is shown in Figure 87.

In the sand impacts, the impacting structure penetrated beneath the initial plane of the surface a distance of about 1-3/4 inches. In this distance the entire momentum of the body was expended. In the case of water impact, however, the impulse delivered to the body during the high deceleration phase of breaking through the surface of the water is only a portion of the initial impact momentum of the body. The impact for our purposes can be described in two phases, at least from a consideration of the axial loading imposed on the structure. The first is the high force-short time interval encountered during the initial phase of impact. As obtained from Test W2A, this is a curve having a shape approximated by a half-sine, with an amplitude of about 1600 g's and a duration of 400 μ sec. For this example the momentum extracted from the body is only 1/3 of its total. Following this phase is a gradual deceleration through several feet of water. During this interval, the body plows through the water with a trailing cavity which is maintained for a considerable portion of the gradual deceleration phase. As the body is slowed down, principally by the drag forces imposed on its front surface, the cavity contracts laterally towards the body and finally collapses over it. When this occurs the body is subjected to distributed lateral loading and may readily buckle if a thin shell structure is involved. These phenomena were observed in high speed motion pictures taken during this program.

In summary, the initial impact phase contributes the major axial loading whereas the cavity collapse produces a significant lateral loading. If a structure is to withstand water entry, it must be designed to resist both types of loading.

Tests W-7, 8 (.008 in., 43 ft/sec)

Deceleration records for plates A and B are shown in Figures 85 and 86, respectively. Again the great difference in the deceleration between the two positions is evident. A faired version of the W-7 B curve and the W-8 B curve as-is are plotted together with the rigid body curve. The peak decelerations for W-7 and W-8 are 250 and 400 g's respectively and occur at 350 μ sec and 230 μ sec. The corresponding forces (buckling loads) are 2400 and 3840 lb. The buckling stress for W-7 is therefore $\sigma = 16,700$ and $\bar{\sigma} = .562$ and for W-8 is $\sigma = 26700$ and $\bar{\sigma} = .890$.

Contrails

Specimen W-7 shown in Figure 88 left, collapsed at the impacted end in a triangular pattern consisting of from 5-6 full waves. At the opposite end two rows of triangular buckles having a full circumferential wave number of 12 extend completely around the shell.

Specimen W-8 has an interesting type of collapse adjacent to the clamping station at the end opposite the impact. See Figure 89 upper end. This may account for its unusual buckling characteristics. Apparently what has happened is that a cross section of the shell initially 3/4 in. away from the clamping station moved 1/2 in. toward that station; in so doing, the material between the two sections folded inward and under the material immediately adjacent to the clamping station. The action can further be described as an attempt by the shell to buckle symmetrically inward resulting in the formation of twelve full waves around the circumference. By contrast, the collapse at the impacted end was small and considerably smaller than that of specimen W-7. The indication that the collapse configuration of specimen W-8 was of a higher energy mode than that of W-7 is further strengthened by the large difference between their changes of length. Specimen W-7 shortened by 1.64 in whereas W-8 shortened by only .46 inch.

Tests W-9, 10, 11

The records for plate B for tests W-9, 10, and 11 together with that of plate A of test W-9 are shown in Figures 90 and 91. In each case, as before, the abrupt change in the deceleration following a clearly defined pulse shows the effect of shell buckling. Plots of the smoothed records of plates B are shown in Figure 92 together with the rigid body deceleration curve obtained from test W-2A. The peak values of all three curves are very close to each other and except for that of W-11, resemble the general size and shape of the other data obtained on the .016 in. thickness shells (neglecting S-17 which was prebuckled). The curves yield the following values:

For W-9: $P = 7810$ lb at $360 \mu\text{sec}$. $\sigma = 27,200$ psi, $\bar{\sigma} = .457$

For W-10: $P = 7410$ lb at $380 \mu\text{sec}$. $\sigma = 25,700$ psi, $\bar{\sigma} = .433$

For W-11: $P = 6620$ lb at $510 \mu\text{sec}$. $\sigma = 23,000$ psi, $\bar{\sigma} = .388$

Specimens W-9 and W-11 are shown in Figure 93 at the left and right, respectively. In both cases, the larger amount of deformation occurs at the impacted end, which is the lower end in the figure. It is noted that the deformational modes of the two shells are distinctly different. Specimen W-9 has a triangular pattern of 10 full circumferential waves, whereas specimen W-11 displays a partially transformed ring deformation which is similar to that of specimen S-14.

In general, the water impacts produced less damage to the specimens than the sand impacts at the same velocity. Specimen W-9 and W-11 shortened by only .02 in. and .10 in respectively as compared to .72 in. in Specimen S-12.

Contrails

The results of the water impact tests are summarized in Table 9 below.

TABLE 9 - WATER IMPACT TEST RESULTS

Test No.	V_o ft/sec	h in.	p lb.	σ psi	$\bar{\sigma}$	nf	ΔL in	t_{cr} sec
W-7	43	.008	2400	16,700	.562	12 5-6	1.64	350
W-8	43	.008	3840	26,700	.890	12	.46	230
W-9	43	.016	7810	27,200	.457	10	.02	360
W-10	43	.016	7410	25,700	.433	--	--	380
W-11	43	.016	6620	23,000	.388	ring	.10	510

PART II. ANALYTICAL INVESTIGATION

8. ELASTIC BEHAVIOR OF AXIALLY LOADED CYLINDRICAL SHELLS

Reference 18 presented a nonlinear analysis of the problem of dynamic buckling of an axially compressed cylindrical shell stabilized by constant internal pressure. In that investigation it was assumed that the rate of end shortening was constant. Initial imperfections were considered and the various deflection parameters were taken to be completely free and their values were determined by an approximate solution of the equations of motion. This is in contrast to earlier work of Volmir (Ref. 5) wherein certain of these parameters were assumed to have the same values indicated by static analysis. The ends of the shell were elastically supported which essentially implies that the analysis should not be applied to extremely short cylindrical shells.

The present study is concerned with a different type of condition, namely one where the dynamic axial loading is prescribed as a function of time. The shell is assumed to be thin, i. e., the thickness is small compared to the radius. Further, the velocity at which the struck end of the shell moves is assumed to be small in comparison with the velocity of propagation of sound in the material. The following analysis is based upon the use of a coordinate system consisting of a coordinate x along a generator, y , in the circumferential direction, and z in the inward radial direction. The components of displacement of a point in the middle surface of the shell in these directions are designated by u , v , and w respectively. Further L denotes the length of the shell, R the radius to the middle surface, h the wall thickness, P the total axial compressive force, σ the mean axial stress, and q the intensity of internal pressure. Lastly let M denote the mass of the object striking the impacted end of the shell and ρ be the mass density of the shell material.

We shall obtain the equations of motion of the shell by employing the Lagrange equations

$$\frac{d}{dt} \frac{\partial E_k}{\partial \dot{\rho}_i} - \frac{\partial E_k}{\partial \rho_i} + \frac{\partial \Pi}{\partial \rho_i} = 0 \quad (20)$$

where

- E_k = kinetic energy of the system
- Π = potential energy
- ρ_i = generalized coordinates
- t = time

It is assumed that initial imperfections are present in the shell and that they are represented by $w_0(x, y)$. The total deflection is represented by $w_1(x, y)$ and consequently the net deflection by $w = w_1 - w_0$. We select for

w_0 and w_1 the functions

$$\begin{aligned} w_0 &= f_0 \sin \alpha x \sin \beta y + \psi_0 \sin^2 \alpha x \sin^2 \beta y \\ w_1 &= g_1 + f_1 \sin \alpha x \sin \beta y + \psi_1 \sin^2 \alpha x \sin^2 \beta y \end{aligned} \quad (21)$$

where $\alpha = m\pi/L$ and $\beta = n/R$. Here m is the number of half waves in the axial direction of the shell and n the number of half waves in the circumferential direction. Further, f_0 and ψ_0 are initial deflection parameters of the shell which are considered to be known. Also, g_1 , f_1 , and ψ_1 are time-dependent deflection parameters of the deformed shell. The relations, Equation (21), imply diamond shaped buckles and correspond to an elastically supported shell, i. e., one whose ends are neither clamped nor simply supported.

We shall employ the following approximate nonlinear strain-displacement relations to describe the membrane strains in the shell:

$$\begin{aligned} \epsilon_x &= \frac{\partial u}{\partial x} + \frac{1}{2} \left(\frac{\partial w_1}{\partial x} \right)^2 - \frac{1}{2} \left(\frac{\partial w_0}{\partial x} \right)^2 \\ \epsilon_y &= \frac{\partial v}{\partial y} + \frac{1}{2} \left(\frac{\partial w_1}{\partial y} \right)^2 - \frac{1}{2} \left(\frac{\partial w_0}{\partial y} \right)^2 + \frac{w_1}{R} - \frac{w_0}{R} \\ \epsilon_{xy} &= \frac{\partial u}{\partial y} + \frac{\partial v}{\partial x} + \frac{\partial w_1}{\partial x} \cdot \frac{\partial w_1}{\partial y} - \frac{\partial w_0}{\partial x} \cdot \frac{\partial w_0}{\partial y} \end{aligned} \quad (22)$$

where ϵ_x and ϵ_y denote normal strains of the middle surface and ϵ_{xy} the shearing strain of that surface. We now introduce the Airy function $\phi(x, y)$ of the membrane stresses. This function is defined by the relations

$$\begin{aligned} \sigma_x &= \frac{\partial^2 \phi}{\partial y^2} \\ \sigma_y &= \frac{\partial^2 \phi}{\partial x^2} \\ \sigma_{xy} &= -\frac{\partial^2 \phi}{\partial x \partial y} \end{aligned} \quad (23)$$

Contrails

where σ_x and σ_y denote normal stresses of the middle surface and τ_{xy} represents the shearing stress of that surface. In Reference 18 it is demonstrated that for a biaxial stress field the relations (22) and (23) may be combined to yield the compatibility equation

$$\frac{1}{E} \Delta^4 \phi \left[\left(\frac{\partial^2 w_1}{\partial x \partial y} \right)^2 - \frac{\partial^2 w_1}{\partial x^2} \cdot \frac{\partial^2 w_1}{\partial y^2} \right] - \left[\left(\frac{\partial^2 w_o}{\partial x \partial y} \right)^2 - \frac{\partial^2 w_o}{\partial x^2} \cdot \frac{\partial^2 w_o}{\partial y^2} \right] - \frac{1}{R} \left[\frac{\partial^2 w_1}{\partial x^2} - \frac{\partial^2 w_o}{\partial x^2} \right] \quad (24)$$

where

$$\Delta^4 = \frac{\partial^4}{\partial x^4} + 2 \frac{\partial^4}{\partial x^2 \partial y^2} + \frac{\partial^4}{\partial y^4}$$

and E represents Young's modulus.

If the Relations (21) are substituted in (24) we obtain the following solution of (24) for the Airy stress function

$$\begin{aligned} \phi &= K_1 \sin \alpha x \sin \beta y + K_2 \sin 3 \alpha x \sin \beta y \\ &+ K_3 \sin \alpha x \sin 3 \beta y + K_4 \cos 2 \alpha x + K_5 \cos 2 \beta y \\ &+ K_6 \cos 2 \alpha x \cos 2 \beta y + K_7 \cos 4 \alpha x + K_8 \cos 4 \beta y \\ &+ K_9 \cos 4 \alpha x \cos 2 \beta y + K_{10} \cos 2 \alpha x \cos 4 \beta y \\ &- \frac{\sigma_y^2}{2} + \frac{qR}{2h} x^2 \end{aligned} \quad (25)$$

where

$$K_1 = \frac{(f_1 - f_o) \left(\frac{\alpha^2}{R} \right) - (f_1 \psi_1 - f_o \psi_o) \alpha^2 \beta^2}{A_1}$$

$$K_2 = \frac{3 (f_1 \psi_1 - f_o \psi_o) \alpha^2 \beta^2}{2A_2}$$

Contrails

$$K_3 = \frac{3 (f_1 \psi_1 - f_0 \psi_0) \alpha^2 \beta^2}{2A_3}$$

$$K_4 = \frac{(f_1^2 - f_0^2 + \psi_1^2 - \psi_0^2) \left(\frac{\alpha^2 \beta^2}{2}\right) - (\psi_1 - \psi_0) \left(\frac{\alpha^2}{R}\right)}{A_4}$$

$$K_5 = \frac{(f_1^2 - f_0^2 + \psi_1^2 - \psi_0^2) \alpha^2 \beta^2}{2A_5}$$

$$K_6 = \frac{(\psi_1 - \psi_0) \left(\frac{\alpha^2}{R}\right) - (\psi_1^2 - \psi_0^2) \alpha^2 \beta^2}{A_6}$$

$$K_7 = -\frac{(\psi_1^2 - \psi_0^2) \alpha^2 \beta^2}{2A_7}$$

$$K_8 = -\frac{(\psi_1^2 - \psi_0^2) \alpha^2 \beta^2}{2A_8}$$

$$K_9 = \frac{(\psi_1^2 - \psi_0^2) \alpha^2 \beta^2}{2A_9}$$

$$K_{10} = \frac{(\psi_1^2 - \psi_0^2) \alpha^2 \beta^2}{2A_{10}}$$

(26)

and

$$A_1 = \frac{(\alpha^2 + \beta^2)^2}{E}$$

$$A_2 = \frac{(9\alpha^2 + \beta^2)^2}{E}$$

$$A_3 = \frac{(\alpha^2 + 9\beta^2)^2}{E}$$

$$A_4 = \frac{16 \alpha^4}{E}$$

$$\begin{aligned}
 A_5 &= \frac{16 \beta^4}{E} \\
 A_6 &= \frac{16 (\alpha^2 + \beta^2)^2}{E} \\
 A_7 &= \frac{256 \alpha^4}{E} \\
 A_8 &= \frac{256 \beta^4}{E} \\
 A_9 &= \frac{16 (4\alpha^2 + \beta^2)^2}{E} \\
 A_{10} &= \frac{16 (\alpha^2 + 4\beta^2)^2}{E}
 \end{aligned}
 \tag{27}$$

It is necessary to enforce the condition that the circumferential displacements be periodic. From Equations (22) and (23) it is possible to obtain

$$\frac{\partial v}{\partial y} = \frac{1}{E} \left(\frac{\partial^2 \phi}{\partial x^2} - \nu \frac{\partial^2 \phi}{\partial y^2} \right) + \frac{w}{R} - \frac{1}{2} \left(\frac{\partial w}{\partial y} \right)^2
 \tag{28}$$

Substitution of Equations (21) and (25) into (28) and then setting the terms that are non-harmonic in y to zero reveals that g_1 is not an independent parameter but instead is a function of f_1 and ψ_1 .

The kinetic energy of the shell is given by

$$E_{k_1} = \frac{\rho h}{2} \int_0^L \int_0^{2\pi R} \left(\frac{\partial w}{\partial t} \right)^2 dx dy
 \tag{29}$$

which is equivalent to assuming that tangential displacements and their first derivatives are small in comparison with normal displacements and their first derivatives throughout the shell. This assumption is satisfactory if the

number of circumferential waves is not too small. If the buckling configuration 21 is substituted in 29 one obtains

$$E_{k_1} = \frac{\rho h}{2} (\pi R L) \left[2 \left(\frac{\partial g_1}{\partial t} \right)^2 + \frac{1}{2} \left(\frac{\partial f_1}{\partial t} \right)^2 + 3 \left(\frac{\partial \psi_1}{\partial t} \right)^2 + \frac{\partial g_1}{\partial t} \cdot \frac{\partial \psi_1}{\partial t} \right] \quad (30)$$

In Reference 18, it is demonstrated that the end shortening of the shell is given by

$$e = - \int_0^L \frac{\partial u}{\partial x} dx \quad (31)$$

where

$$\frac{\partial u}{\partial x} = \frac{1}{E} \frac{\partial^2 \phi}{\partial y^2} - \frac{\nu}{E} \frac{\partial^2 \phi}{\partial x^2} - \frac{1}{2} \left(\frac{\partial w_1}{\partial x} \right)^2 + \frac{1}{2} \left(\frac{\partial w_0}{\partial x} \right)^2 \quad (32)$$

where ν represents Poisson's ratio.

The kinetic energy of the mass M which strikes the impacted end of the cylindrical shell is found from Equations 31 and 32 to be

$$E_{k_2} = \frac{ML^2}{2} \left[\frac{1}{E} \left(\frac{\partial \sigma}{\partial t} \right)^2 + \frac{\alpha^4}{16} f_1^2 \left(\frac{\partial f_1}{\partial t} \right)^2 + \frac{9\alpha^4}{256} \psi_1^2 \left(\frac{\partial \psi_1}{\partial t} \right)^2 + \frac{\alpha^2}{2E} f_1 \frac{\partial f_1}{\partial t} \cdot \frac{\partial \sigma}{\partial t} + \frac{3\alpha^2}{8E} \psi_1 \frac{\partial \psi_1}{\partial t} \cdot \frac{\partial \sigma}{\partial t} + \frac{3\alpha^4}{32} f_1 \psi_1 \frac{\partial f_1}{\partial t} \cdot \frac{\partial \psi_1}{\partial t} \right] \quad (33)$$

We next calculate the total potential energy. This is composed of (a) bending energy of the shell, (b) membrane energy of the shell, and (c) the potential of the loads P and q . For (a) we employ the well-known expression

$$\begin{aligned}
 U_B = \frac{D}{2} \int_0^L \int_0^{2\pi R} & \left[\left(\frac{\partial^2 w}{\partial x^2} + \frac{\partial^2 w}{\partial y^2} \right)^2 \right. \\
 & \left. - 2(1-\nu) \left(\frac{\partial^2 w}{\partial x^2} \cdot \frac{\partial^2 w}{\partial y^2} - \left(\frac{\partial^2 w}{\partial x \partial y} \right)^2 \right) \right] dx dy
 \end{aligned} \tag{34}$$

which becomes with the aid of Equation 21

$$\begin{aligned}
 U_B = \frac{D}{2} (\pi R L) & \left[\frac{1}{2} (f_1 - f_0)^2 (\alpha^2 + \beta^2)^2 \right. \\
 & \left. + \frac{1}{2} (\psi_1 - \psi_0)^2 (\alpha^2 + \beta^2)^2 + (\psi_1 - \psi_0)^2 (\alpha^4 + \beta^4) \right]
 \end{aligned}$$

where $D = Eh^3/12(1-\nu^2)$

For (b), the membrane energy of the shell, we have

$$\begin{aligned}
 U_m = \frac{h}{2E} \int_0^L \int_0^{2\pi R} & \left[(\sigma_x + \sigma_y)^2 - 2(1+\nu) (\sigma_x \sigma_y - \sigma_{xy}^2) \right] dx dy \\
 & = \frac{h}{2E} \int_0^L \int_0^{2\pi R} \left[\left(\frac{\partial^2 \phi}{\partial y^2} + \frac{\partial^2 \phi}{\partial x^2} \right)^2 - 2(1+\nu) \left(\frac{\partial^2 \phi}{\partial y^2} \cdot \frac{\partial^2 \phi}{\partial x^2} \right. \right. \\
 & \quad \left. \left. - \left\{ \frac{\partial^2 \phi}{\partial x \partial y} \right\}^2 \right) \right]
 \end{aligned} \tag{36}$$

If ϕ as given by Equation (25) is substituted in (36) the latter becomes

$$U_m = \frac{\pi R L h}{4E} \left[K_1^2 (\beta^2 + \alpha^2)^2 + K_2^2 (9\alpha^2 + \beta^2)^2 + K_3^2 (\alpha^2 + 9\beta^2)^2 \right]$$

Contraills

$$\begin{aligned}
 & + K_4^2 (32\alpha^4) + K_5^2 (32\beta^4) + 16 K_6^2 (\alpha^2 + \beta^2)^2 \\
 & + 512 K_7^2 \alpha^4 + 512 K_8^2 \beta^4 + K_9^2 (16\alpha^2 + 4\beta^2)^2 \\
 & + K_{10}^2 (4\alpha^2 + 16\beta^2)^2 + 4\sigma^2 + \frac{4q^2 R^2}{h^2} - 8(1 + \nu) \frac{\sigma q R}{h} \Big]
 \end{aligned} \tag{37}$$

For (c) the potential energy of the external loads is found for the internal pressure q to be

$$U_q = \int_0^L \int_0^{2\pi R} q w \, dx \, dy \tag{38}$$

and for the axial load to be

$$U_p = - \sigma (2\pi R h) e \tag{39}$$

Using the values of w and e given earlier these become

$$U_q = q \left[g_1 (2\pi R L) + \psi_1 \left(\frac{\pi R L}{2} \right) \right] \tag{40}$$

$$\begin{aligned}
 U_p = - \sigma (2\pi R h) \left[\frac{\sigma L}{E} + \frac{\nu q R L}{E h} + \frac{1}{8} \alpha^2 L (f_1^2 + \frac{3}{4} \psi_1^2) \right. \\
 \left. - \frac{1}{8} \alpha^2 L (f_0^2 + \frac{3}{4} \psi_0^2) \right] \tag{41}
 \end{aligned}$$

It is now possible to formulate the equations of motion by employing the Lagrange Equations 20 where the E_k and π are now completely defined by Equations 30, 33, 35, 37, 40, and 41. The first equation is obtained by regarding f_1 as the first generalized coordinate and is found to be

Contrails

$$\begin{aligned}
 & \frac{\rho h}{2} (\pi R L) \frac{\partial^2 f_1}{\partial t^2} + \frac{M L^2}{2} \left[\frac{\alpha^4}{8} f_1^2 \frac{\partial^2 f_1}{\partial t^2} + \frac{\alpha^4}{4} f_1 \left(\frac{\partial f_1}{\partial t} \right)^2 \right. \\
 & + \frac{\alpha^2}{2E} f_1 \frac{\partial^2 \sigma}{\partial t^2} + \frac{\alpha^2}{2E} \frac{\partial f_1}{\partial t} \frac{\partial \sigma}{\partial t} + \frac{3\alpha^4}{32} \left(f_1 \psi_1 \cdot \frac{\partial^2 \psi_1}{\partial t^2} + \frac{\partial \psi_1}{\partial t} f_1 \frac{\partial \psi_1}{\partial t} \right. \\
 & \left. \left. + \frac{\partial \psi_1}{\partial t} \psi_1 \frac{\partial f_1}{\partial t} \right) \right] - \frac{M L^2}{2} \left[\frac{\alpha^4}{8} f_1 \left(\frac{\partial f_1}{\partial t} \right)^2 + \frac{\alpha^2}{2E} \frac{\partial f_1}{\partial t} \frac{\partial \sigma}{\partial t} \right. \\
 & \left. + \frac{3\alpha^4}{32} \psi_1 \frac{\partial f_1}{\partial t} \frac{\partial \psi_1}{\partial t} \right] + \frac{D(\pi R L)}{2} \left[(f_1 - f_0) (\alpha^2 + \beta^2)^2 \right] \\
 & + \frac{\pi R L h}{4E} \left[\left\{ 2(f_1 - f_0) \frac{\alpha^4}{R^2} + 2(f_1 \psi_1 - f_0 \psi_0) \psi_1 \alpha^4 \beta^4 \right. \right. \quad (42) \\
 & \left. \left. - (f_1 - f_0) \frac{2\alpha^4 \beta^2 \psi_1}{R} - \frac{2\alpha^4 \beta^2}{R} (f_1 \psi_1 - f_0 \psi_0) \right\} \frac{E^2}{(\alpha^2 + \beta^2)^2} \right. \\
 & \left. + \frac{9}{2} (f_1 \psi_1 - f_0 \psi_0) \psi_1 \alpha^4 \beta^4 \frac{E^2}{(9\alpha^2 + \beta^2)^2} + \frac{9}{2} (f_1 \psi_1 - f_0 \psi_0) \psi_1 \alpha^4 \beta^4 \frac{E^2}{(\alpha^2 + 9\beta^2)^2} \right. \\
 & \left. + \left\{ (f_1^2 - f_0^2 + \psi_1^2 - \psi_0^2) f_1 \alpha^4 \beta^4 - \frac{2 f_1 \alpha^4 \beta^2}{R} (\psi_1 - \psi_0) \right\} \frac{E^2}{8\alpha^4} \right. \\
 & \left. + (f_1^2 - f_0^2 + \psi_1^2 - \psi_0^2) f_1 \left(\frac{\alpha^4 E^2}{8} \right) - \frac{\sigma \pi R h \alpha^2 L f_1}{2} = 0 \right.
 \end{aligned}$$

Contrails

The second equation is found by regarding ψ_1 as the second generalized coordinate and is found to be

$$\begin{aligned}
 & \frac{\rho h}{2} (\pi R L) \left[9 \frac{\partial^2 \psi_1}{\partial t^2} \right] + \frac{M L^2}{2} \left[\frac{9 \alpha^4}{128} \psi_1^2 \frac{\partial^2 \psi_1}{\partial t^2} + \frac{9}{64} \alpha^4 \psi_1 \left(\frac{\partial \psi_1}{\partial t} \right)^2 \right. \\
 & + \left. \frac{3 \alpha^2}{8 E} \psi_1 \frac{\partial^2 \sigma}{\partial t^2} + \frac{3 \alpha^2}{8 E} \frac{\partial \psi_1}{\partial t} \frac{\partial \sigma}{\partial t} + \frac{3 \alpha^4}{32} \left(f_1 \frac{\partial f_1}{\partial t} \frac{\partial \psi_1}{\partial t} + \psi_1 \left(\frac{\partial f_1}{\partial t} \right)^2 + f_1 \psi_1 \frac{\partial^2 f_1}{\partial t^2} \right) \right] \\
 & + \frac{D(\pi R L)}{2} \left[(\psi_1 - \psi_0) (\alpha^2 + \beta^2)^2 + 2 (\psi_1 - \psi_0) (\alpha^4 + \beta^4) \right] \\
 & + \frac{\pi R L h}{4 E} \left[2 (f_1 \psi_1 - f_0 \psi_0) f_1 \alpha^4 \beta^4 - 2 (f_1 - f_0) \frac{\alpha^4 \beta^2}{R} f_1 \right] \frac{E^2}{(\alpha^2 + \beta^2)^2} \\
 & + \frac{9}{2} (f_1 \psi_1 - f_0 \psi_0) f_1 \alpha^4 \beta^4 \frac{E^2}{(9 \alpha^2 + \beta^2)^2} + \frac{9}{2} (f_1 \psi_1 - f_0 \psi_0) f_1 \alpha^4 \beta^4 \frac{E^2}{(\alpha^2 + 9 \beta^2)^2} \\
 & + \left\{ (f_1^2 - f_0^2 + \psi_1^2 - \psi_0^2) \psi_1 \alpha^4 \beta^4 + (\psi_1 - \psi_0) \frac{2 \alpha^4}{R^2} \right. \tag{43} \\
 & - \left. (f_1^2 - f_0^2 + \psi_1^2 - \psi_0^2) \frac{\alpha^4 \beta^2}{R} - \frac{2 \psi_1 \alpha^4 \beta^2}{R} (\psi_1 - \psi_0) \right\} \frac{E^2}{8 \alpha^4} \\
 & + (f_1^2 - f_0^2 + \psi_1^2 - \psi_0^2) \frac{\psi_1 E^2 \alpha^4}{8} + \left\{ (\psi_1 - \psi_0) \frac{2 \alpha^4}{R^2} + 4 (\psi_1^2 - \psi_0^2) \psi_1 \alpha^4 \beta^4 \right. \\
 & - \left. 4 (\psi_1 - \psi_0) \frac{\alpha^4 \beta^2}{R} \psi_1 - \frac{2 \alpha^4 \beta^2}{R} (\psi_1^2 - \psi_0^2) \right\} \frac{E^2}{16 (\alpha^2 + \beta^2)^2} \\
 & + (\psi_1^2 - \psi_0^2) \psi_1 \beta^4 \left(\frac{E^2}{128} \right) + (\psi_1^2 - \psi_0^2) \psi_1 \alpha^4 \beta^4 \frac{E^2}{16 (4 \alpha^2 + \beta^2)^2} \\
 & + (\psi_1^2 - \psi_0^2) \psi_1 \alpha^4 \left(\frac{E^2}{128} \right) + (\psi_1^2 - \psi_0^2) \psi_1 \alpha^4 \beta^4 \frac{E^2}{16 (\alpha^2 + 4 \beta^2)^2} - \frac{3}{8} \sigma \pi R h \alpha^2 L \psi_1 = 0
 \end{aligned}$$

Contraails

Equations (42) and (43) are the governing equations for finite deflection of a thin elastic cylindrical shell subject to a rapidly applied axial loading which is prescribed as a function of time. Because of the complexity of these equations it is desirable to proceed from this stage onward only by numerical techniques. The equations (42) and (43) are coupled nonlinear equations in the unknowns f_1 and ψ_1 and no closed-form solution is known to exist. However, if initial conditions are specified, these two equations may be integrated numerically by the Runge-Kutte method. We shall investigate the initial conditions

$$\begin{aligned}f_1 &= f_0 \\ \psi_1 &= \psi_0 \\ \frac{df_1}{dt} &= 0 \\ \frac{d\psi_1}{dt} &= 0\end{aligned}\tag{44}$$

The numerical solutions of equations (42) and (43) have been carried out on IBM 1620 computer for a shell characterized by the following parameters and subject to the following loading rates:

$$\begin{aligned}E &= 10.6 \times 10^6 \text{ lb/in}^2 && \text{Loading Rate, } \frac{d\sigma}{dt}, 10^6 \text{ psi/sec} \\ \nu &= 0.33 \\ L &= 22.8 \text{ in} && = 61.2, 419, 1419 (.008 \text{ in shell}) \\ R &= 2.85 \text{ in} \\ h &= 0.008 \text{ in, } .016 \text{ in} && = 30.5, 214, 708 (.016 \text{ in shell}) \\ f_0 &= \psi_0 = h/2\end{aligned}$$

Further, α was taken equal to β , which implies a wave aspect ratio of unity. Results of these computations are shown in Figures 94 through 103 for the above axial loading rates. Since each of these families of curves contains load-deflection relations for a variety of values of n , the number of half waves in the circumferential direction, it is necessary to formulate a criterion for selection of the significant value of n in each case. The criterion employed is that the curve corresponding to the true value of n is that one in which the post-buckling load (characterized by a vertical tangent to the $\bar{\sigma} - \zeta$ curve) is achieved in a minimum time. It is to be observed that there are in each family a few curves which do not have any point corresponding to a postbuckling load so naturally these curves are eliminated from further consideration. Also, it is to be observed that the inflection point of any curve possessing a vertical tangent essentially corresponds to the dynamic buckling load of the system and because of the nature of the curves in any one family, that curve in which post-buckling is achieved in minimum time is also the same curve in which the inflection point is reached in minimum time. Also, at the inflection point, the

Contrails

rate of change of load with respect to lateral deflection is maximum for the curve corresponding to the true mode of collapse, i. e., the desired value of n . All of these facts make the selection of the proper value of n possible and all are in fact synonymous with buckling, i. e., a rather sudden change in the nature of the behavior of the system.

9. PLASTIC BEHAVIOR OF AXIALLY LOADED CYLINDRICAL SHELLS

To date only a very limited amount of work has been done in the general area of dynamic plasticity of shells (Refs. 34, 35, 36). This is due largely to the rather considerable mathematical complexities of the problem. In the present analysis an approximate method for predicting large plastic deformation of axially loaded cylindrical shells is developed through use of energy criteria.

It is assumed that the shell is subjected to a dynamically applied axial load of short time duration. This essentially reduces the problem to one of considering a structure having an initial kinetic energy. If the energy absorbed by the shell is considered as a function of lateral deflection, then according to Reference 36, there can be a region of instability in the elastic region which corresponds to snap buckling of the shell, or, if this does not occur then when the structure becomes plastic there could be a point of plastic instability. If no such point exists and the shell is loaded further then there exists a point at which a slight increment of energy will lead to a very large deformation of the shell. This last possibility is termed collapse.

For an elasto-plastic material the work done by the internal forces per unit volume is given by

$$V = \int_0^{\epsilon_i} \sigma_i d\epsilon_i + \frac{k\Xi^2}{2} \tag{45}$$

where the repeated index implies summation and

$$\begin{aligned} \sigma_i &= \frac{\sqrt{2}}{2} \sqrt{(\sigma_x - \sigma_y)^2 + (\sigma_y - \sigma_z)^2 + (\sigma_z - \sigma_x)^2 + \sigma(\tau_{xy}^2 + \tau_{yz}^2 + \tau_{xz}^2)} \\ \epsilon_i &= \frac{\sqrt{2}}{3} \sqrt{(\epsilon_x - \epsilon_y)^2 + (\epsilon_y - \epsilon_z)^2 + (\epsilon_z - \epsilon_x)^2 + \frac{3}{2}(\epsilon_{xy}^2 + \epsilon_{yz}^2 + \epsilon_{xz}^2)} \end{aligned} \tag{46}$$

$$\Xi = \epsilon_x + \epsilon_y + \epsilon_z$$

k = bulk modulus of the material

For a thin shell of incompressible material ($\Xi = 0$) these relations become

$$V = \int_0^{\epsilon_i} \sigma_i d\epsilon_i$$

$$\sigma_i = \sqrt{\sigma_x^2 - \sigma_x \sigma_y + \sigma_y^2 + 3\tau_{xy}^2} \quad (47)$$

$$\epsilon_i = \frac{2}{\sqrt{3}} \sqrt{\epsilon_x^2 + \epsilon_x \epsilon_y + \epsilon_y^2 + \frac{1}{4} \epsilon_{xy}^2}$$

where the integration is extended over the volume of the shell.

The strains at any distance z from the middle surface are given by

$$\begin{aligned} \epsilon_x' &= \epsilon_x - z\kappa_1 \\ \epsilon_y' &= \epsilon_y - z\kappa_2 \\ \epsilon_{xy}' &= \epsilon_{xy} - 2z\tau \end{aligned} \quad (48)$$

where ϵ_x , ϵ_y , ϵ_{xy} are given by Equations (22) and κ_1 , κ_2 , and τ are the usual curvatures and twist defined by

$$\begin{aligned} \kappa_1 &= \frac{\partial^2 w}{\partial x^2} \\ \kappa_2 &= \frac{1}{R^2} \cdot \frac{\partial^2 w}{\partial \lambda^2} + \frac{1}{R^2} \frac{\partial v}{\partial \lambda} \\ \tau &= \frac{1}{R} \frac{\partial^2 w}{\partial x \partial \lambda} + \frac{1}{R} \frac{\partial v}{\partial x} \end{aligned} \quad (49)$$

where λ is the central angle defined by the relation

$$dy = R d\lambda \quad (49a)$$

Next, a deformation-type elasto-plastic stress-strain law can be written as

$$\begin{aligned} \sigma_x &= \frac{4}{3} \frac{\sigma_i}{\epsilon_i} \left(\epsilon_x + \frac{1}{2} \epsilon_y \right) \\ \sigma_y &= \frac{4}{3} \frac{\sigma_i}{\epsilon_i} \left(\epsilon_y + \frac{1}{2} \epsilon_x \right) \\ \tau_{xy} &= \frac{1}{3} \frac{\sigma_i}{\epsilon_i} \epsilon_{xy} \end{aligned} \quad (50)$$

for $\nu = .5$ and where

$$\frac{\sigma_i}{\epsilon_i} = E \left[1 - \omega(\epsilon_i) \right]$$

For the elastic region $\omega(\epsilon_i)$ vanishes. For very large deformations we may reasonably neglect all terms involving u and v as well as their derivatives as being small compared to w and its derivatives in which case

$$\begin{aligned} \epsilon'_x &= \frac{1}{2} \left(\frac{\partial w}{\partial x} \right)^2 - z \frac{\partial^2 w}{\partial x^2} \\ \epsilon'_y &= \frac{1}{2} \left(\frac{\partial w}{R \partial \lambda} \right)^2 - \frac{w}{R} - \frac{z}{R^2} \frac{\partial^2 w}{\partial \lambda^2} \\ \epsilon'_{xy} &= \frac{1}{R} \frac{\partial w}{\partial x} \cdot \frac{\partial w}{\partial \lambda} - 2 \frac{z}{R} \cdot \frac{\partial^2 w}{\partial x \partial \lambda} \end{aligned} \tag{51}$$

We shall consider an elastic linear hardening material which is incompressible and whose stress-strain relations are given by

$$\begin{aligned} \omega(\epsilon_i) &= 0 \text{ for } \epsilon_i < \epsilon_s \text{ (elastic region)} \\ \omega(\epsilon_i) &= \eta \left(1 - \frac{\epsilon_s}{\epsilon_i} \right) \text{ for } \epsilon_i > \epsilon_s \text{ (plastic region)} \end{aligned} \tag{52}$$

where ϵ_s is the strain at which yielding occurs in uniaxial tension and

$$\eta = 1 - \frac{1}{E} \frac{d\sigma_i}{d\epsilon_i} \tag{53}$$

With these last relations the work done by the internal forces (Equation 45) becomes

$$\begin{aligned} V &= \int_0^L \int_0^{2\pi R} \left\{ \frac{2}{3} E (1 - \eta) \left[h \gamma(x, \lambda) + \frac{h^3}{4} \delta(x, \lambda) \right] \right. \\ &\quad \left. + \frac{2}{3} \cdot \frac{2\gamma E \epsilon_s}{\sqrt{3}} \left[\frac{\left\{ \gamma(x, \lambda) + z \delta(x, \lambda) \right\}^{3/2}}{\delta(x, \lambda)} \right] \right\} dx dy \\ &\quad \begin{matrix} z = \frac{h}{2} \\ z = -\frac{h}{2} \end{matrix} \end{aligned} \tag{54}$$

Contrails

where

$$\begin{aligned} \gamma(x, \lambda) &= \frac{1}{4} \left(\frac{\partial w}{\partial x} \right)^4 + \frac{1}{2} \left(\frac{\partial w}{\partial x} \right)^2 \left(\frac{\partial w}{\partial y} \right)^2 - \frac{1}{2} \frac{w}{R} \left(\frac{\partial w}{\partial x} \right)^2 \\ &\quad + \frac{1}{4} \left(\frac{\partial w}{\partial y} \right)^4 - \frac{w}{R} \left(\frac{\partial w}{\partial y} \right)^2 + \frac{w^2}{R^2} \\ \delta(x, \lambda) &= \left(\frac{\partial^2 w}{\partial x^2} \right)^2 + \frac{1}{R^2} \cdot \frac{\partial^2 w}{\partial x^2} \cdot \frac{\partial^2 w}{\partial \lambda^2} + \frac{1}{R^4} \left(\frac{\partial^2 w}{\partial \lambda^2} \right)^2 + \frac{1}{R^2} \left(\frac{\partial^2 w}{\partial x \partial \lambda} \right)^2 \end{aligned} \quad (55)$$

For extremely large deformations the terms in Equation (54) which correspond to bending strains can be neglected and the work becomes

$$V = \int_0^L \int_0^{2\pi R} \left\{ \frac{2}{3} E (1 - \eta) \left[h \gamma(x, \lambda) \right] + \frac{2\eta E \epsilon_s}{\sqrt{3}} h \sqrt{\gamma(x, \lambda)} \right\} dx dy \quad (56)$$

For a perfectly plastic material, $\eta = 1$ and for this case Equation (56) becomes

$$V = \int_0^L \int_0^{2\pi R} \frac{2\eta E \epsilon_s}{\sqrt{3}} h \sqrt{\gamma(x, \lambda)} dx dy \quad (57)$$

If I denotes the impulse per unit mass imparted to the shell by the axial loading, then from impulse-momentum relations one can write for an elemental mass dm

$$\left(\frac{\partial w}{\partial t} \right) dm = I dm$$

or

$$I = \frac{\partial w}{\partial t} \quad (58)$$

The kinetic energy of the shell, from Equation (29) now becomes

$$E_{k1} = \frac{1}{2} \int \rho h I^2 da \quad (59)$$

Contrails

where the integration extends over the entire middle surface of the shell. Thus, any specified form of impulse can now be substituted in Equation (59) to yield the kinetic energy of the shell. Let us take this in the form $I(x, y) = I_1 f(x, y)$. Then it is possible to equate the initial kinetic energy (Equation 59) to the work done by the internal forces (Equation 57).

At this point in the analysis it is necessary to assume a deflection configuration. One excellent possibility is to utilize that offered in Reference 8 which related the geometry of the triangular plane surfaces which form upon collapse to the geometric parameters of the shell. In this manner the impulse required to cause collapse, i. e. a specified lateral deflection is determined. Because of the complexity of these relations it is almost essential that these calculations be carried out on a digital computer.

PART III - COMPARISON OF THEORETICAL PREDICTIONS WITH EXPERIMENTAL RESULTS

10. RIGID IMPACT OF PRESSURIZED CYLINDRICAL SHELLS

A comparison between the theoretical predictions with the experimental results as obtained under this program are summarized in Table 10. The comparison is made for a 5052 H-38 A1 shell having the following dimensions: Mean diameter, 5.716; length 22.8 in., wall thickness .016 in.

TABLE 10. COMPARISON OF THEORETICAL AND
EXPERIMENTAL RESULTS - PHASE 1

V_o Ft/sec	q psig	$\bar{\sigma}_{crT}$	$\bar{\sigma}_{crE}$	$(n_f)_T$	$(n_f)_E$	t_{crT}	t_{crE}	Test No.
11.5	17	.355	.450	6	5	325	560	G-2
11.5	17	.355	.672 ⁽²⁾				600	G-8 ⁽¹⁾
		.355	.520					
11.5	34	.380	.482	6	5	370	570	G-3
23	17	.437	.417	6		140	260	G-6
23	34	.448	.370	6		205	250	G-7

(2) Measured near the impacted end with one pair of opposite strain gages

(1) Specimen had supported impacted end condition. All other tests utilized free end condition.

11. NON-RIGID IMPACT

Comparison is made for two shell thicknesses on the basis of three constant rates of axial stress rise, $\frac{d\sigma}{dt}$. The rates determined from the rigid body sand impact tests are as follows:

For the .016 in. shell:

$$\frac{d\sigma}{dt} = 30.5 \times 10^6, 214 \times 10^6, \text{ and } 708 \times 10^6 \text{ psi/sec.}$$

$$f_o = \psi_o = .008 = \frac{h}{2}$$

Contrails

For the .008 in. shell:

$$\frac{d\sigma}{dt} = 61.2 \times 10^6, 419 \times 10^6, \text{ and } 1417 \times 10^6 \text{ psi/sec.}$$

$$f_o = \psi_o = .008 \text{ in.} = h$$

The comparison is shown in Table 11.

TABLE 11. COMPARISON OF THEORETICAL AND
EXPERIMENTAL RESULTS - PHASE 3

$\frac{d\sigma}{dt}$ psi/sec $\times 10^{-6}$	h in.	$\bar{\sigma}_{cr_T}$	$\bar{\sigma}_{cr_E}$	$(n_f)_T$	$(n_f)_E$	t_{cr_T} μsec	t_{cr_E} μsec	Test No.	<i>✓</i> <i>41/500</i>
30.5	.016	.462	.271 ⁽¹⁾	7	---	900	500 ⁽¹⁾	S-17	23
214	.016	.41	.446	6	6	114	300	S-14	33
708	.016	.75	.462	8	10	77	260	S-13	43
61.2	.008	.37	.394	5	7 5-6	179	380	S-16	23
419	.008	.62	.728	11	10	44	220	S-19	33
1417	.008	1.30	.741	14	5	28	200	S-15	43

(1) Prebuckled

The following comparison applies to the $h = .008$ in shell with $f_o = \psi_o = 2h = .016$ in.

$\frac{d\sigma}{dt}$ psi/sec $\times 10^{-6}$	$\bar{\sigma}_{cr_T}$	$\bar{\sigma}_{cr_E}$	$(n_f)_T$	$(n_f)_E$	t_{cr_T} μsec	t_{cr_E} μsec
61.2	.20	.394	6	5-6	92	380
419	.57	.728	9	10	41	220

The values corresponding to the $f_o = 2h$ imperfection factor are probably more applicable to the .008 in thickness cylindrical shells tested in this program. As determined in the preceding program, these shells were imperfect by a factor of two wall thicknesses whereas the .016 in. shells were imperfect by a factor between $h/2$ and h . What needs to be done in order to obtain a valid comparison is a measurement of each shell in its test fixture prior to testing as was done in the pressurized shell experiments during this program.

12. SUMMARY DISCUSSION AND CONCLUSIONS

12.1 Rigid Impact

Except for test no. G-8 in which the specimen was supported by the circular plate at the impacted end, the experimentally obtained values of $\bar{\sigma}_{cr}$ ranged from 82 to 127% of the theoretically predicted values. Risking making conclusions based on a small number of tests, it is observed that at $V_0 = 11.5$ ft/sec, $(\bar{\sigma}_{cr})_E / (\bar{\sigma}_{cr})_T = 1.27$ (Test nos. G-2 and G-3) whereas at $V_0 = 23$ ft/sec.

$\frac{(\bar{\sigma}_{cr})}{(\bar{\sigma}_{cr})} = .955$ and $.826$ (Tests nos. G-6 and G-7, respectively). Also, in the

latter pair, specimen G-7 had a lower $(\bar{\sigma}_{cr})_E$ than specimen G-6 despite the fact that its internal pressure was twice as high as G-6. This trend in the experiments, which runs contrary to theoretical predictions, is due largely to the effect of the asymmetry of the applied impact loading. This conclusion is drawn from the observation that the variation of the peak values among the three measurements of axial strain made in each test is larger in specimens G-6 and G-7 than in G-2 and G-3. A comparison of the ratio of the largest deviation of a local value from the average of the three values to the average value shows: G-2: 10%, G-3: 3%, G-6: 13%, G-7: 25%. The results of test no. G-4 may be recalled at this time in which the observed asymmetrical impact produced low axial strains. The flatness of the impact, as obtained from the apparatus employed for these tests, was less at higher impact velocities. It may be concluded, therefore, that a small axial asymmetry of the impact, significantly reduces the buckling stress. A large non-uniformity results in local deformations occurring where the impact is applied and a buckling response is not present, at least initially. Relatively low axial loads are introduced during this initial phase, but when the impact is later applied to the entire cross section, the shell undergoes a collapse process which is similar to the case of a uniformly applied impact.

The edge support condition has an important effect on the buckling behavior of an axially impacted shell. The comparison between test nos. G-8 and G-2 show that a substantial increase in the buckling stress resulted by preventing local buckling from occurring at the impacted end. In both tests, the impacted edge was initially free of restraint prior to the impact, and the internal pressurization produced no initial deformations at that end. The effect tested therefore was that of inward rotation of the shell wall at the impacted end, specimen G-2 being free to rotate and G-8 restrained against inward rotation.

For the case of an internally pressurized right circular cylindrical shell subject to axially symmetric impact by a rigid body, a nonlinear theory incorporating effects of initial imperfections has been presented which predicts dynamic buckling loads with good accuracy. The theory predicts the number of circumferential waves with considerable accuracy and also indicates correctly

the experimentally observed trend of decreasing time required to reach the buckling load with increasing impact velocity for like shells with equal pressurization. Further, it correctly predicts the experimentally observed trend of increasing time required to reach the buckling load when the internal pressure is increased for constant impact velocities.

12.2 High Velocity Impact

Over the velocity range 216-271 ft/sec covered in tests HV-4, -6, and -7, an inverse trend of both axial strain and axial force with velocity was observed. The values of the first peak of the strain records obtained at the mid-length position are as follows (Each value is the average of two measurements): HV-4 ($V_0 = 216$ ft/sec), $\epsilon = 3450 \mu$ in/in; HV-6 ($V_0 = 225$ ft/sec), $\epsilon = 2700 \mu$ in/in. A similar trend was noted also in the average values of the strain and (separately) acceleration records. Considering the gross average of the strain and acceleration measurements (taken together) the following values for the average force sustained by the shells during a large portion of the collapse process are: $P = 2150$ lb for $V_0 = 220$ ft/sec (average of Test nos. HV-4 and -6) and $P = 1890$ lb for $V_0 = 271$ ft/sec (Test No. HV-7). The corresponding dimensionless stresses, $\bar{\sigma} = .127$ and $.112$.

Further experimentation is required to substantiate the observed inverse trend of axial force with impact velocity and to determine whether this trend is continuous for a given shell or whether it is interrupted by the occurrence of changing buckle and collapse modes.

The fact that the high strain levels sustained for substantial times (referring to Figures 86 and 93) at the forward gage position were not transmitted to the mid-length positions is puzzling. Further work should be done to explain this phenomenon.

As noted previously, a ring collapse mode was obtained in Test No. HV-8 conducted at $V_0 = 392$ ft/sec. It is believed that this is the first time such a configuration has been observed in a thin shell. Further work is needed to determine what is the critical, postbuckling, and collapse behavior of a shell when it undergoes this type of response. It is expected that the ring mode should dominate in the high velocity loading regime. What is the mode of response at even higher velocities? Obviously, there are thresholds of velocity which separate distinctly different regimes of response in a shell such as a cylinder or cone under axial impact. Exploration of these regimes should prove interesting and meaningful to the structures field.

12.3 Non-Rigid Impact

Axial impact of a right circular cylindrical shell into a non-rigid medium was studied experimentally with the aid of a calibration obtained from a rigid body force-time penetration curve for the same medium. Agreement of test results from impact of cylindrical shells into sand with predictions of a nonlinear theory incorporating effects of initial imperfections is moderately good with regard to mean axial buckling stress. This applies to thin shells ($R/h = 356$) which were known to possess initial geometric imperfections of approximately twice the wall thickness. For the thicker shells ($R/h = 178$) possessing initial imperfections varying from half the shell thickness to the full shell thickness, agreement of

Contrails

buckling stresses was again moderately good, being much better for lower impact velocities. In all cases the nonlinear theory predicts the number of circumferential waves with rather good accuracy. Further, it predicts correctly the experimentally observed trend of decreasing time required to reach the buckling load with increasing impact velocity.

It would appear, from the moderately good agreement between the theoretical and experimental results obtained herein, that reasonable estimates of buckling stress for non-rigid impact can be made, provided that the following conditions are met: (1) the force-time curve of the impacted medium has an approximately linear initial rise to the peak value; (2) the frontal structure which makes the initial contact with the medium is sufficiently rugged to remain rigid during the impact. In order to apply the analysis, the rigid body force-time characteristic for the impacted medium must be determined and the slope representing the initial rise to the peak obtained. Values of $\bar{\sigma}$ and ζ are then computed for particular values of n . Plots of $\bar{\sigma}$ vs ζ are made for various values of n , and that curve which is the first (in time) to reach a clearly defined peak in ζ is selected as the pertinent curve. The value of $\bar{\sigma}$ at the inflection point of this curve corresponds to the buckling stress. Since the applied load varies linearly with time, the time corresponding to buckling is easily obtained.

As with rigid impact the initial imperfections of the shell, especially at the ends, must be known if accuracy of prediction is to be obtained. The methods for measuring and computing actual imperfections, described previously, are recommended as both accurate and convenient for this purpose.

13. REFERENCES

1. Fung, Y. C., and Sechler, E. E., "Instability of Thin Elastic Shells," published in Structural Mechanics-Proceedings of the First Symposium on Naval Structural Mechanics, Pergamon Press, New York, 1960, pp. 115-168.
2. Thielemann, W. F., "New Developments in the Nonlinear Theories of the Buckling of Thin Cylindrical Shells," Aeronautics and Astronautics, Proceedings of the Durand Centennial Conference, Pergamon Press, New York, 1960.
3. Schmitt, A. F., "Dynamic Buckling Tests of Aluminum Shells," Aeronautical Engineering Review, September, 1956, pp. 54-58.
4. Volmir, A. S., "Investigation of the Stability of Plates and Cylindrical Shells Subject to Dynamic Loading," Collected Scientific Works of the Military Air Engineering Academy in honor of N. E. Zhukov, Moscow, 1957 (in Russian). Unavailable in the U.S.A.
5. Volmir, A. S., "On the Stability of Dynamically Loaded Cylindrical Shells," Doklady Akademii Nauk SSSR, Vol. 123, No. 5, 1958, pp. 806-808, (in Russian). Translated in Soviet Physics-Doklady, Vol. 3, 1958, pp. 1287-1289.
6. Agamirov, V. L., and Volmir, A. S., "Behavior of Cylindrical Shells Under Dynamic Loadings by Hydrostatic Pressure or Axial Compression," Izvestiya Akademii Nauk SSSR Otdelenie Tekhnicheskii Nauk, 1959, No. 3, pp. 78-83, (in Russian). Translated in the Journal of the American Rocket Society, Vol. 31, No. 1, 1961, pp. 98-101.
7. Volmir, A. S., and Mineev, V. E., "An Experimental Investigation of the Buckling of a Shell Under Dynamic Load," Doklady Akademii Nauk SSSR, Vol. 125, No. 5, 1959, pp. 1002-1003, (in Russian). Translated in Soviet Physics-Doklady, Vol. 4, No. 2, 1959, pp. 464-465.
8. Coppa, A. P., "On the Mechanism of Buckling of a Circular Cylindrical Shell under Longitudinal Impact," General Electric Co. TIS Report R60SD494, Proceedings of Tenth International Congress of Applied Mechanics, PP274-276, Mechanics (USSR) - Periodical Selection of Translations of Foreign Articles, No. 6, 1961.
9. Slepov, B. I., "Dynamic Stability of Circular Cylindrical Shells Subject to the Action of Shock Wave Loading," Works of the Conference on the Theory of Plates and Shells, Kazan, USSR, 1960, pp. 353-357, (in Russian).

Contrails

10. Pertsev, A. K., and Kadashevich, Yu. I., "Stability of Cylindrical Shells Submerged in a Liquid and Subjected to Short-Time Dynamic Loads," Works of the Conference on the Theory of Plates and Shells, Kazan, USSR, 1960, pp. 271-277 (in Russian).
11. Blokhina, A. I., "Dynamic Stability of Cylindrical Shells with Initial Bending Subject to a Given Velocity of Approach of the Ends," Inzhenernyi Sbornik, Vol. XXXI, 1961, pp. 196-201. (in Russian)
12. Yao, J. C., "The Stability of a Cylinder Due to Dynamic Radial Pressure," Douglas Aircraft Co., Inc., Santa Monica, California, Report No. SM-38702, February 27, 1961. Also published in Journal of the American Rocket Society, Vol. 31, No. 12, 1961, pp. 1705-1708.
13. Kadashevich, Yu. I., and Pertsev, A. K., "Loss of Stability of a Cylindrical Shell Under Dynamic Loads," Izvestiya Akademii Nauk SSSR, Otdelenie Tekhnicheskikh Nauk Mekhanika i Mashinostroenie, No. 3, 1960, pp. 30-33, (in Russian). Translated in the Journal of the American Rocket Society, Vol. 32, No. 1, 1962, pp. 140-143.
14. Goodier, J. N., and McIvor, I. K., "Dynamic Stability and Nonlinear Oscillations of Cylindrical Shells (Plane Strain) Subjected to Impulsive Pressure," Division of Engineering Mechanics, Stanford University, Technical Report No. 132, June 1962.
15. Abrahamson, G. R., and Goodier, J. N., "Dynamic Plastic Flow Buckling of a Cylindrical Shell From Uniform Radial Impulse," Proceedings of the Fourth U. S. National Congress of Applied Mechanics, Berkeley, California, 1962.
16. Koval, L. R., and O'Neill, J. P., "Stability of Axially-Loaded Thin Cylindrical Shells under Dynamic Lateral Pressures," Space Technology Laboratories Report EM 13-20, Redondo Beach, California, October, 1963.
17. Roth, R. S., and Klosner, J. M., "Nonlinear Response of Cylindrical Shells with Initial Imperfections Subjected to Dynamic Axial Loads," Avco Corp. RAD-TM-63-43, 31 July, 1963.
18. Coppa, A. P., and Nash, W. A., "Dynamic Buckling of Shell Structures Subject to Longitudinal Impact," General Electric Co., Space Sciences Laboratory, TIS Report R62SD77, August, 1962. (ASD-TDR-62-774, Dec. 1962).
19. Suhara, J., "Snapping of Shallow Spherical Shell under Static and Dynamic Loadings," AFOSR TN (60)-813, Massachusetts Institute of Technology, ASRL TR 76-4, June, 1960.

20. Humphrey, J. S., and Bodner, S. R., "Dynamic Buckling of Shells under Impulsive Loading," Journal of the Engineering Mechanics Division, American Society of Civil Engineers, Vol. 88, No. EM 2, 1962.
21. Budiansky, B., and Roth, R. S., "Axisymmetric Dynamic Buckling of Clamped Shallow Spherical Shells," NASA TN D-1510, 1962, pp. 597-604.
22. Koval, L. R., and Bhuta, P. G., "Dynamic Response of Shallow Spherical Shells," Space Technology Laboratories, Redondo Beach, California, Report EM13-31, October, 1963.
23. Ho, F. H., and Nash, W. A., "Dynamic Buckling of Shallow Spherical Caps," scheduled for publication in the Proceedings of the Symposium on Non-Classical Problems, International Association of Shell Structures, Warsaw, 1963.
24. Ho, F. H., "Transitional Instability of Spherical Shells Under Dynamic Loadings," Ph.D. Dissertation, University of Florida, Gainesville, Florida, April, 1964.
25. Bolotin, V. V., "Dynamic Stability of Elastic Systems," Gostekhizdat, Moscow, 1956 (in Russian).
26. Bolotin, V. V., Biochenko, G. A., Makarov, B. P., Sudakova, N. I., and Shveiko, Yu. Yu., "Loss of Stability of Thin Elastic Shells Under the Effect of Impulsive Loads," Stroitel'naya Mekhanika i Raschet Sooruzhenii, No. 2, 1959, pp. 9-16, (in Russian). Translated by Space Technology Laboratories, Redondo Beach, California, Translation No. 73, January, 1963.
27. Mishenkov, G. V., "Dynamic Stability of Shallow Cylindrical Shells," Work of the Conference on the Theory of Plates and Shells, Kazan, USSR, 1960, pp. 239-245, (in Russian).
28. Mishenkov, G. V., "Dynamic Stability of Shallow Elastic Shells," Inzhenernyy Zhurnal, Vol. 1, No. 2, 1961, pp. 112-118, (in Russian).
29. Gnuni, V. Ts., "Theory of Nonlinear Dynamic Stability of Shells," Izvestiya Akademii Nauk SSSR, Otdelenie Tekhnicheskikh Nauk Mekhanika i Mashinostroenie, No. 4, 1961, pp. 181-182, (in Russian).
30. Gnuni, V. Ts., "Theory of Dynamic Stability of Laminated Anisotropic Shells," Izvestiya Akademii Nauk Armentian SSR, Seriya Fiz-mat. Nauk, Vol. 13, No. 1, 1960, pp. 18-24.

Contrails

31. Bolotin, V. V., and Boychenko, G. A., "Investigation of thin Elastic Shells Subject to the Action of Dynamic Loads," *Raschet na Prochnost*, Vol. 5, Moscow, 1960, pp. 259-282, (in Russian).
32. "Final Report on Buckling of Shells Under Dynamic Loads," Engineering Mechanics Laboratory, Space Technology Laboratories, Redondo Beach, California, October 1961.
33. Yao, J. C., "Dynamic Stability of Cylindrical Shells under Static and Periodic Axial and Radial Loads," *Journal of the American Institute of Aeronautics and Astronautics*, Vol. 1, No. 6, 1963, pp. 1391-1396.
34. Witmer, S., "Response of Plates and Shells to Intense External Loads of Short Duration," WADD Technical Report 60-433, April 1960.
35. Pian, T. H. H., "Dynamic Response of Thin Shell Structures," *Proceedings of the Second Symposium on Naval Structural Mechanics*, 1960.
36. Radkowski, P. P., "Studies on the Dynamic Response of Shell Structures and Materials to a Pressure Pulse," Avco Corp., 1961, AFSWS-TR-61-31 (II).

€ = .001

APPENDIX A

ϵ unit and starting	n_f #	γ	K^+	
1.0000000E-03	5.0000000E-00	0.0000000E-99	1.3760377E-01	
$\gamma + \alpha$	$\gamma - \beta$	α	β	γ
4.4725087E-02	4.4725087E-02	4.4725087E-02	4.4725087E-02	0
U/D	W_1/D	W_2/D	K^-	
1.5103780E-00	3.4479666E-02	6.7596867E-02	1.3760377E-01	
α/β	α^0	β^0		
1.0000000E-00	2.5625587E-00	2.5625587E-00		
1.0000000E-03	5.0000000E-00	8.7266460E-02	1.4758770E-02	
9.8034113E-02	7.0731290E-02	1.0767653E-02	1.6535169E-02	5
6.2536408E-00	1.6185917E-01	1.4910079E-00	6.9631476E-02	
6.5119704E-01	6.1694109E-01	9.4739542E-01		
1.0000000E-03	1.0000000E+01	0.0000000E-99	2.8228895E-01	
4.4725087E-02	4.4725087E-02	4.4725087E-02	4.4725087E-02	0
3.6998380E-01	8.3203692E-03	1.6558600E-02	2.8228895E-01	
1.0000000E-00	2.5625587E-00	2.5625587E-00		
1.0000000E-03	1.0000000E+01	8.7266460E-02	5.9057506E-02	
9.8034113E-02	7.5056737E-02	1.0767653E-02	1.2209722E-02	5
1.5318985E-00	1.2143383E-02	3.5278255E-02	8.6585180E-02	
8.8189176E-01	6.1694109E-01	6.9956555E-01		
1.0000000E-03	1.0000000E+01	1.7453292E-01	1.7537847E-02	
1.8011584E-01	1.6612330E-01	5.5829269E-03	8.4096172E-03	10
2.9208458E-00	3.3696791E-02	2.7493215E-01	7.2214371E-02	
6.6387407E-01	3.1987815E-01	4.8183557E-01		
1.0000000E-03	2.0000000E+01	0.0000000E-99	5.6809667E-01	
4.4725087E-02	4.4725087E-02	4.4725087E-02	4.4725087E-02	0
9.2037131E-02	2.0621019E-03	4.1191156E-03	5.6809667E-01	
1.0000000E-00	2.5625587E-00	2.5625587E-00		
1.0000000E-03	2.0000000E+01	8.7266460E-02	1.3270617E-01	
9.8034113E-02	7.6131134E-02	1.0767653E-02	1.1135325E-02	5
3.8107490E-01	2.2690819E-03	4.9863583E-03	1.4666390E-01	
9.6698149E-01	6.1694109E-01	6.3800714E-01		
1.0000000E-03	2.0000000E+01	1.7453292E-01	6.2900875E-02	10
1.8011584E-01	1.6824021E-01	5.5829269E-03	6.2927016E-03	
7.2658928E-01	2.9144276E-03	8.3231389E-03	9.0339268E-02	

8.8720668E-01 3.1987815E-01 3.6054524E-01
 1.0000000E-03 2.0000000E+01 3.4906585E-01 1.9077158E-02
 3.5180303E-01 3.4500201E-01 2.7371885E-03 4.0638342E-03 20
 1.4141126E-00 7.3981669E-03-5.6244248E-02 7.2928122E-02
 6.7354827E-01 1.5682934E-01 2.3284054E-01

$\epsilon = .002$

ϵ	n	γ	K^+	
2.0000000E-03	5.0000000E-00	0.0000000E-99	1.9455244E-01	
$\gamma + \alpha$	$\gamma - \beta$	α	β	γ
6.3256098E-02	6.3256098E-02	6.3256098E-02	6.3256098E-02	0
U/D	W_1/D	W_2/D	K^-	
1.0671964E-00	3.4479666E-02	6.7596867E-02	1.9455244E-01	
α/β	α in deg.	β in deg.		
1.0000000E-00	3.6243074E-00	3.6243074E-00		
2.0000000E-03	5.0000000E-00	8.7266460E-02	4.4688743E-02	
1.0773394E-01	6.1001034E-02	2.0467489E-02	2.6265425E-02	5
3.2896187E-00	7.6535574E-02	3.3231563E-01	9.9749469E-02	
7.7925597E-01	1.1727007E-00	1.5048980E-00		
2.0000000E-03	1.0000000E+01	0.0000000E-99	3.9911699E-01	
6.3256098E-02	6.3256098E-02	6.3256098E-02	6.3256098E-02	0
2.6142157E-01	8.3203692E-03	1.6558600E-02	3.9911699E-01	
1.0000000E-00	3.6243074E-00	3.6243074E-00		
2.0000000E-03	1.0000000E+01	8.7266460E-02	1.2044591E-01	
1.0773394E-01	6.5329349E-02	2.0467489E-02	2.1937110E-02	5
8.0582849E-01	1.0195237E-02	2.4774522E-02	1.4832282E-01	
9.3300756E-01	1.1727007E-00	1.2569038E-00		
2.0000000E-03	1.0000000E+01	1.7453292E-01	5.2222208E-02	
1.8553261E-01	1.6068810E-01	1.0999695E-02	1.3844811E-02	10
1.4824392E-00	1.6778374E-02	6.7913293E-02	1.0713509E-01	
7.9449950E-01	6.3023613E-01	7.9324925E-01		
2.0000000E-03	1.0000000E+01	3.4906585E-01	6.9635664E-04	
3.5451996E-01	3.3828895E-01	5.4541168E-03	1.0776896E-02	20
2.8528615E-00	1.2147383E-00	3.7337644E+02	1.0856873E-01	
5.0609345E-01	3.1249787E-01	6.1747068E-01		

Contrails

$\epsilon = .002$

2.0000000E-03 2.0000000E+01 0.0000000E-99 8.0320904E-01
6.3256098E-02-6.3256098E-02 6.3256098E-02 6.3256098E-02 0
6.5031202E-02 2.0621019E-03-4.1191156E-03 8.0320904E-01
1.0000000E-00 3.6243074E-00 3.6243074E-00
2.0000000E-03 2.0000000E+01 8.7266460E-02 2.5624239E-01
1.0773394E-01 6.6404487E-02 2.0467489E-02 2.0861972E-02 5
2.0045780E-01 2.1695280E-03-4.5410678E-03 2.7088397E-01
9.8109082E-01 1.1727007E-00 1.1953029E-00
2.0000000E-03 2.0000000E+01 1.7453292E-01 1.3268887E-01
1.8553261E-01 1.6280693E-01 1.0999695E-02 1.1725985E-02 10
3.6877142E-01 2.4541567E-03-5.8770248E-03 1.6055347E-01
9.3806151E-01 6.3023613E-01 6.7184948E-01
2.0000000E-03 2.0000000E+01 3.4906585E-01 5.5768293E-02
3.5451996E-01 3.4227567E-01 5.4541168E-03 6.7901761E-03 20
7.0967753E-01 3.8104220E-03-1.4863033E-02 1.0987395E-01
8.0323642E-01 3.1249787E-01 3.8904843E-01
2.0000000E-03 2.0000000E+01 6.9813170E-01 5.7773801E-03
7.0051183E-01 6.9371492E-01 2.3801337E-03 4.4167738E-03 40
1.3257320E-00 2.9200951E-02-1.0718168E-00 1.0715346E-01
5.3888513E-01 1.3637161E-01 2.5306249E-01

Contrails

ϵ	n	γ	K^+	
5.0000000E-03	5.0000000E-00	0.0000000E-99	3.0738340E-01	
$\gamma + \alpha$	$\gamma - \beta$	α	β	γ
1.0004171E-01	-1.0004171E-01	1.0004171E-01	1.0004171E-01	
U/D	W_1/D	W_2/D	K^-	0
6.7343114E-01	3.4479666E-02	-6.7596867E-02	3.0738340E-01	
α/β	α in deg.	β in deg.		
1.0000000E-00	5.7319679E-00	5.7319679E-00		
5.0000000E-03	5.0000000E-00	8.7266460E-02	1.2144643E-01	
1.3265874E-01	3.5924567E-02	4.5392289E-02	5.1341892E-02	5
1.4824849E-00	5.0041421E-02	-1.4077606E-01	1.7744409E-01	
8.8411795E-01	2.6007865E-00	2.9416737E-00		
5.0000000E-03	5.0000000E-00	1.7453292E-01	4.5471317E-02	
2.0091835E-01	1.3663672E-01	2.6385437E-02	3.7896194E-02	10
2.5223940E-00	1.1570471E-01	-7.6166950E-01	1.5578867E-01	
6.9625558E-01	1.5117741E-00	2.1712920E-00		
5.0000000E-03	1.0000000E+01	0.0000000E-99	6.3058543E-01	
1.0004171E-01	-1.0004171E-01	1.0004171E-01	1.0004171E-01	0
1.6496440E-01	8.3203692E-03	-1.6558600E-02	6.3058543E-01	
1.0000000E-00	5.7319679E-00	5.7319679E-00		
5.0000000E-03	1.0000000E+01	8.7266460E-02	2.7788117E-01	
1.3265874E-01	4.0258385E-02	4.5392289E-02	4.7008074E-02	5
3.6315108E-01	9.1547832E-03	-1.9782188E-02	3.0760986E-01	
9.6562749E-01	2.6007865E-00	2.6933642E-00		
5.0000000E-03	1.0000000E+01	1.7453292E-01	1.5054372E-01	
2.0091835E-01	1.4519360E-01	2.6385437E-02	2.9339315E-02	10
6.1788832E-01	1.1220737E-02	-3.0024891E-02	2.0685157E-01	
8.9932013E-01	1.5117741E-00	1.6810189E-00		
5.0000000E-03	1.0000000E+01	3.4906585E-01	5.4538278E-02	
3.6255373E-01	3.3018440E-01	1.3487885E-02	1.8881442E-02	20
1.1535575E-00	2.3286258E-02	-1.3583675E-01	1.6336352E-01	
7.1434612E-01	7.7279889E-01	1.0818269E-00		
5.0000000E-03	2.0000000E+01	0.0000000E-99	1.2690312E-00	
1.0004171E-01	-1.0004171E-01	1.0004171E-01	1.0004171E-01	0
4.1036528E-02	2.0621019E-03	-4.1191156E-03	1.2690312E-00	
1.0000000E-00	5.7319679E-00	5.7319679E-00		

Contrails

5.0000000E-03 2.0000000E+01 8.7266460E-02 5.7306041E-01
1.3265874E-01 4.1334963E-02 4.5392289E-02 4.5931496E-02 5
9.0337423E-02 2.1155853E-03-4.2758588E-03 5.9139166E-01
9.8826061E-01 2.6007865E-00 2.6316809E-00
5.0000000E-03 2.0000000E+01 1.7453292E-01 3.3052047E-01
2.0091835E-01 1.4731753E-01 2.6385437E-02 2.7215388E-02 10
1.5370583E-01 2.2125661E-03-4.7191662E-03 3.6105976E-01
9.6950435E-01 1.5117741E-00 1.5593268E-00
5.0000000E-03 2.0000000E+01 3.4906585E-01 1.6404463E-01
3.6255373E-01 3.3418242E-01 1.3487885E-02 1.4883421E-02 20
2.8695883E-01 2.5867101E-03-6.7641066E-03 2.1975942E-01
9.0623553E-01 7.7279889E-01 8.5275721E-01
5.0000000E-03 2.0000000E+01 6.9813170E-01 6.4631048E-02
7.0406949E-01 6.9012623E-01 5.9377938E-03 8.0054615E-03 40
5.3140756E-01 4.0601542E-03-2.0501843E-02 1.6703817E-01
7.4171786E-01 3.4021052E-01 4.5867916E-01
5.0000000E-03 2.0000000E+01 1.1344640E-00 2.2478500E-02
1.1367942E-00 1.1305351E-00 2.3302744E-03 3.9288646E-03 65
7.4704093E-01 6.4011513E-03-9.2499742E-02 1.6634656E-01
5.9311648E-01 1.3351488E-01 2.2510736E-01
5.0000000E-03 2.0000000E+01 1.5707963E-00 1.2471655E-02
1.5707963E-00 1.5707962E-00 1.3218857E-10 2.5359475E-10 90
8.3495319E-01 7.2208171E-10-2.0578602E-08 1.7119425E-01
5.2125913E-01 7.5738477E-09 1.4529908E-08

Contrails

ϵ	n	γ	K^+	
1.0000000E-02	5.0000000E-00	0.0000000E-99	4.3416069E-01	
$\gamma + \alpha$	$\gamma - \beta$	α	β	γ
1.4153947E-01	1.4153947E-01	1.4153947E-01	1.4153947E-01	
U/D	W_1/D	W_2/D	K^-	0
4.7438967E-01	3.4479666E-02	6.7596867E-02	4.3416069E-01	
α/β	α^o	β^o		
1.0000000E-00	8.1096144E-00	8.1096144E-00		
1.0000000E-02	5.0000000E-00	8.7266460E-02	2.2410234E-01	
1.6612618E-01	2.0862387E-03	7.8859725E-02	8.5180221E-02	5
8.5214589E-01	4.3095810E-02	1.0308051E-01	2.8238769E-01	
9.2579854E-01	4.5183294E-00	4.8804671E-00		
1.0000000E-02	5.0000000E-00	1.7453292E-01	1.1793692E-01	
2.2425668E-01	1.1294656E-01	4.9723763E-02	6.1586356E-02	10
1.3376913E-00	6.5829195E-02	2.4261227E-01	2.3045555E-01	
8.0738277E-01	2.8489617E-00	3.5286382E-00		
1.0000000E-02	5.0000000E-00	3.4906585E-01	1.4039696E-02	
3.7557818E-01	3.0071541E-01	2.6512330E-02	4.8350433E-02	20
2.3953153E-00	5.2966339E-01	1.6499123E+01	2.3302169E-01	
5.4833697E-01	1.5190446E-00	2.7702757E-00		
1.0000000E-02	1.0000000E+01	0.0000000E-99	8.9066425E-01	
1.4153947E-01	1.4153947E-01	1.4153947E-01	1.4153947E-01	0
1.1620699E-01	8.3203692E-03	1.6558600E-02	8.9066425E-01	
1.0000000E-00	8.1096144E-00	8.1096144E-00		
1.0000000E-02	1.0000000E+01	8.7266460E-02	4.8843542E-01	
1.6612618E-01	6.4231639E-03	7.8859725E-02	8.0843296E-02	5
2.0874256E-01	8.8392257E-03	1.8200527E-02	5.2281682E-01	
9.7546400E-01	4.5183294E-00	4.6319796E-00		
1.0000000E-02	1.0000000E+01	1.7453292E-01	2.9909083E-01	
2.2425668E-01	1.2152978E-01	4.9723763E-02	5.3003138E-02	10
3.2768228E-01	9.7966448E-03	2.2473424E-02	3.5957091E-01	
9.3812867E-01	2.8489617E-00	3.0368561E-00		
1.0000000E-02	1.0000000E+01	3.4906585E-01	1.4147785E-01	
3.7557818E-01	3.1694429E-01	2.6512330E-02	3.2121555E-02	2
5.8675900E-01	1.3872592E-02	4.7300169E-02	2.5320610E-01	
8.2537505E-01	1.5190446E-00	1.8404295E-00		

1.0000000E-02 1.0000000E+01 6.9813170E-01 2.9757044E-02
7.0996605E-01 6.7795167E-01 1.1834359E-02 2.0180026E-02 40
1.0717970E-00 4.9784397E-02-7.5090186E-01 2.3592244E-01
5.8643924E-01 6.7805884E-01 1.1562303E-00
1.0000000E-02 2.0000000E+01 0.0000000E-99 1.7924307E-00
1.4153947E-01-1.4153947E-01 1.4153947E-01 1.4153947E-01 0
2.8907640E-02 2.0621019E-03-4.1191156E-03 1.7924307E-00
1.0000000E-00 8.1096144E-00 8.1096144E-00
1.0000000E-02 2.0000000E+01 8.7266460E-02 9.9677353E-01
1.6612618E-01 7.5006118E-03 7.8859725E-02 7.9765848E-02 5
5.1926777E-02 2.1037970E-03-4.1728159E-03 1.0244454E-00
9.8864021E-01 4.5183294E-00 4.5702464E-00
1.0000000E-02 2.0000000E+01 1.7453292E-01 6.2941040E-01
2.2425668E-01 1.2366051E-01 4.9723763E-02 5.0872403E-02 10
8.1514208E-02 2.1455946E-03-4.3562115E-03 6.6816782E-01
9.7742116E-01 2.8489617E-00 2.9147739E-00
1.0000000E-02 2.0000000E+01 3.4906585E-01 3.3888049E-01
3.7557818E-01 3.2096021E-01 2.6512330E-02 2.8105636E-02 20
1.4596210E-01 2.2731436E-03-5.1144732E-03 3.9994511E-01
9.4331009E-01 1.5190446E-00 1.6103343E-00
1.0000000E-02 2.0000000E+01 6.9813170E-01 1.6178539E-01
7.0996605E-01 6.8413064E-01 1.1834359E-02 1.4001052E-02 40
2.6662012E-01 2.5895102E-03-8.1717709E-03 2.6748307E-01
8.4524784E-01 6.7805884E-01 8.0220121E-01
1.0000000E-02 2.0000000E+01 1.1344640E-00 9.2056362E-02
1.1391220E-00 1.1281640E-00 4.6580347E-03 6.2999062E-03 65
3.7372003E-01 2.2332721E-03-1.1055914E-02 2.3853586E-01
7.3938160E-01 2.6688573E-01 3.6095803E-01
1.0000000E-02 2.0000000E+01 1.5707963E-00 7.5963718E-02
1.5707963E-00 1.5707962E-00 2.6755223E-10 3.9019104E-10 95
4.1252234E-01 1.6625424E-10-1.0332429E-09 2.3720204E-01
6.8569548E-01 1.5329613E-08 2.2356300E-08

Contrails

ϵ	n	γ	K^+	
5.0000000E-02	5.0000000E-00	0.0000000E-99	9.6100637E-01	
$\gamma + \alpha$	$\gamma - \beta$	α	β	
3.1756042E-01	3.1756042E-01	3.1756042E-01	3.1756042E-01	0
U/D	W_1/D	W_2/D	K^-	
2.0565906E-01	3.4479666E-02	6.7596867E-02	9.6100637E-01	
α/β	α	β		
1.0000000E-00	1.8194872E+01	1.8194872E+01		
5.0000000E-02	5.0000000E-00	8.7266460E-02	7.1322418E-01	
3.2894103E-01	1.6529893E-01	2.4167457E-01	2.5256539E-01	5
2.7319167E-01	3.8079361E-02	7.5475434E-02	7.9928988E-01	
9.5687920E-01	1.3846933E+01	1.4470931E+01		
5.0000000E-02	5.0000000E-00	1.7453292E-01	5.3332807E-01	
3.6093407E-01	2.9683871E-02	1.8640115E-01	2.0421679E-01	10
3.5298670E-01	4.2595766E-02	9.1380743E-02	6.8275714E-01	
9.1276114E-01	1.0679999E+01	1.1700760E+01		
5.0000000E-02	5.0000000E-00	3.4906585E-01	3.0735325E-01	
4.6747720E-01	2.0317559E-01	1.1841135E-01	1.4589025E-01	20
5.3392786E-01	5.7230527E-02	1.6905728E-01	5.6341829E-01	
8.1164677E-01	6.7844707E-00	8.3588957E-00		
5.0000000E-02	5.0000000E-00	6.9813170E-01	9.1814802E-02	
7.5577209E-01	6.0282344E-01	5.7640390E-02	9.5308258E-02	40
8.9737151E-01	1.4533456E-01	1.3504866E-00	5.4038780E-01	
6.0477854E-01	3.3025510E-00	5.4607609E-00		
5.0000000E-02	1.0000000E+01	0.0000000E-99	1.9714682E-00	
3.1756042E-01	3.1756042E-01	3.1756042E-01	3.1756042E-01	0
5.0378464E-02	8.3203692E-03	1.6558600E-02	1.9714682E-00	
1.0000000E-00	1.8194872E+01	1.8194872E+01		
5.0000000E-02	1.0000000E+01	8.7266460E-02	1.4916576E-00	
3.2894103E-01	1.6101956E-01	2.4167457E-01	2.4828602E-01	5
6.6921322E-02	8.7070369E-03	1.6550606E-02	1.5837459E-00	
9.7337161E-01	1.3846933E+01	1.4225741E+01		

Contrails

5.0000000E-02 1.0000000E+01 1.7453292E-01 1.1506003E-00
3.6093407E-01-2.1044105E-02 1.8640115E-01 1.9557702E-01 10
8.6467998E-02 8.9932870E-03-1.6972596E-02 1.2860092E-00
9.5308306E-01 1.0679999E+01 1.1205738E+01
5.0000000E-02 1.0000000E+01 3.4906585E-01 7.4142092E-01
4.6747720E-01 2.1983080E-01 1.1841135E-01 1.2923504E-01 20
1.3079153E-01 9.4684010E-03-1.8975646E-02 9.2310873E-01
9.1624802E-01 6.7844707E-00 7.4046225E-00
5.0000000E-02 1.0000000E+01 6.9813170E-01 3.9728258E-01
7.5577209E-01 6.2901975E-01 5.7640390E-02 6.9111940E-02 40
2.1982108E-01 1.0092912E-02-2.6387340E-02 6.5531033E-01
8.3401493E-01 3.3025510E-00 3.9598224E-00
5.0000000E-02 1.0000000E+01 1.1344640E-00 2.4465451E-01
1.1576560E-00 1.1033652E-00 2.3192061E-02 3.1098798E-02 65
3.0168566E-01 7.8910851E-03-2.9603491E-02 5.7877453E-01
7.4575427E-01 1.3288072E-00 1.7818298E-00
5.0000000E-02 1.0000000E+01 1.5707963E-00 2.0545193E-01
1.5707963E-00 1.5707962E-00 1.3390524E-09 1.8855349E-09 90
3.3134323E-01 5.8009542E-10-2.5612987E-09 5.6830933E-01
7.1017111E-01 7.6722056E-08 1.0803319E-07
5.0000000E-02 2.0000000E+01 0.0000000E-99 3.9675111E-00
3.1756042E-01-3.1756042E-01 3.1756042E-01 3.1756042E-01 0
1.2532141E-02 2.0621019E-03-4.1191156E-03 3.9675111E-00
1.0000000E-00 1.8194872E+01 1.8194872E+01
5.0000000E-02 2.0000000E+01 8.7266460E-02 3.0156280E-00
3.2894103E-01-1.5995594E-01 2.4167457E-01 2.4722240E-01 5
1.6647340E-02 2.1297033E-03-4.0070845E-03 3.1597793E-00
9.7755936E-01 1.3846933E+01 1.4164800E+01 89

Contrails

5.0000000E-02 2.0000000E+01 1.7453292E-01 2.3427228E-00
3.6093407E-01-1.8897685E-02 1.8640115E-01 1.9343060E-01 10
2.1509769E-02 2.1564391E-03-3.9417679E-03 2.5318343E-00
9.6365903E-01 1.0679999E+01 1.1082757E+01
5.0000000E-02 2.0000000E+01 3.4906585E-01 1.5453686E-00
4.6747720E-01 2.2395633E-01 1.1841135E-01 1.2510951E-01 29
3.2535688E-02 2.1332295E-03-3.8665631E-03 1.7440851E-00
9.4646164E-01 6.7844707E-00 7.1682469E-00
5.0000000E-02 2.0000000E+01 6.9813170E-01 8.9952257E-01
7.5577209E-01 6.3543570E-01 5.7640390E-02 6.2695996E-02 40
5.4682667E-02 1.8745307E-03-3.6012855E-03 1.1011915E-00
9.1936316E-01 3.3025510E-00 3.5922160E-00
5.0000000E-02 2.0000000E+01 1.1344640E-00 6.3350348E-01
1.1576560E-00 1.1083970E-00 2.3192061E-02 2.6066934E-02 65
7.5047292E-02 1.1342092E-03-2.3959049E-03 8.5441793E-01
8.8971187E-01 1.3288072E-00 1.4935253E-00
5.0000000E-02 2.0000000E+01 1.5707963E-00 5.7029478E-01
1.5707963E-00 1.5707962E-00 1.3390524E-09 1.5373953E-09 90
8.2424906E-02 7.4040258E-11-1.6603021E-10 8.0103320E-01
8.7098775E-01 7.6722056E-08 8.8086262E-08

Contrails

ϵ	n	γ	K^+	
1.0000000E-01	5.0000000E-00	0.0000000E-99	1.3415311E-00	
$\gamma + \alpha$	$\gamma - \beta$	α	β	γ
4.5102681E-01	4.5102681E-01	4.5102681E-01	4.5102681E-01	
U/D	W_1/D	W_2/D	K^-	0
1.3957006E-01	3.4479666E-02	6.7596867E-02	1.3415311E-00	
α/β	α^0	β^0		
1.0000000E-00	2.5841932E+01	2.5841932E+01		
1.0000000E-01	5.0000000E-00	8.7266460E-02	1.0850040E-00	
4.5882113E-01	3.0213571E-01	3.7155467E-01	3.8940217E-01	5
1.7281959E-01	3.7784447E-02	7.0497774E-02	1.2118993E-00	
9.5416691E-01	2.1288514E+01	2.2311101E+01		
1.0000000E-01	5.0000000E-00	1.7453292E-01	8.8247181E-01	
4.8144445E-01	1.6114954E-01	3.0691153E-01	3.3568246E-01	10
2.1004911E-01	4.0983115E-02	7.6689325E-02	1.0981702E-00	
9.1429122E-01	1.7584735E+01	1.9233188E+01		
1.0000000E-01	5.0000000E-00	3.4906585E-01	5.9773055E-01	
5.6287704E-01	9.4748568E-02	2.1381119E-01	2.5431728E-01	20
2.9254485E-01	4.8001793E-02	1.0182413E-01	9.3843130E-01	
8.4072618E-01	1.2250479E+01	1.4571306E+01		
1.0000000E-01	5.0000000E-00	6.9813170E-01	2.9651465E-01	
8.1008067E-01	5.3834223E-01	1.1194897E-01	1.5978946E-01	40
4.6061790E-01	6.6580892E-02	2.3731411E-01	8.2892591E-01	
7.0060295E-01	6.4142037E-00	9.1552621E-00		
1.0000000E-01	5.0000000E-00	1.1344640E-00	1.3376455E-01	
1.1806146E-00	1.0542032E-00	4.6150646E-02	8.0260763E-02	65
6.1856959E-01	7.9783207E-02	6.2680982E-01	8.4644257E-01	
5.7500881E-01	2.6442372E-00	4.5986030E-00		
1.0000000E-01	5.0000000E-00	1.5707963E-00	8.7336903E-02	
1.5707963E-00	1.5707962E-00	2.6785121E-09	5.0342818E-09	90
6.7621536E-01	7.8236154E-09	9.5618241E-08	8.6902235E-01	
5.3205446E-01	1.5346744E-07	2.8844310E-07		
1.0000000E-01	1.0000000E+01	0.0000000E-99	2.7521004E-00	
4.5102681E-01	4.5102681E-01	4.5102681E-01	4.5102681E-01	0
3.4189231E-02	8.3203692E-03	1.6558600E-02	2.7521004E-00	
1.0000000E-00	2.5841932E+01	2.5841932E+01		

Contrails

1.0000000E-01 1.0000000E+01 8.7266460E-02 2.2542035E-00
4.5882113E-01-2.9799254E-01 3.7155467E-01 3.8525900E-01 5
4.2334072E-02 8.8038256E-03-1.6046156E-02 2.4317188E-00
9.6442828E-01 2.1288514E+01 2.2073714E+01
1.0000000E-01 1.0000000E+01 1.7453292E-01 1.8663093E-00
4.8144445E-01-1.5261313E-01 3.0691153E-01 3.2714605E-01 10
5.1453855E-02 9.1208255E-03-1.5805198E-02 2.1389012E-00
9.3814834E-01 1.7584735E+01 1.8744088E+01
1.0000000E-01 1.0000000E+01 3.4906585E-01 1.3353581E-00
5.6287704E-01 1.1169271E-01 2.1381119E-01 2.3737313E-01 20
7.1662099E-02 9.3996565E-03-1.5895309E-02 1.6860811E-00
9.0073881E-01 1.2250479E+01 1.3600478E+01
1.0000000E-01 1.0000000E+01 6.9813170E-01 8.1284297E-01
8.1008067E-01 5.6566938E-01 1.1194897E-01 1.3246231E-01 40
1.1283345E-01 8.9040427E-03-1.6659010E-02 1.2207120E-00
8.4513826E-01 6.4142037E-00 7.5895317E-00
1.0000000E-01 1.0000000E+01 1.1344640E-00 5.6409920E-01
1.1806146E-00 1.0761938E-00 4.6150646E-02 5.8270187E-02 65
1.5152546E-01 5.8486269E-03-1.3093040E-02 1.0262007E-00
7.9201129E-01 2.6442372E-00 3.3386357E-00
1.0000000E-01 1.0000000E+01 1.5707963E-00 4.9985652E-01
1.5707963E-00 1.5707962E-00 2.6785121E-09 3.4795396E-09 90
1.6564643E-01 3.9803494E-10-9.6884232E-10 9.8470541E-01
7.6978922E-01 1.5346744E-07 1.9936293E-07
1.0000000E-01 2.0000000E+01 0.0000000E-99 5.5385062E-00
4.5102681E-01-4.5102681E-01 4.5102681E-01 4.5102681E-01 0
8.5049094E-03 2.0621019E-03-4.1191156E-03 5.5385062E-00
1.0000000E-00 2.5841932E+01 2.5841932E+01
1.0000000E-01 2.0000000E+01 8.7266460E-02 4.5501527E-00
4.5882113E-01-2.9696239E-01 3.7155467E-01 3.8422885E-01 5
1.0531019E-02 2.1633850E-03-3.9208144E-03 4.8670477E-00
9.6701399E-01 2.1288514E+01 2.2014691E+01

Contrails

1.0000000E-01 2.0000000E+01 1.7453292E-01 3.7827928E-00
4.8144445E-01-1.5049089E-01 3.0691153E-01 3.2502381E-01 10
1.2799655E-02 2.2161116E-03-3.7681269E-03 4.2485583E-00
9.4427398E-01 1.7584735E+01 1.8622493E+01
1.0000000E-01 2.0000000E+01 3.4906585E-01 2.7397790E-00
5.6287704E-01 1.1589458E-01 2.1381119E-01 2.3317126E-01 20
1.7826655E-02 2.2119184E-03-3.5302117E-03 3.2762625E-00
9.1697060E-01 1.2250479E+01 1.3359729E+01
1.0000000E-01 2.0000000E+01 6.9813170E-01 1.7336805E-00
8.1008067E-01 5.7236938E-01 1.1194897E-01 1.2576231E-01 40
2.8068437E-02 1.9055402E-03-3.0020769E-03 2.2259753E-00
8.9016313E-01 6.4142037E-00 7.2056497E-00
1.0000000E-01 2.0000000E+01 1.1344640E-00 1.2731028E-00
1.1806146E-00 1.0814950E-00 4.6150646E-02 5.2968965E-02 65
3.7693458E-02 1.1052854E-03-1.8057425E-03 1.7325923E-00
8.7127709E-01 2.6442372E-00 3.0348981E-00
1.0000000E-01 2.0000000E+01 1.5707963E-00 1.1587301E-00
1.5707963E-00 1.5707962E-00 2.6681479E-09 3.1233328E-09 90
4.1366250E-02 7.0478293E-11-1.2118984E-10 1.6131716E-00
8.5426307E-01 1.5287361E-07 1.7895379E-07

Contrails

ϵ	n	γ	K^+	
5.0000000E-01	5.0000000E-00	0.0000000E-99	2.6653521E-00	
$\gamma + \alpha$	$\gamma - \beta$	α	β	γ
1.0471975E-00	-1.0471975E-00	1.0471975E-00	1.0471975E-00	
U/D	W_1/D	W_2/D	K^-	0
3.9027069E-02	3.4479666E-02	-6.7596867E-02	2.6653521E-00	
α/β	α_o	β_o		
1.0000000E-00	6.0000000E+01	6.0000000E+01		
5.0000000E-01	5.0000000E-00	8.7266460E-02	2.4009778E-00	
1.0493931E-00	-9.5886403E-01	9.6212669E-01	1.0461304E-00	5
4.6931720E-02	4.0007963E-02	-6.0277647E-02	2.8279948E-00	
9.1970045E-01	5.5125798E+01	5.9938862E+01		
5.0000000E-01	5.0000000E-00	1.7453292E-01	2.1763170E-00	
1.0559468E-00	-8.6268094E-01	8.8141389E-01	1.0372138E-00	10
5.4873477E-02	4.4818966E-02	-5.3424070E-02	3.0013770E-00	
8.4978992E-01	5.0501296E+01	5.9427977E+01		
5.0000000E-01	5.0000000E-00	3.4906585E-01	1.8193639E-00	
1.0816796E-00	-6.4737496E-01	7.3261381E-01	9.9644081E-01	20
7.0606663E-02	5.1967590E-02	-4.1466571E-02	3.3797670E-00	
7.3523063E-01	4.1975679E+01	5.7091853E+01		
5.0000000E-01	5.0000000E-00	6.9813170E-01	1.3569000E-00	
1.1777305E-00	-1.3043607E-01	4.7959881E-01	8.2856777E-01	40
9.9561818E-02	5.5049836E-02	-2.4650959E-02	4.2472157E-00	
5.7882871E-01	2.7478987E+01	4.7473436E+01		
5.0000000E-01	5.0000000E-00	1.1344640E-00	1.0651907E-00	
1.3578821E-00	6.6190897E-01	2.2341817E-01	4.7255502E-01	65
1.2573174E-01	3.6778769E-02	-1.1709657E-02	5.3616190E-00	
4.7278765E-01	1.2800918E+01	2.7075408E+01		
5.0000000E-01	5.0000000E-00	1.5707963E-00	9.7858058E-01	
1.5707963E-00	1.5707962E-00	1.3393404E-08	3.0520096E-08	90
1.3523455E-01	2.4885092E-09	-7.4103237E-10	5.8996801E-00	
4.3883885E-01	7.6738553E-07	1.7486727E-06		

5.0000000E-01 1.0000000E+01 0.0000000E-99 5.4678692E-00
1.0471975E-00-1.0471975E-00 1.0471975E-00 1.0471975E-00 0
9.5601124E-03 8.3203692E-03-1.6558600E-02 5.4678692E-00
1.0000000E-00 6.0000000E+01 6.0000000E+01
5.0000000E-01 1.0000000E+01 8.7266460E-02 4.9533553E-00
1.0493931E-00-9.5636823E-01 9.6212669E-01 1.0436346E-00 5
1.1496444E-02 9.5210393E-03-1.4280623E-02 5.7624855E-00
9.2189987E-01 5.5125798E+01 5.9795863E+01
5.0000000E-01 1.0000000E+01 1.7453292E-01 4.5185601E-00
1.0559468E-00-8.5704132E-01 8.8141389E-01 1.0315742E-00 10
1.3441865E-02 1.0517605E-02-1.2156331E-02 6.0712211E-00
8.5443572E-01 5.0501296E+01 5.9104850E+01
5.0000000E-01 1.0000000E+01 3.4906585E-01 3.8340851E-00
1.0816796E-00-6.3371702E-01 7.3261381E-01 9.8278287E-01 20
1.7295883E-02 1.1840865E-02-8.4758394E-03 6.7218358E-00
7.4544828E-01 4.1975679E+01 5.6309310E+01
5.0000000E-01 1.0000000E+01 6.9813170E-01 2.9655274E-00
1.1777305E-00-9.8551920E-02 4.7959881E-01 7.9668362E-01 40
2.4388769E-02 1.1756289E-02-3.5110068E-03 8.0694138E-00
6.0199406E-01 2.7478987E+01 4.5646609E+01
5.0000000E-01 1.0000000E+01 1.1344640E-00 2.4354548E-00
1.3578821E-00 6.9722739E-01 2.2341817E-01 4.3723660E-01 65
3.0799381E-02 7.2922639E-03-8.0060912E-04 9.4991207E-00
5.1097775E-01 1.2800918E+01 2.5051812E+01
5.0000000E-01 1.0000000E+01 1.5707963E-00 2.2823529E-00
1.5707963E-00 1.5707962E-00 1.3374762E-08 2.7809398E-08 90
3.3173373E-02 4.7681265E-10-3.4243575E-11 1.0089339E+01
4.8094397E-01 7.6631744E-07 1.5933611E-06
5.0000000E-01 2.0000000E+01 0.0000000E-99 1.1003896E+01
1.0471975E-00-1.0471975E-00 1.0471975E-00 1.0471975E-00 0
2.3781725E-03 2.0621019E-03-4.1191156E-03 1.1003896E+01
1.0000000E-00 6.0000000E+01 6.0000000E+01

Contrails

5.0000000E-01 2.0000000E+01 8.7266460E-02 9.9818455E-00
1.0493931E-00-9.5574680E-01 9.6212669E-01 1.0430132E-00 5
2.8598541E-03 2.3517584E-03-3.5238006E-03 1.1577804E+01
9.2244914E-01 5.5125798E+01 5.9760258E+01
5.0000000E-01 2.0000000E+01 1.7453292E-01 9.1193562E-00
1.0559468E-00-8.5563469E-01 8.8141389E-01 1.0301676E-00 10
3.3437969E-03 2.5891495E-03-2.9702472E-03 1.2176145E+01
8.5560240E-01 5.0501296E+01 5.9024256E+01
5.0000000E-01 2.0000000E+01 3.4906585E-01 7.7647296E-00
1.0816796E-00-6.3030471E-01 7.3261381E-01 9.7937056E-01 20
4.3025220E-03 2.8943256E-03-2.0160520E-03 1.3423646E+01
7.4804556E-01 4.1975679E+01 5.6113800E+01
5.0000000E-01 2.0000000E+01 6.9813170E-01 6.0547826E-00
1.1777305E-00-9.0634277E-02 4.7959881E-01 7.8876597E-01 40
6.0669474E-03 2.8299420E-03-7.5047425E-04 1.5924934E+01
6.0803689E-01 2.7478987E+01 4.5192961E+01
5.0000000E-01 2.0000000E+01 1.1344640E-00 5.0199734E-00
1.3578821E-00 7.0580038E-01 2.2341817E-01 4.2866361E-01 65
7.6616507E-03 1.7256602E-03-1.1262743E-04 1.8409041E+01
5.2119697E-01 1.2800918E+01 2.4560615E+01
5.0000000E-01 2.0000000E+01 1.5707963E-00 4.7244897E-00
1.5707963E-00 1.5707962E-00 1.3352426E-08 2.7274461E-08 90
8.2660089E-03 1.1159917E-10-3.4701498E-12 1.9398475E+01
4.8955784E-01 7.6503769E-07 1.5627115E-06

Contrails

ϵ	n	γ	K^+	
1.0000000E-00	5.0000000E-00	0.0000000E-99	3.0776835E-00	
$\gamma + \alpha$	$\gamma - \beta$	α	β	γ
1.5707963E-00	1.5707963E-00	1.5707963E-00	1.5707963E-00	0
U/D	W_1/D	W_2/D	K^-	
3.7024328E-11	3.4479666E-02	6.7596867E-02	3.0776835E-00	
α/β	α^o	β^o		
1.0000000E-00	8.9999999E+01	8.9999999E+01		
1.0000000E-00	5.0000000E-00	8.7266460E-02	2.8131723E-00	
1.5707963E-00	1.5707963E-00	1.4835298E-00	1.6580627E-00	5
5.8914549E-03	4.3909780E-02	5.1730194E-02	3.3908908E-00	
8.9473684E-01	8.5000000E+01	9.4999999E+01		
1.0000000E-00	5.0000000E-00	1.7453292E-01	2.5881079E-00	
1.5707963E-00	1.5707963E-00	1.3962634E-00	1.7453292E-00	10
1.1738072E-02	5.2971649E-02	3.5245914E-02	3.7650631E-00	
8.0000000E-01	8.0000000E+01	9.9999999E+01		
1.0000000E-00	5.0000000E-00	3.4906585E-01	2.2296410E-00	
1.5707963E-00	1.5707963E-00	1.2217304E-00	1.9198621E-00	20
2.3119490E-02	6.8883611E-02	2.3449971E-03	4.7685837E-00	
6.3636363E-01	7.0000000E+01	1.0999999E+02		
1.0000000E-00	5.0000000E-00	6.9813170E-01	1.7624537E-00	
1.5707963E-00	1.5707963E-00	8.7266462E-01	2.2689280E-00	40
4.3450428E-02	8.4766038E-02	4.9363283E-02	8.8735032E-00	
3.8461538E-01	5.0000000E+01	1.2999999E+02		
1.0000000E-00	5.0000000E-00	1.1344640E-00	1.4652012E-00	
1.5707963E-00	1.5707963E-00	4.3633232E-01	2.7052603E-00	65
6.1263566E-02	6.2047487E-02	5.6322464E-02	3.3964181E+01	
1.6129032E-01	2.5000000E+01	1.5499999E+02		
1.0000000E-00	5.0000000E-00	1.5707963E-00	1.3763481E-00	
1.5707963E-00	1.5707687E-00	2.6247174E-08	2.7559134E-05	90
6.9007469E-02	4.1798152E-09	4.0254298E-09	8.5684315E+04	
9.5239471E-04	1.5038522E-06	1.5790221E-03		

Contrails

1.0000000E-00 1.0000000E+01 0.0000000E-99 6.3137515E-00
1.5707963E-00-1.5707963E-00 1.5707963E-00 1.5707963E-00 0
2.7707838E-11 8.3203692E-03-1.6558600E-02 6.3137515E-00
1.0000000E-00 8.9999999E+01 8.9999999E+01
1.0000000E-00 1.0000000E+01 8.7266460E-02 5.7987943E-00
1.5707963E-00-1.5707963E-00 1.4835298E-00 1.6580627E-00 5
1.4431770E-03 1.0489657E-02-1.2300037E-02 6.9261618E-00
8.9473684E-01 8.5000000E+01 9.4999999E+01
1.0000000E-00 1.0000000E+01 1.7453292E-01 5.3626894E-00
1.5707963E-00-1.5707963E-00 1.3962634E-00 1.7453292E-00 10
2.8753707E-03 1.2539167E-02-8.0061004E-03 7.6606633E-00
8.0000000E-01 8.0000000E+01 9.9999999E+01
1.0000000E-00 1.0000000E+01 3.4906585E-01 4.6732652E-00
1.5707963E-00-1.5707963E-00 1.2217304E-00 1.9198621E-00 20
5.6633748E-03 1.6025324E-02 1.8424028E-04 9.6408924E-00
6.3636363E-01 7.0000000E+01 1.0999999E+02
1.0000000E-00 1.0000000E+01 6.9813170E-01 3.7888404E-00
1.5707963E-00-1.5707963E-00 8.7266462E-01 2.2689280E-00 40
1.0643663E-02 1.9074427E-02 1.1867431E-02 1.7803176E+01
3.8461538E-01 5.0000000E+01 1.2999999E+02
1.0000000E-00 1.0000000E+01 1.1344640E-00 3.2391276E-00
1.5707963E-00-1.5707963E-00 4.3633232E-01 2.7052603E-00 65
1.5007188E-02 1.3496663E-02 1.2426705E-02 6.7943081E+01
1.6129032E-01 2.5000000E+01 1.5499999E+02
1.0000000E-00 1.0000000E+01 1.5707963E-00 3.0780487E-00
1.5707963E-00 1.5707963E-00 2.7000000E-08-2.7000000E-08 90
1.6432814E-02 9.3418369E-10 9.3402017E-10-2.8674748E+04
-1.0000000E-00 1.5469860E-06-1.5469860E-06

Contrails

1.0000000E-00 2.0000000E+01 0.0000000E-99 1.2706204E+01
1.5707963E-00-1.5707963E-00 1.5707963E-00 1.5707963E-00 0
7.1345175E-12 2.0621019E-03-4.1191156E-03 1.2706204E+01
1.0000000E-00 8.9999999E+01 8.9999999E+01
1.0000000E-00 2.0000000E+01 8.7266460E-02 1.1683181E+01
1.5707963E-00-1.5707963E-00 1.4835298E-00 1.6580627E-00 5
3.5900457E-04 2.5934458E-03-3.0377620E-03 1.3924141E+01
8.9473684E-01 8.5000000E+01 9.4999999E+01
1.0000000E-00 2.0000000E+01 1.7453292E-01 1.0817818E+01
1.5707963E-00-1.5707963E-00 1.3962634E-00 1.7453292E-00 10
7.1527689E-04 3.0933903E-03-1.9552137E-03 1.5386319E+01
8.0000000E-01 8.0000000E+01 9.9999999E+01
1.0000000E-00 2.0000000E+01 3.4906585E-01 9.4523245E-00
1.5707963E-00-1.5707963E-00 1.2217304E-00 1.9198621E-00 20
1.4088205E-03 3.9372483E-03 8.7445541E-05 1.9333508E+01
6.3636363E-01 7.0000000E+01 1.0999999E+02
1.0000000E-00 2.0000000E+01 6.9813170E-01 7.7074259E-00
1.5707963E-00-1.5707963E-00 8.7266462E-01 2.2689280E-00 40
2.6477164E-03 4.6506811E-03 2.9352144E-03 3.5634415E+01
3.8461538E-01 5.0000000E+01 1.2999999E+02
1.0000000E-00 2.0000000E+01 1.1344640E-00 6.6291051E-00
1.5707963E-00-1.5707963E-00 4.3633232E-01 2.7052603E-00 65
3.7331865E-03 3.2662516E-03 3.0164542E-03 1.3589352E+02
1.6129032E-01 2.5000000E+01 1.5499999E+02
1.0000000E-00 2.0000000E+01 1.5707963E-00 6.3163265E-00
1.5707963E-00 1.5707963E-00 2.7000000E-08-2.7000000E-08 90
4.0878250E-03 2.2535788E-10 2.2522096E-10-1.5875519E+04
-1.0000000E-00 1.5469860E-06-1.5469860E-06

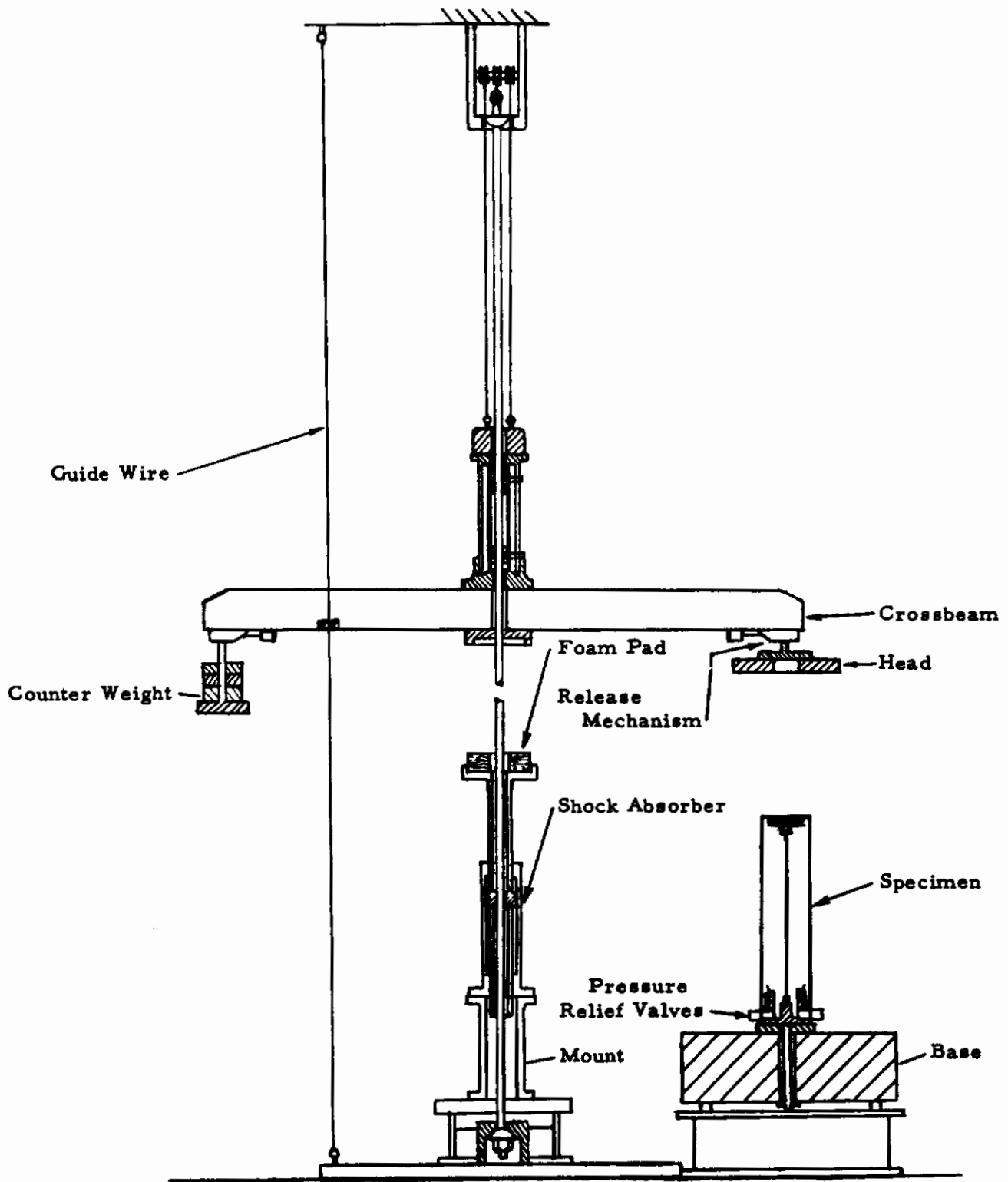


Figure 1. Pressurized Shell Impact Apparatus

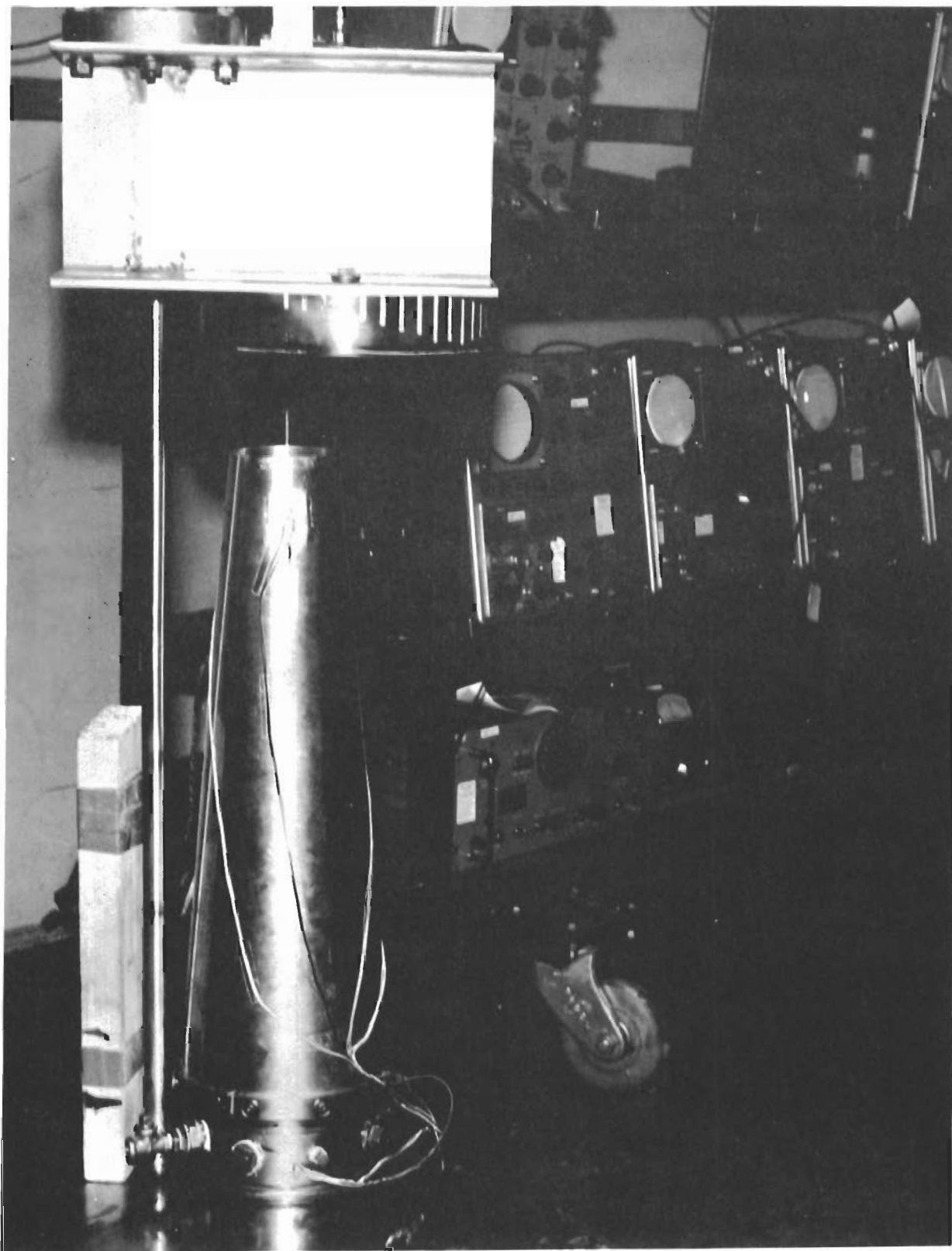


Figure 2. Modified Pressurized Shell Impact Apparatus

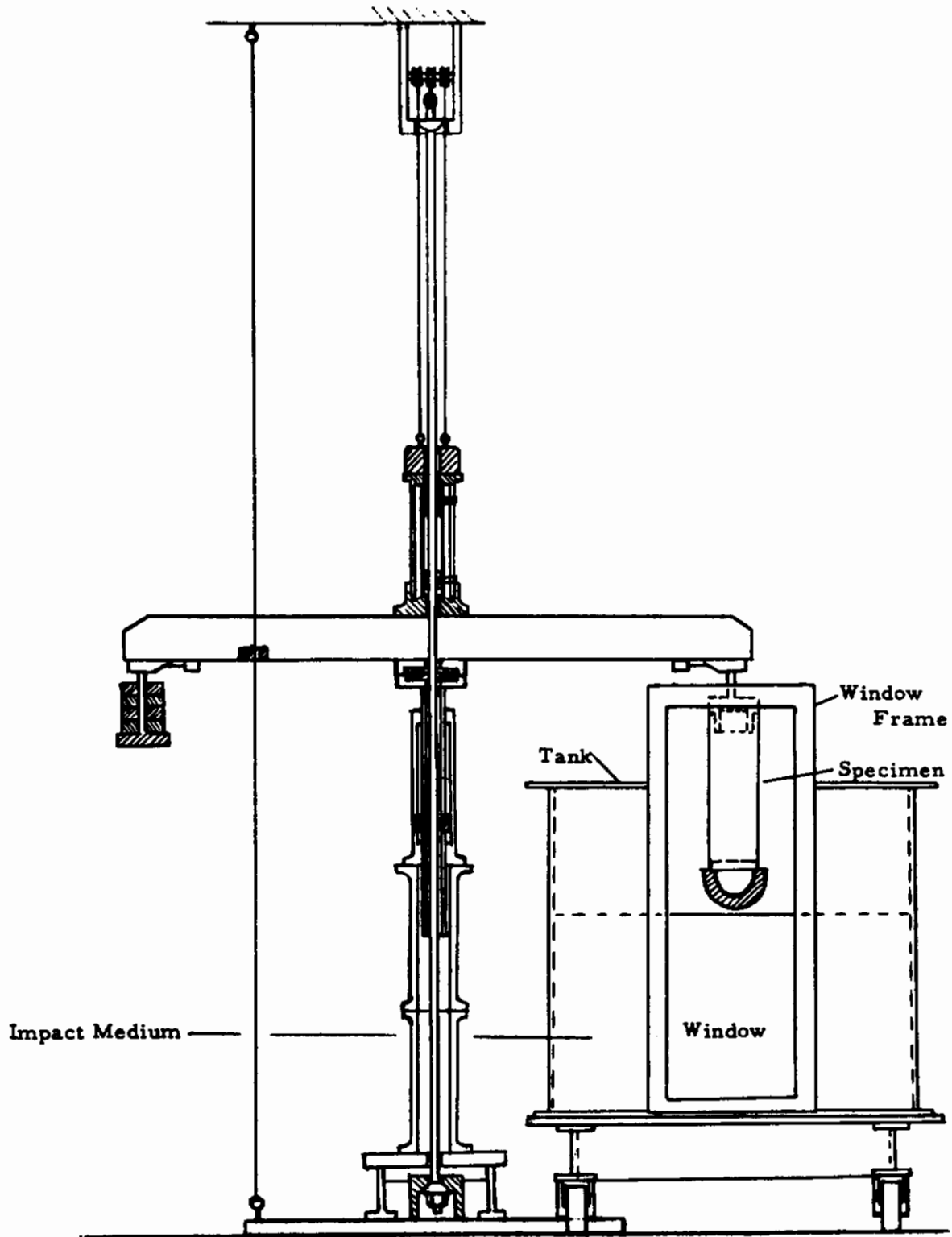


Figure 3. Non-Rigid Impact Test Apparatus

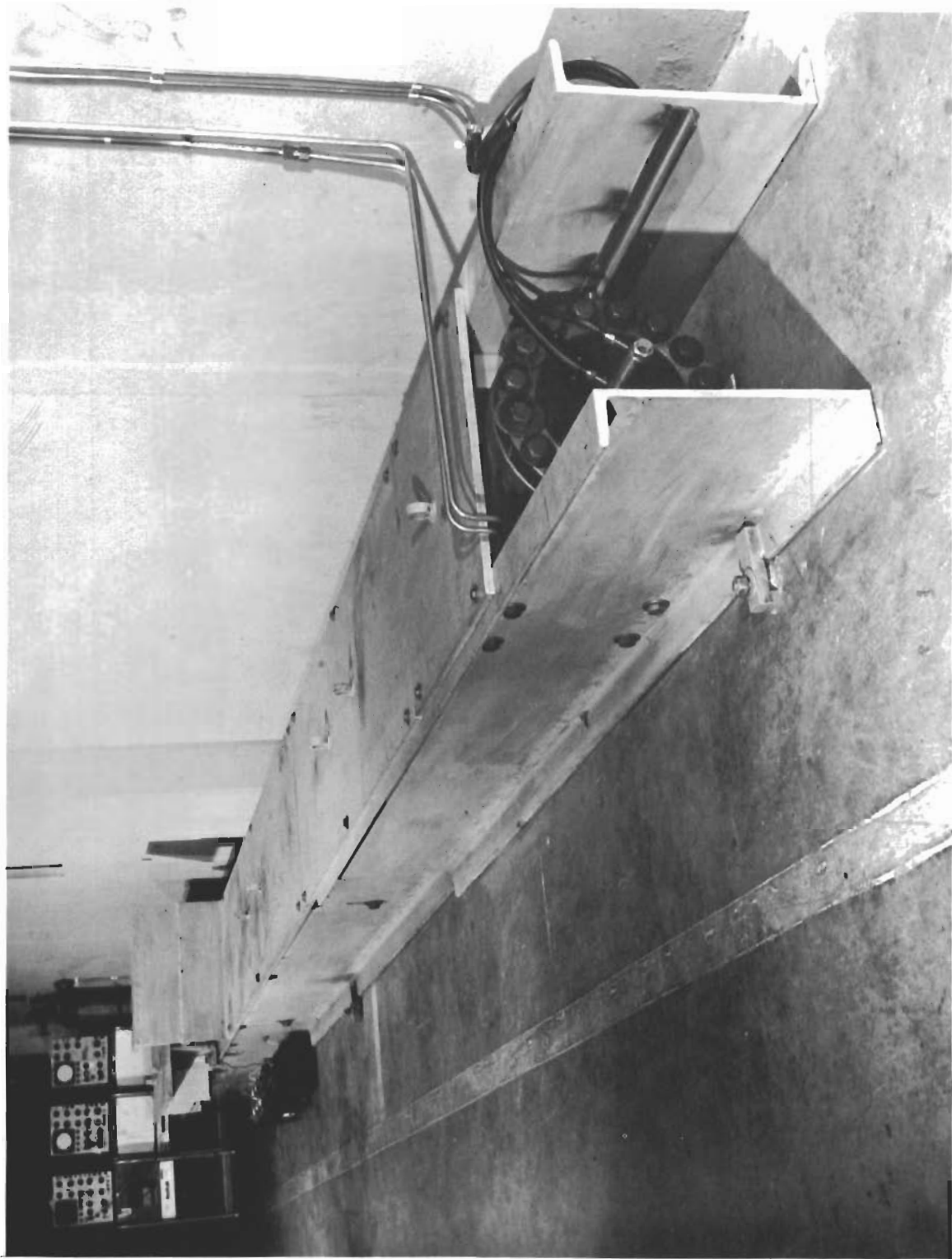


Figure 4. High Velocity Structural Impact Facility

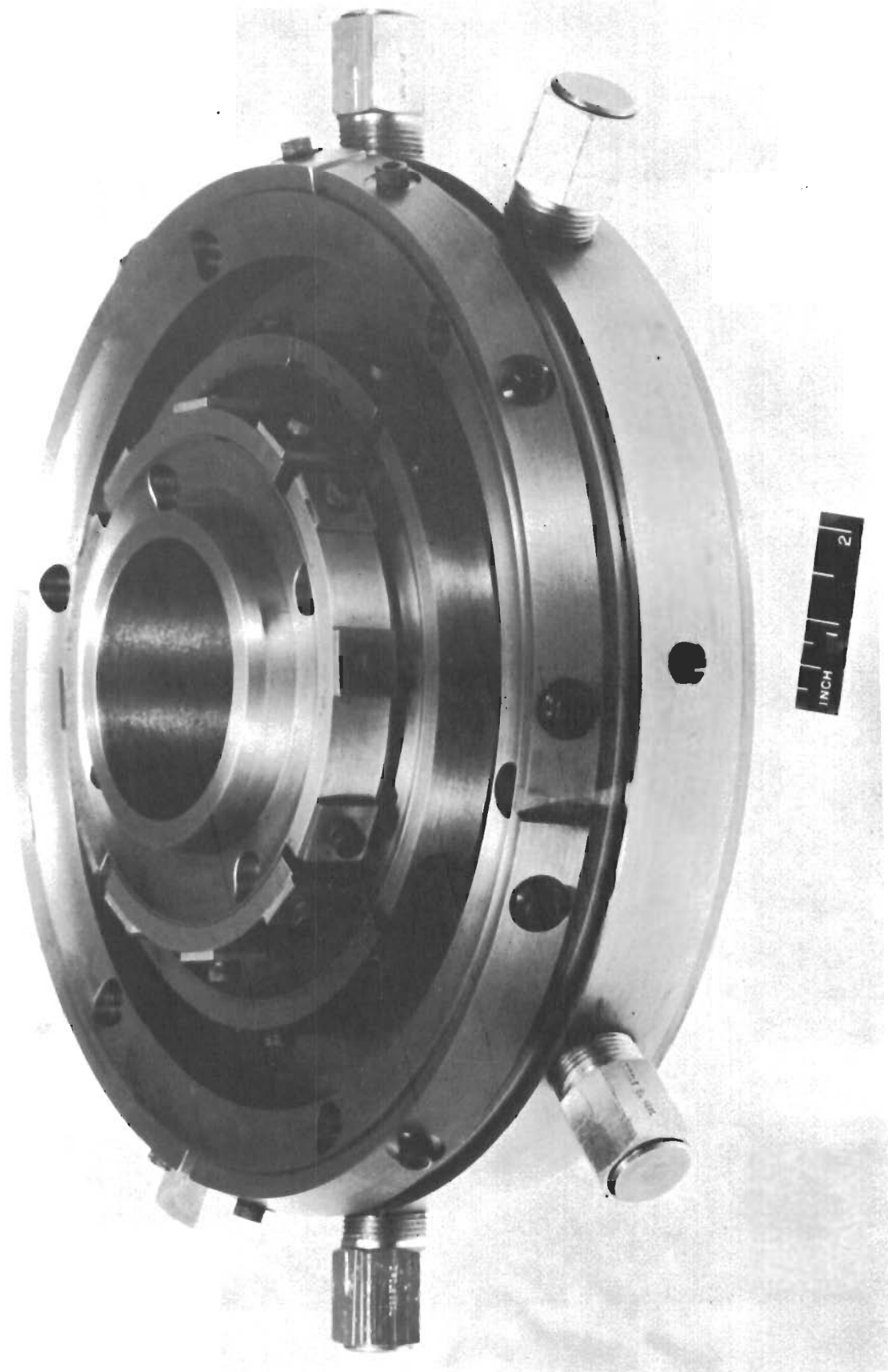


Figure 5. Pressurized Shell Mounting Fixture

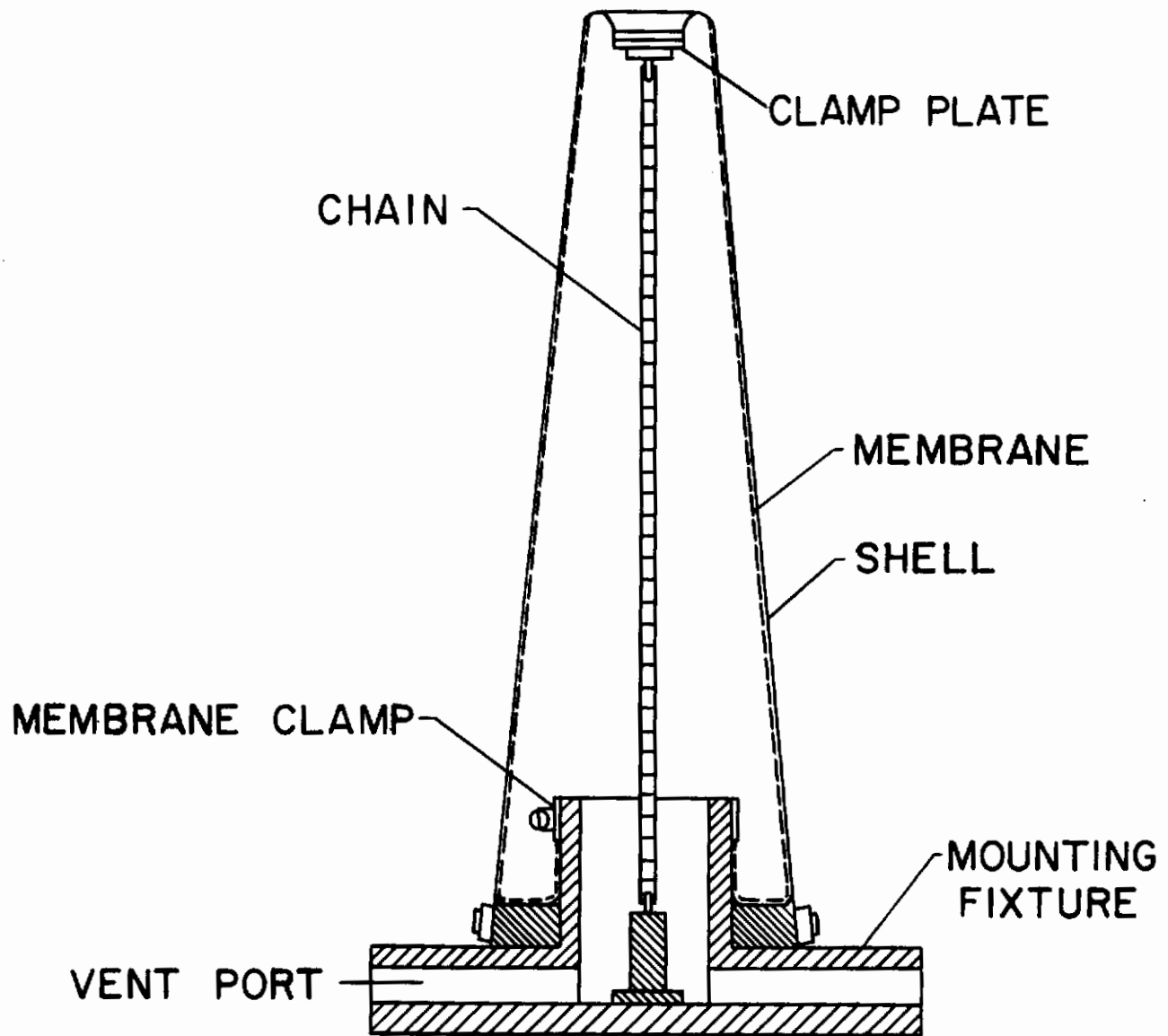


Figure 6. Mounting Arrangement of Pressurized Shell

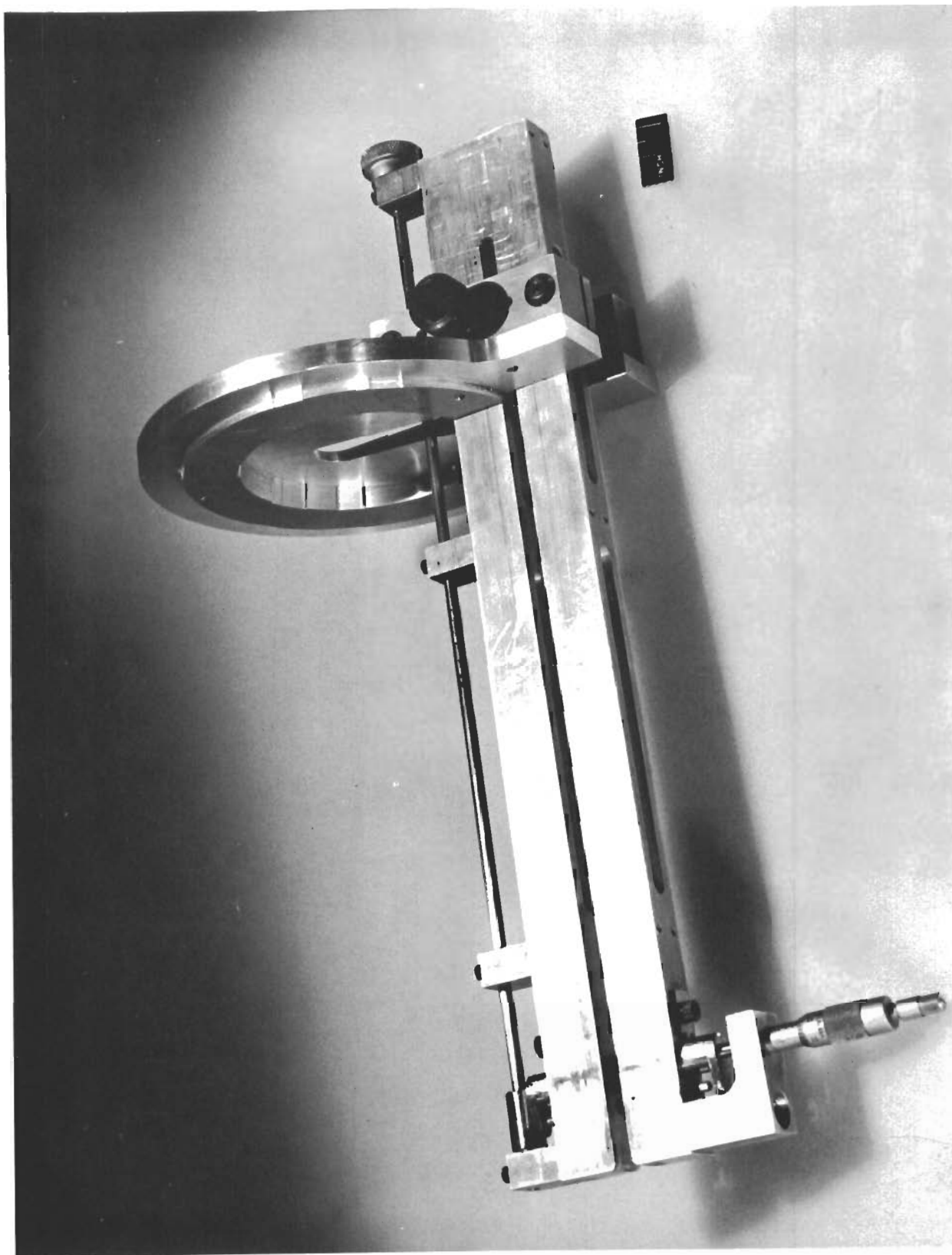


Figure 7. Strain Gage Attachment Fixture

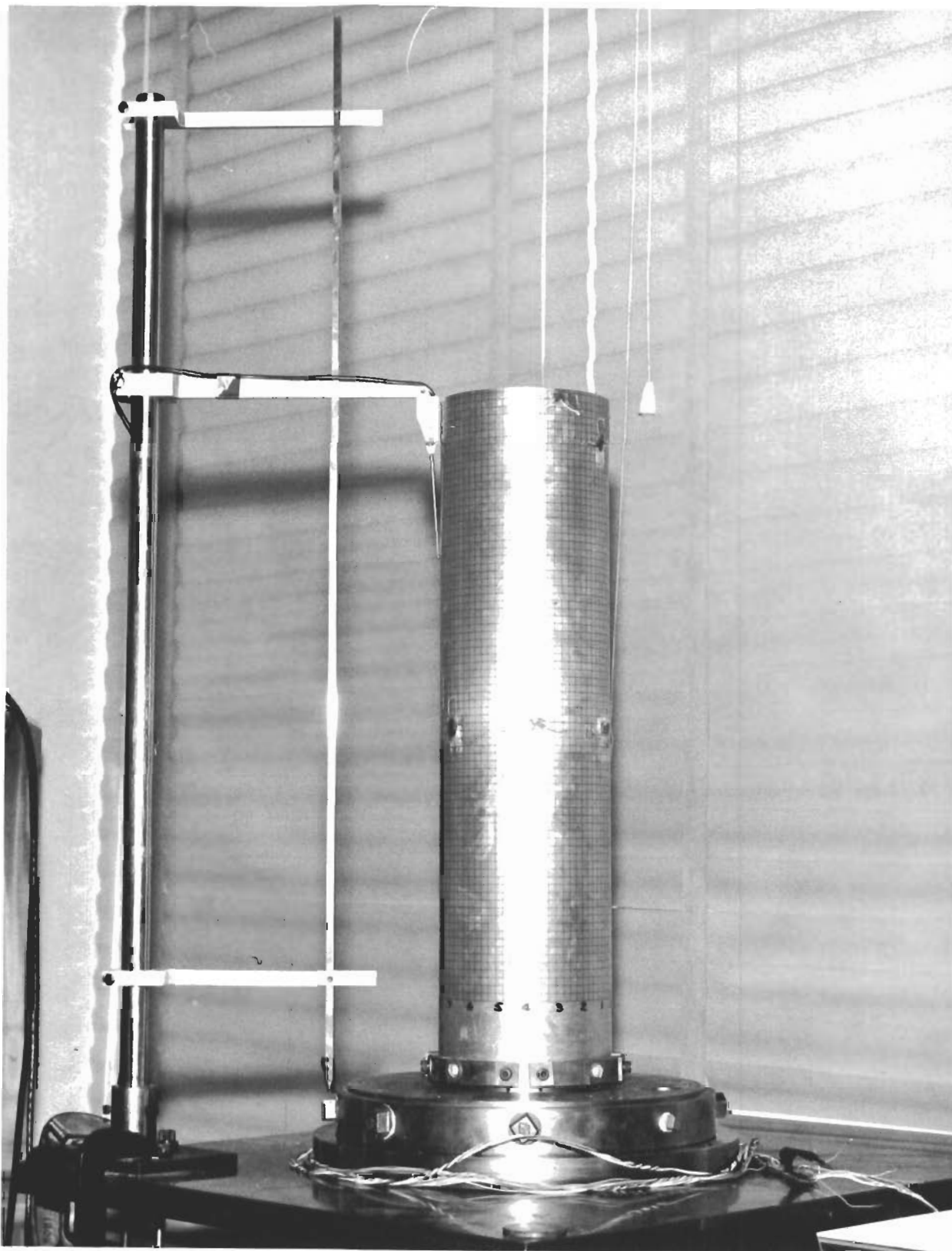


Figure 8. Precision Shell Measurement System

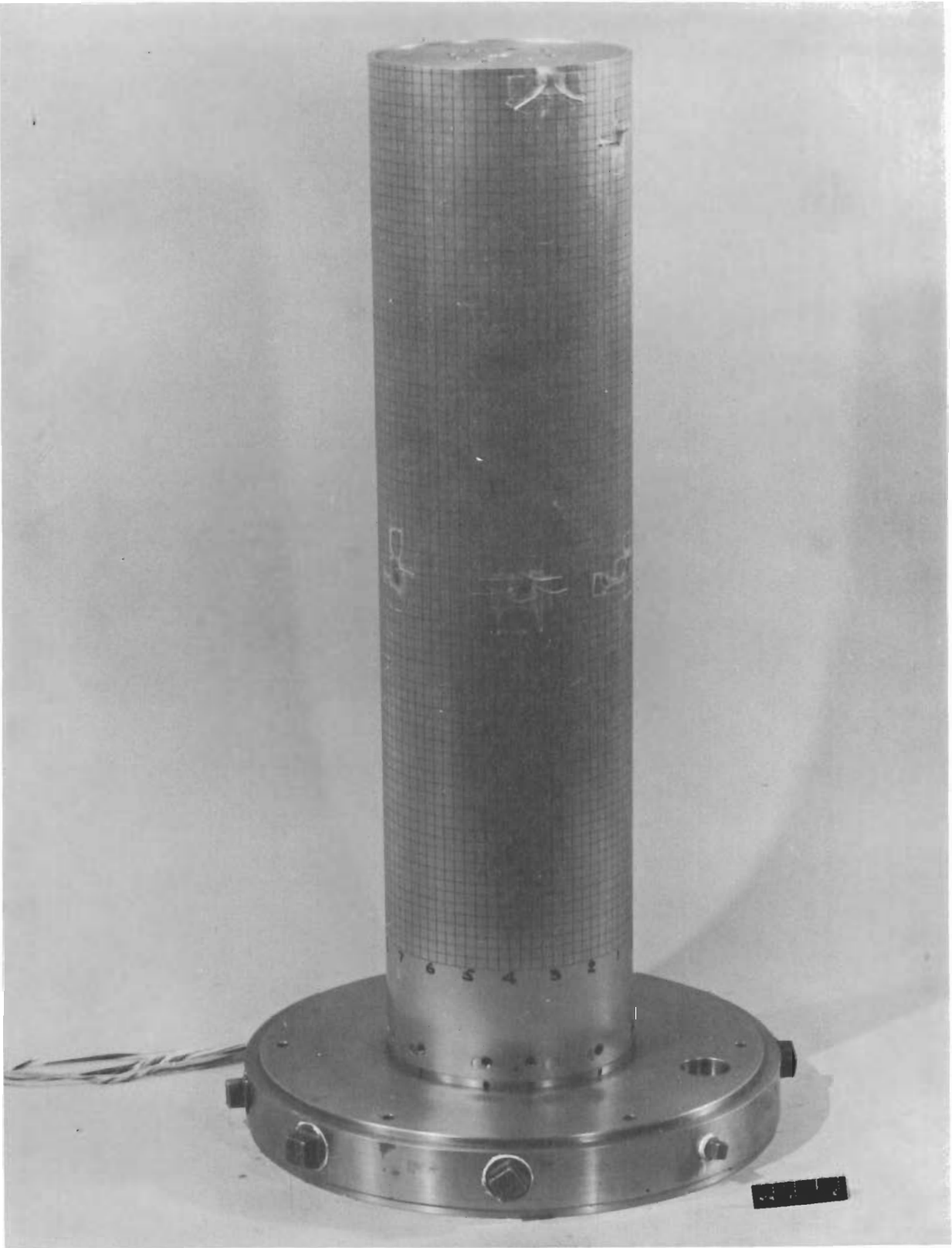


Figure 9. Mounted Instrumented Cylinder

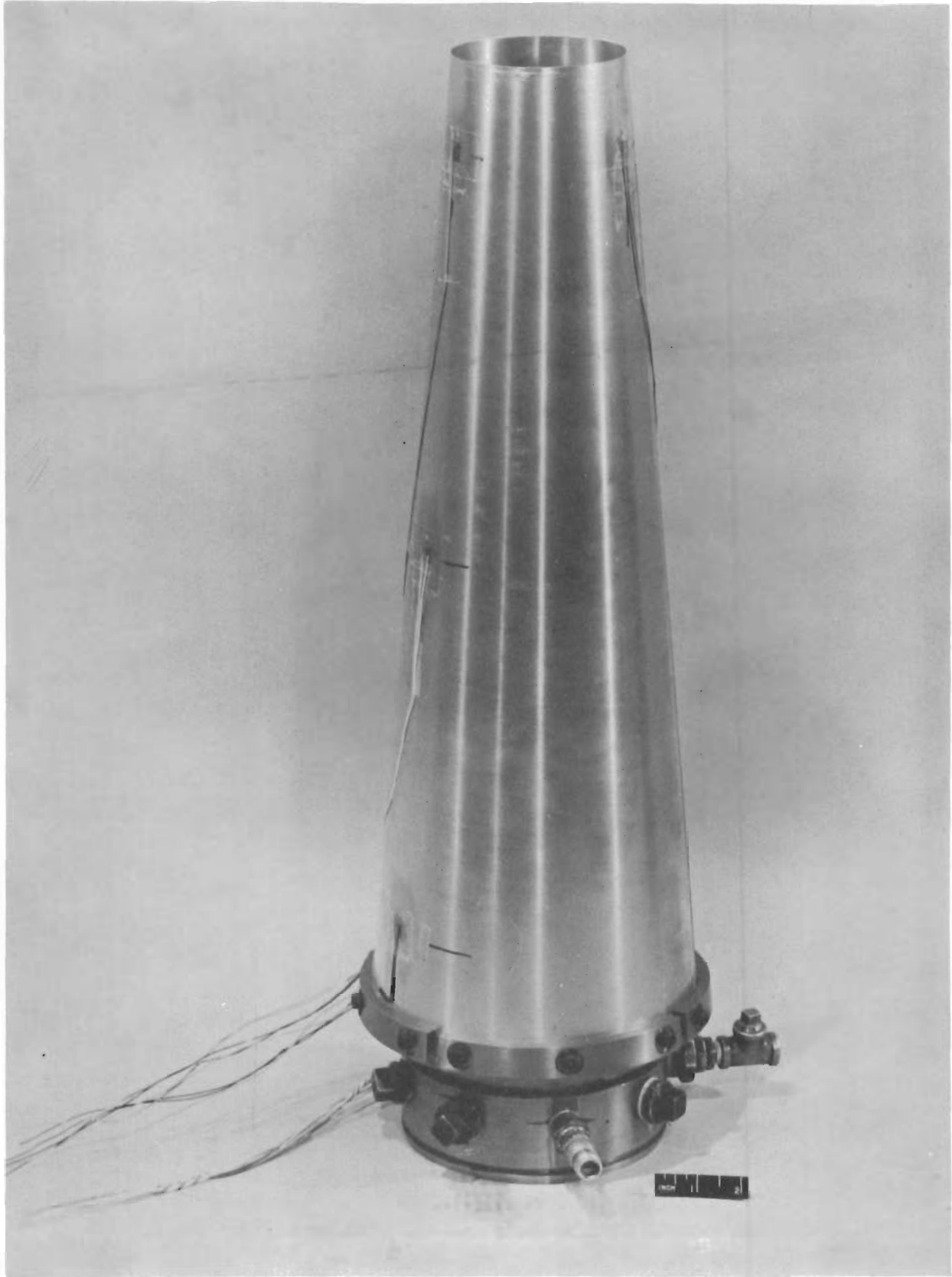
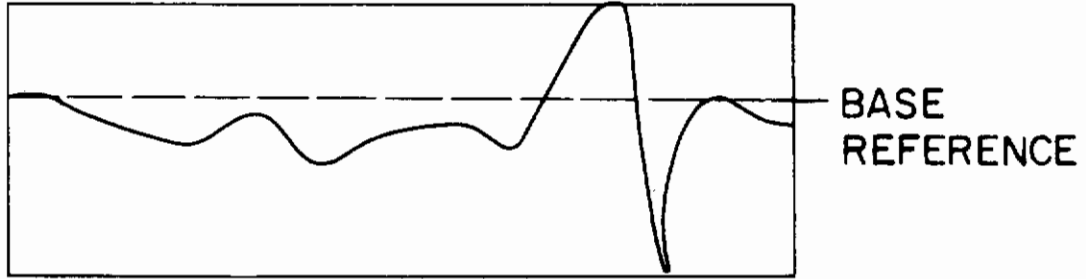
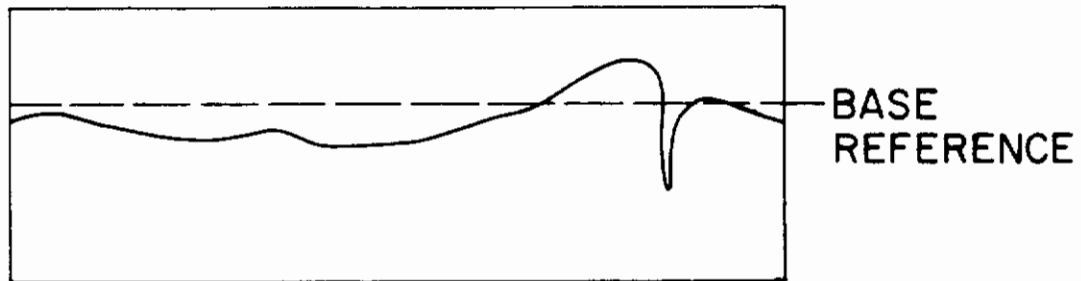


Figure 10. Instrumented Conical Shell



(a) POSITION NO. 9, 0 PSIG



(b) POSITION NO. 9, 17 PSIG

Figure 11. Measured Traverses of Specimen G-8

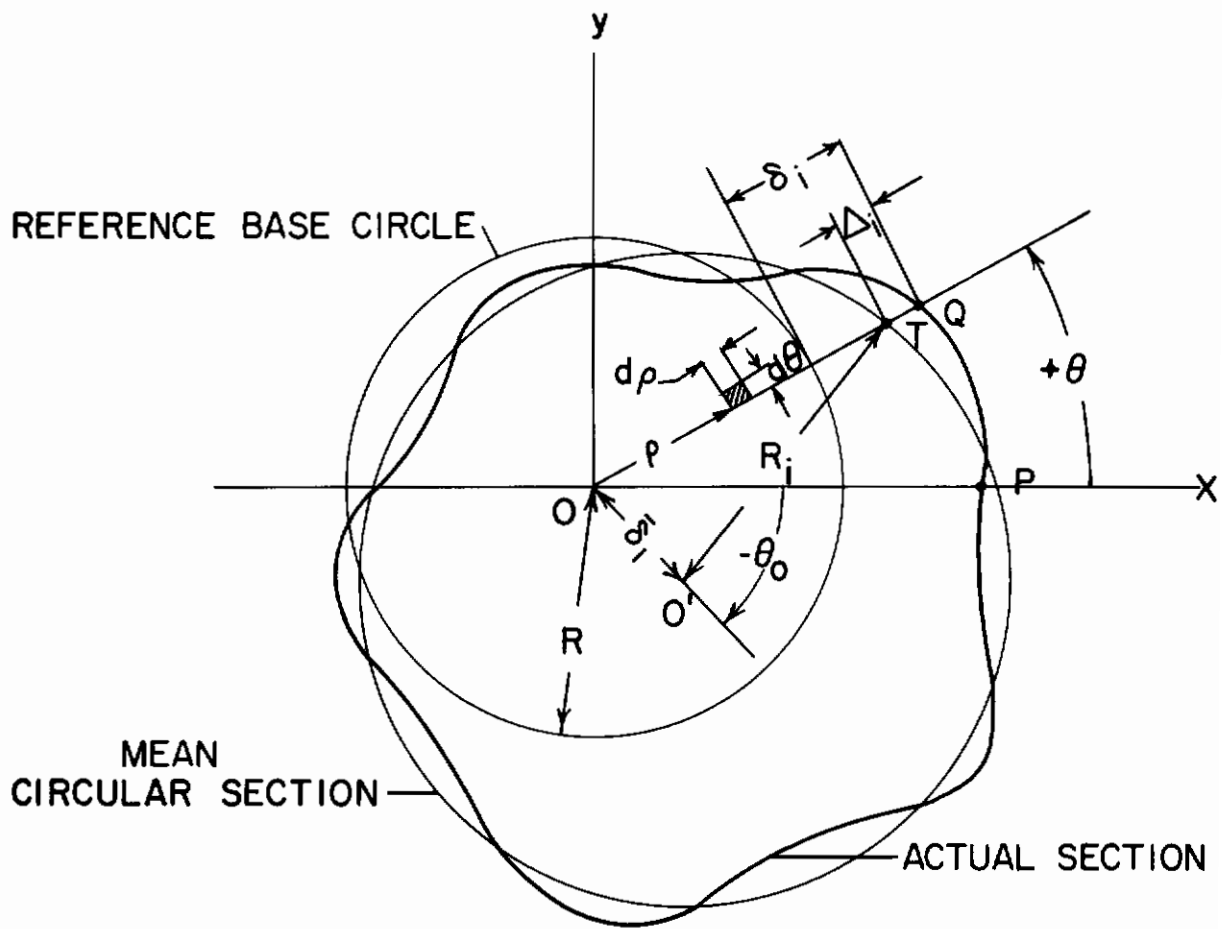


Figure 12. Relationship Between Actual, Mean, and Reference Sections

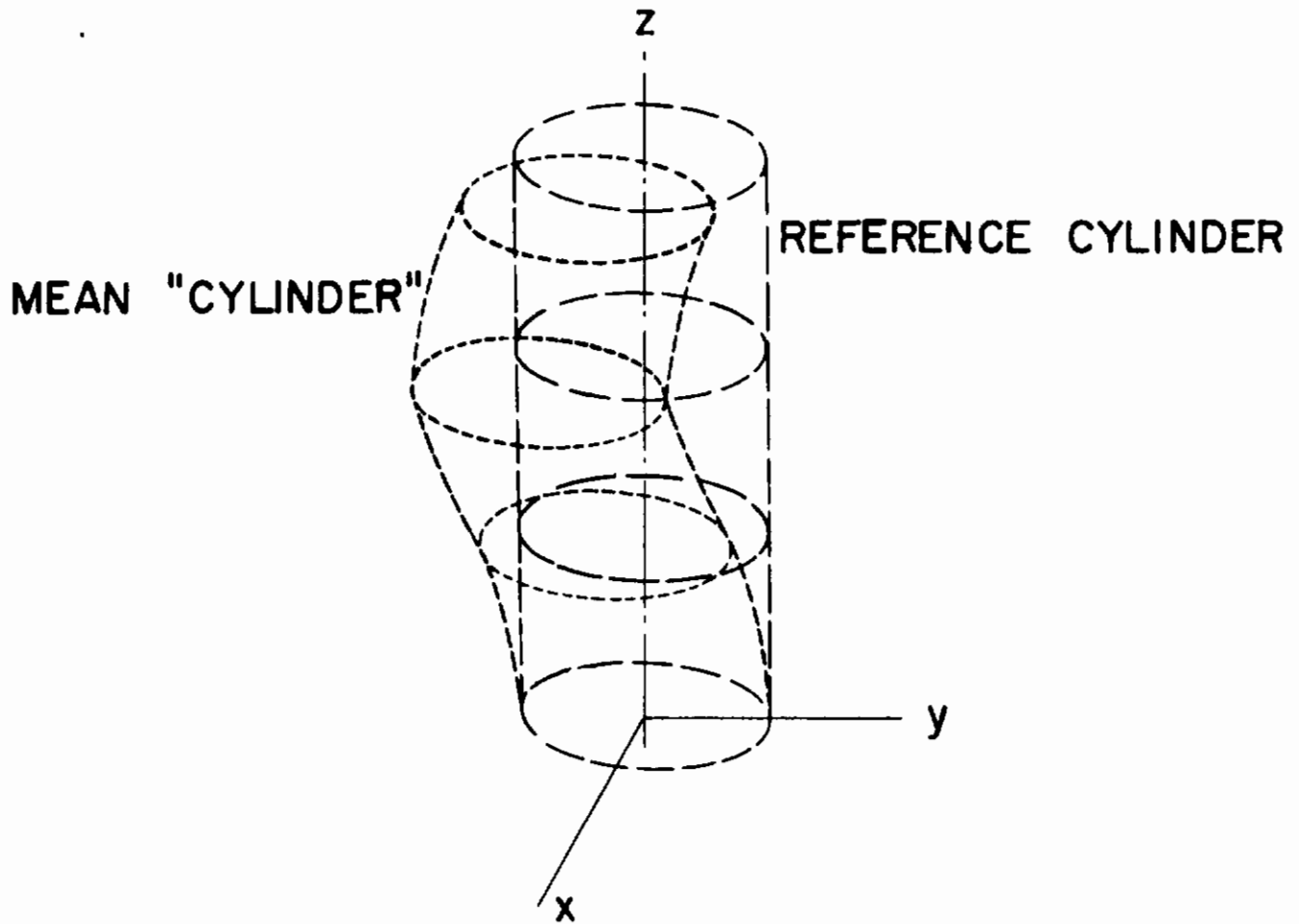


Figure 13. Relationship Between the Mean "Cylinder" and Reference Cylinder

Contrails

AXIAL POSITION

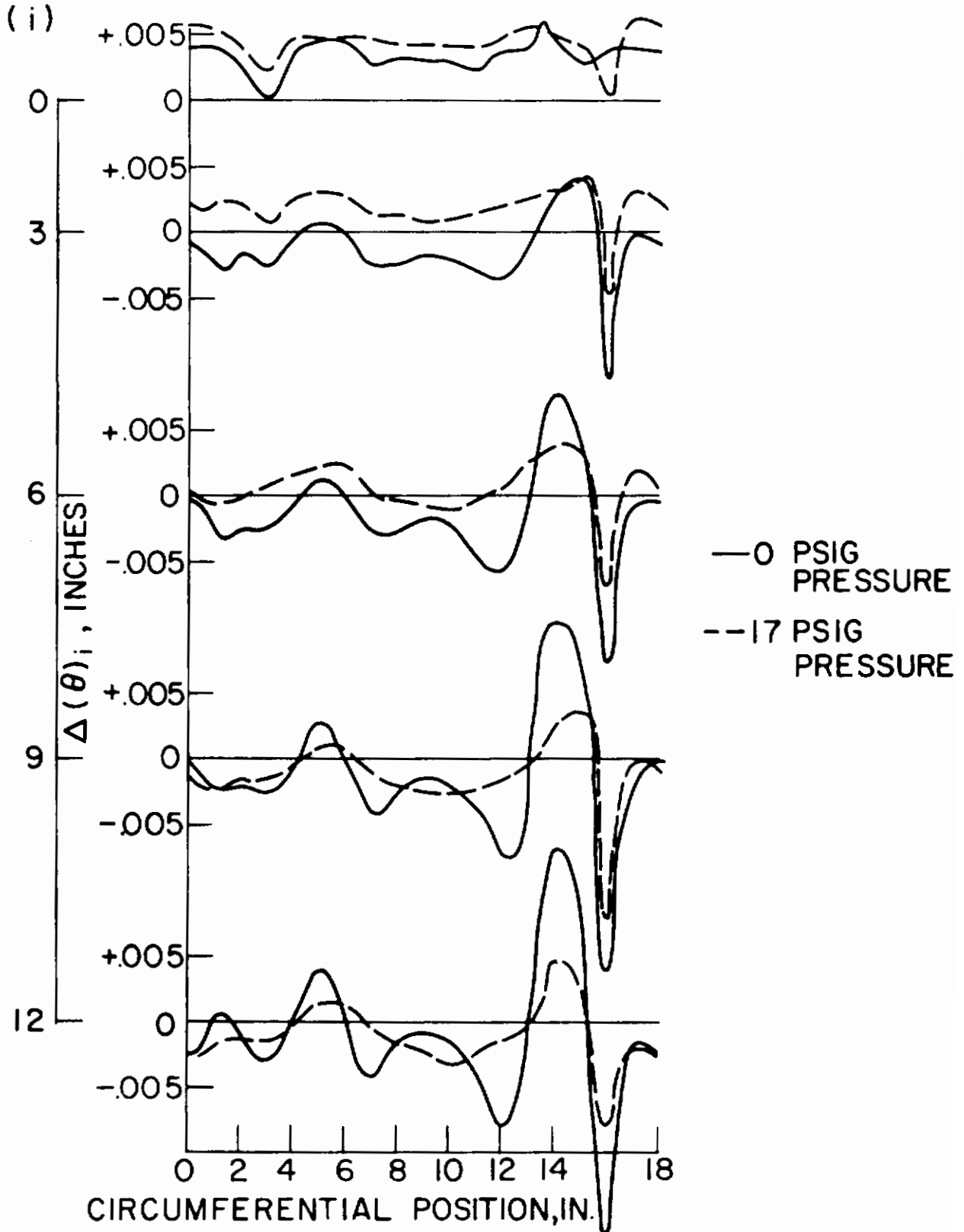


Figure 14. $\Delta(\theta)_i$ Imperfection Components - Specimen G-8

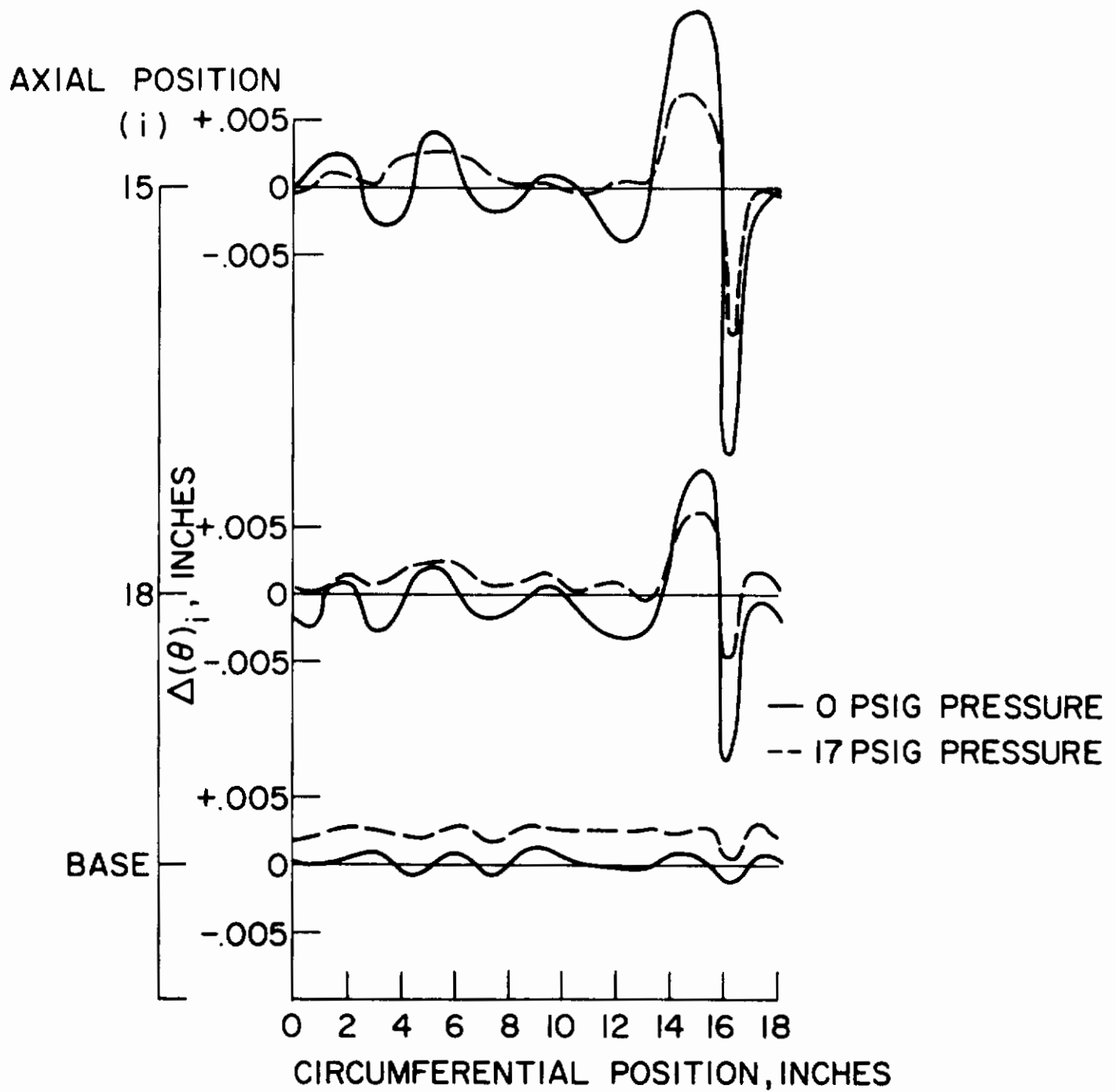


Figure 14. $\Delta(\theta)_i$ Imperfection Components - Specimen G-8 (Cont'd)

CIRCUMFERENTIAL POSITION
($R\theta$), IN.

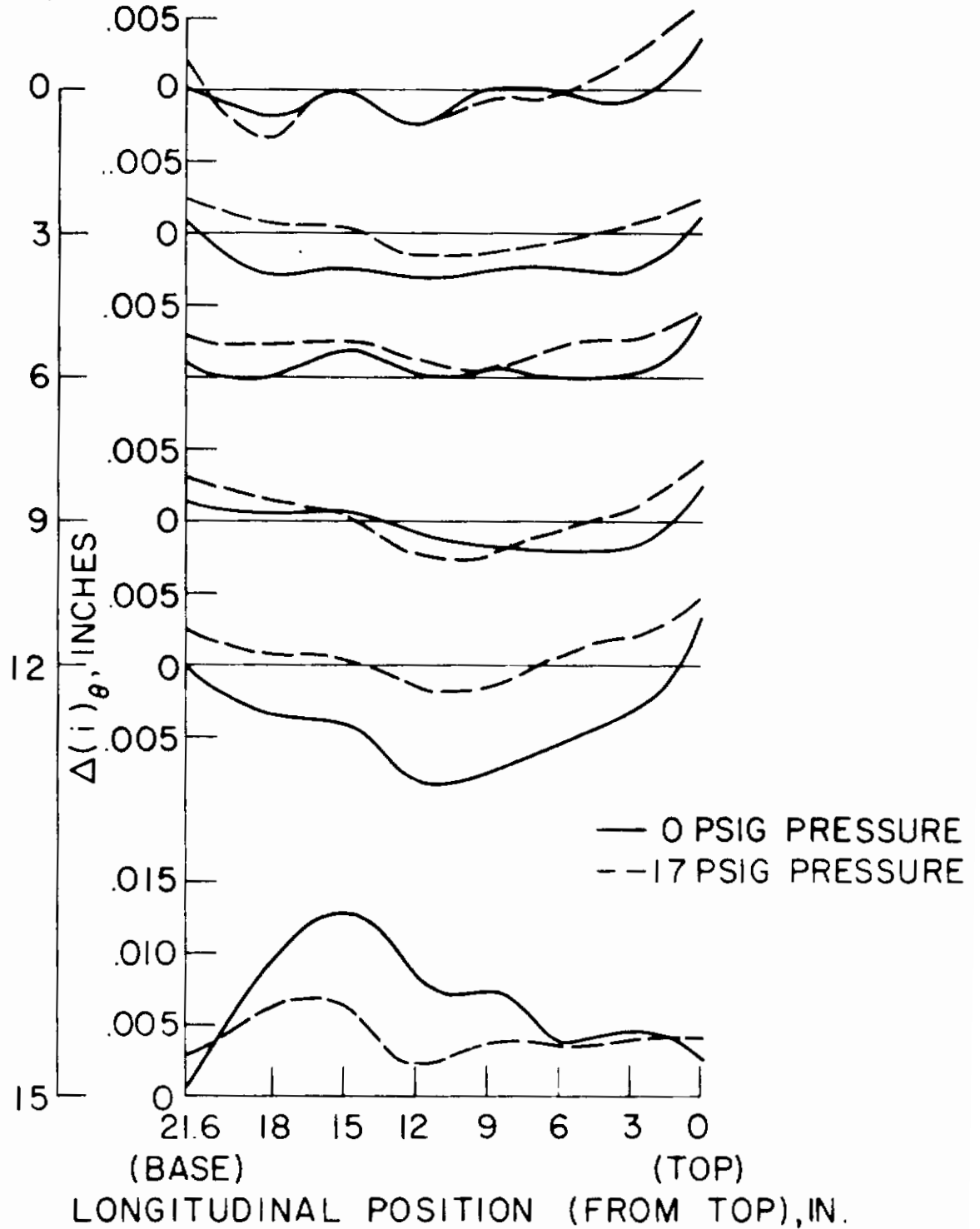


Figure 15. $\Delta(i)_\theta$ Imperfection Components - Specimen G-8

Contrails

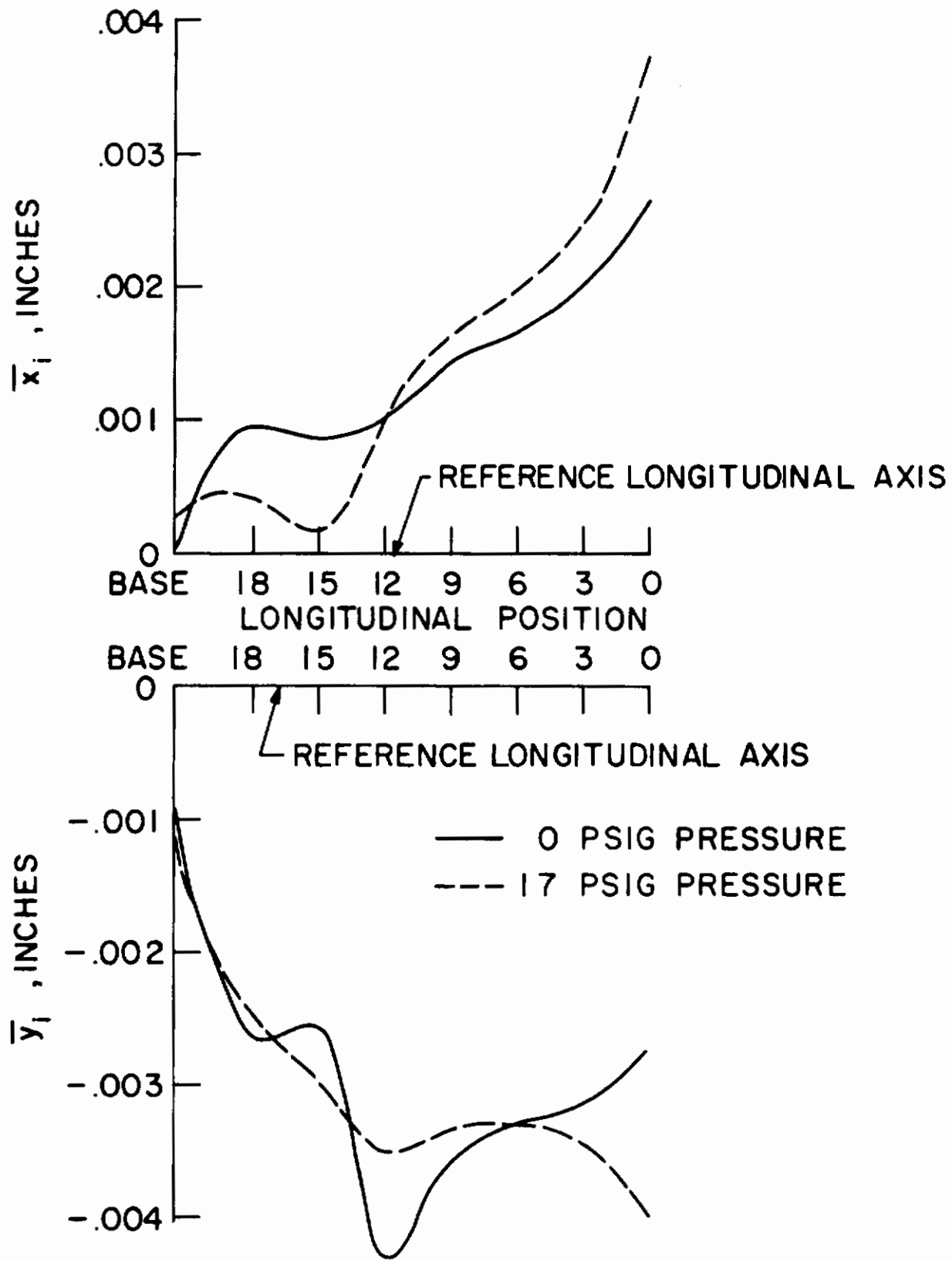


Figure 16. Components of the Centroidal Axis of the Mean Cylinder - Specimen G-8

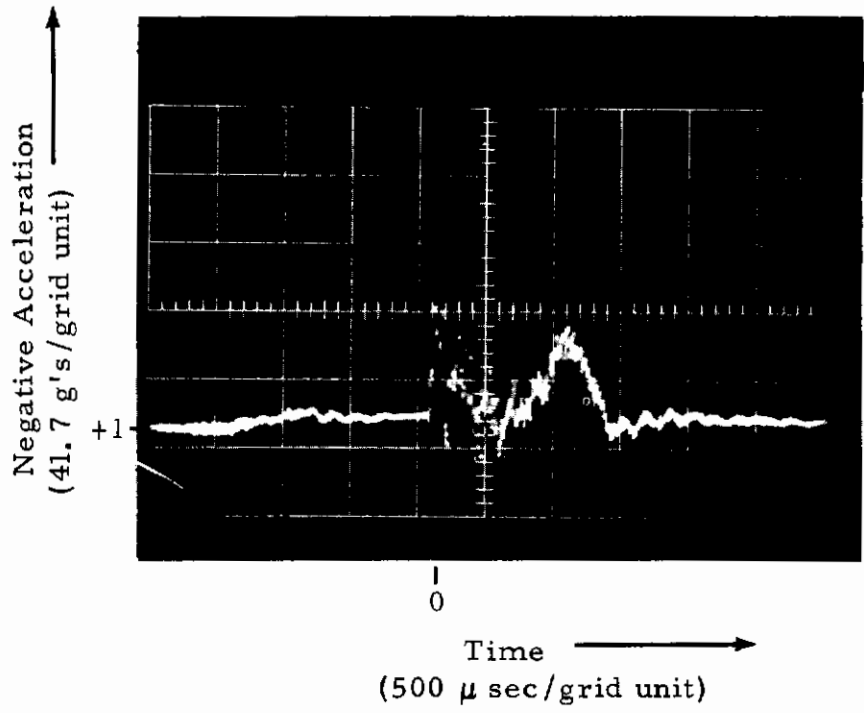
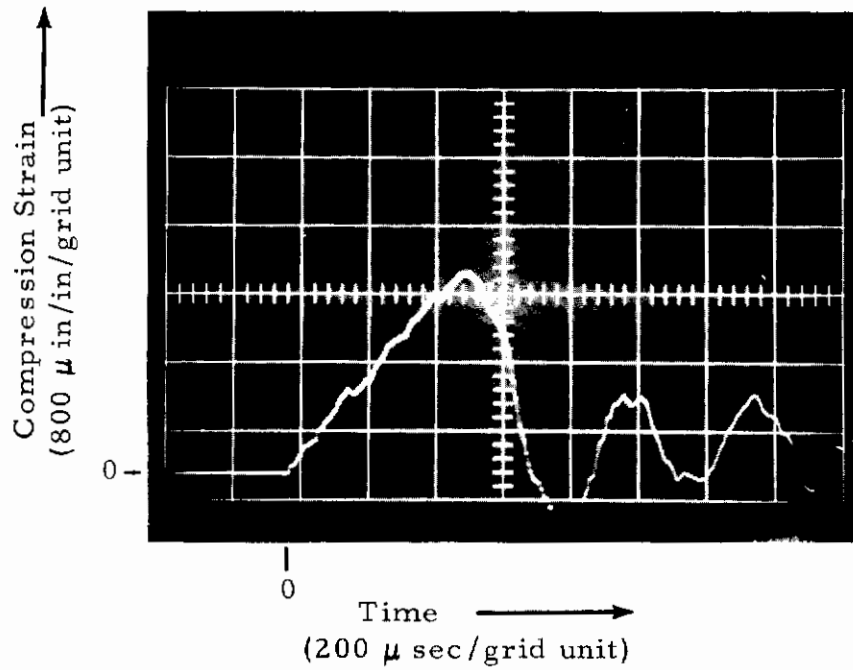
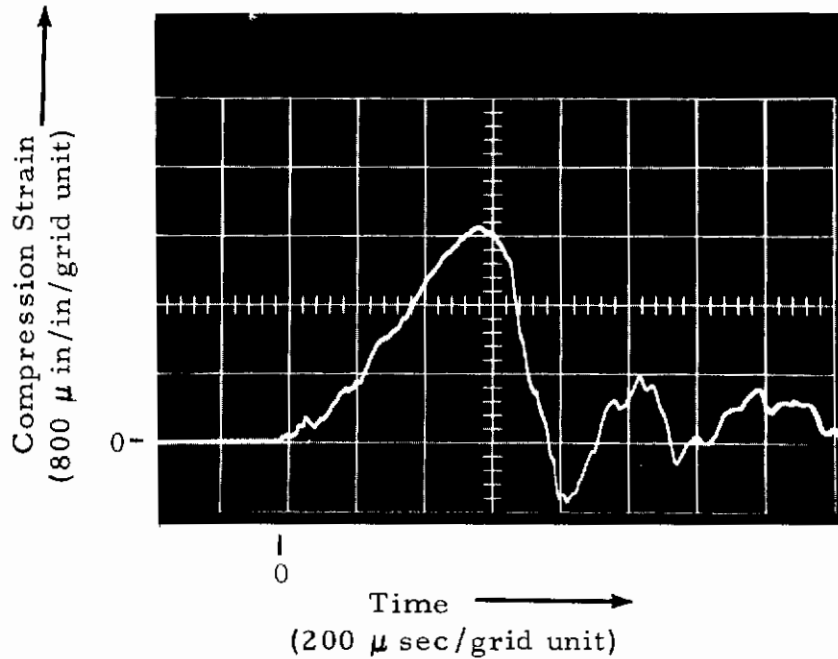


Figure 17. Accelerometer Record - Test No. G-1

Contrails

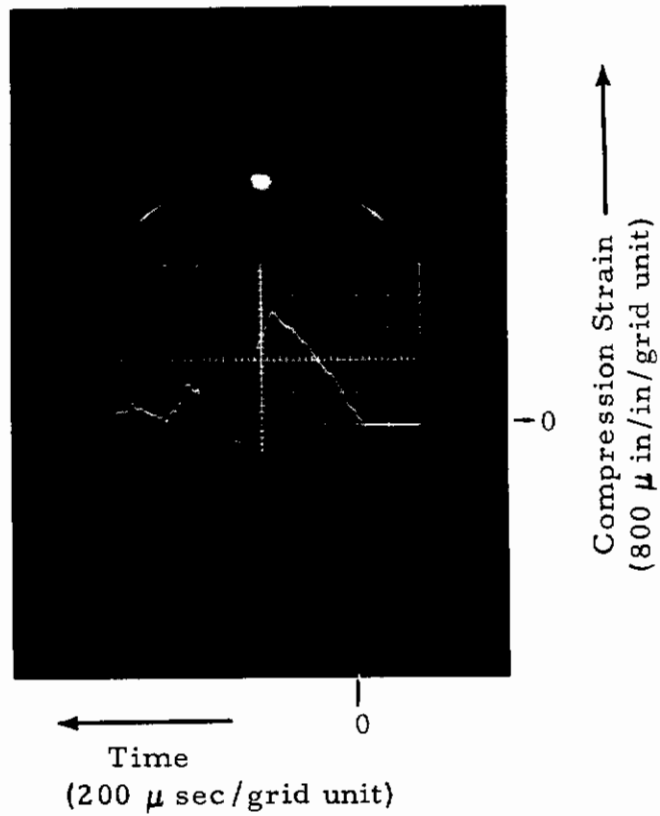


(a)



(b)

Figure 18. Data Records - Test No. G-2



(c)

Figure 18. Data Records - Test No. G-2 (Cont'd)

Contrails

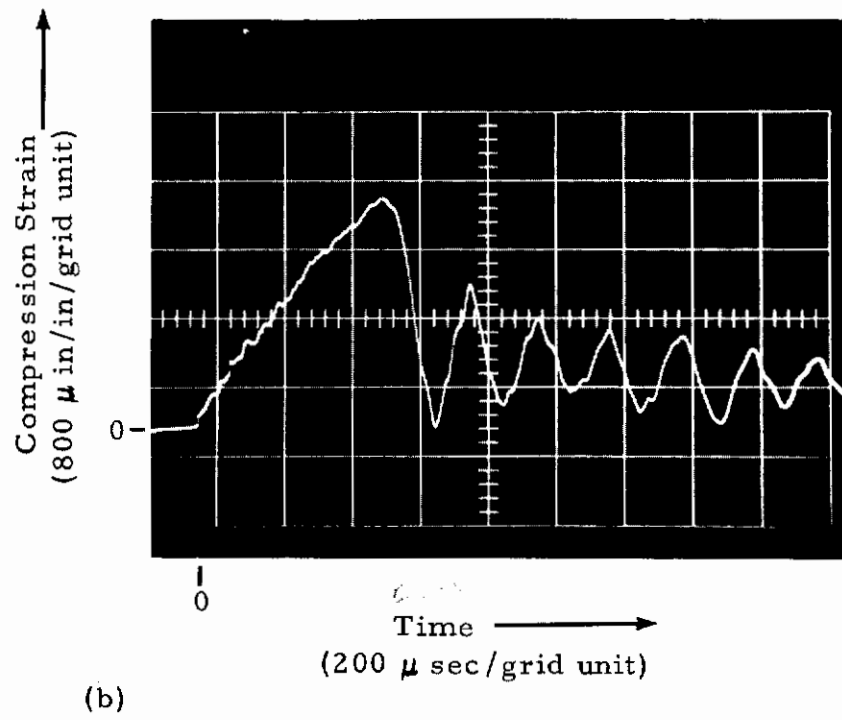
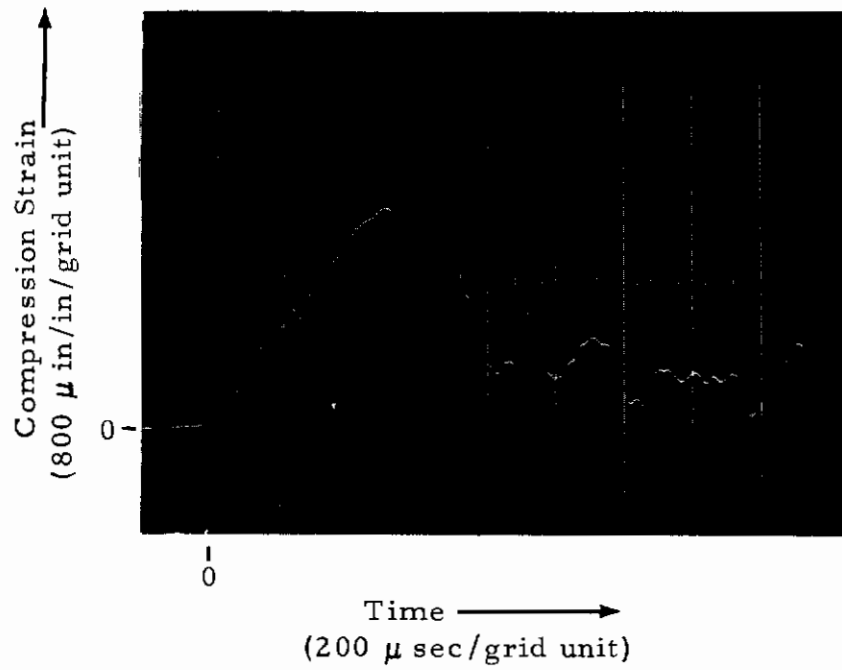


Figure 19. Data Records - Test No. G-3

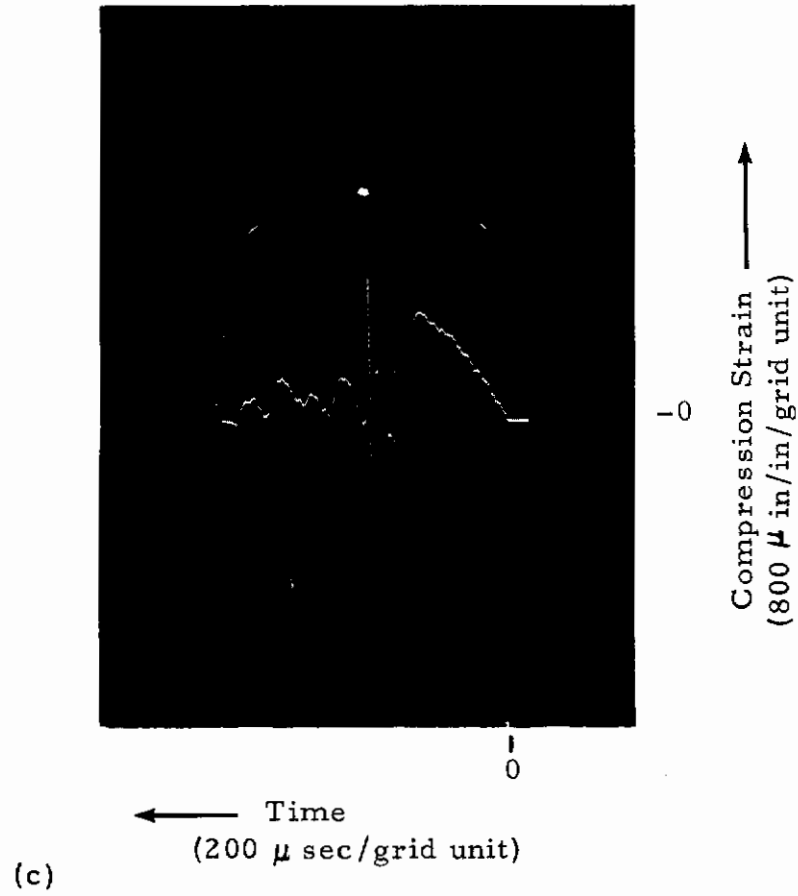


Figure 19. Data Records - Test No. G-3 (Cont'd)

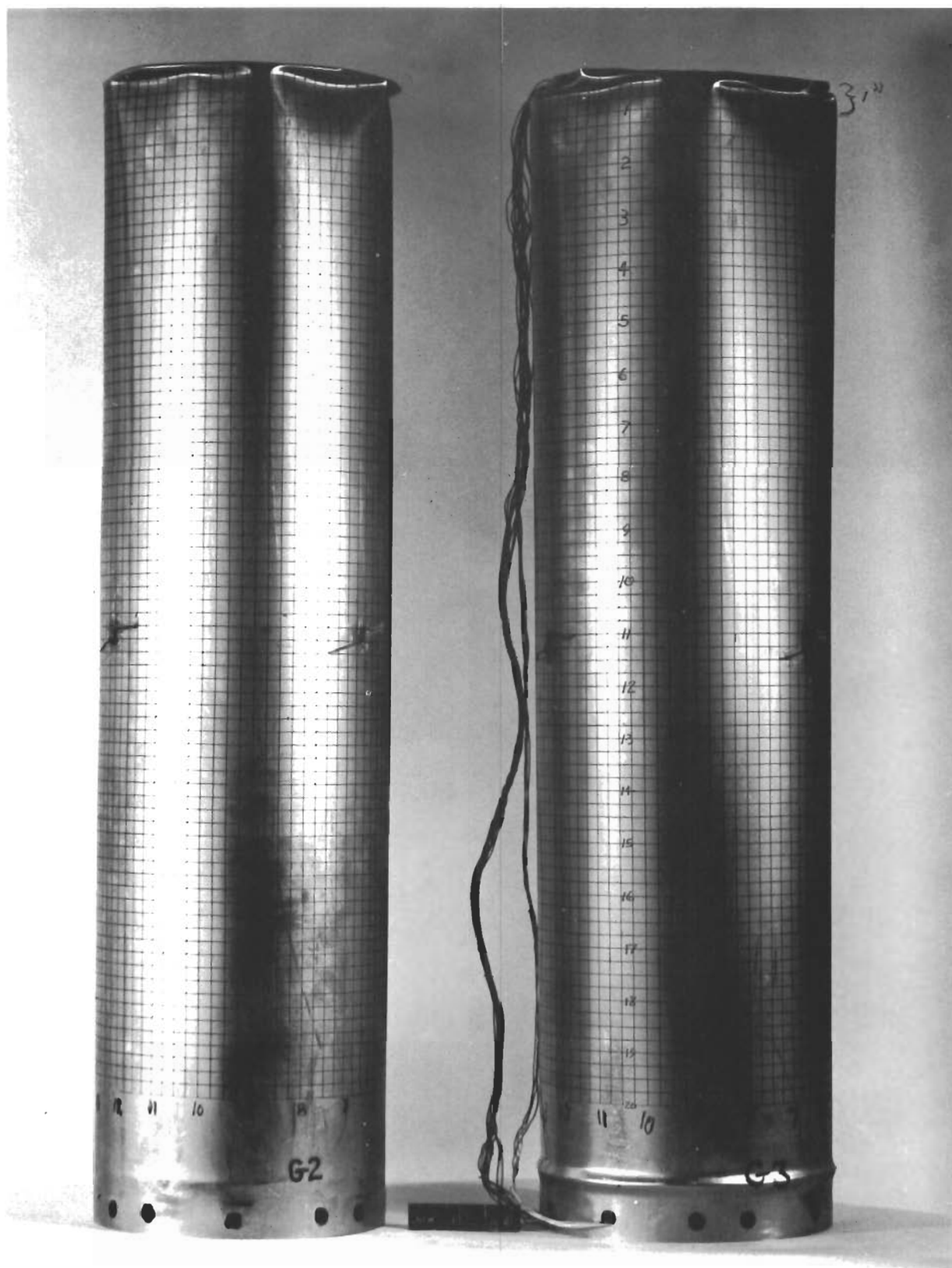
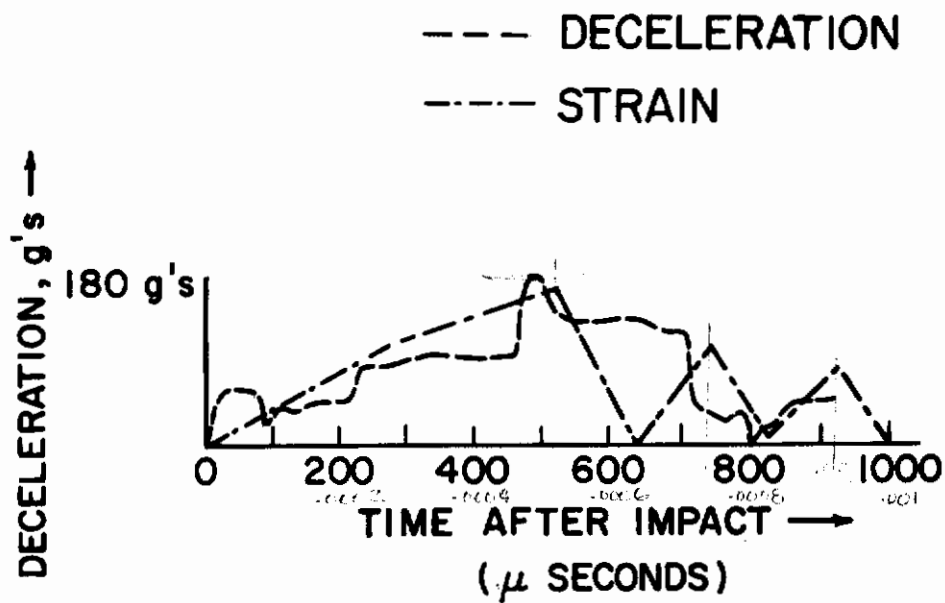


Figure 20. Specimens G-2 and G-3



G-3 Test

Figure 21. Comparison of Data from Accelerometer and Strain Gages

Contrails

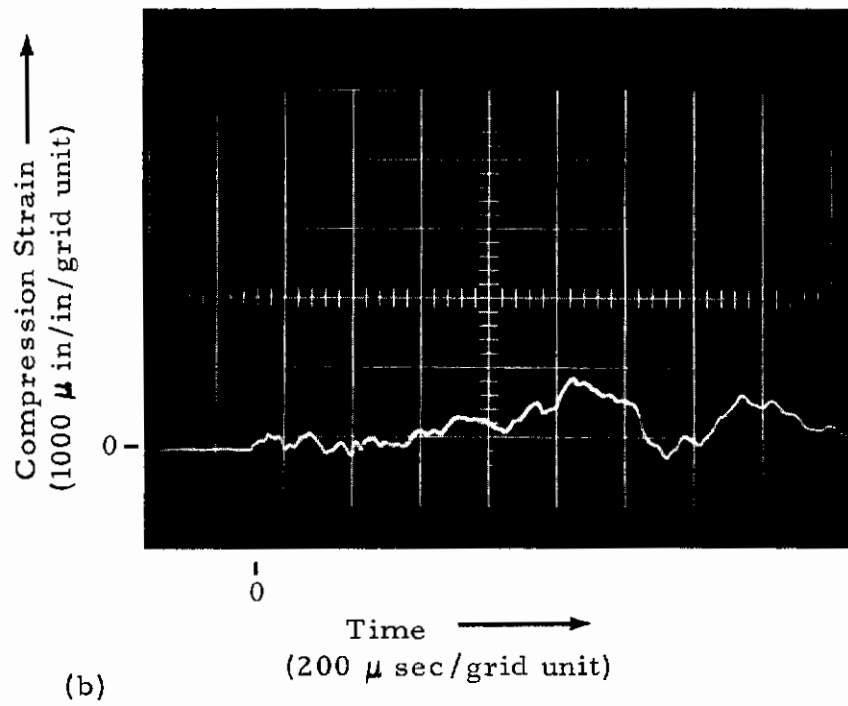
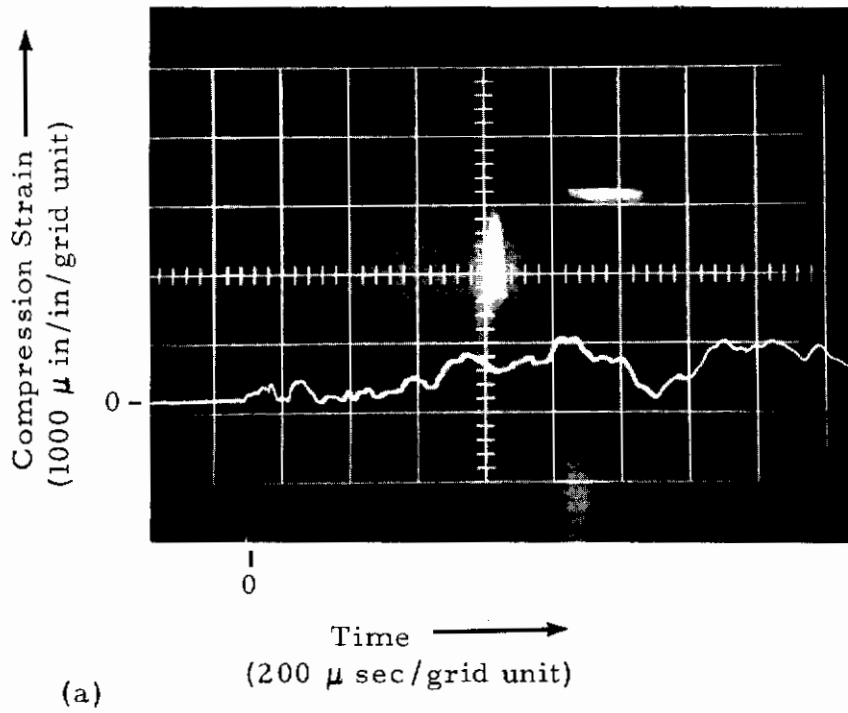


Figure 22. Data Records - Test No. G-4

Contrails

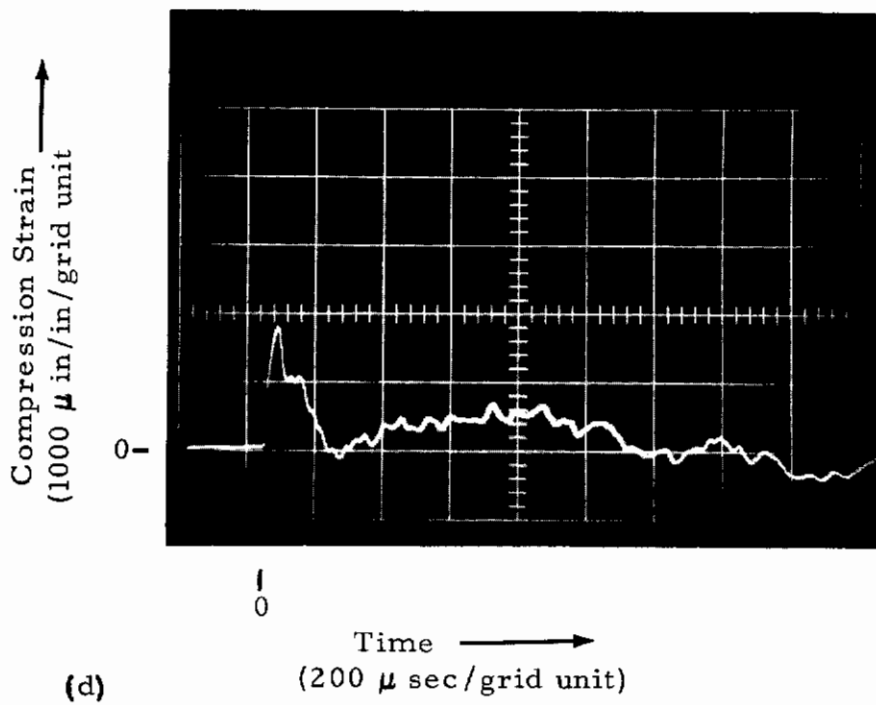
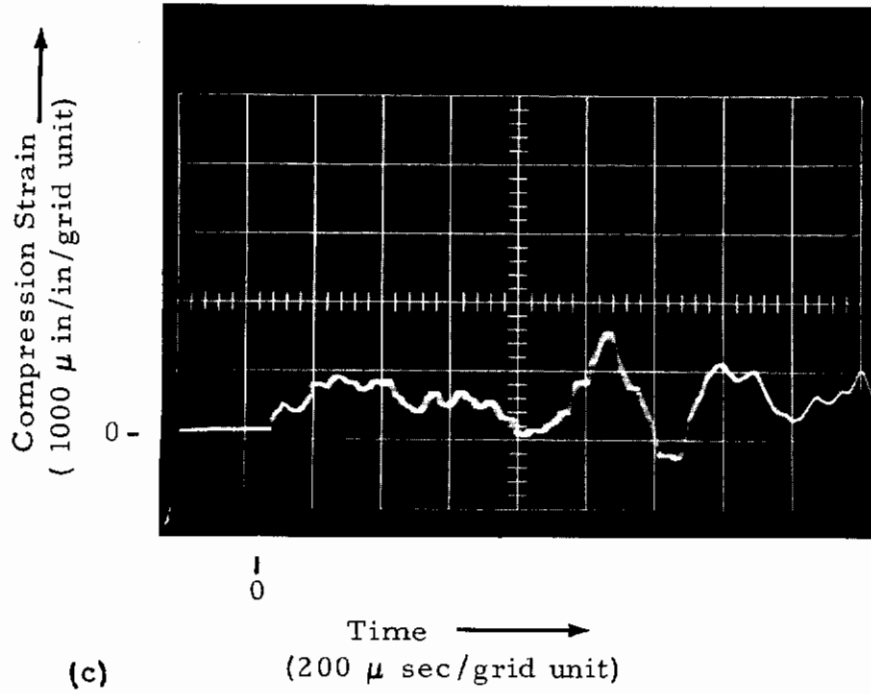


Figure 22. Data Records - Test No. G-4 (Cont'd)

Contrails

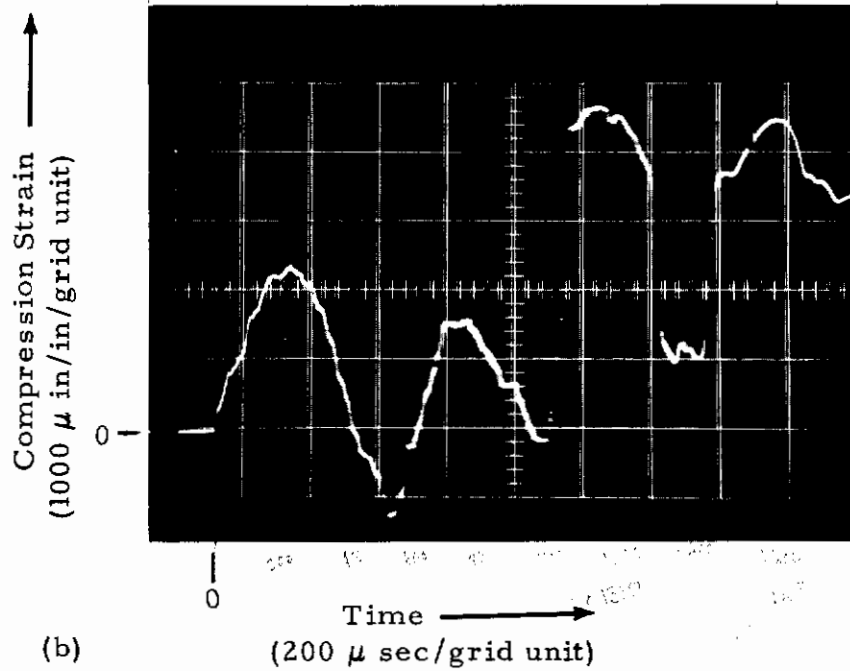
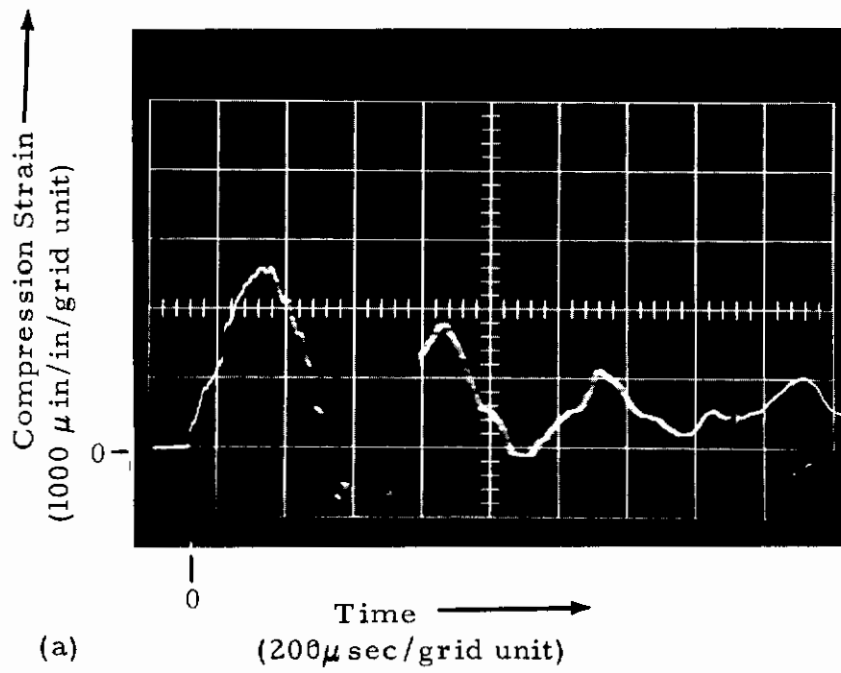


Figure 23. Data Records - Test No. G-6

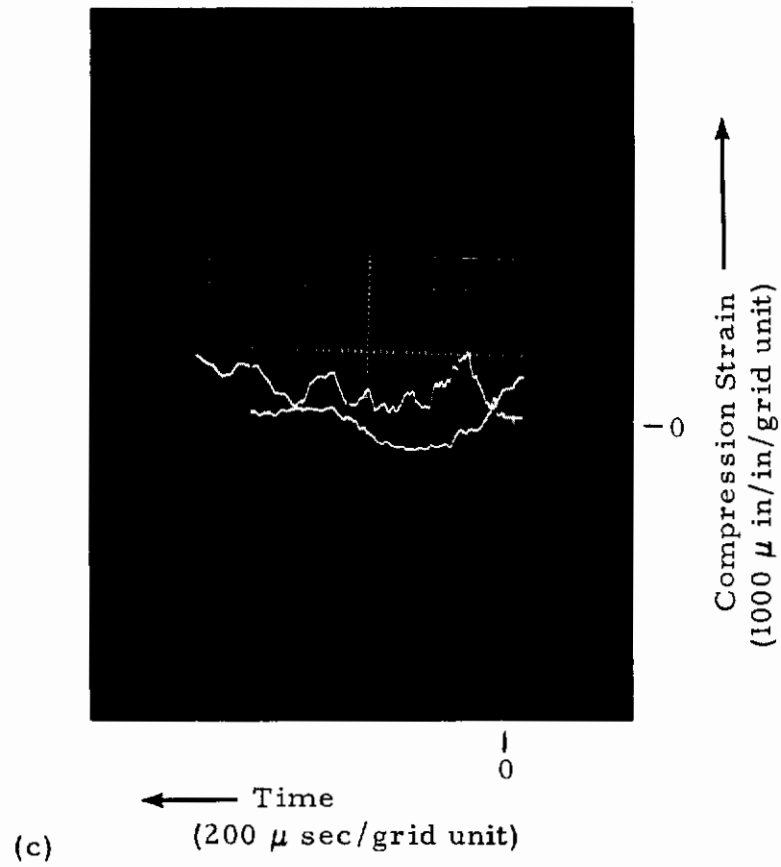
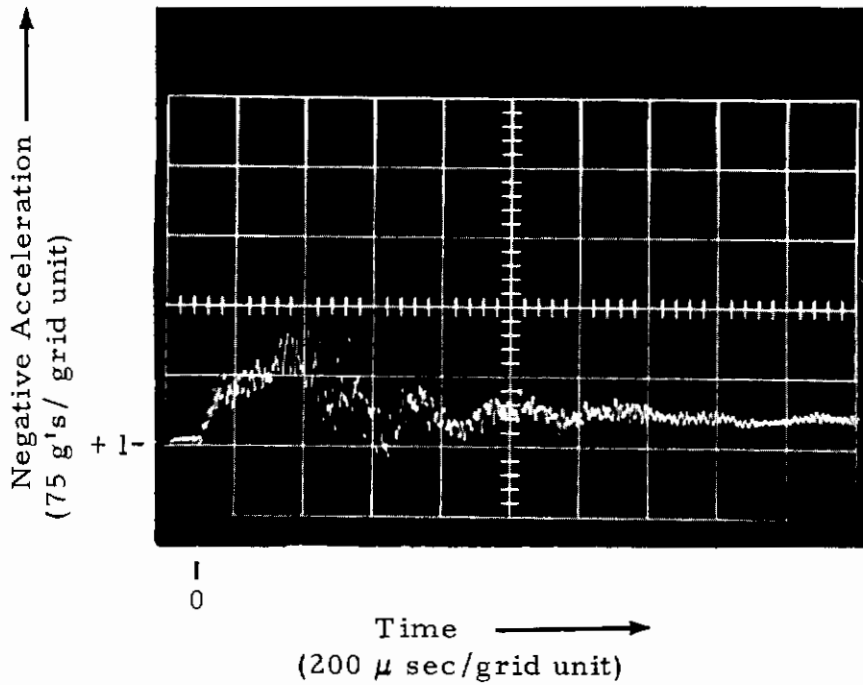


Figure 23. Data Record - Test No. G-6 (Cont'd)



(d)

Figure 23. Data Records - Test No. G-6 (Cont'd)

Contrails

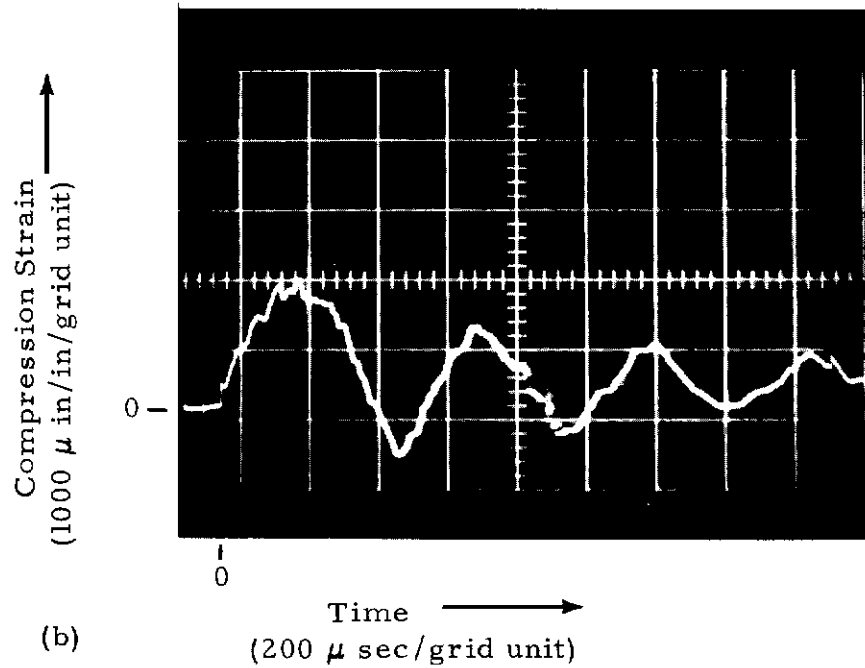
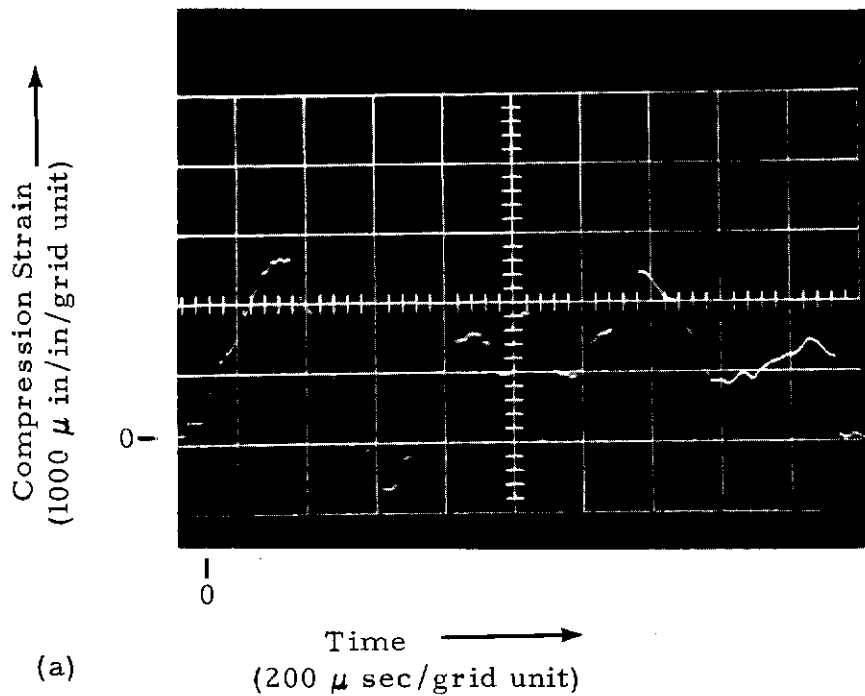


Figure 24. Data Records - Test No. G-7

Contrails

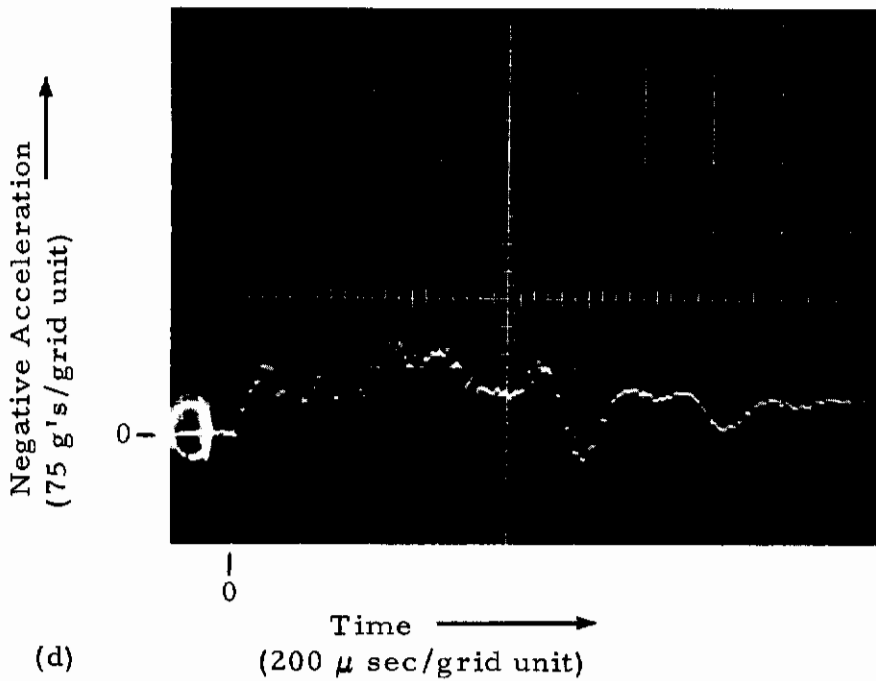
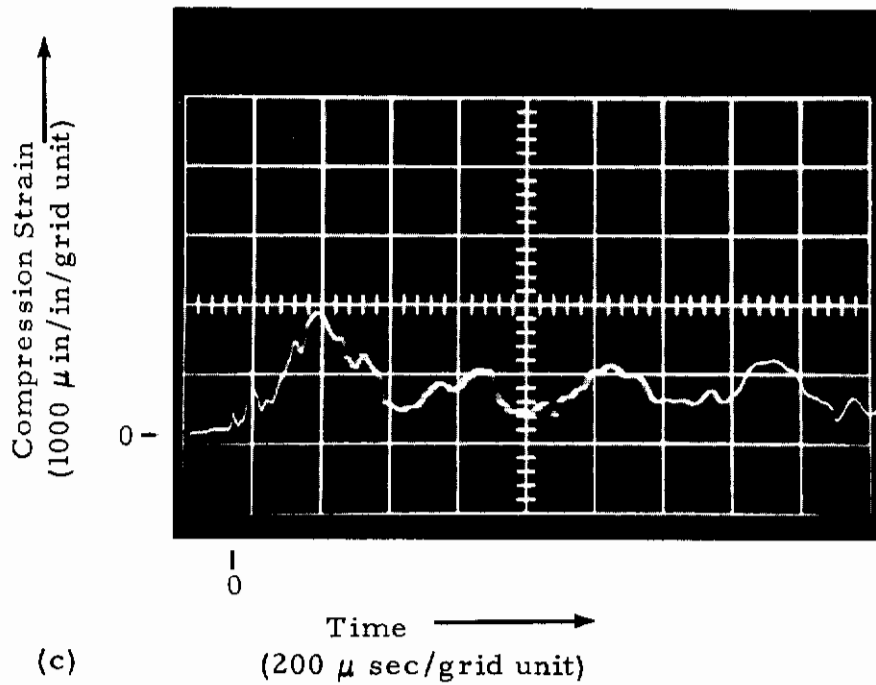


Figure 24. Data Records - Test No. G-7 (Cont'd)

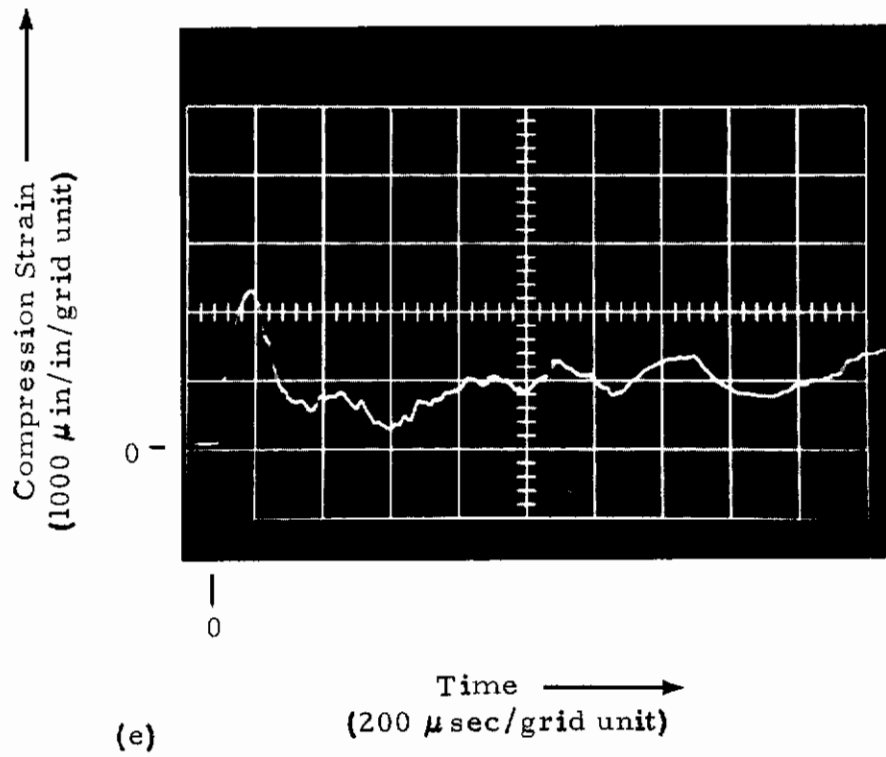


Figure 24. Data Records - Test No. G-7 (Cont'd)

Contrails

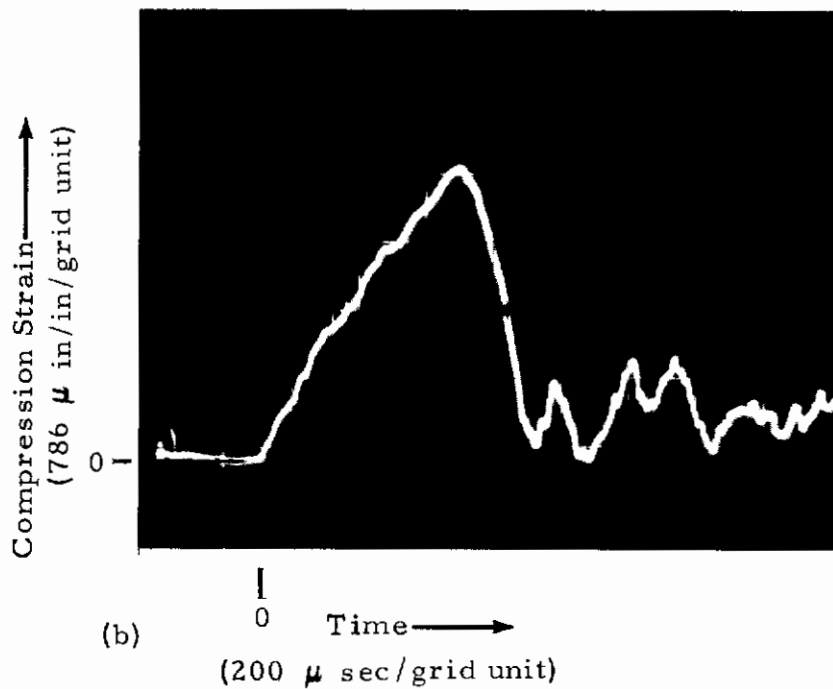
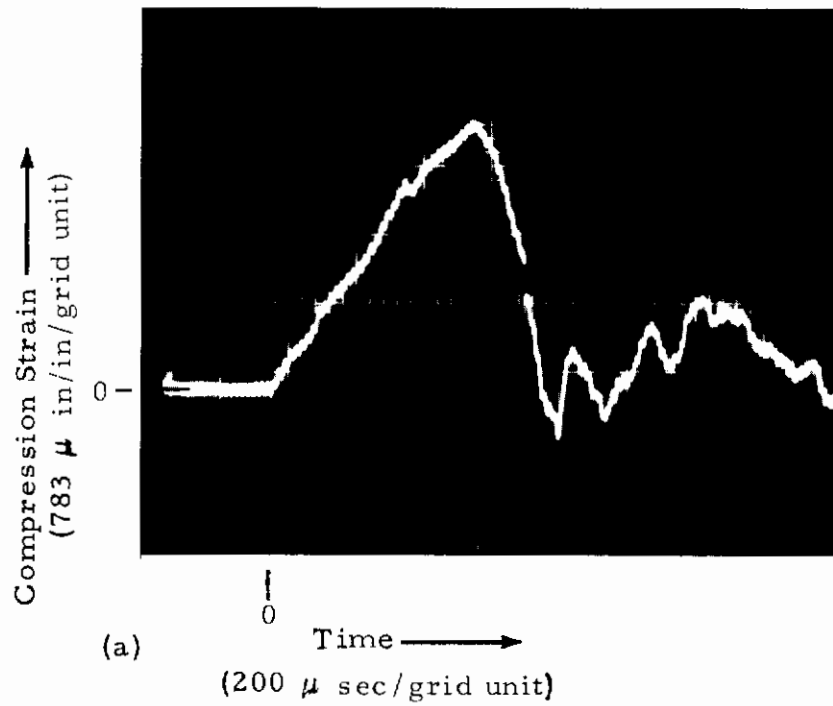


Figure 25. Data Records - Test No. G-8

Contrails

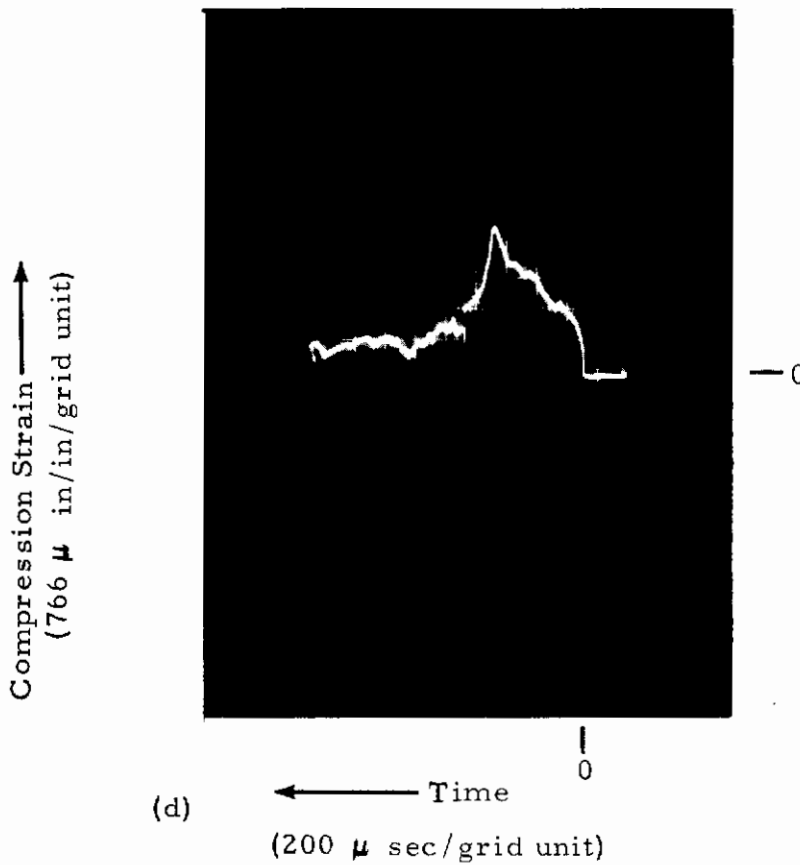
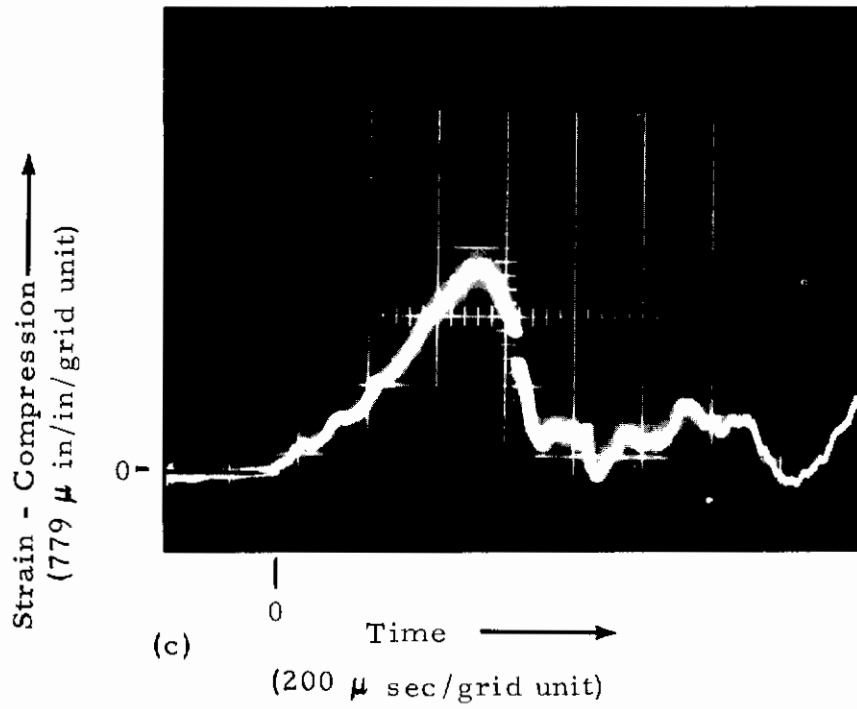
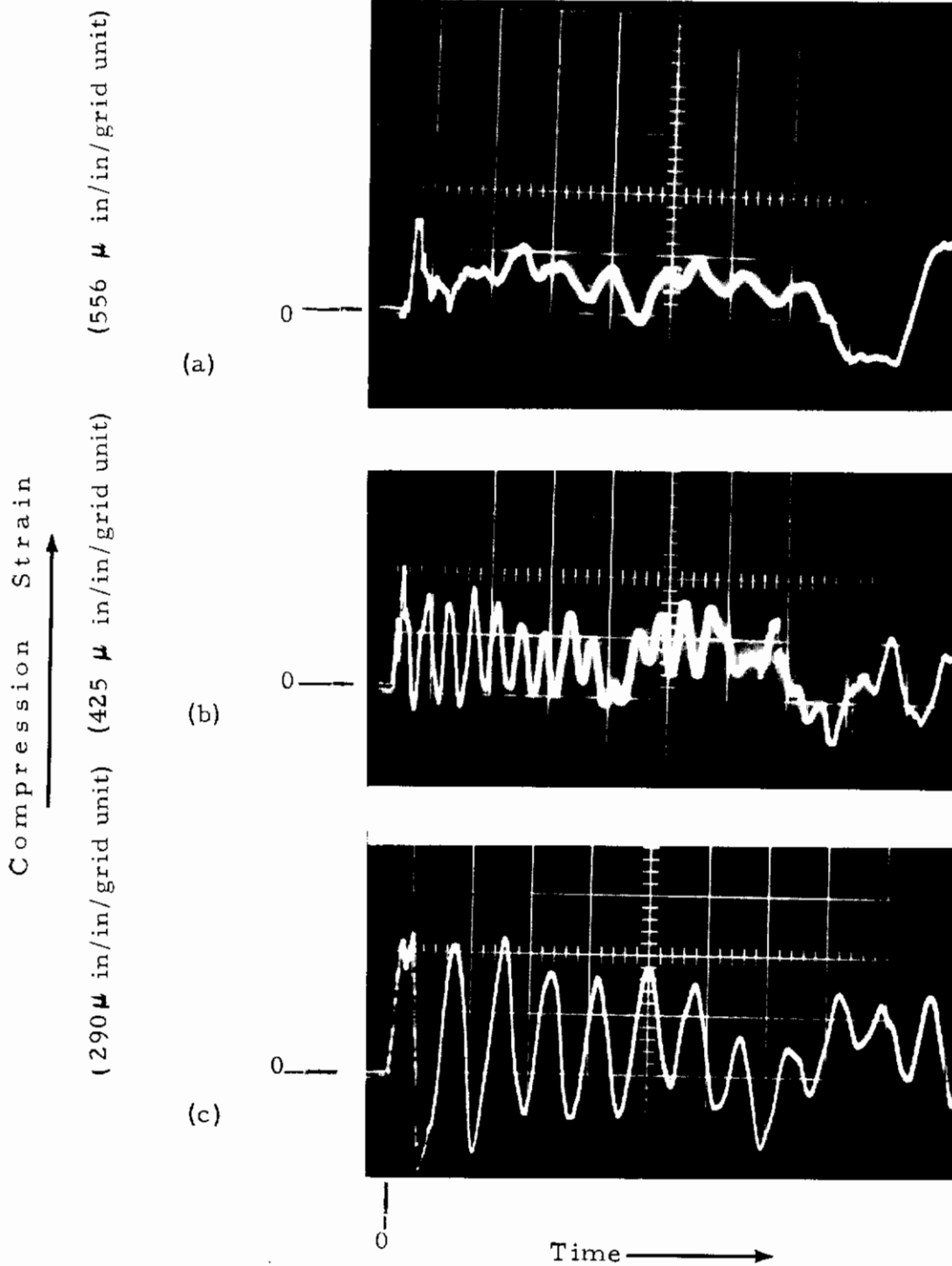


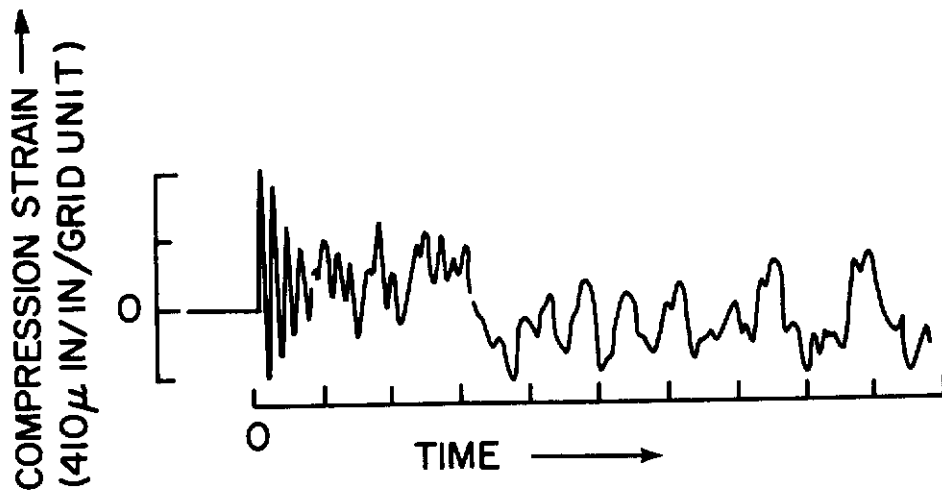
Figure 25. Data Records - Test No. G-8 (Cont'd,)

Contrails

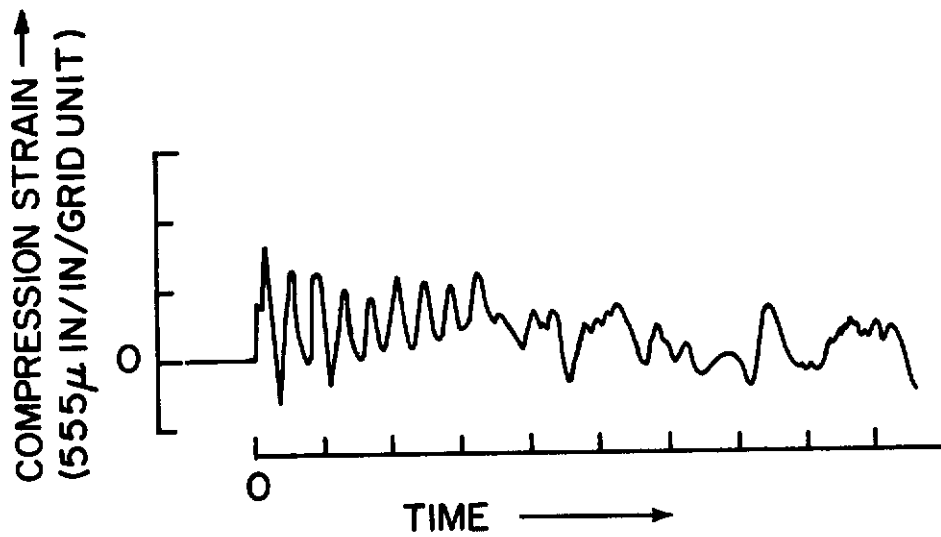


- (a) Forward position, 500 μ sec/grid unit
 - (b) Middle position, .001 sec/grid unit
 - (c) Rear position, 500 μ sec/grid unit
- (All axially aligned)

Figure 26. Strain Data Records Test No. C-3



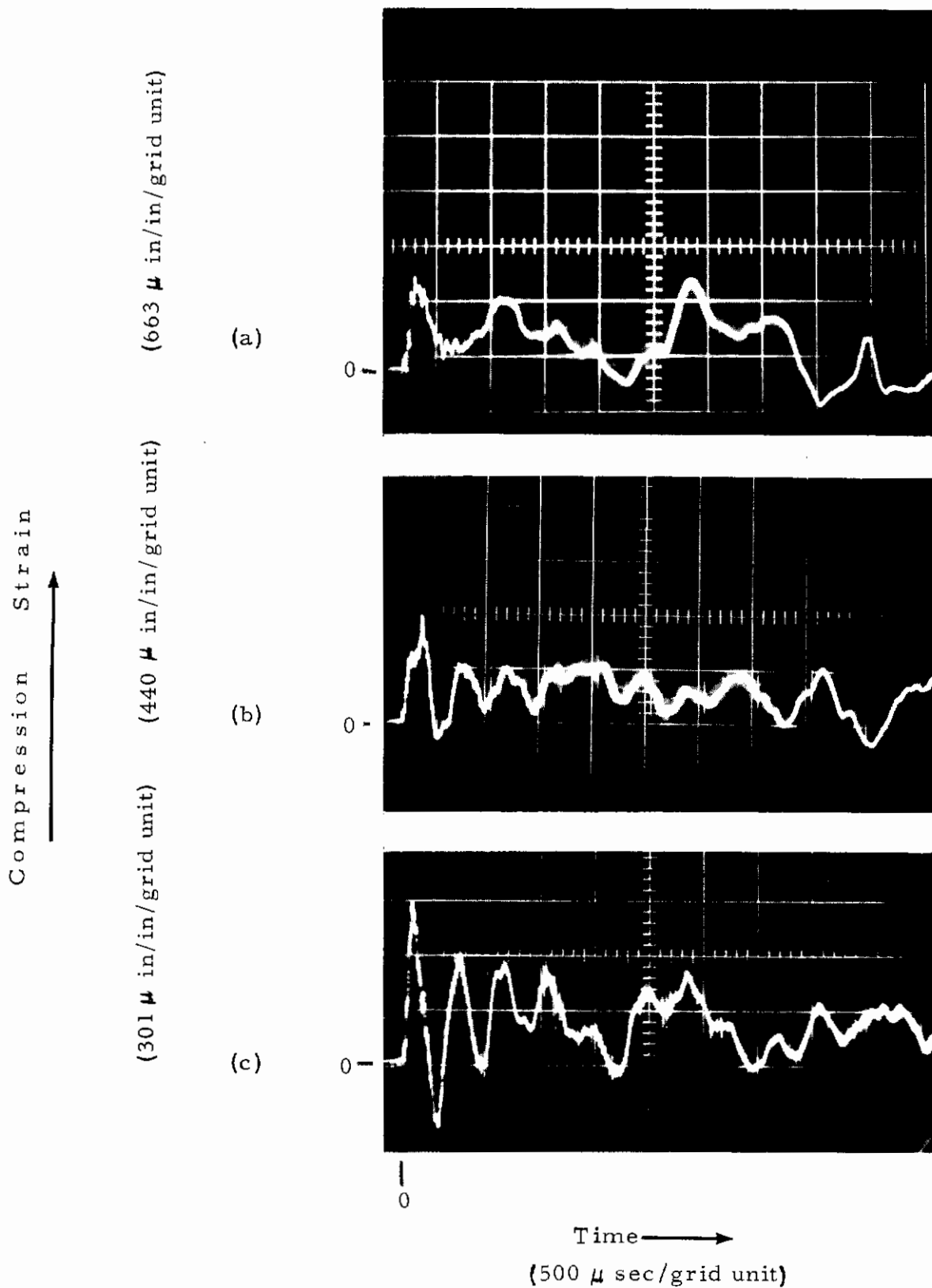
(d)



(e) (d) Middle position, .002 sec/grid unit
(e) Middle position, .001 sec/grid unit

Figure 26. Strain Data Records - Test No. C-3 (Cont'd)

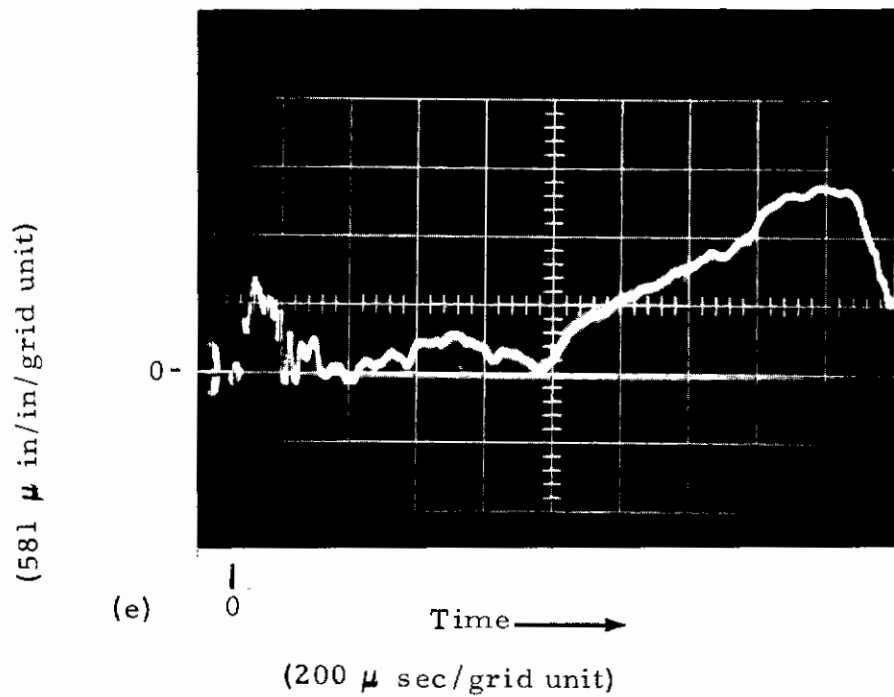
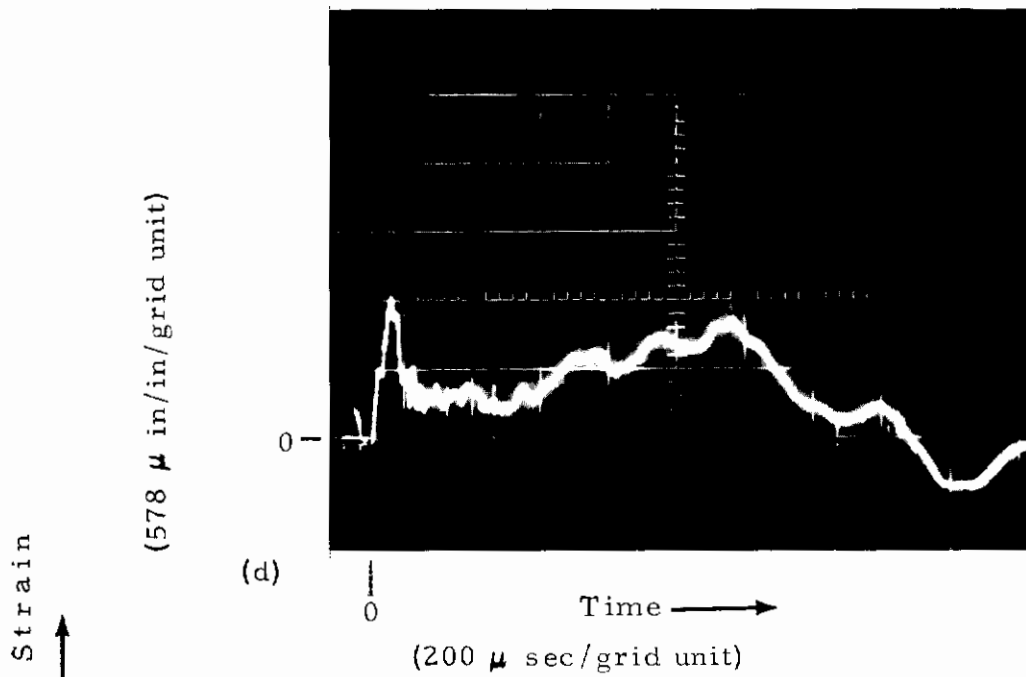
Contrails



(a) Forward position, (b) Middle position,
(c) Rear Position, all axially aligned

Figure 27. Strain Data Records - Test No. C-4

Contrails



(d) and (e) Forward positions

Figure 27. Strain Data Records - Test No. C-4 (Cont'd.)

Contrails

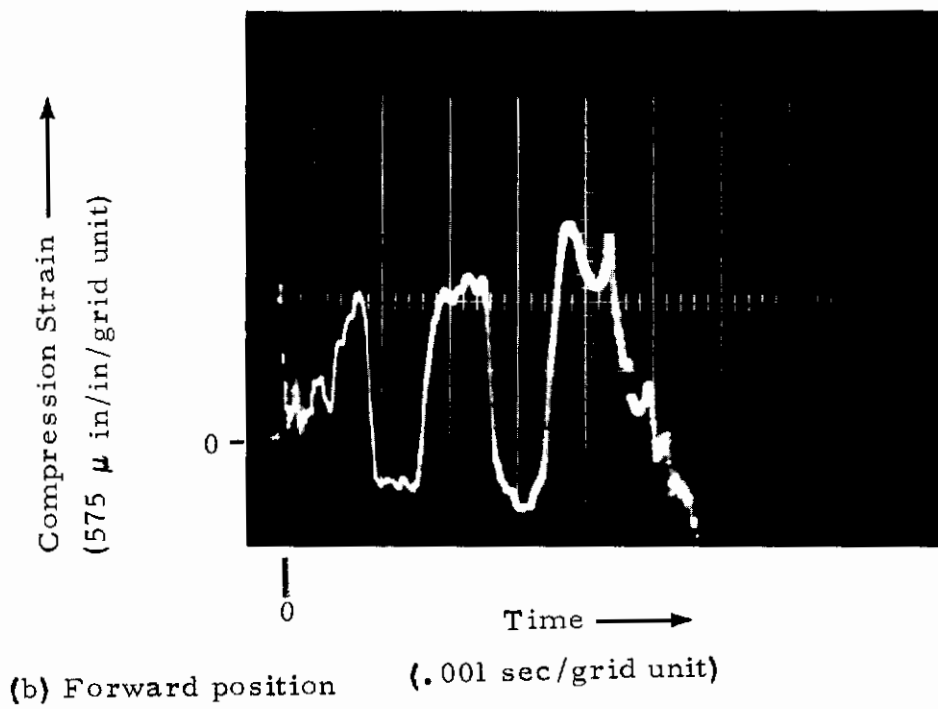
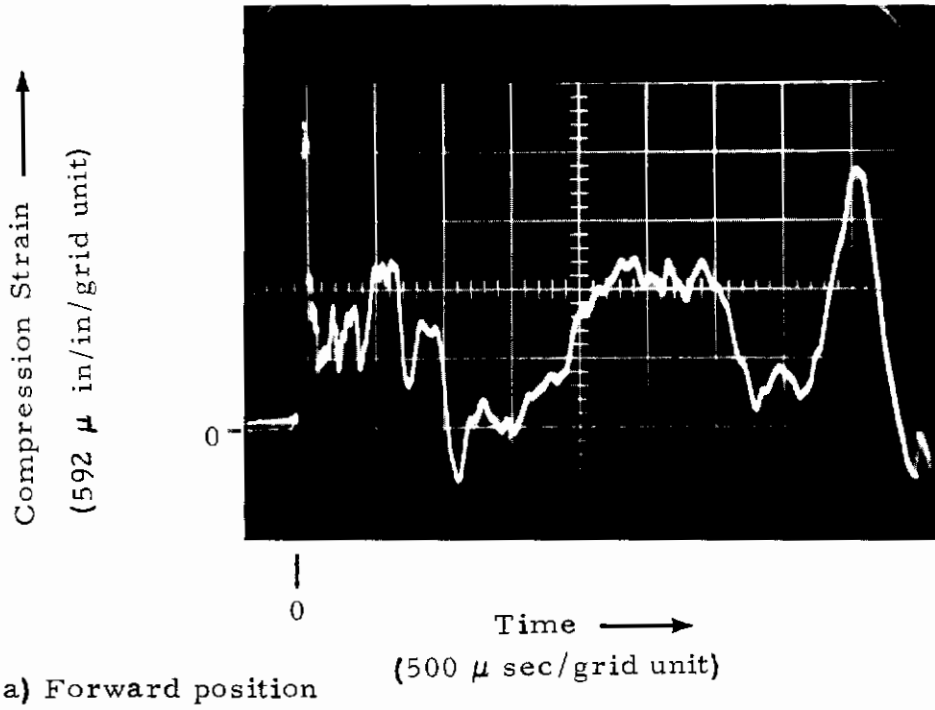
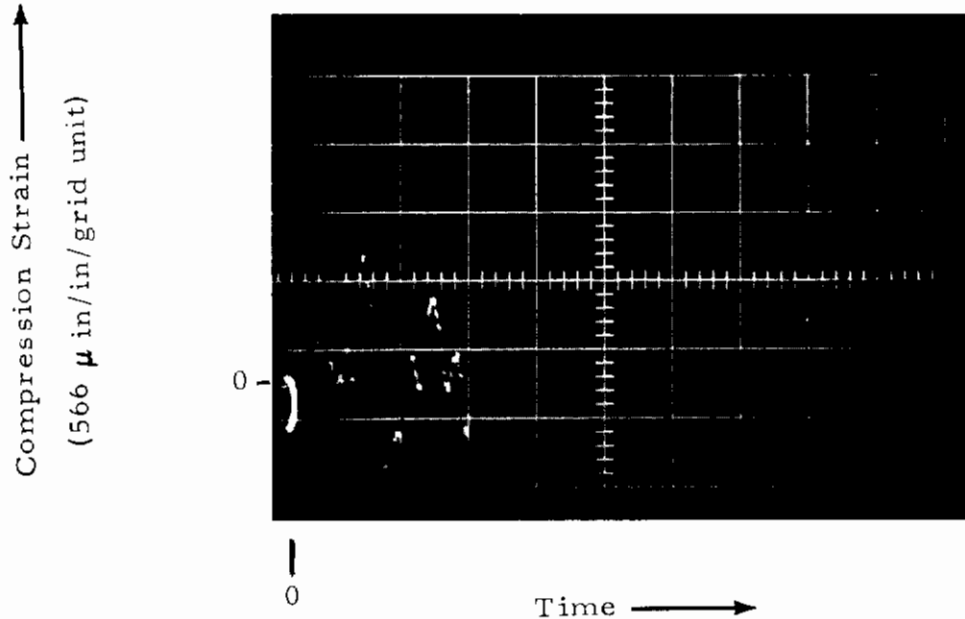
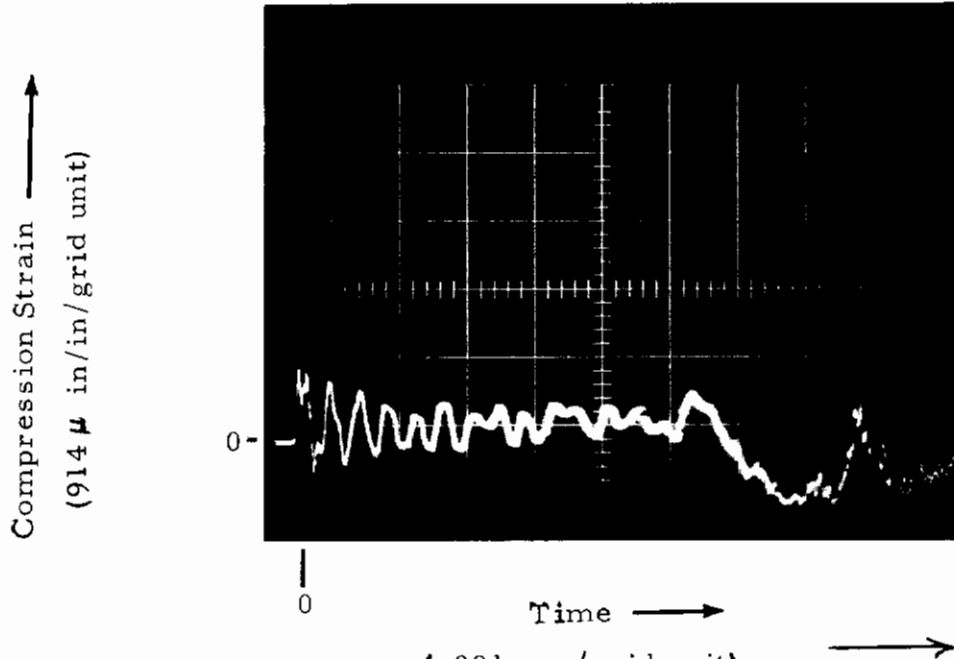


Figure 28. Strain Data Records - Test No. C-6

Contrails



(c) Forward position (.002 sec/grid unit)



(d) Middle position

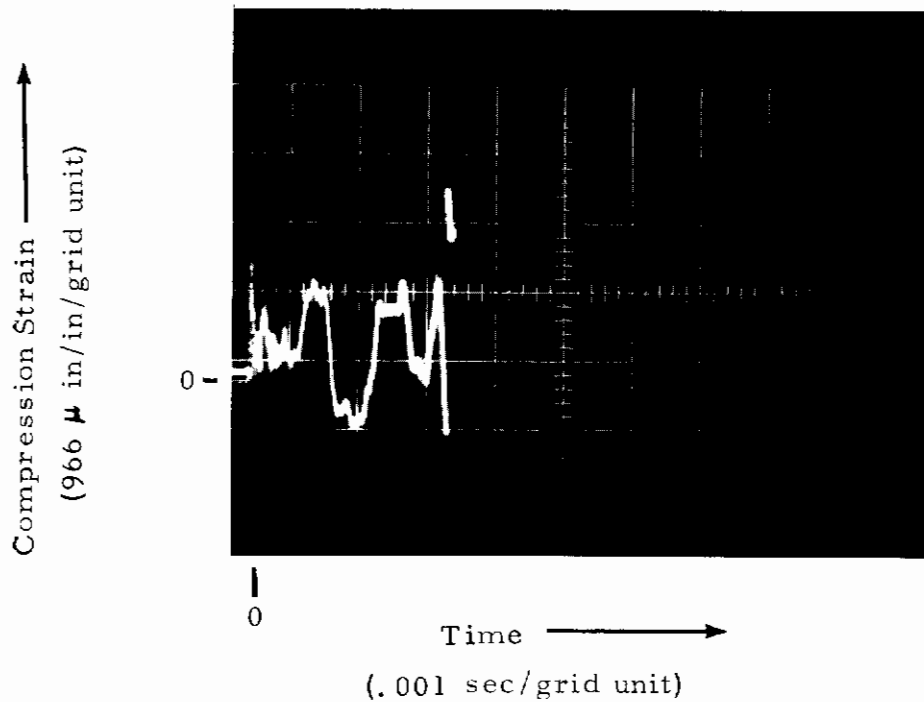
(.001 sec/grid unit)

Figure 28. Strain Data Records - Test No. C-6 (Cont'd)

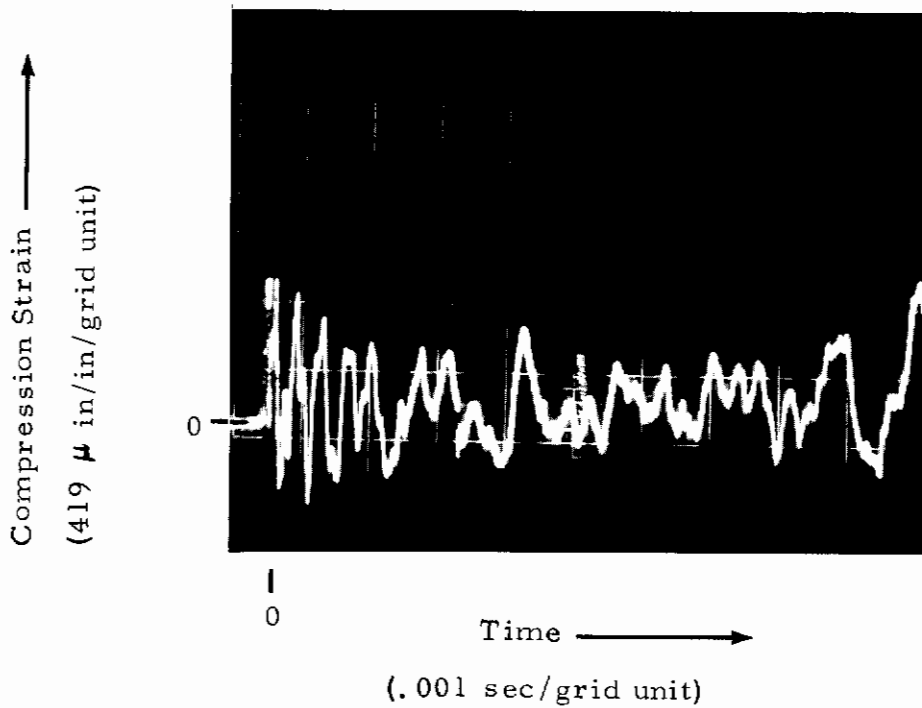


Figure 29. Specimen C-6, Showing Orderly Collapse at End

Contrails



(a) Forward position



(b) Middle position

Figure 30. Strain Data Records - Test No. C-1

Contrails

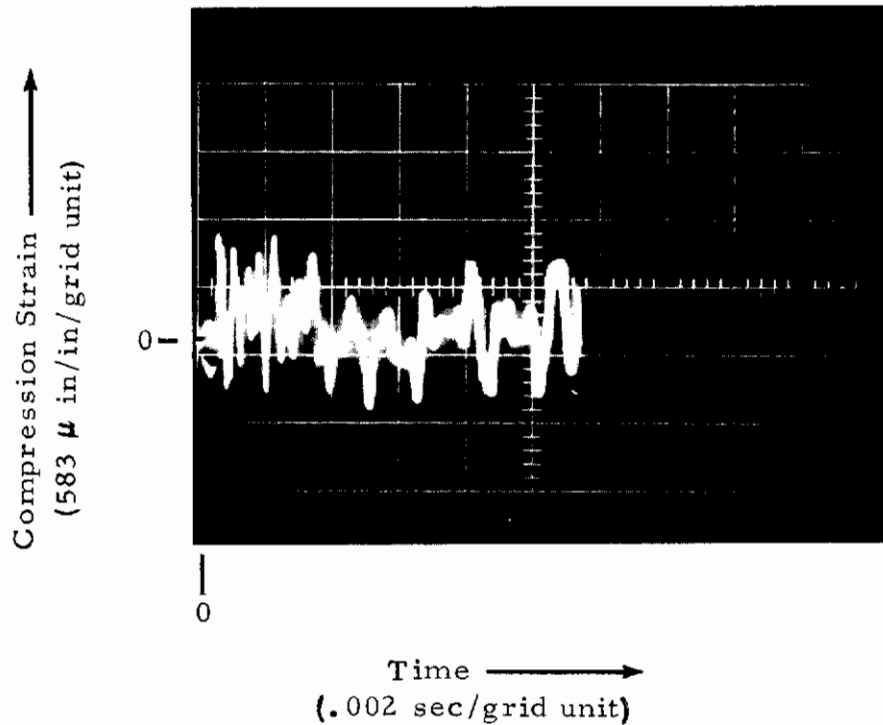
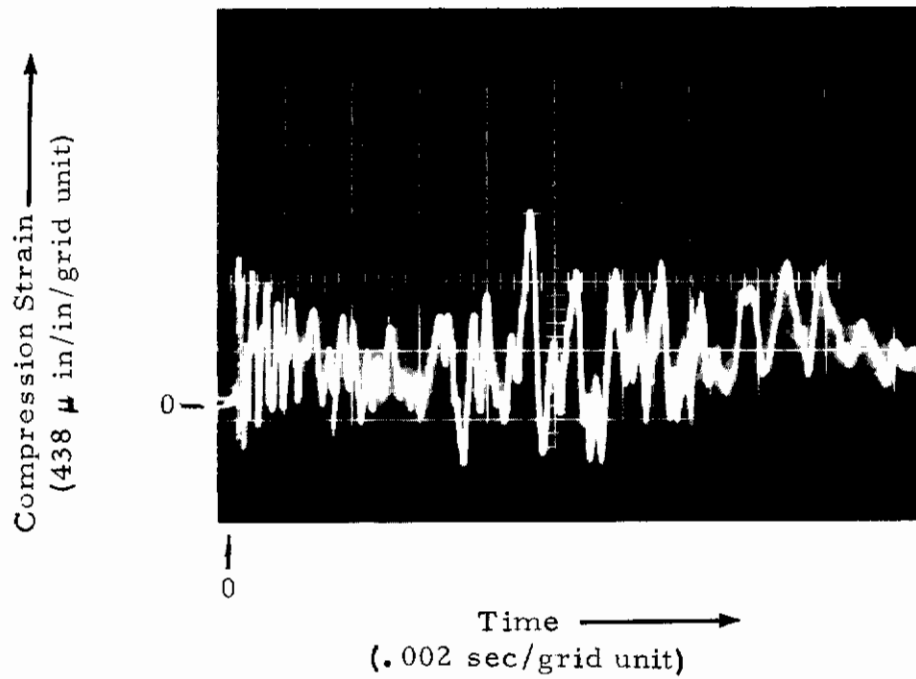


Figure 30. Strain Data Records - Test No. C-1 (Cont'd.)

Contrails

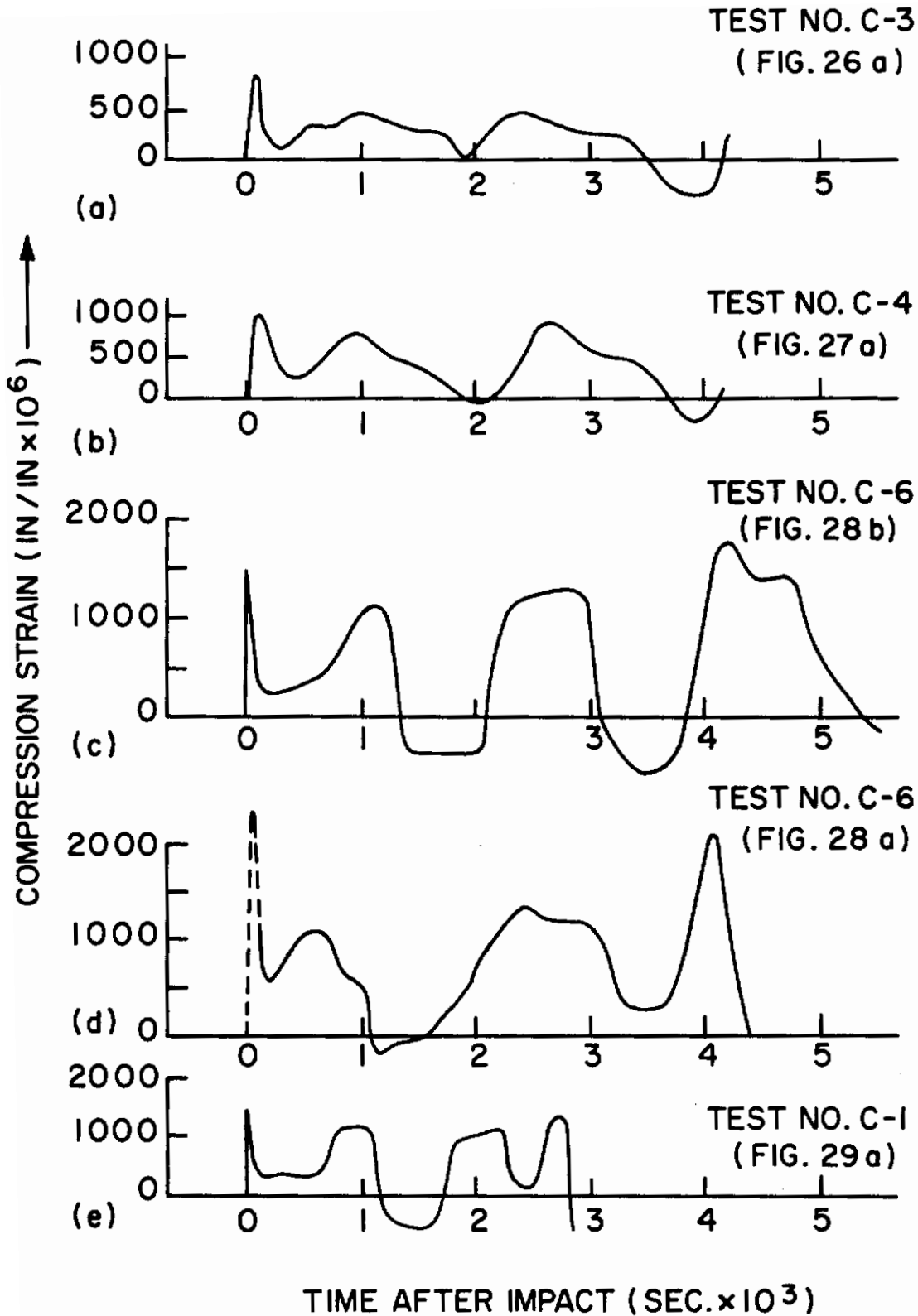


Figure 31. Initial and Postbuckling Strain - Time Pulses



Figure 32. Specimens After Oblique Impact - Type A



Figure 33. Specimens After Oblique Impact - Type B

Contraails

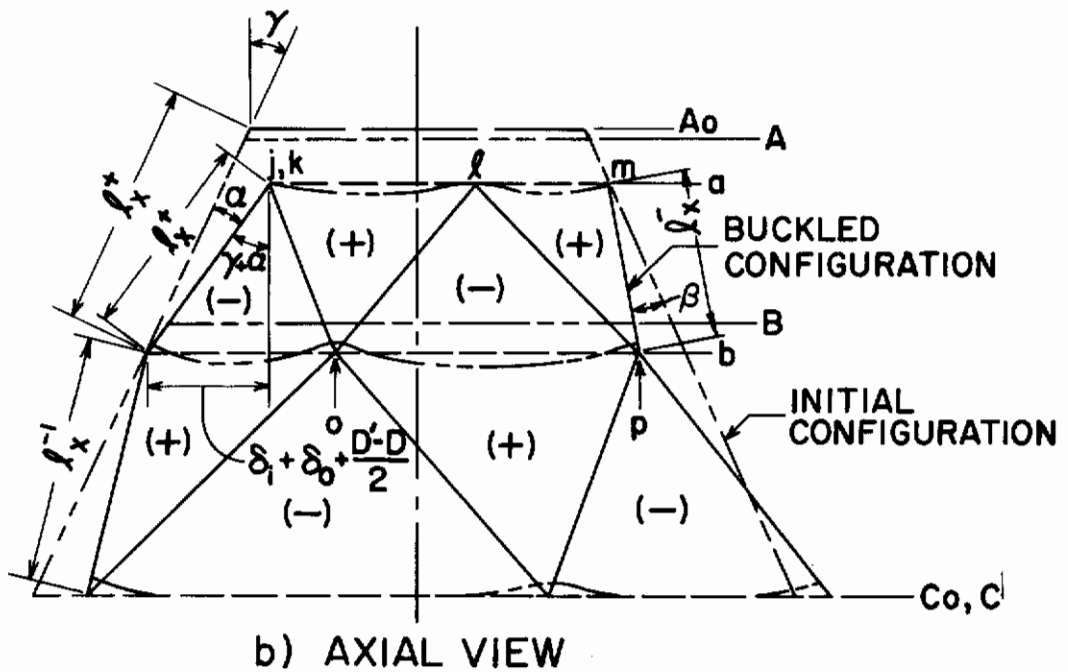
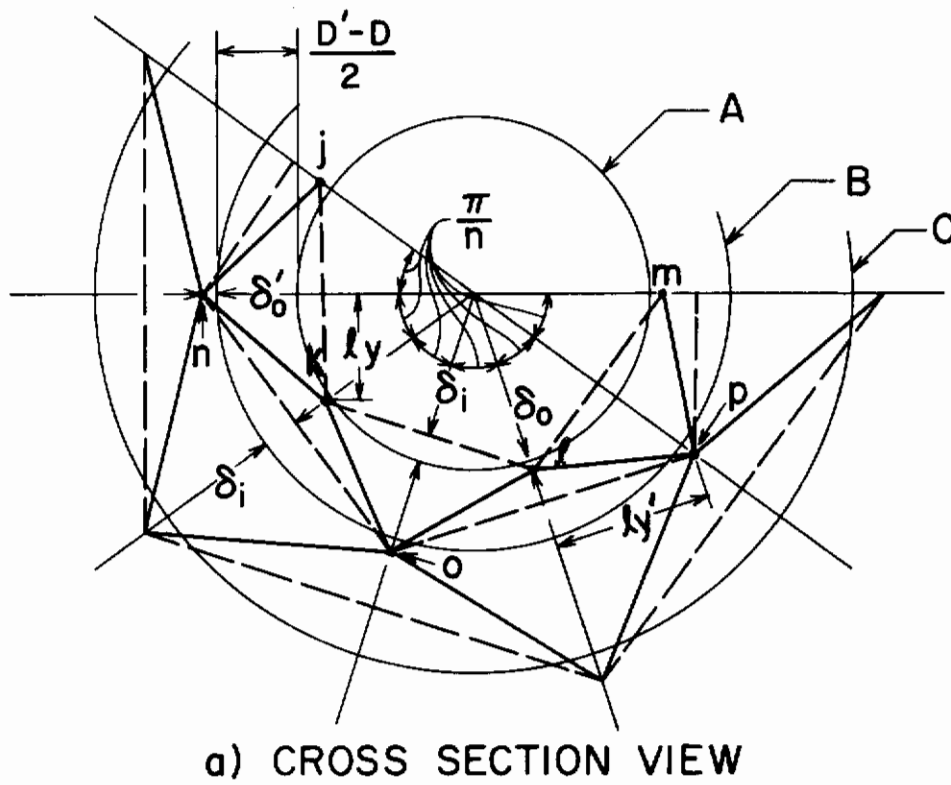


Figure 34. Inextensional Geometry of a Conical Frustum

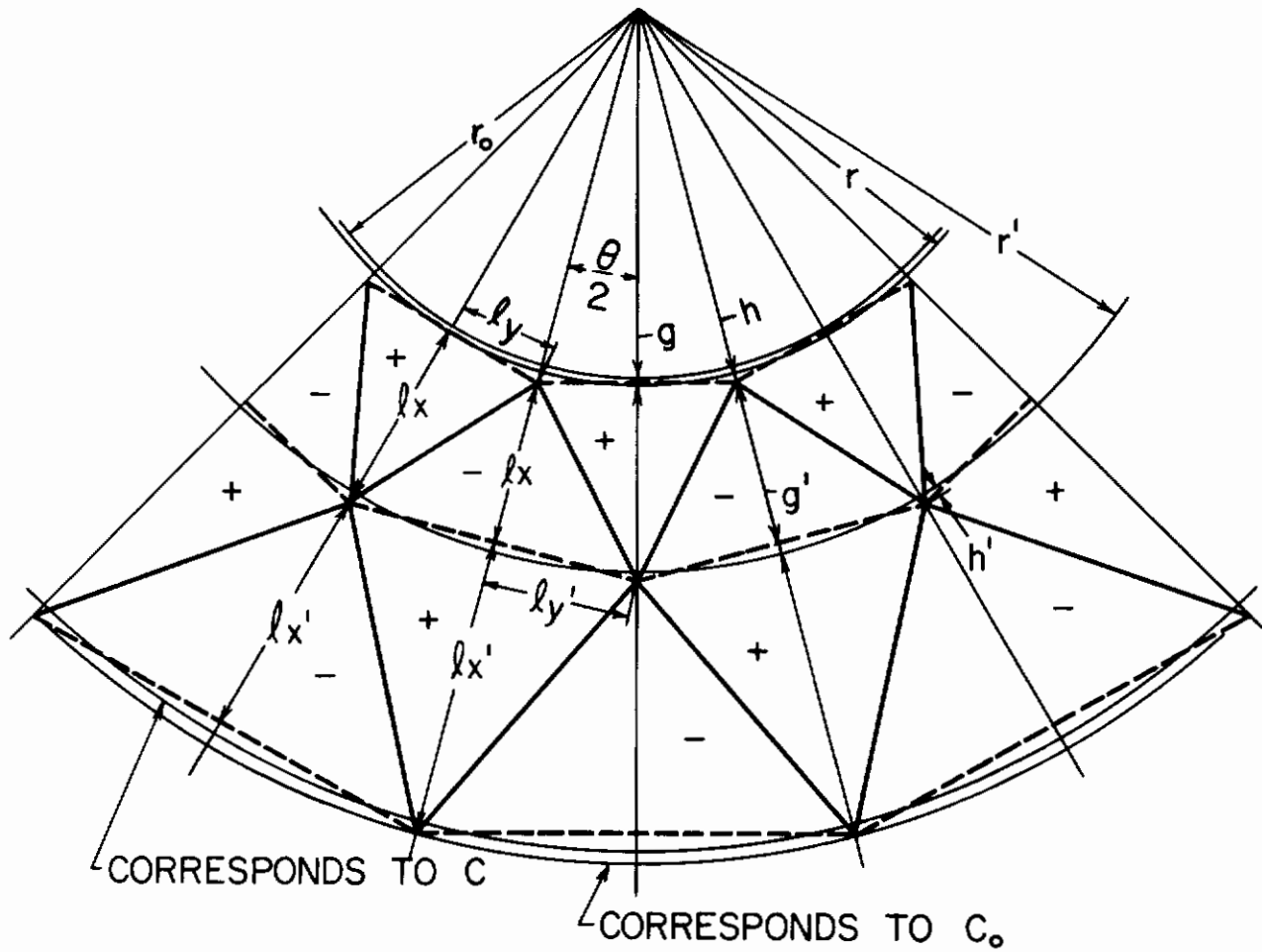
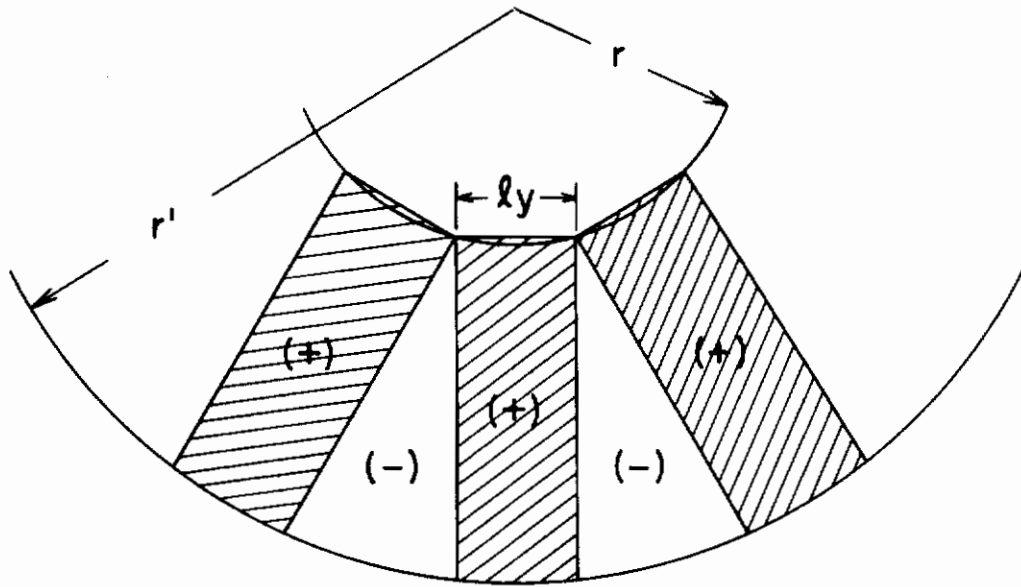
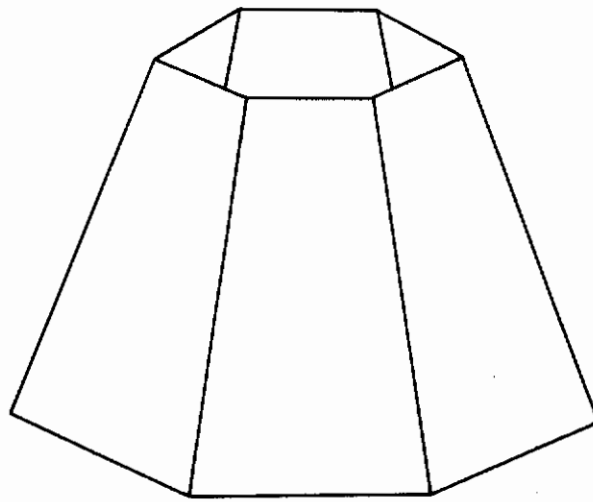


Figure 35. Layout of an Inextensional Pattern for a Cone in the Plane.



(a) PATTERN CORRESPONDING TO $K^+ = 0$ IN THE CONICAL BLANK



(b) PRISMOIDAL INEXTENSIONAL SHORTENING CONFIGURATION FOR A CONICAL SHELL

Figure 36. Prismatic Inextensional Shortening Configuration

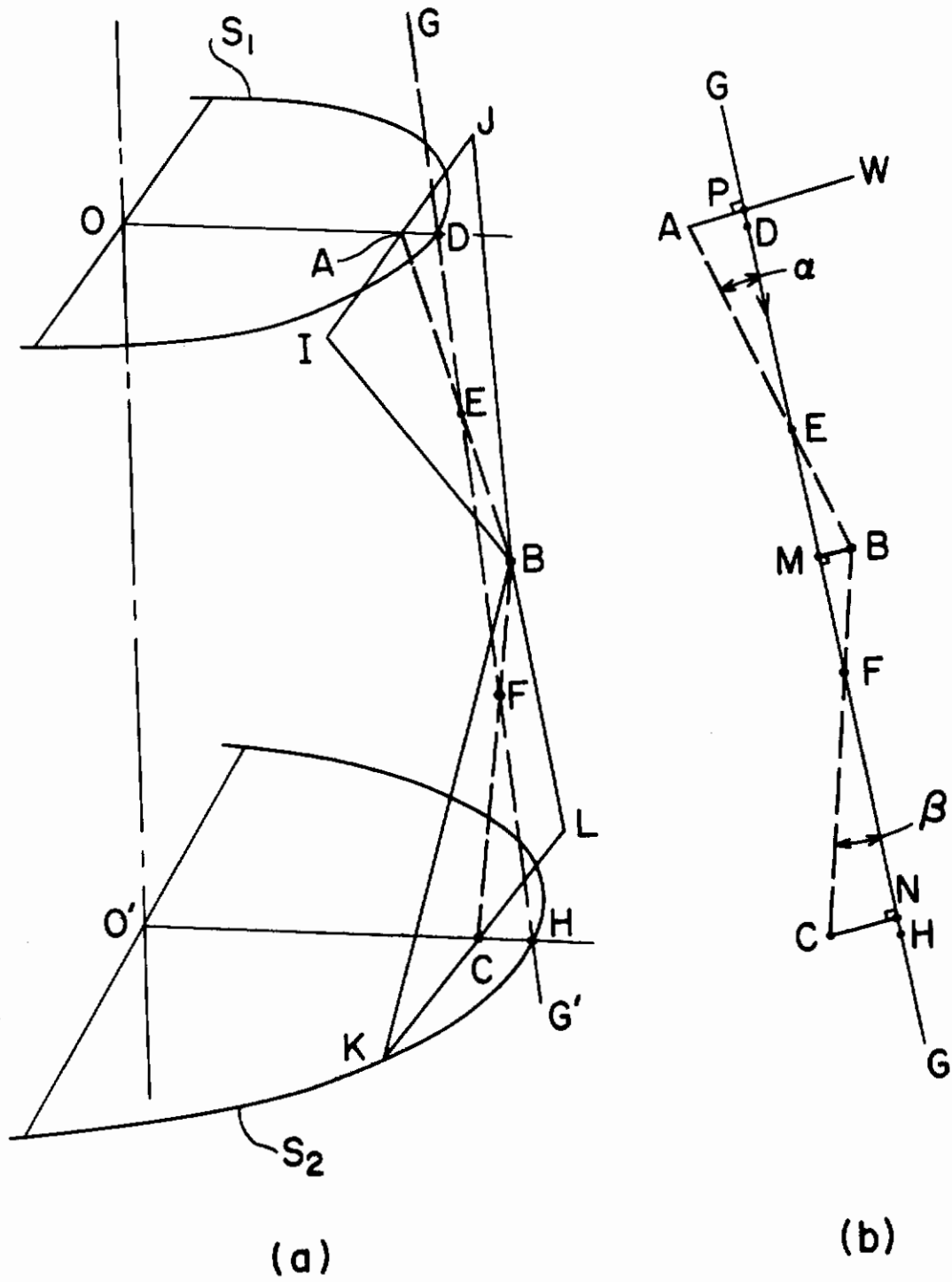


Figure 37. Profile Geometry

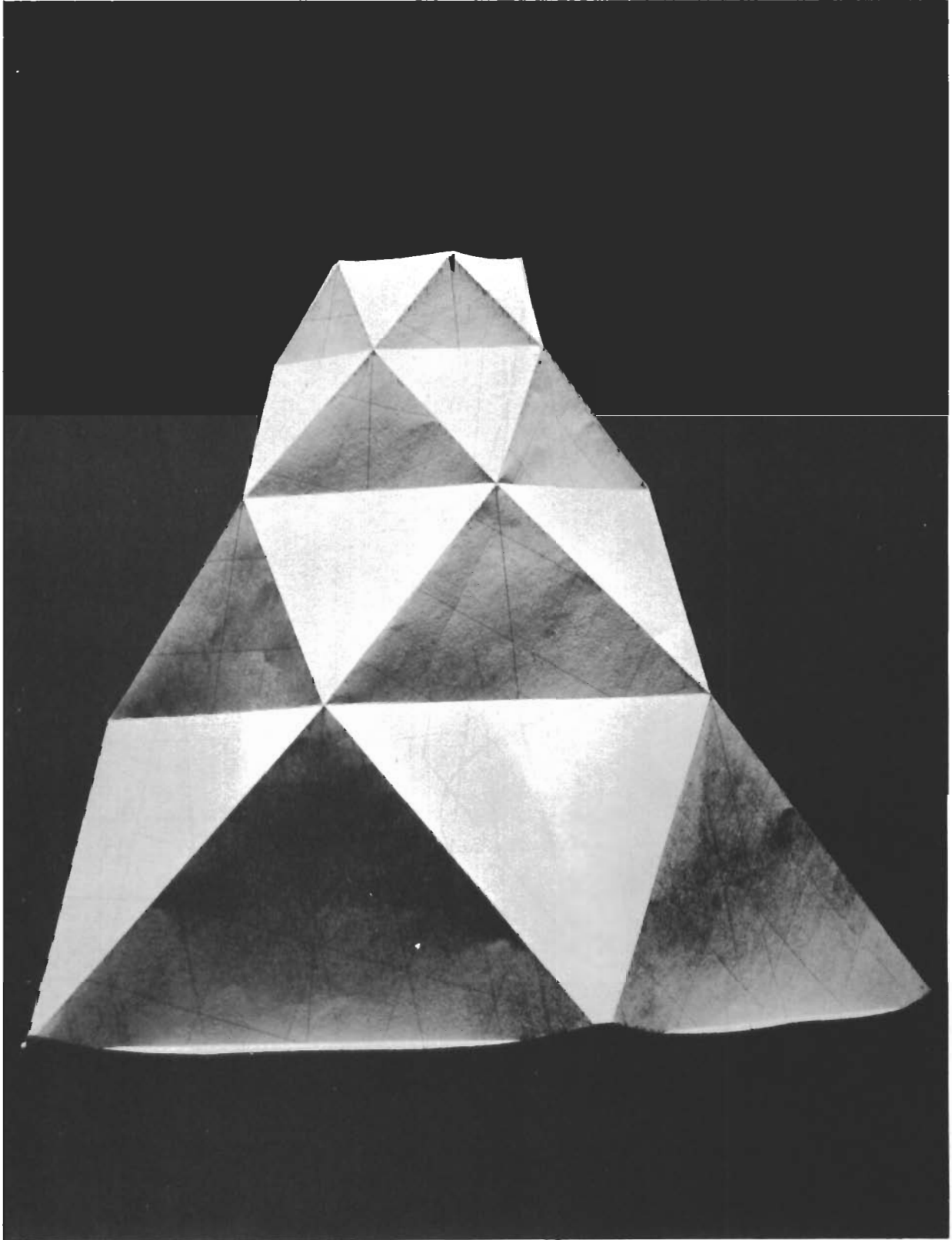


Figure 38. 10% Shortened Inextensional Configuration for a Conical Frustum of $\gamma = 25^\circ$, $n_f = 5$

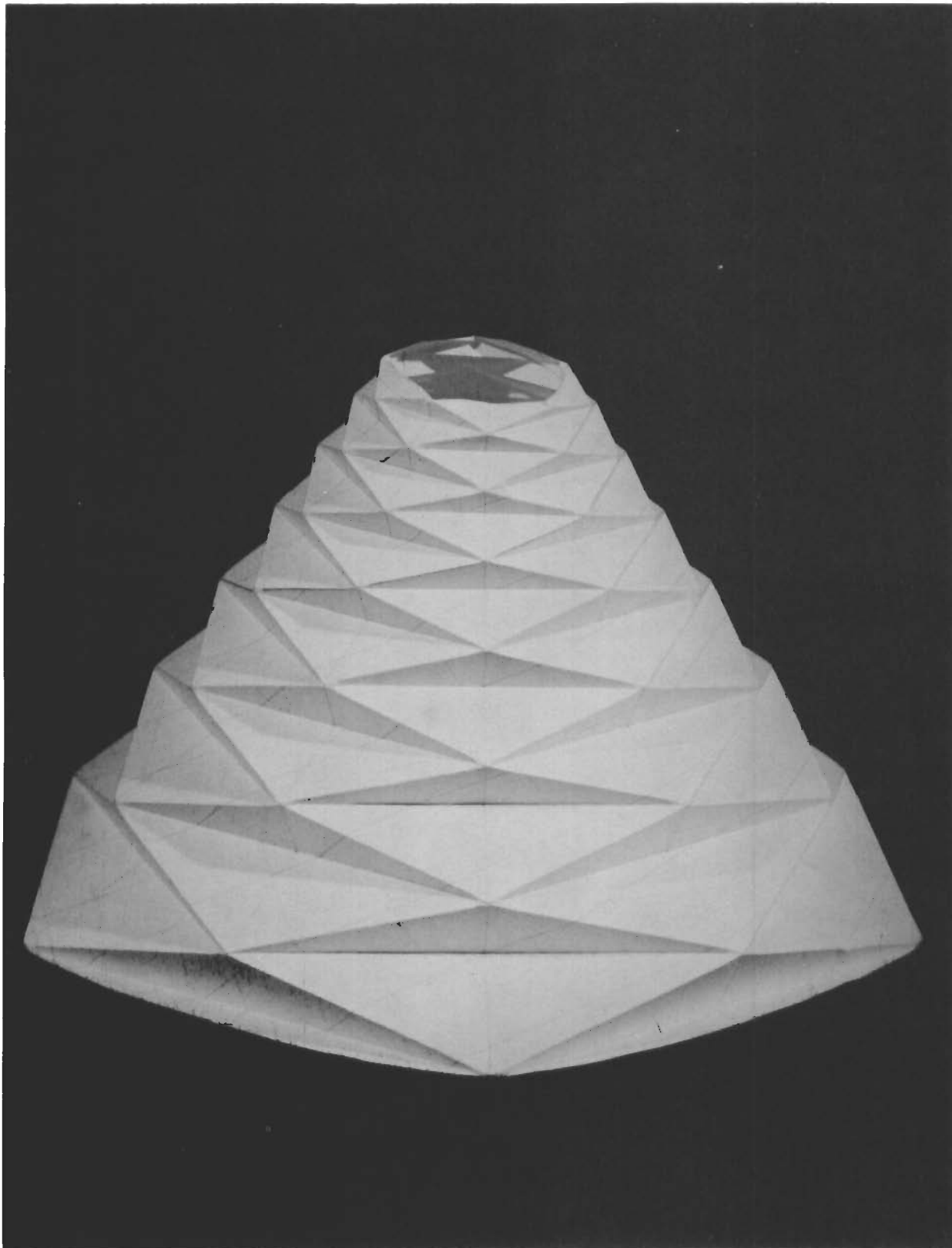


Figure 39. 50% Shortened Inextensional Configuration for a Conical Frustum of $\gamma = 25^\circ$, $n_f = 5$

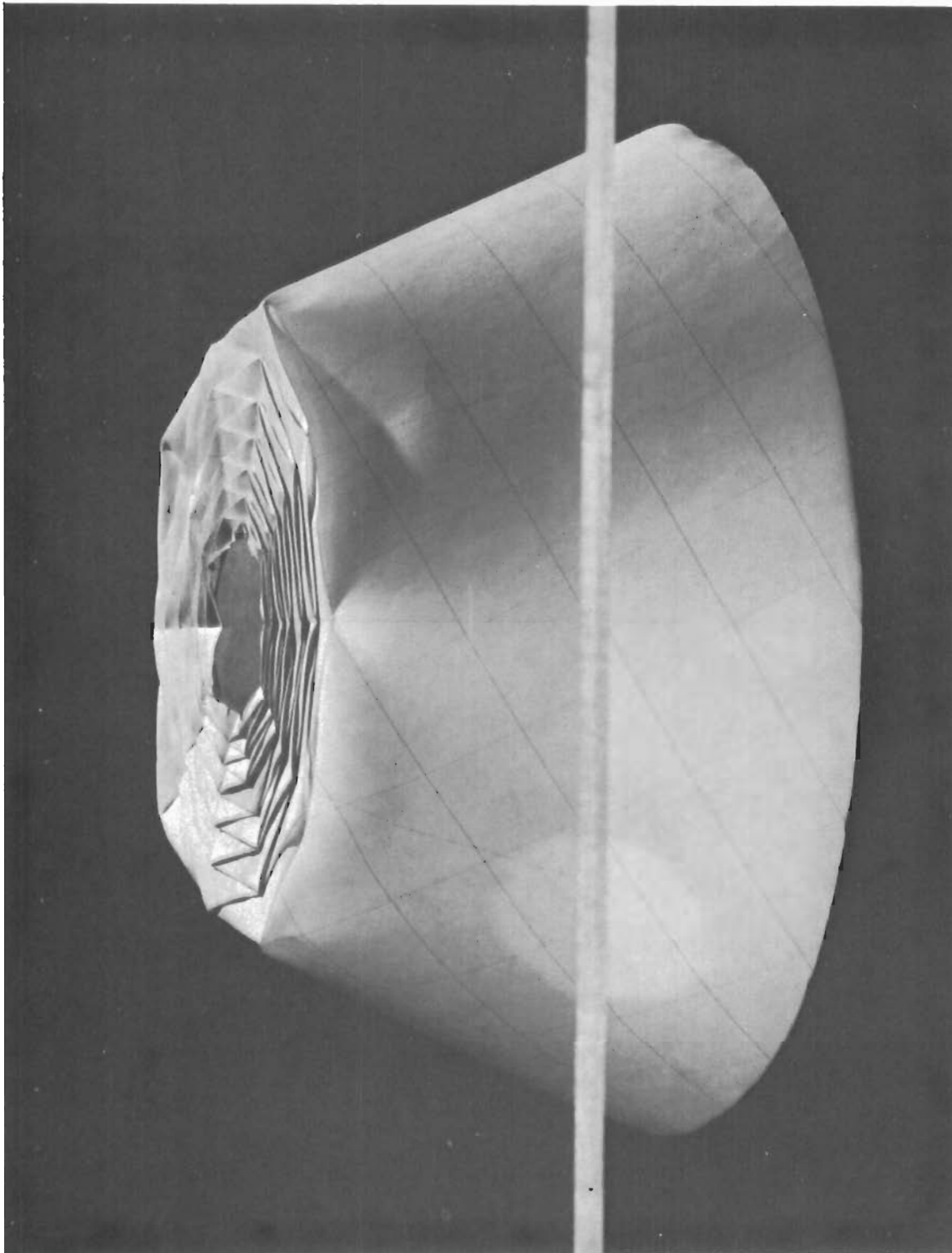


Figure 40. Total Collapse Configuration for a Conical Frustum of $\gamma = 25^\circ$, $n_f = 5$

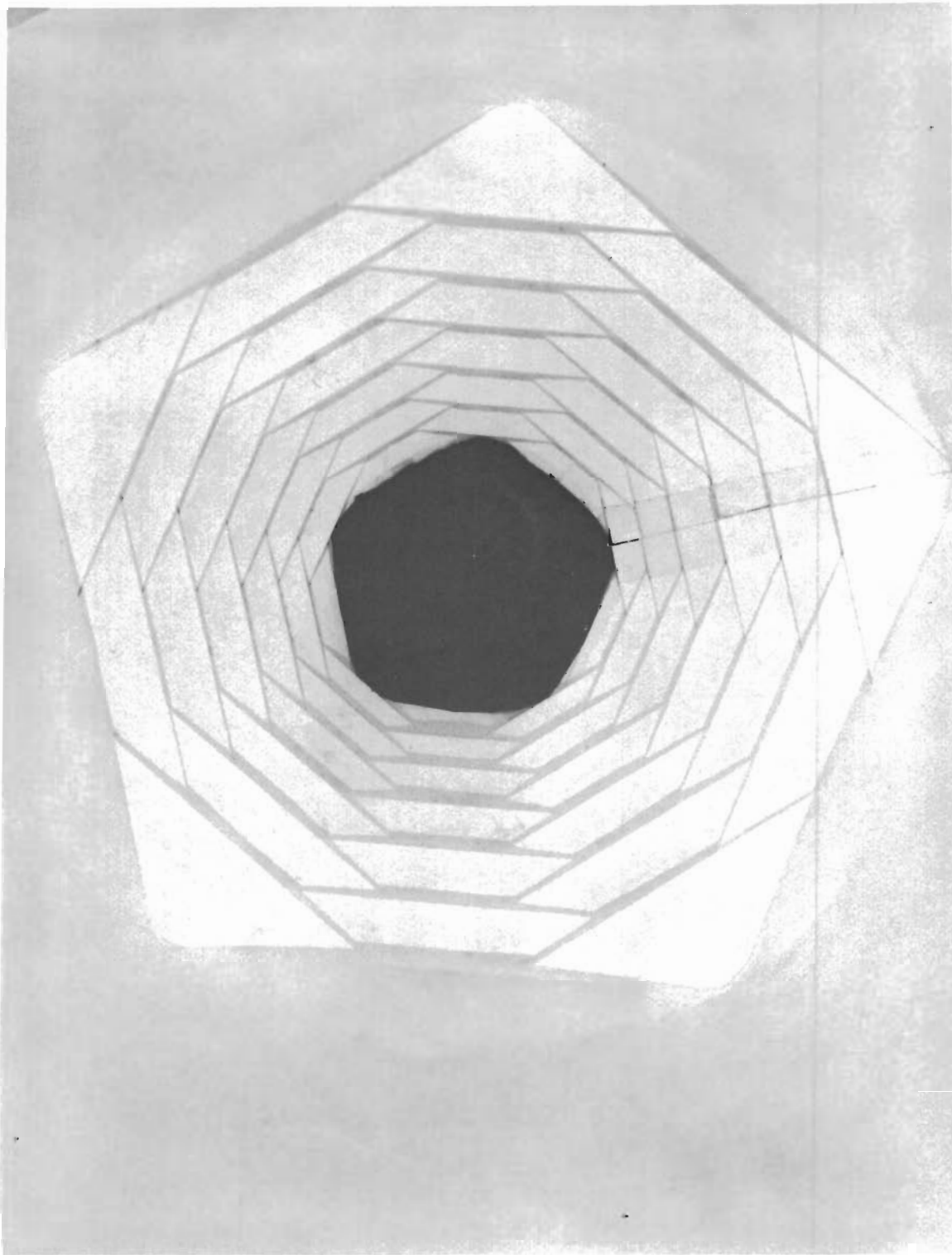


Figure 41. Inside View of the Constructed Total Collapse Pattern,
 $\gamma = 25^\circ$, $n_f = 5$

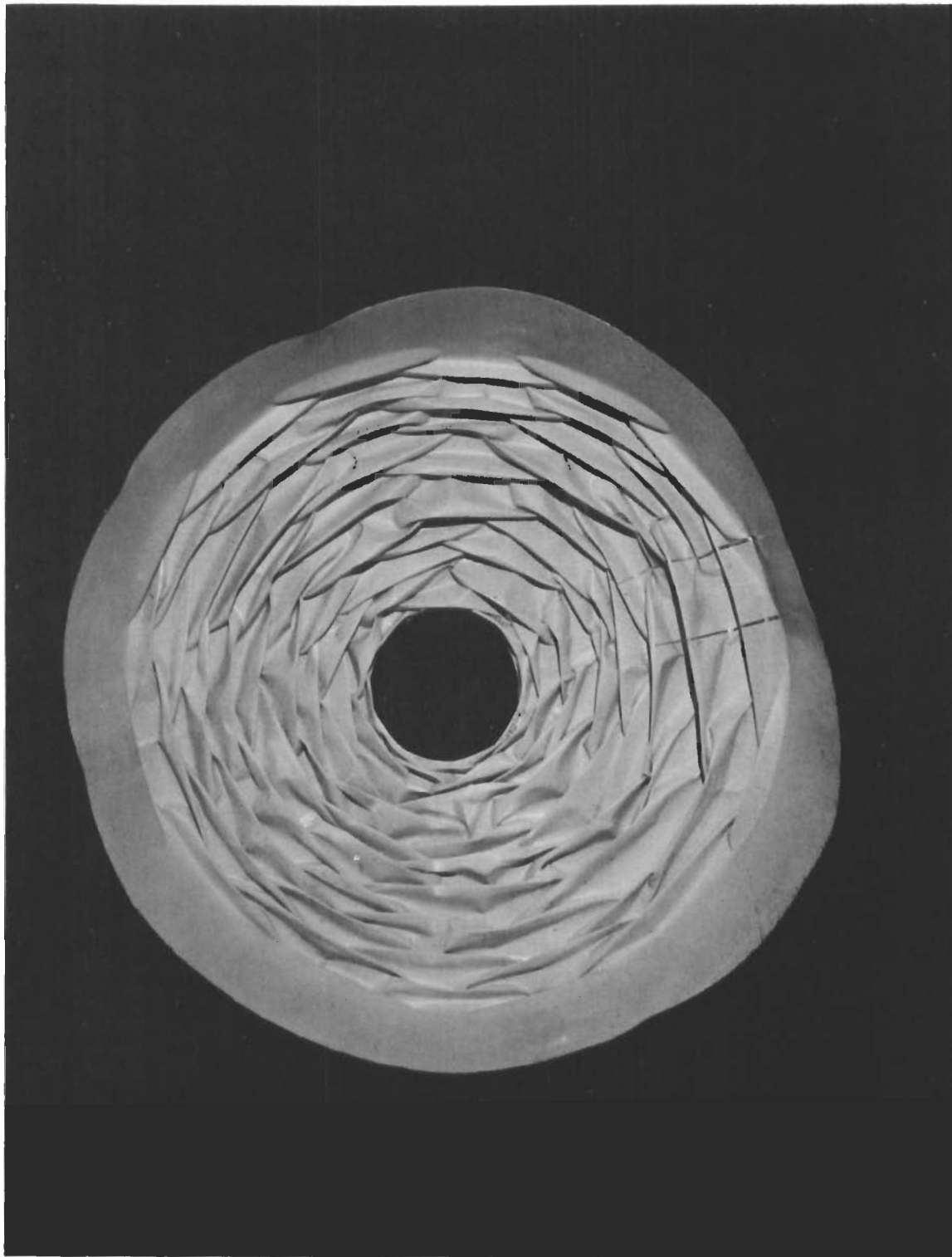


Figure 42. Inside View of Collapsed Conical Frustum Obtained Experimentally ($V_o = 20$ ft/sec, $\gamma = 25^\circ$, $n \approx 5$)



Figure 43. Outside View of a Collapsed Conical Frustum Obtained Experimentally
($V_0 = 20$ ft/sec, $\gamma = 25^\circ$, $n \approx 5$)



Figure 44. Projectile

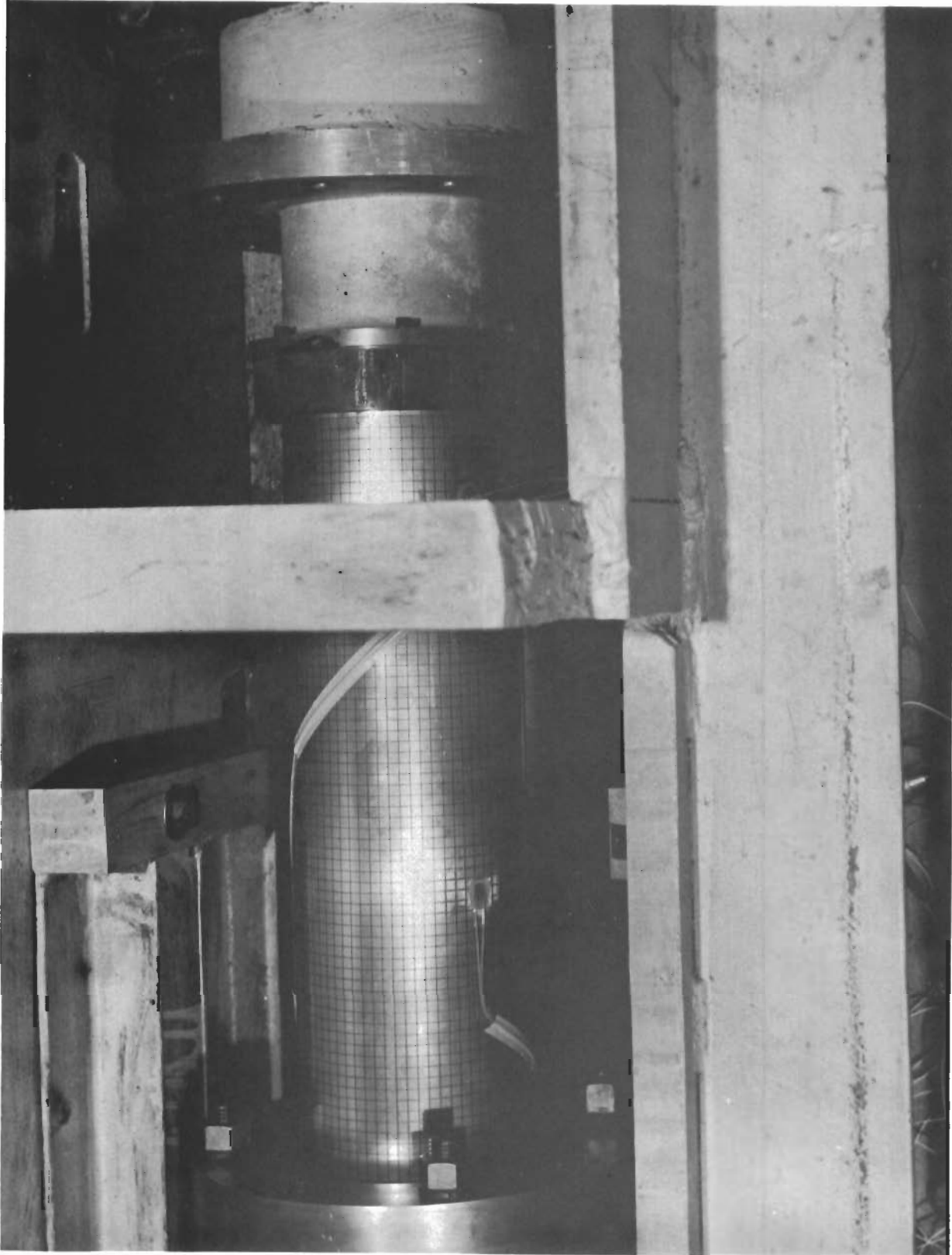


Figure 45. Initial Alignment of the Specimen and Projectile on the High Velocity Impact Facility

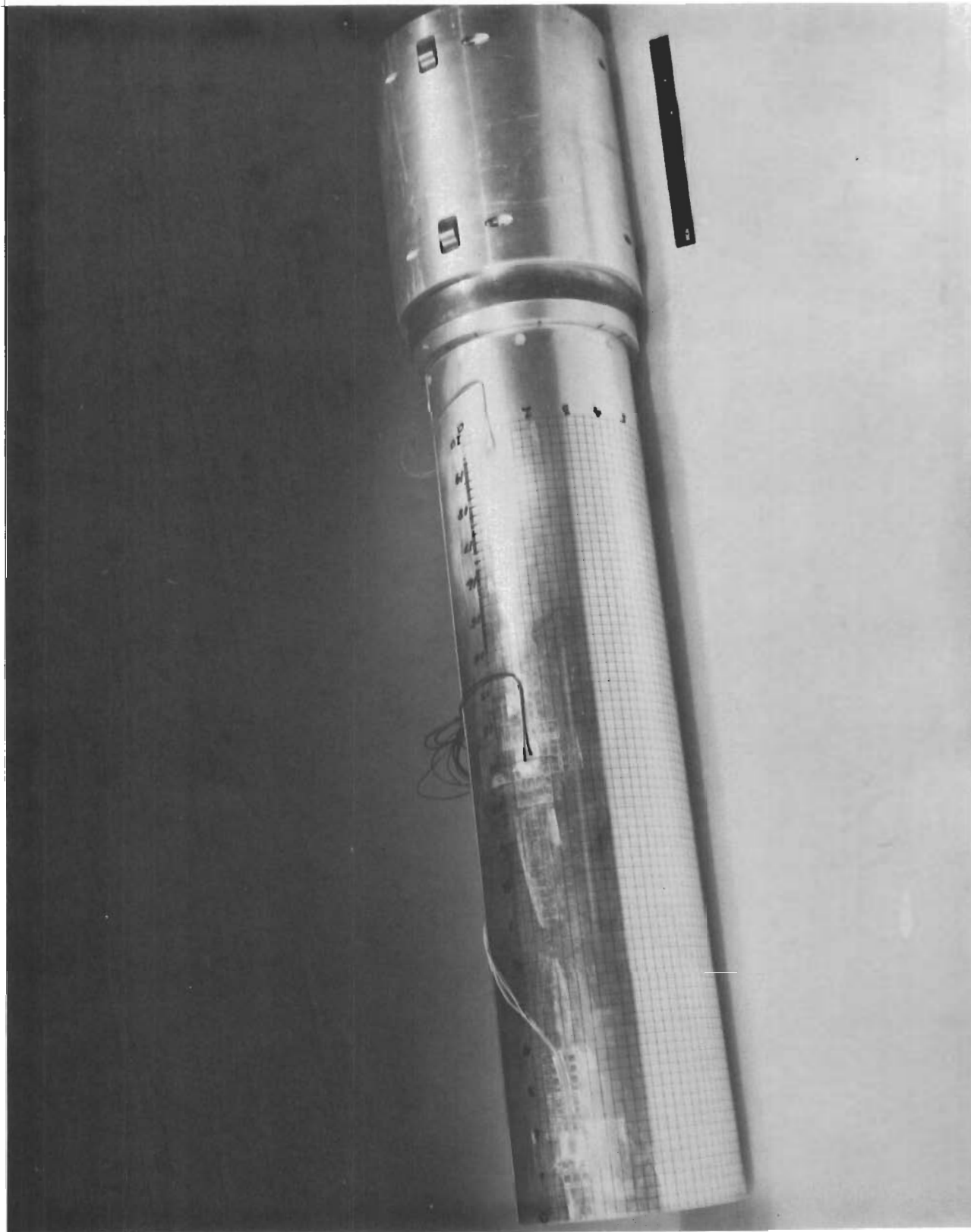


Figure 46. Instrumented Cylindrical Shell Shown Mounted on its Carriage

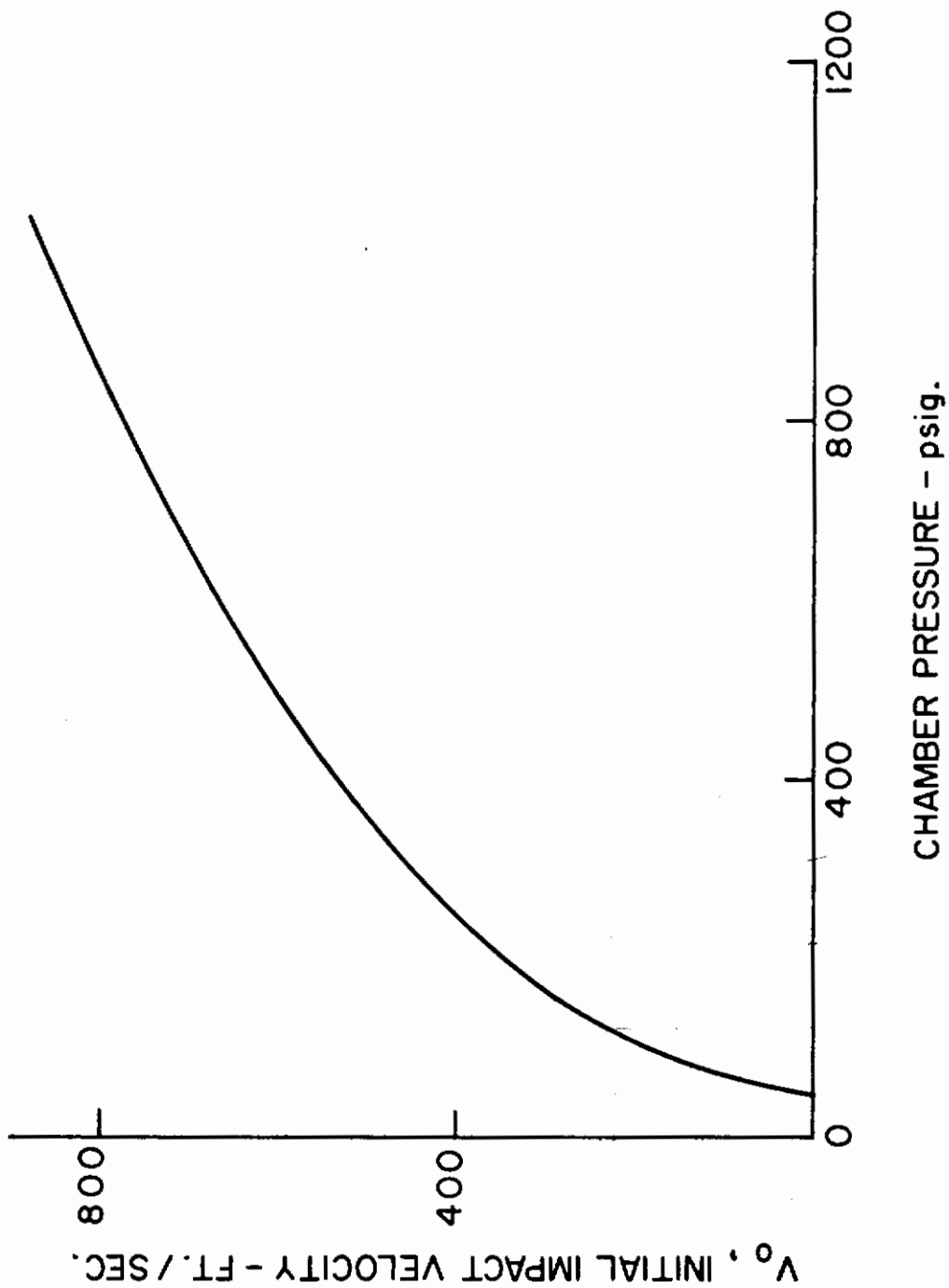
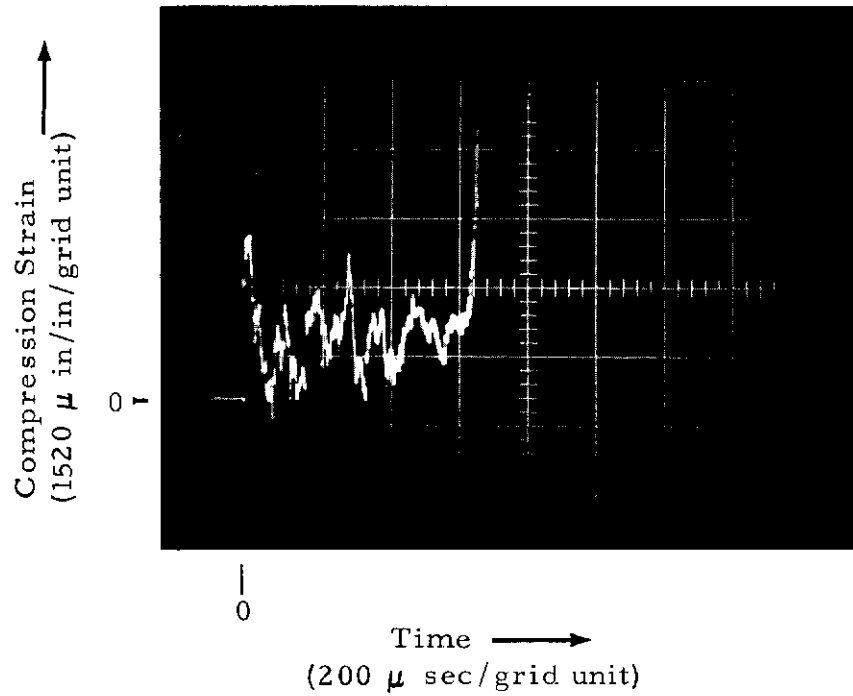
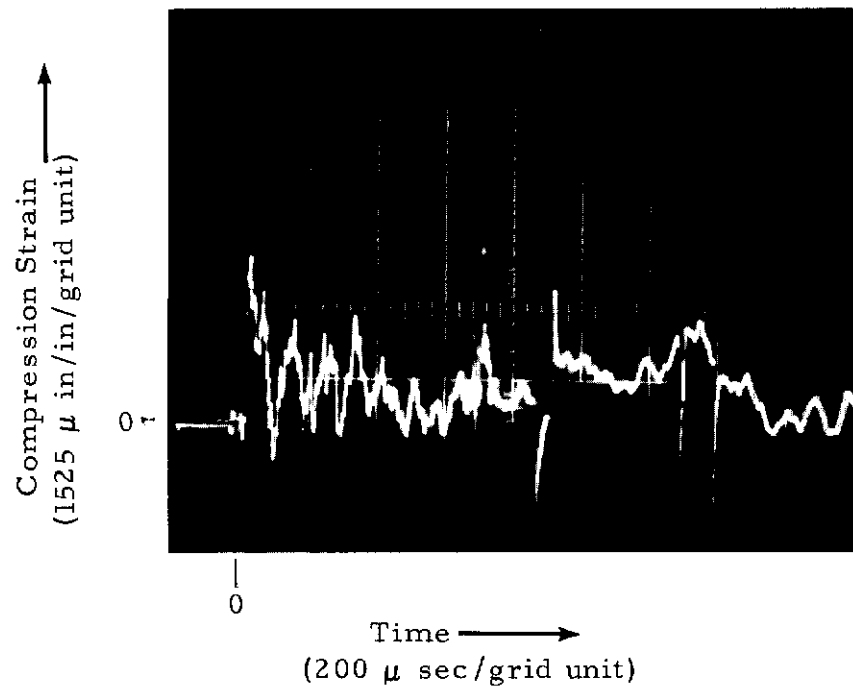


Figure 47. Calculated Velocity-Chamber Pressure Characteristic of the High Velocity Impact Facility - 14 lb. Projectile

Contrails



(a) Forward position



(b) Middle position

Figure 48. Strain Records - Test No. HV-4
($V_0 = 216$ ft/sec, $h = .016$ in)

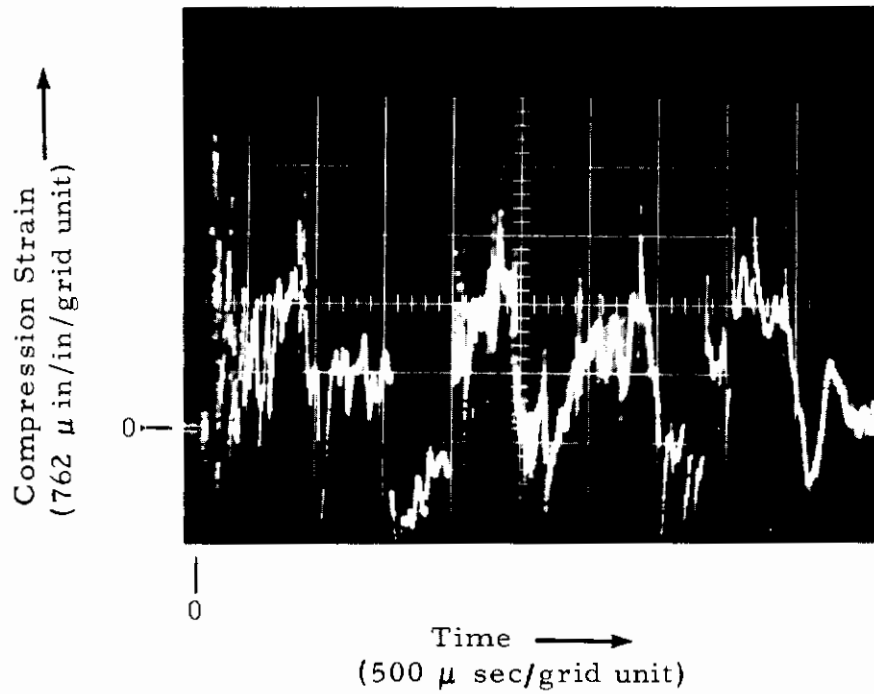


Figure 49. Strain Record, Middle Position - Test No. HV-4
($V_0 = 216$ ft/sec, $h = .016$ in)

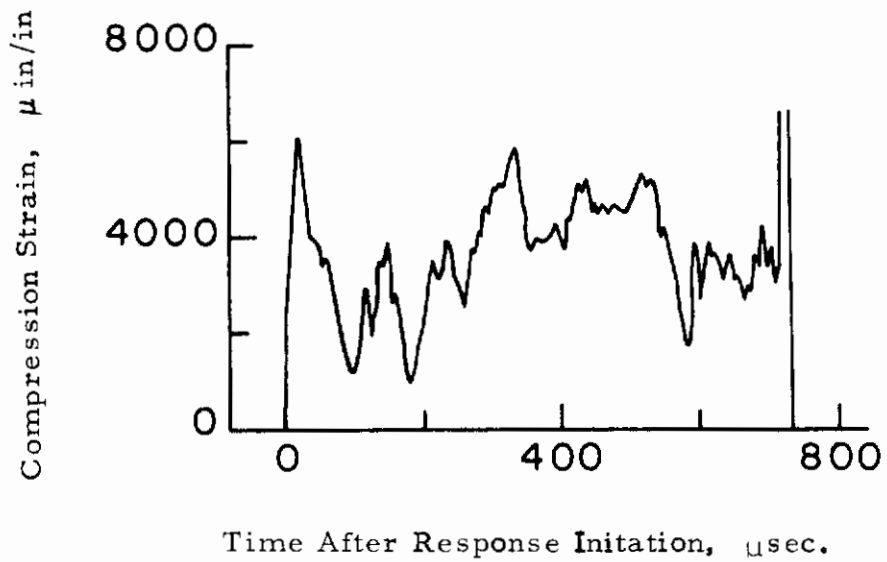


Figure 50. Strain Record, Forward Position - Test No. HV-5
($V_0 = 201$ ft/sec, $h = .016$ in)

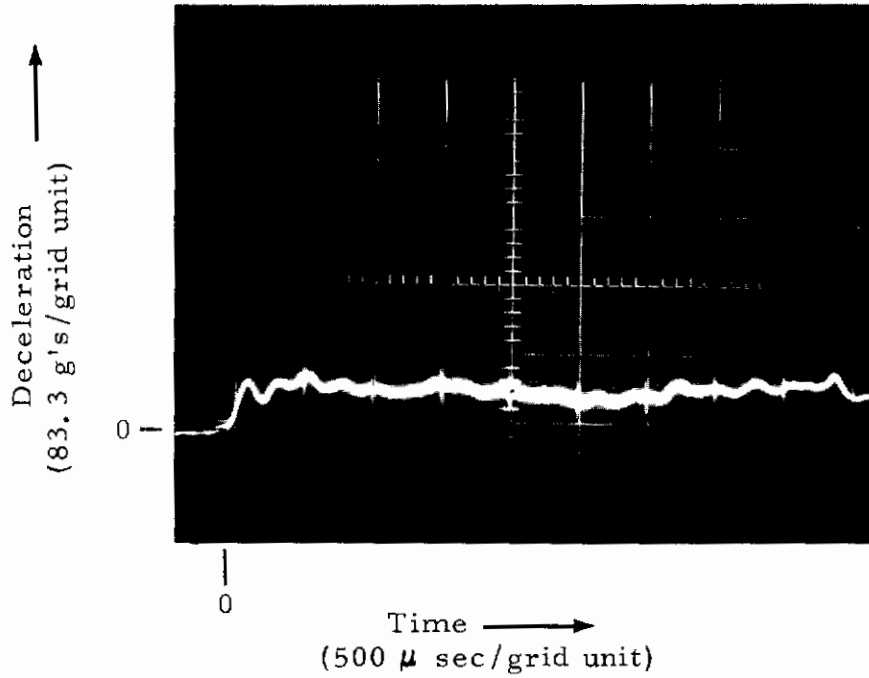


Figure 51. Deceleration Record - Test No. HV-5
 $V_0 = 201$ ft/sec, $h = .016$ in

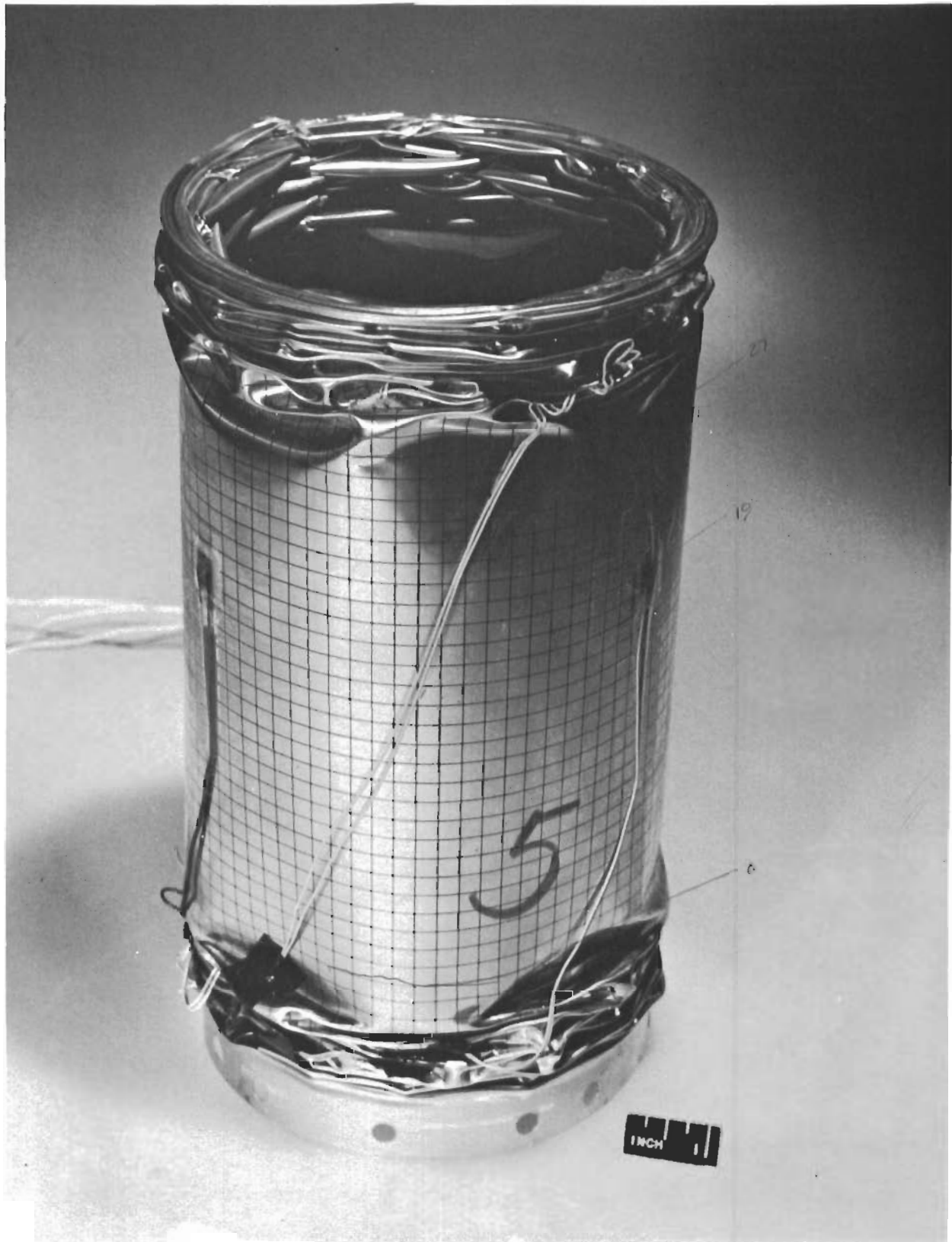


Figure 52. Specimen HV-5 After Impact, $V_0 = 201$ ft/sec, $h = .016$ in

Contrails

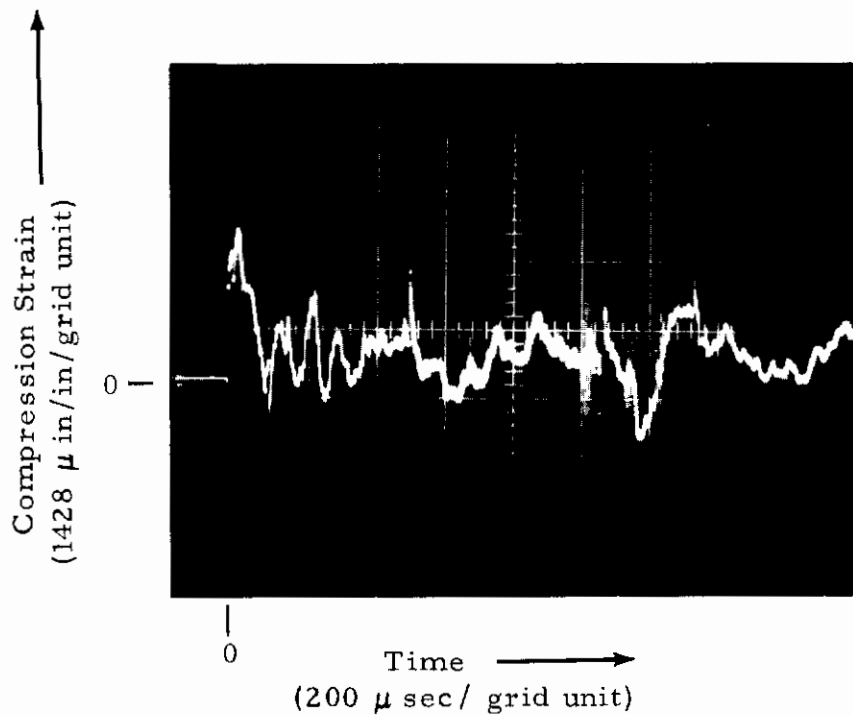
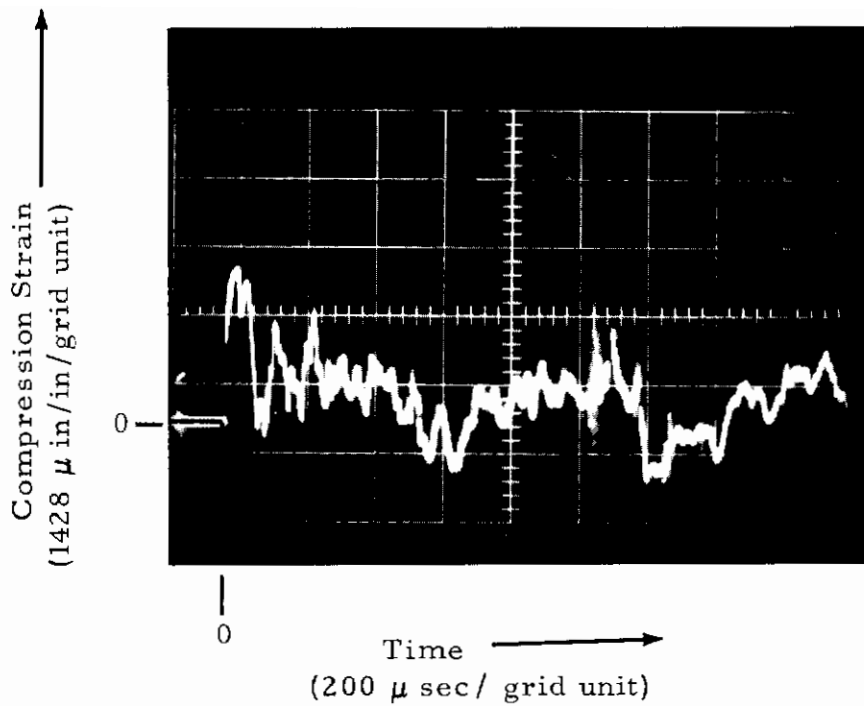


Figure 53. Strain Records, Middle Position - Test No. HV-6
($V_0 = 225$ ft/sec, $h = .016$ in)

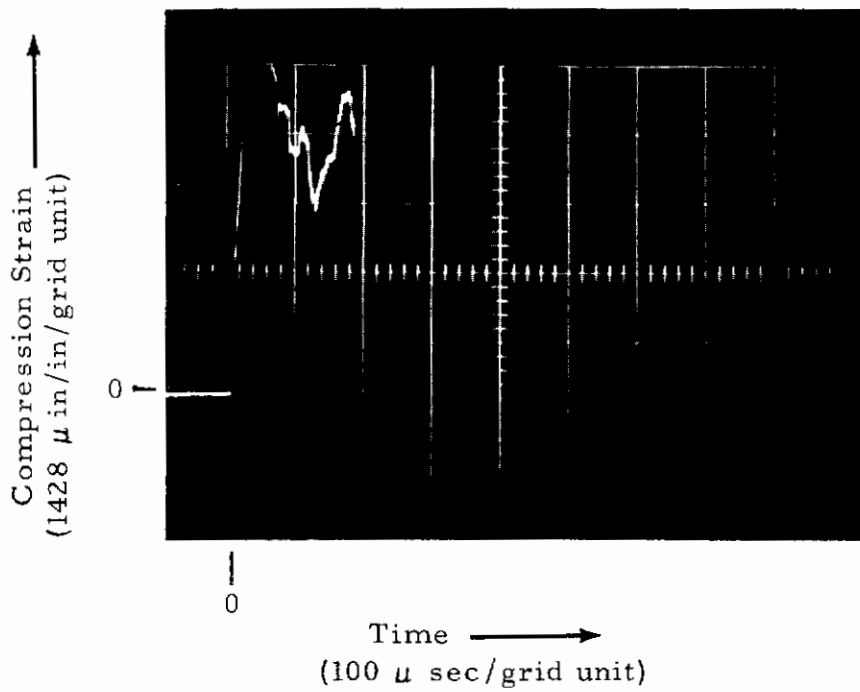


Figure 54. Strain Record, Forward Position - Test No. HV-6
($V_o = 225$ ft/sec, $h = .016$ in)

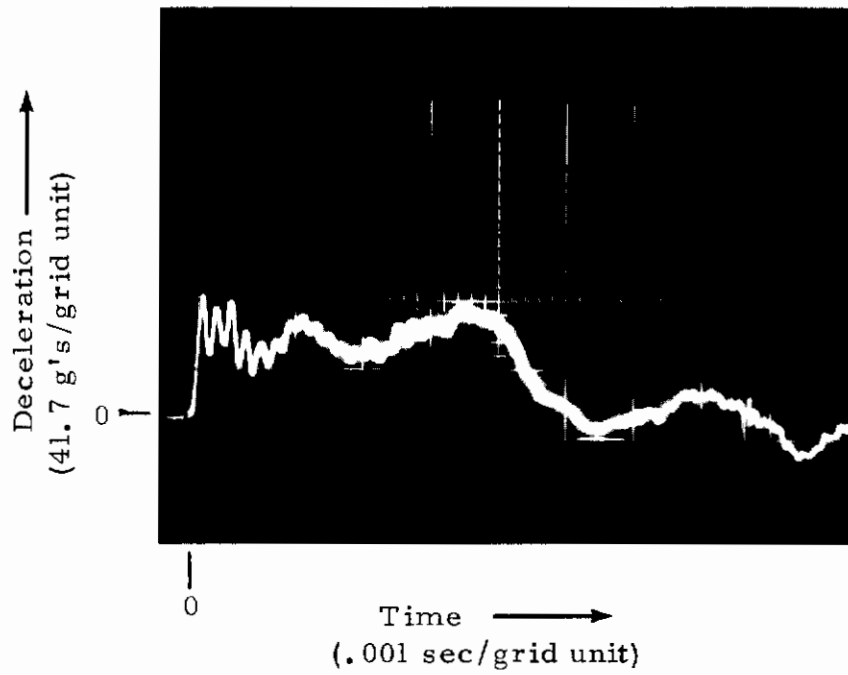


Figure 55. Deceleration Record - Test No. HV-6
($V_o = 225$ ft/sec, $h = .016$ in)

Contrails

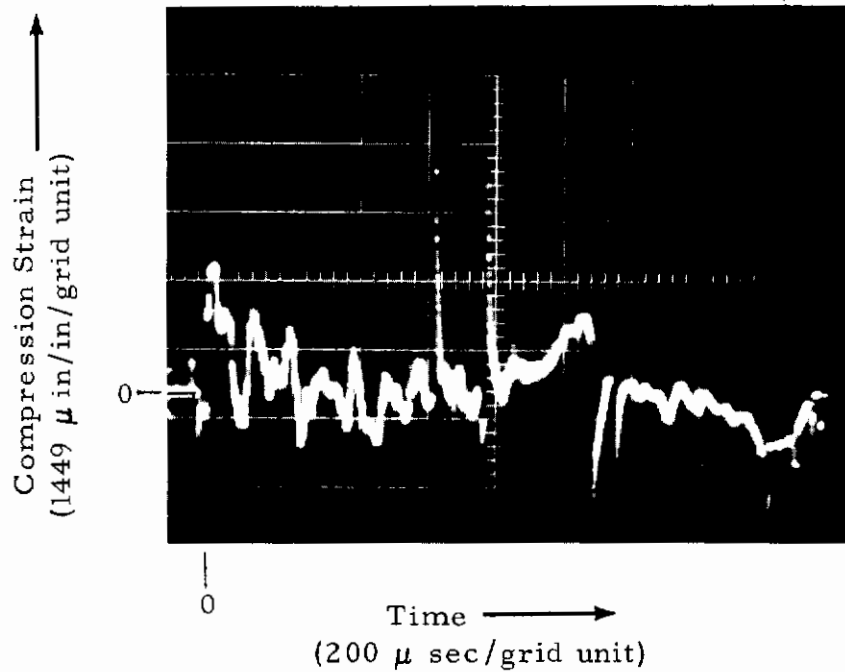
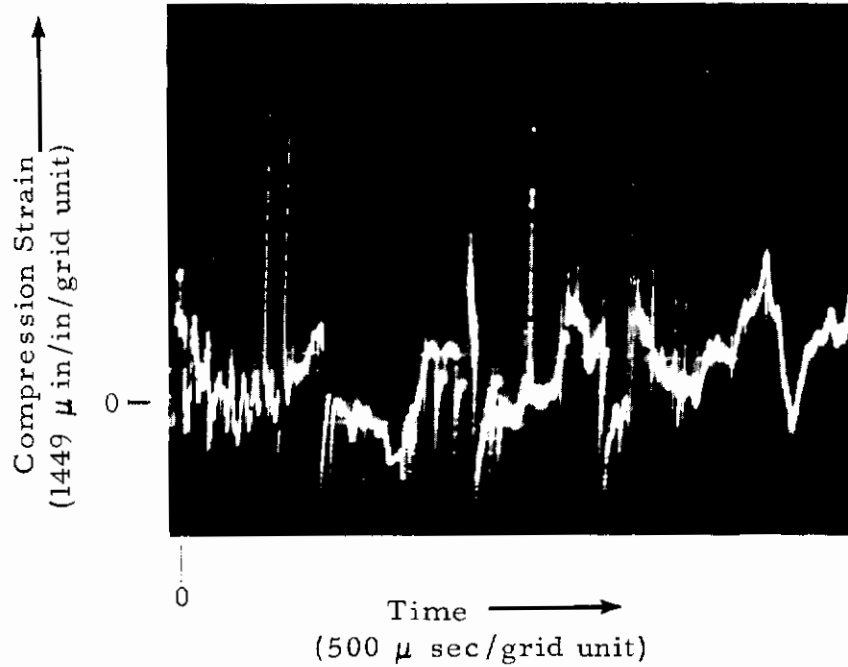


Figure 56. Strain Records, Middle Position - Test No. HV-7
($V_0 = 271$ ft/sec, $h = .016$)

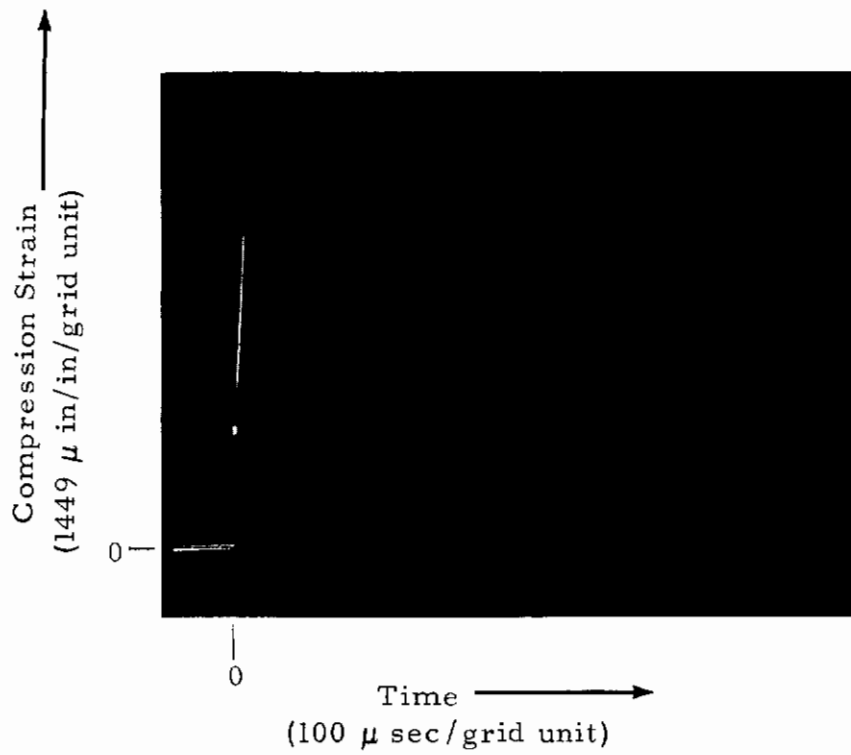


Figure 57. Strain Record, Forward Position - Test No. HV-7
($V_0 = 271$ ft/sec, $h = .016$ in)

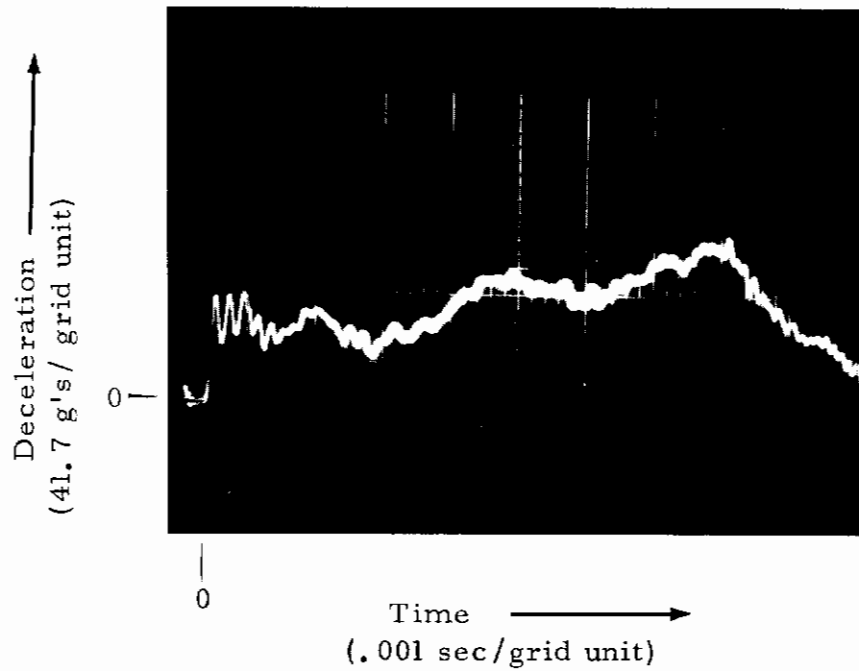


Figure 58. Deceleration Record - Test No. HV-7
($V_0 = 271$ ft/sec, $h = .016$ in)

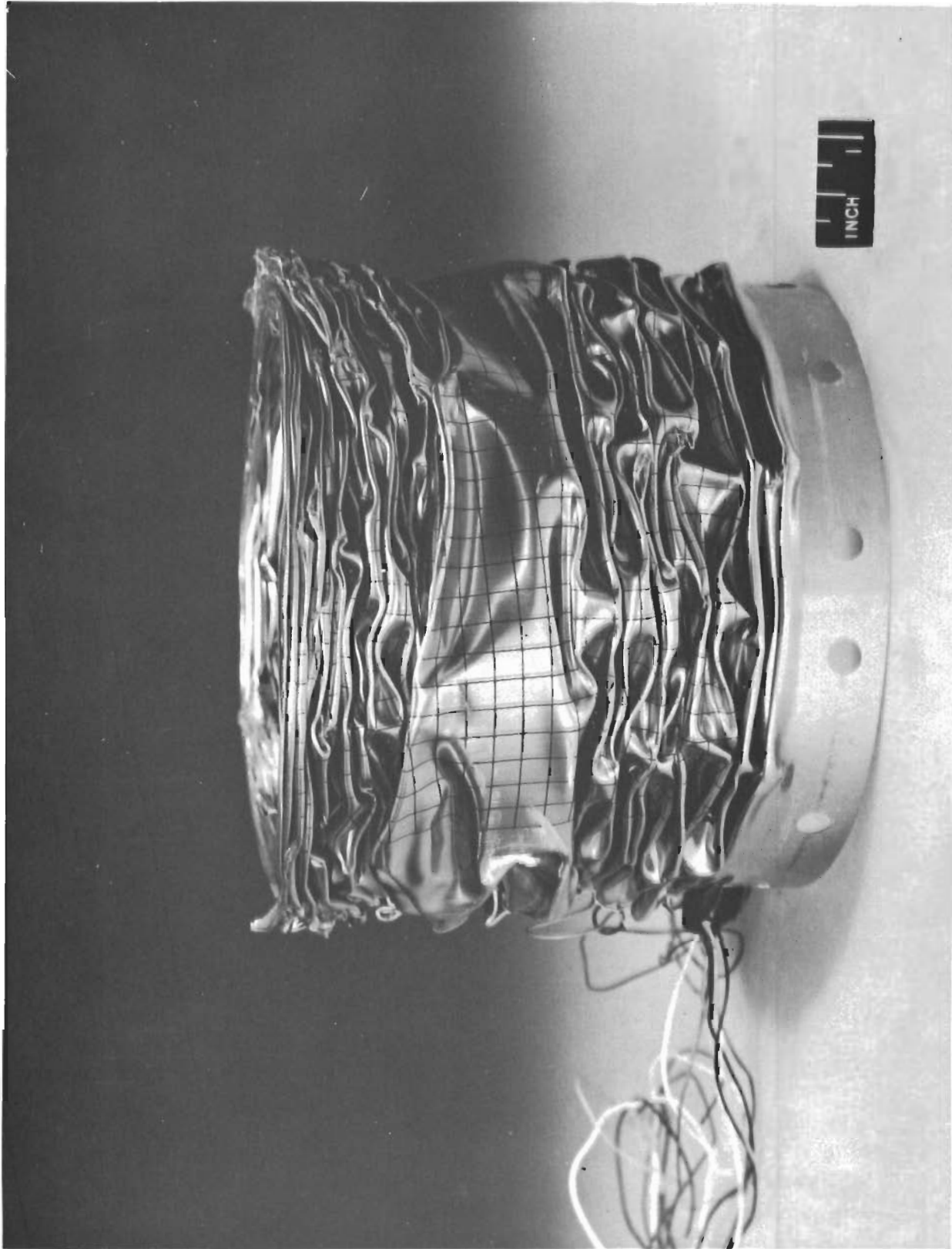


Figure 59. Specimen HV - 7 After Impact, $V_o = 271$ ft/sec, $h = .016$ in

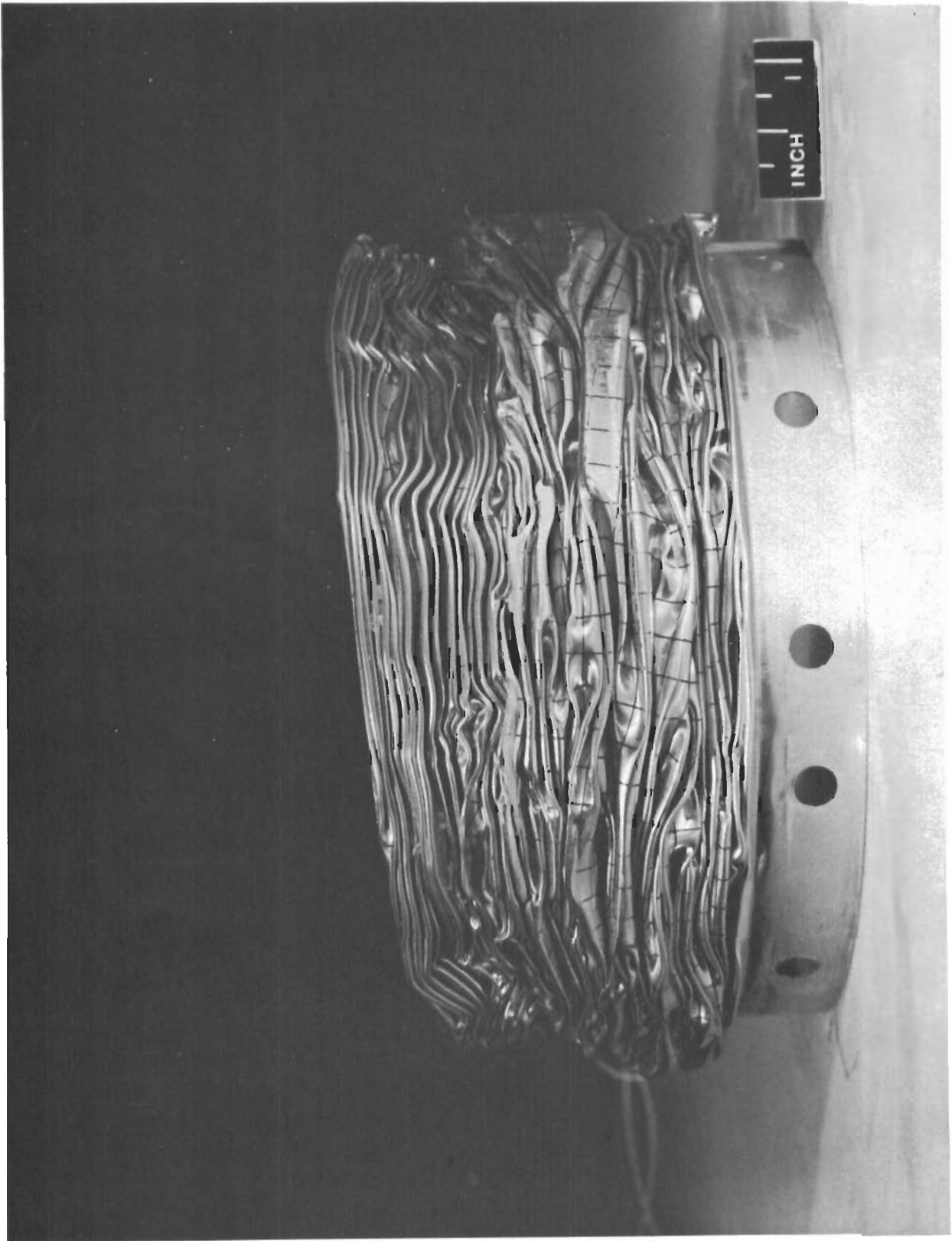


Figure 60. Specimen HV-8 After Impact, $V_0 = 392$ ft/sec, $h = .016$ in.

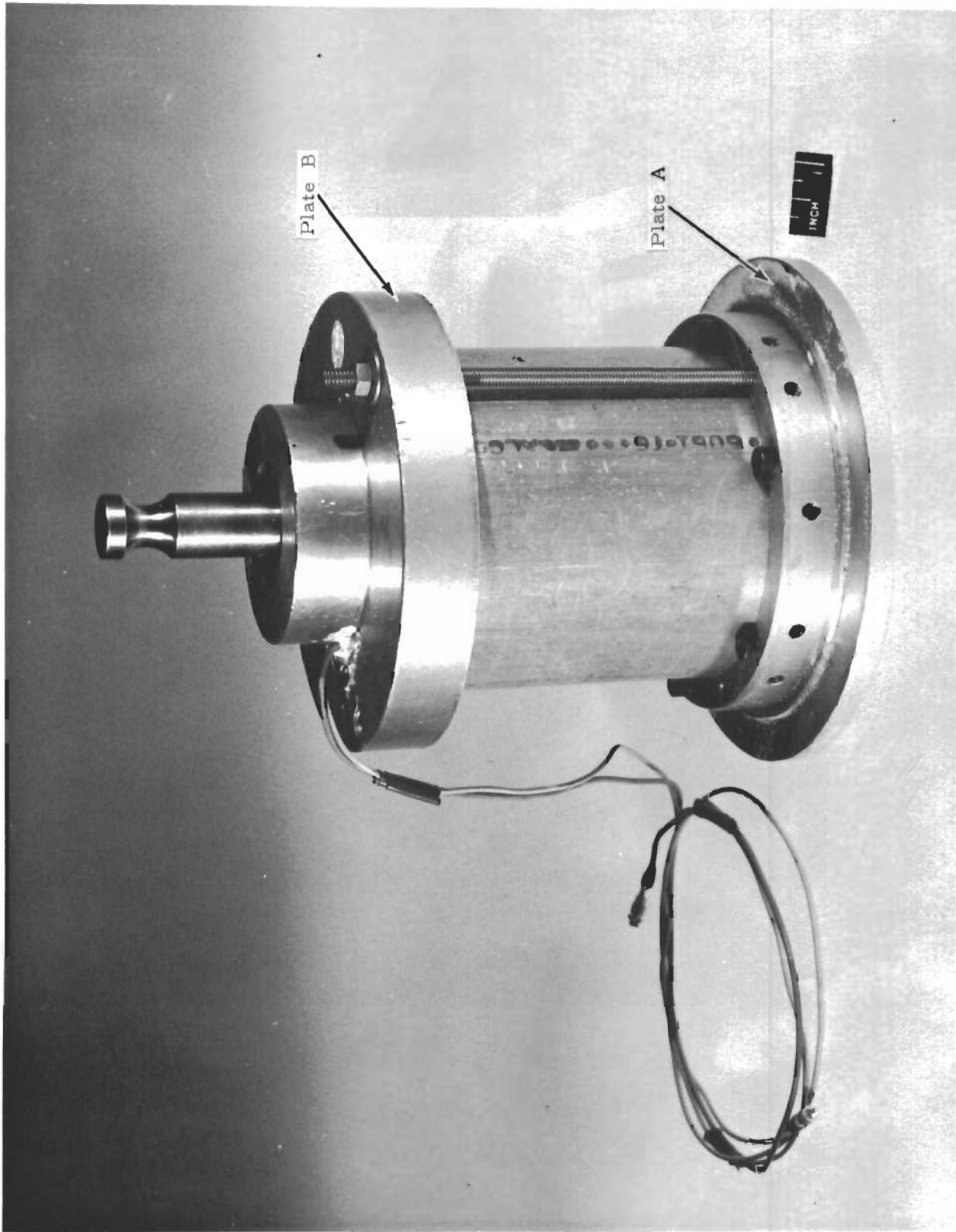


Figure 61. Rigid Body Structure for Non Rigid Impact Experiments

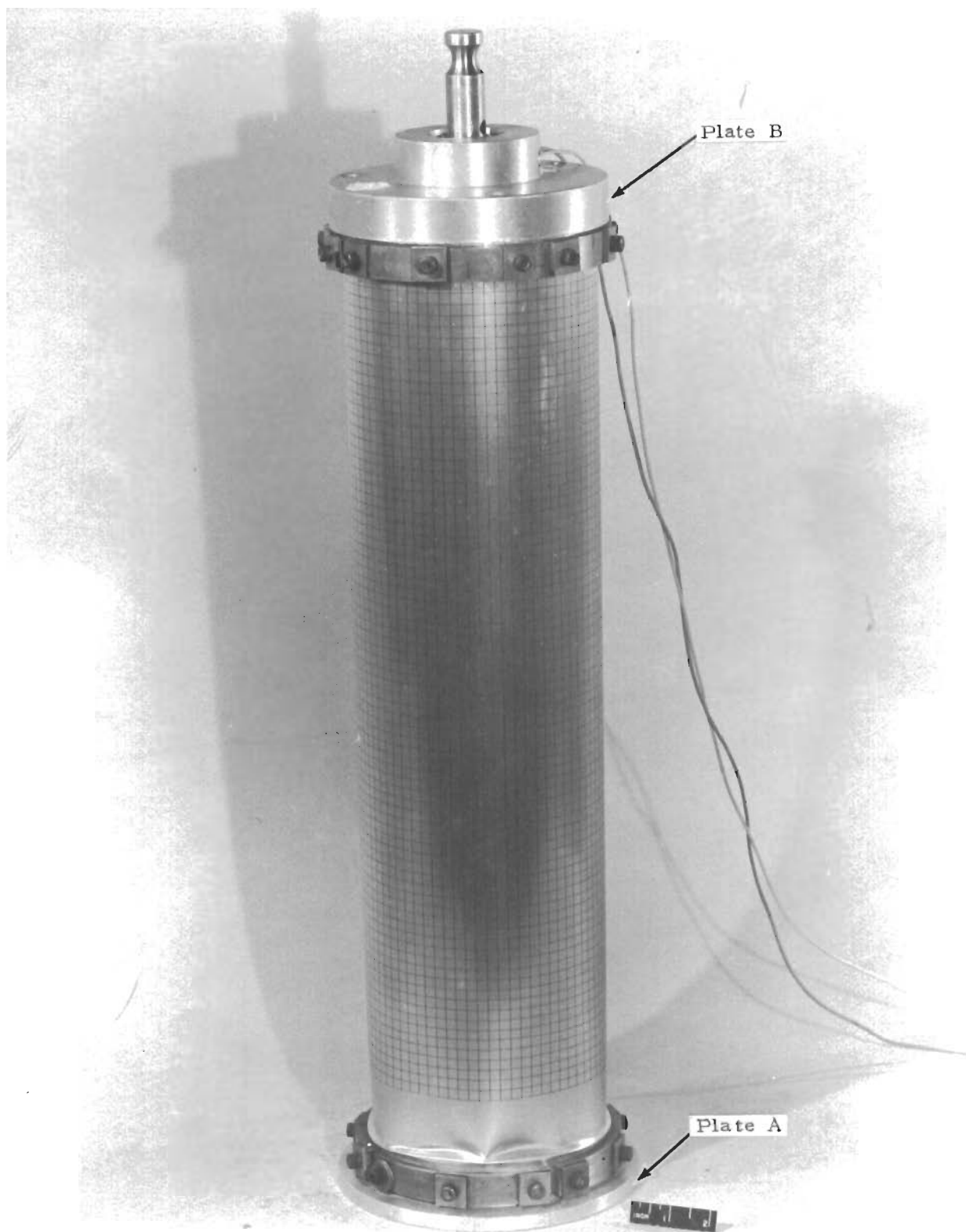


Figure 62. Shell Structure for Non Rigid Impact Experiments
(Showing Some Collapse at Plate A End)

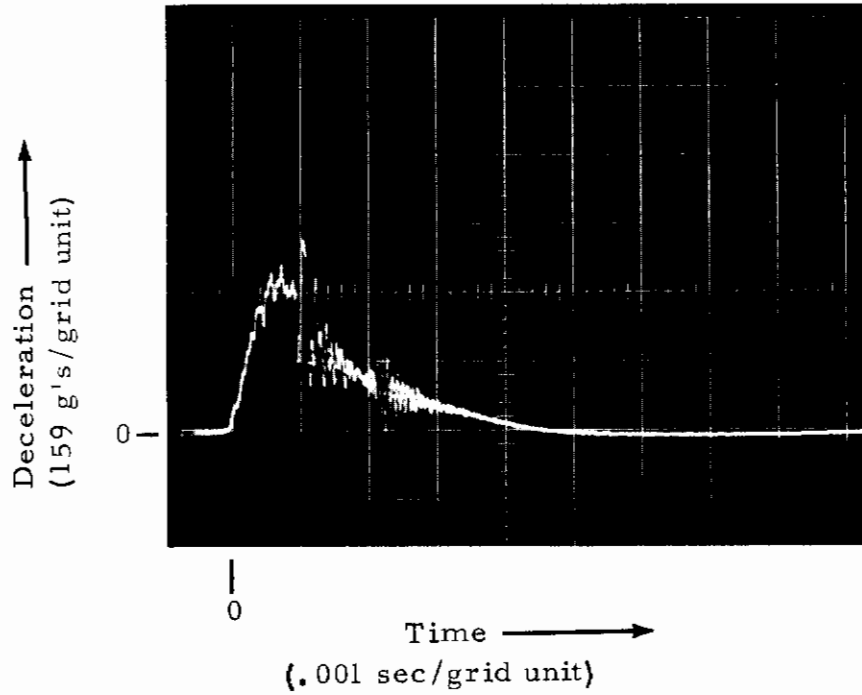


Figure 63. Force-Time Curve for the Rigid Body-Impact on Dry Sand, $V_0 = 23$ ft/sec - Test No. S-4, Plate B

Contrails

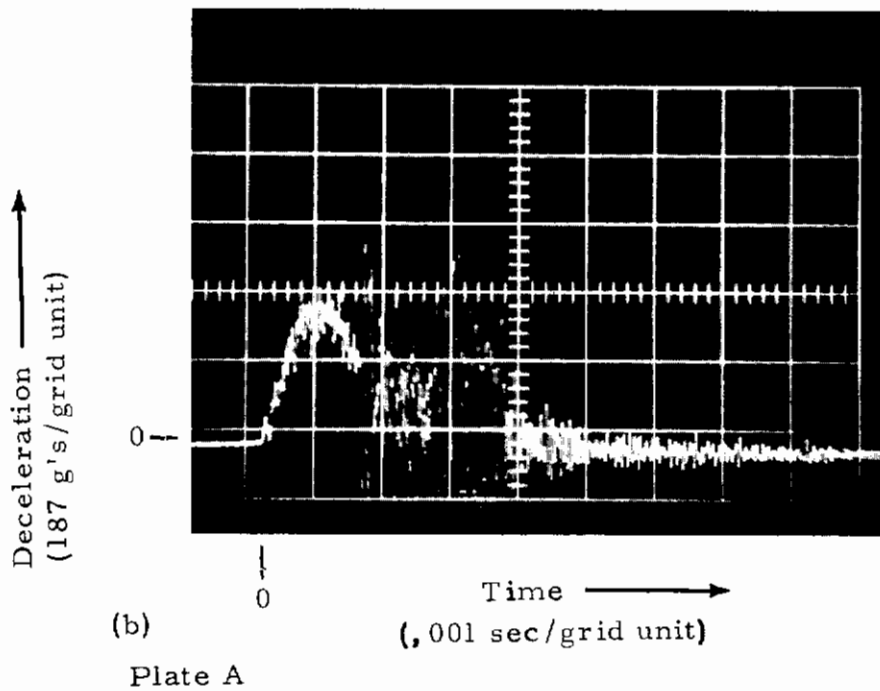
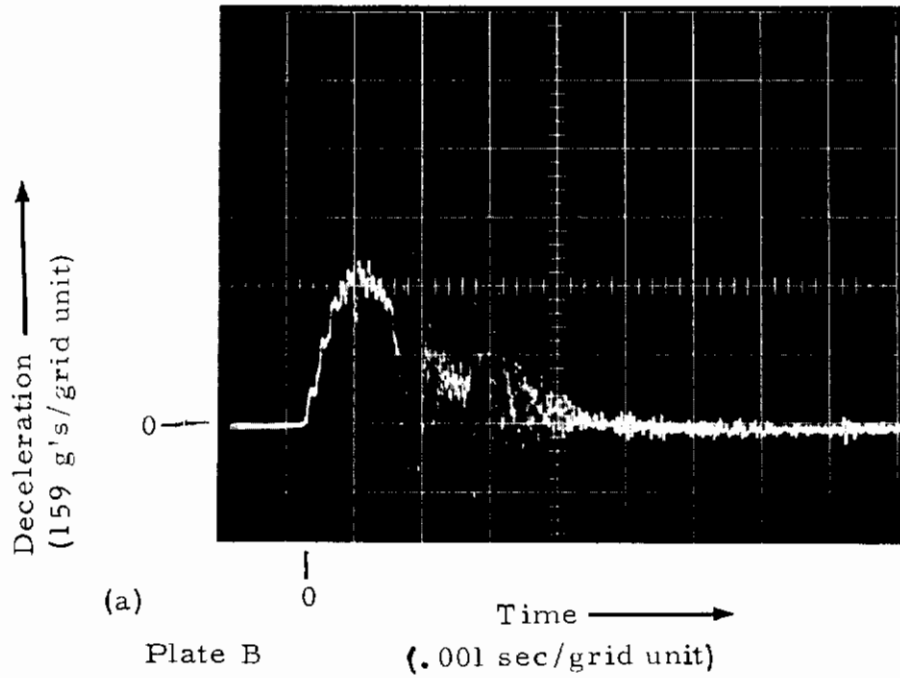
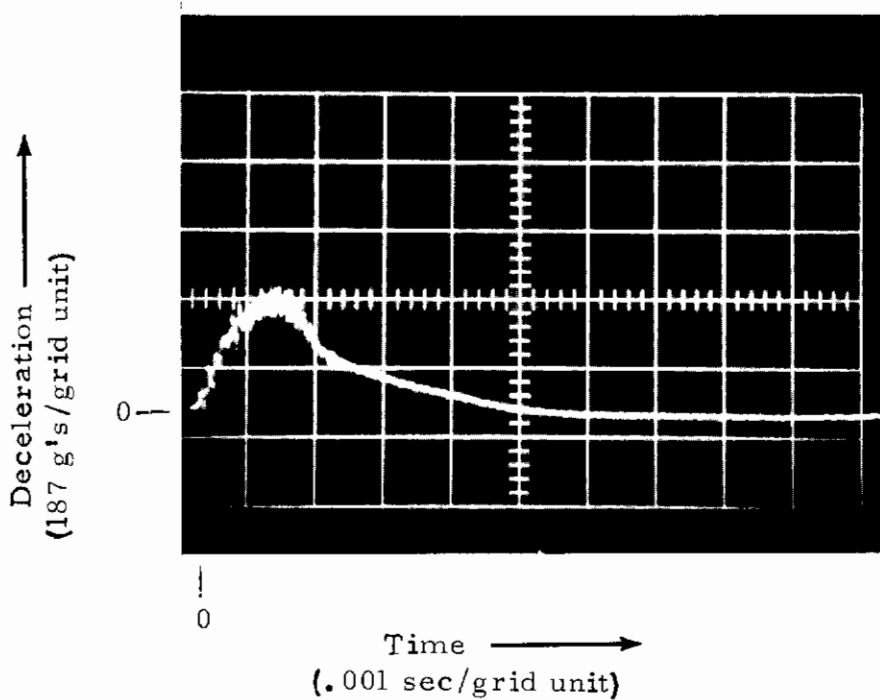
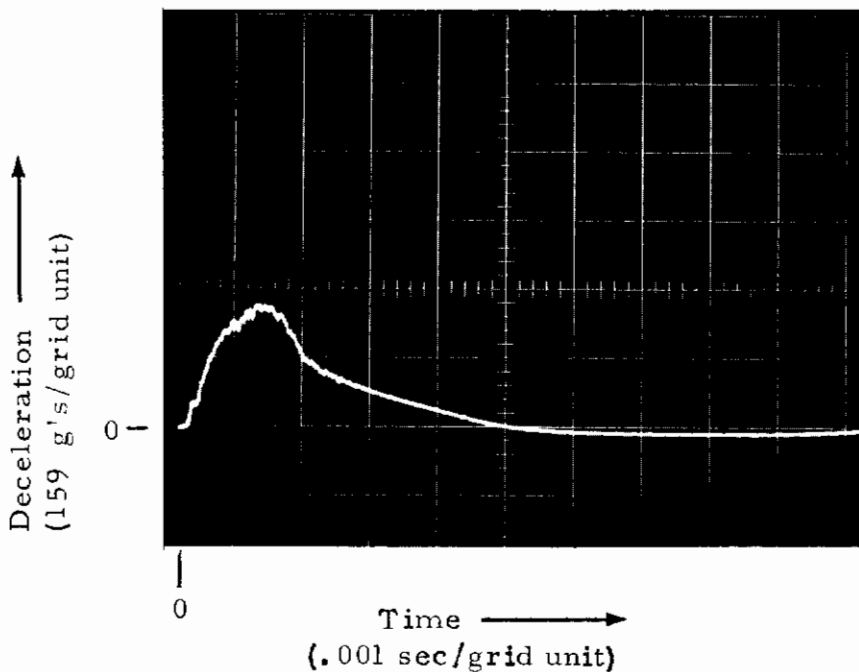


Figure 64. Force-Time Curves for the Rigid Body - Impact on Dry Sand, $V_0 = 23$ ft/sec - Test No. S-5

Contrails



(a) Plate (A)



(b) Plate (B)

Figure 65. Force-Time Curves for the Rigid Body - Impact on Dry Sand, $V_0 = 23$ ft/sec - Test No. S-5

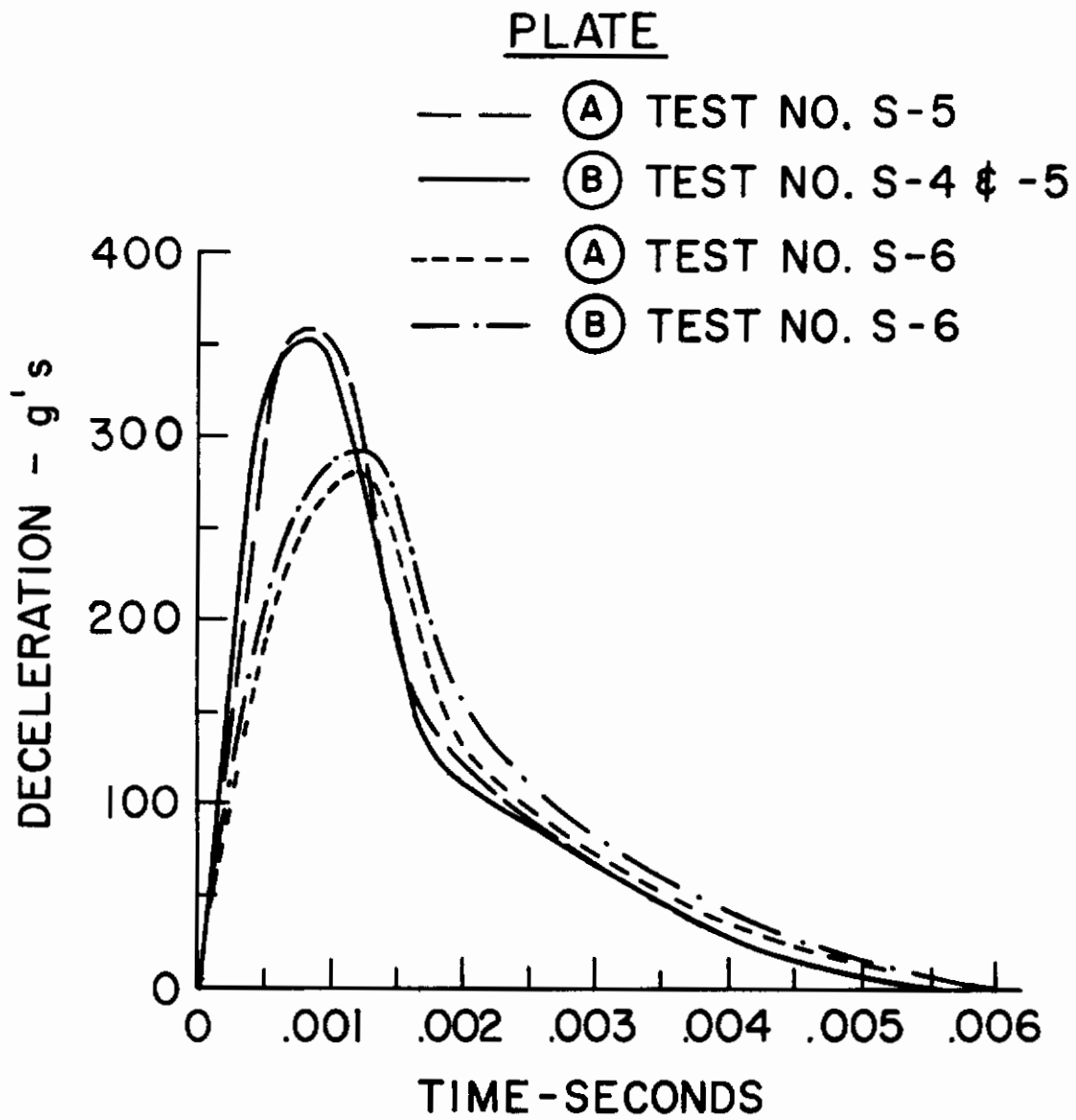
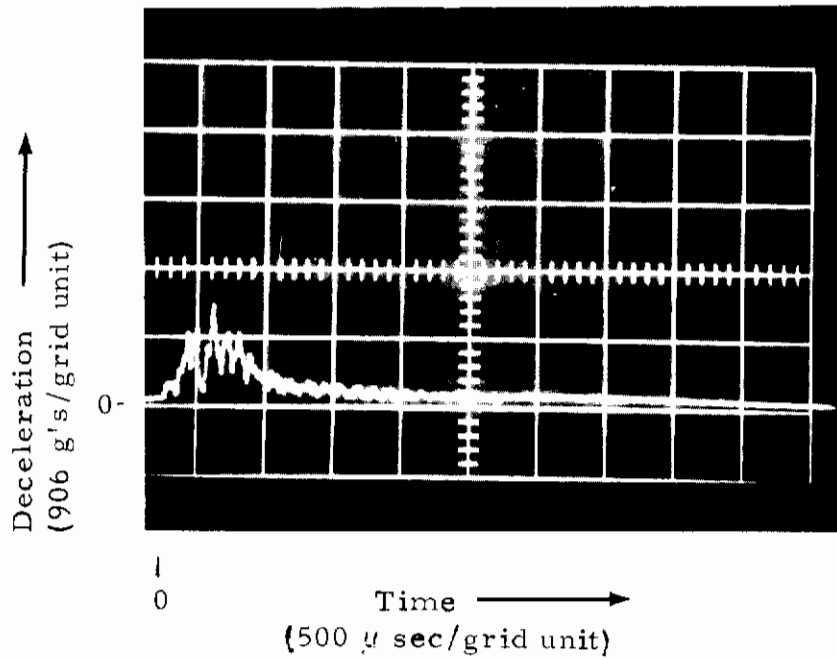
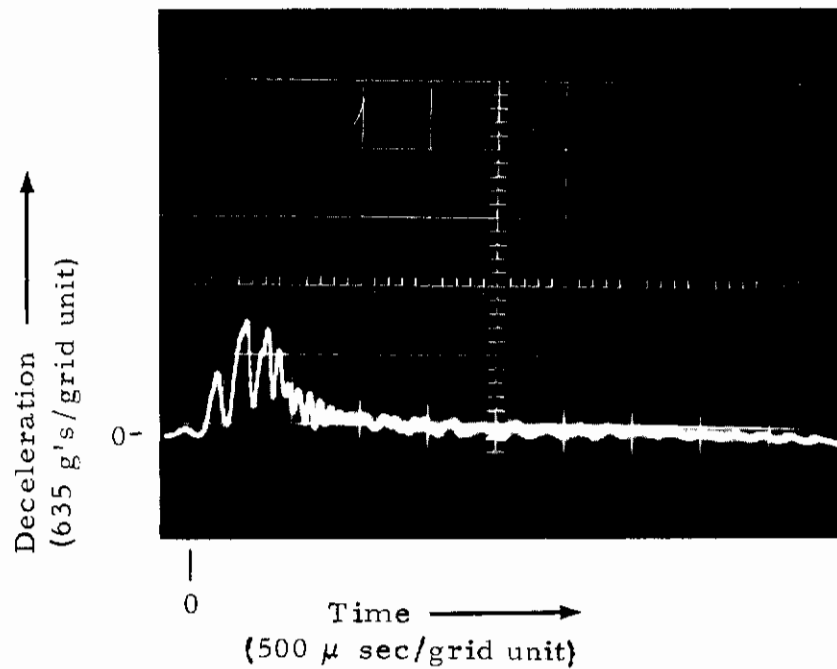


Figure 66. Comparison of Deceleration Measurements of a Rigid Body Impacting on Dry Sand, $V_0 = 23$ ft/sec

Contrails



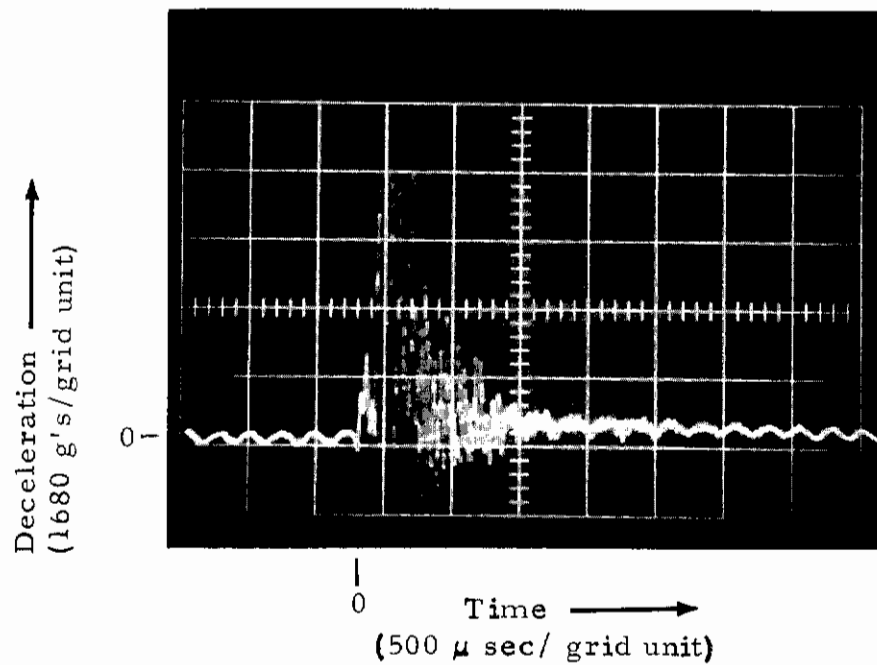
(a) Plate (A)



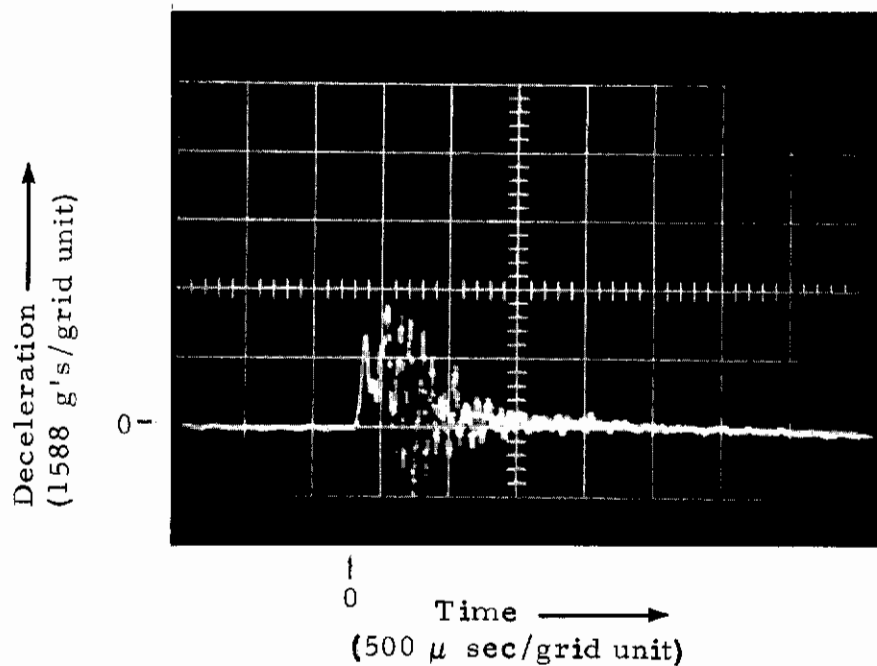
(b) Plate (B)

Figure 67. Force-Time Curves for the Rigid Body - Impact on Dry Sand,
 $V_0 = 33$ ft/sec

Contrails



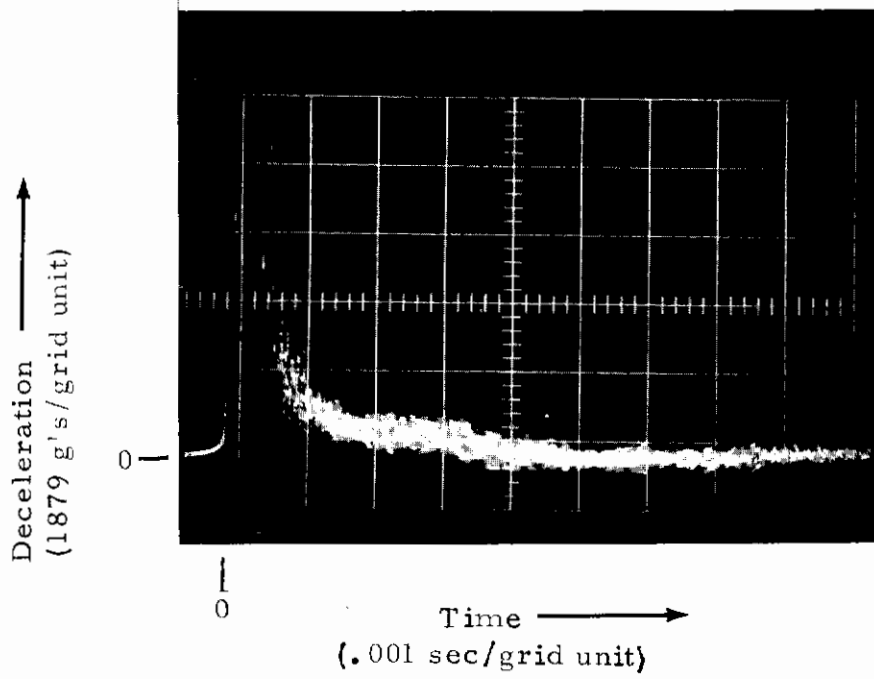
(a) Plate (A)



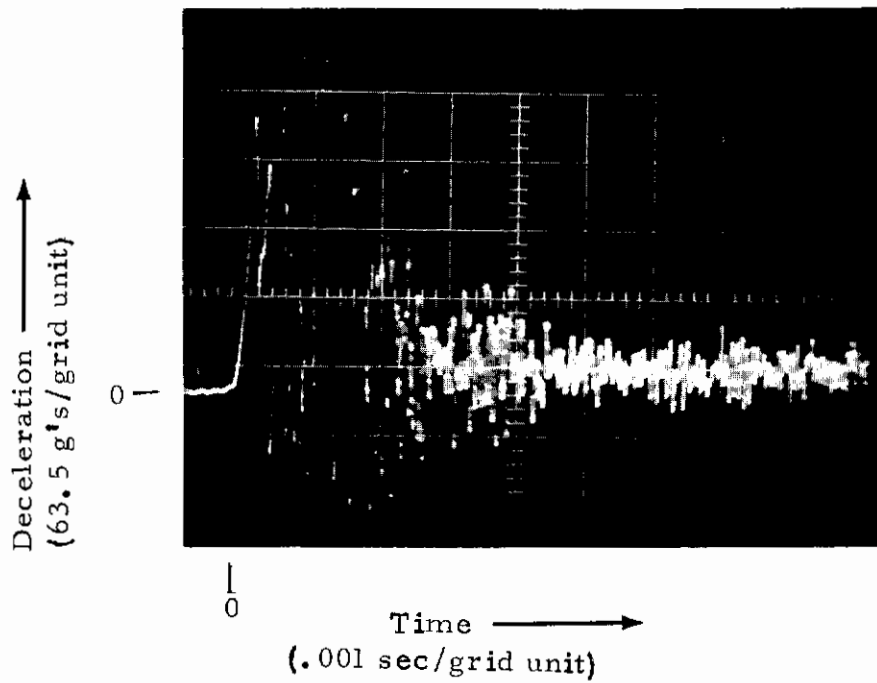
(b) Plate (B)

Figure 68. Force-Time Curves for the Rigid Body - Impact on Dry Sand, $V_0 = 43$ ft/sec

Contrails



(a) Plate (A)



(b) Plate (B)

Figure 69. Force-Time Curves for the Shell Structure - Impact on Dry Sand, $V_0 = 23$ ft/sec

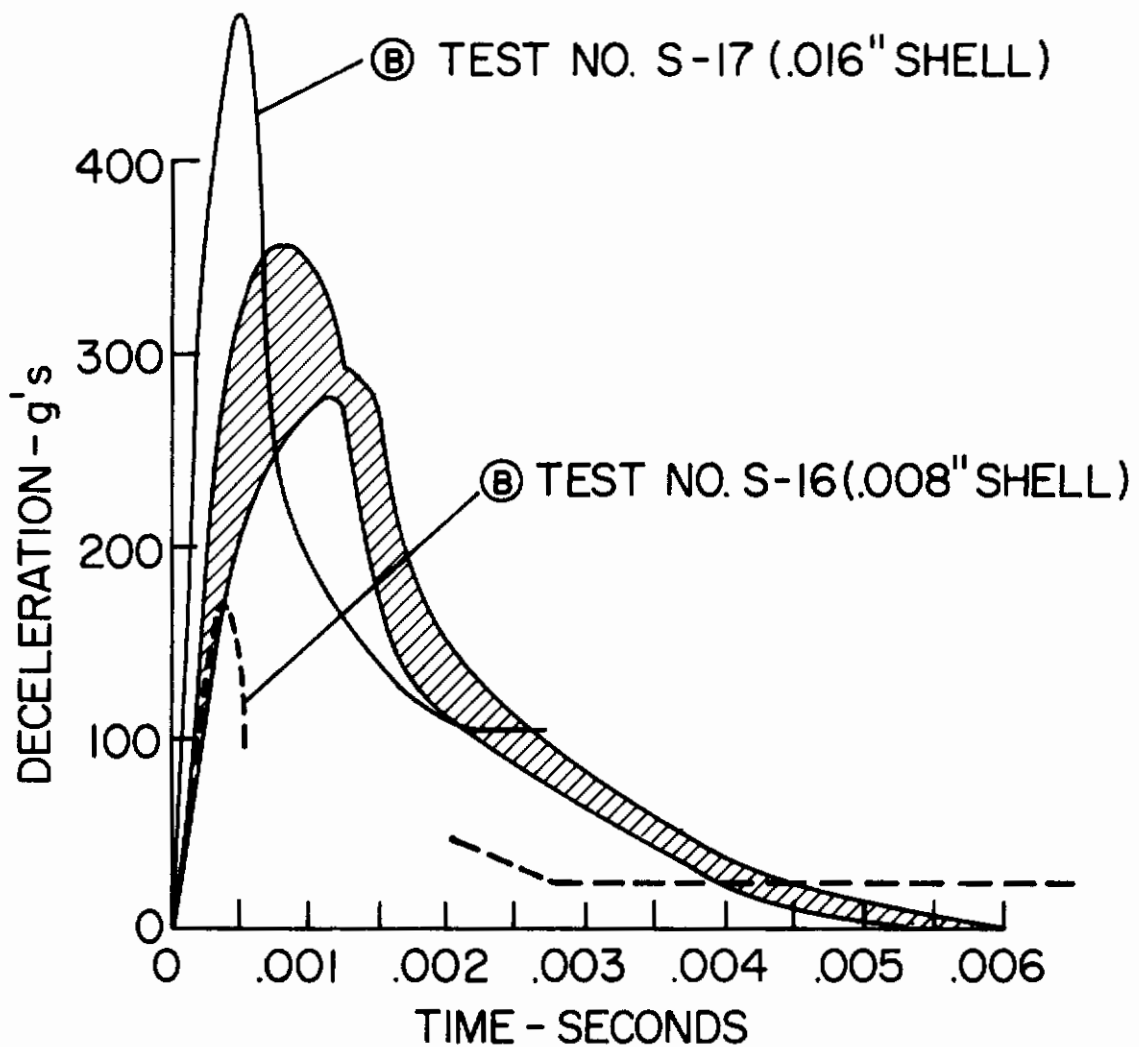


Figure 70. Effect of Shell Buckling on the Deceleration of Plate (B) - Showing a Comparison with the Deceleration of Plate (A) and (B) of the Rigid Body - Vertical Impact into Dry Sand $V_0 = 23$ ft/sec

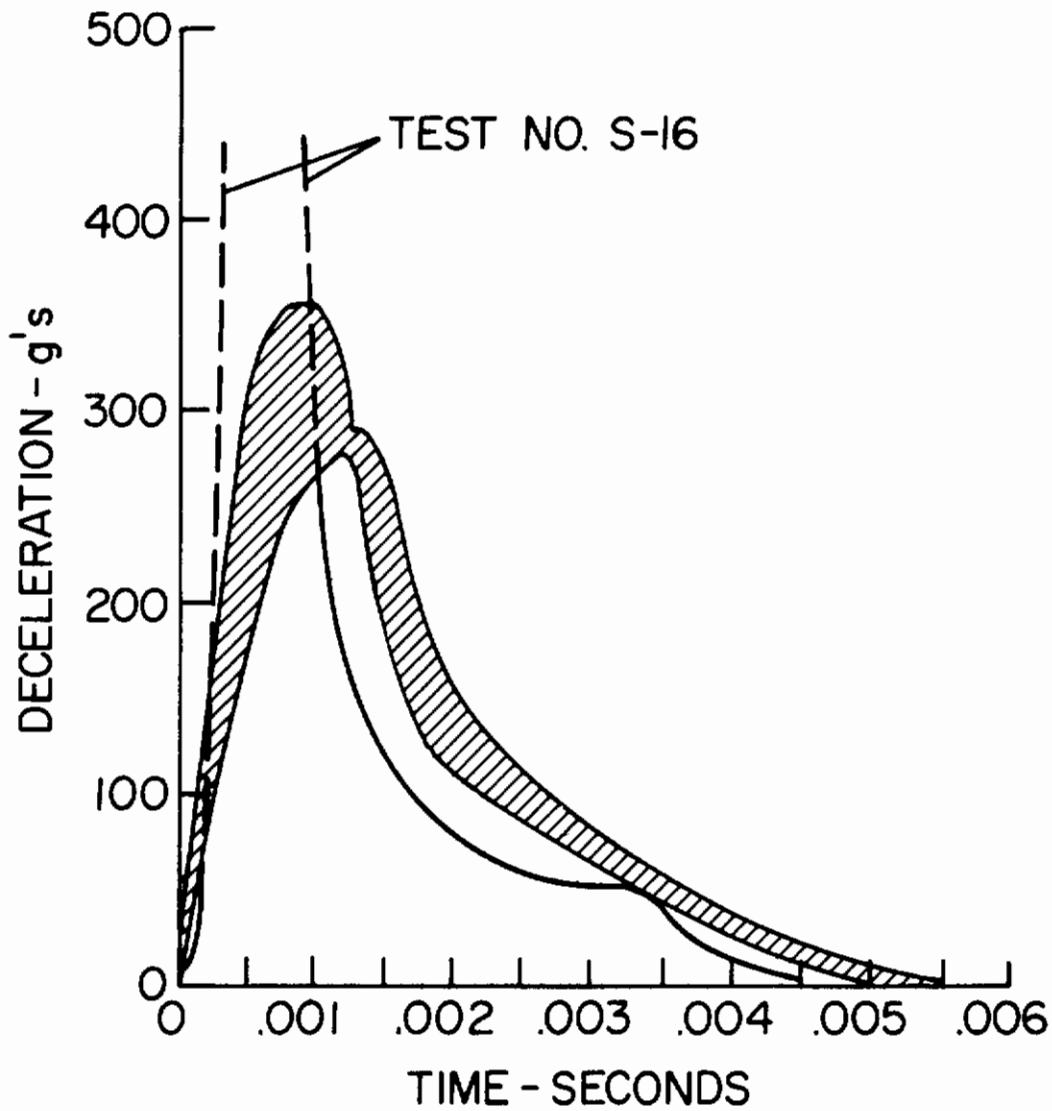


Figure 71. Effect of Shell Buckling on the Deceleration of Plate (A) - $V_0 = 23$ ft/sec

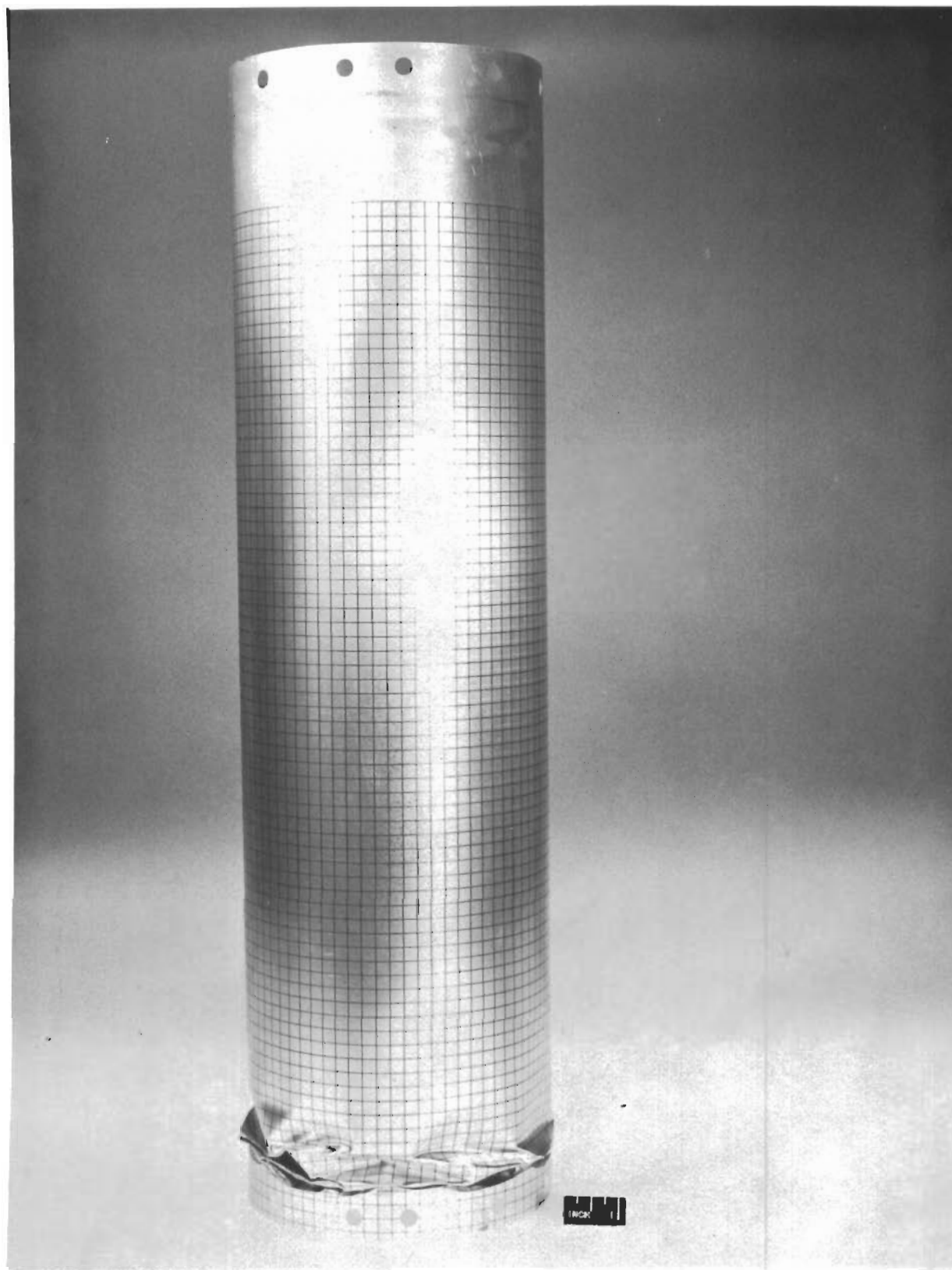


Figure 72. Specimen S-16 After Impact into Dry Sand, $V_0 = 23$ ft/sec,
 $h = .008$ in, Impacted End Down

Contrails

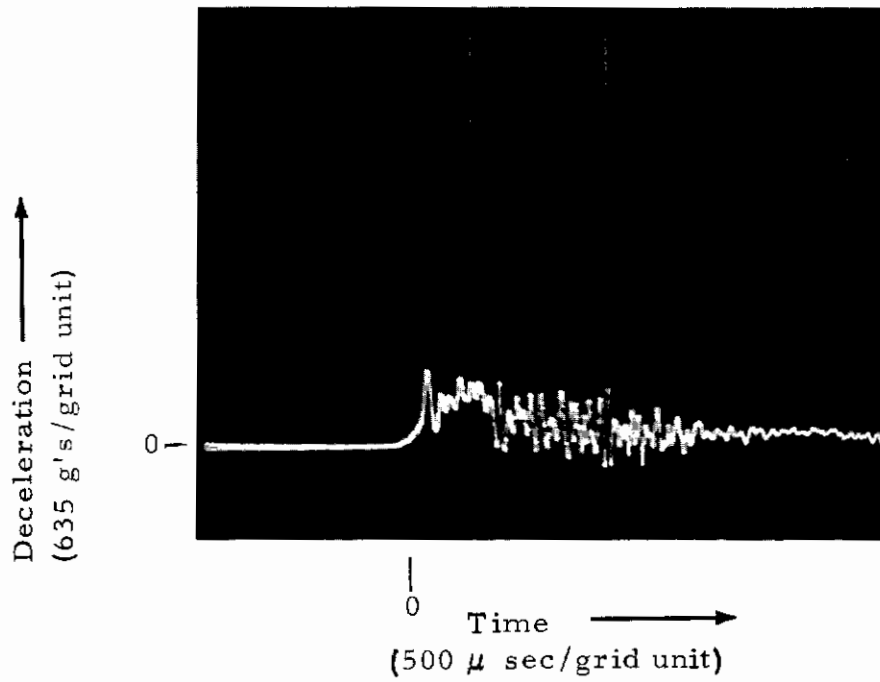
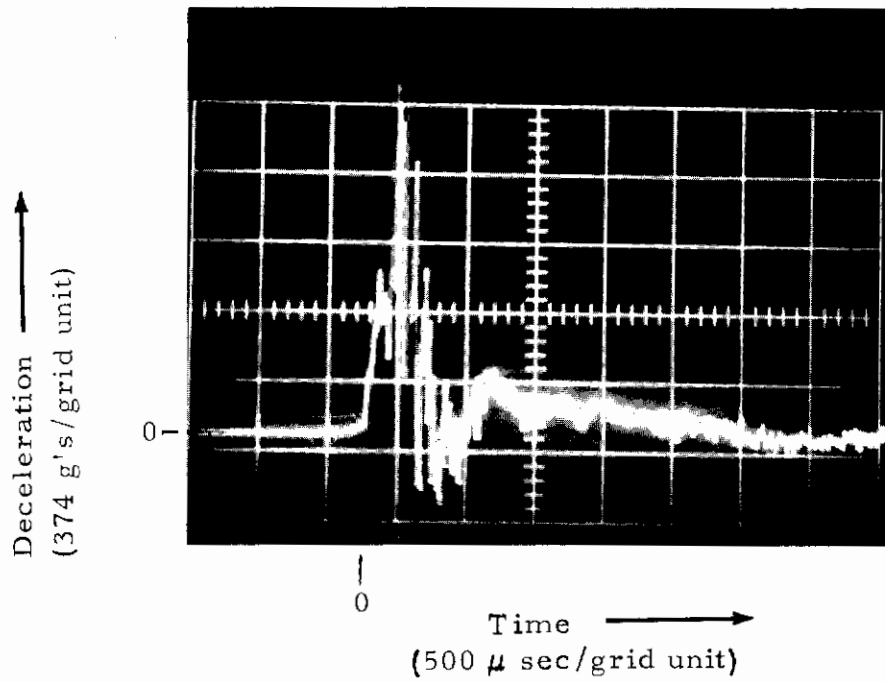
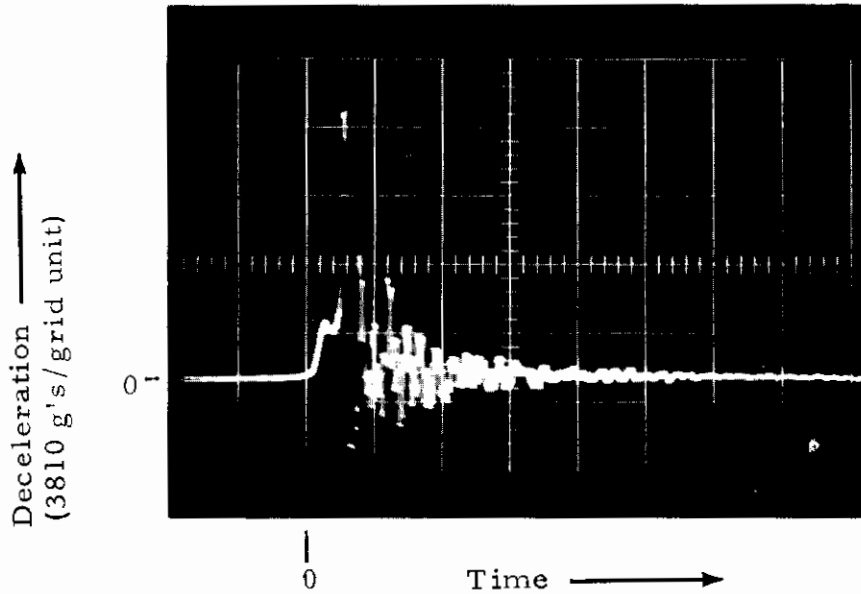
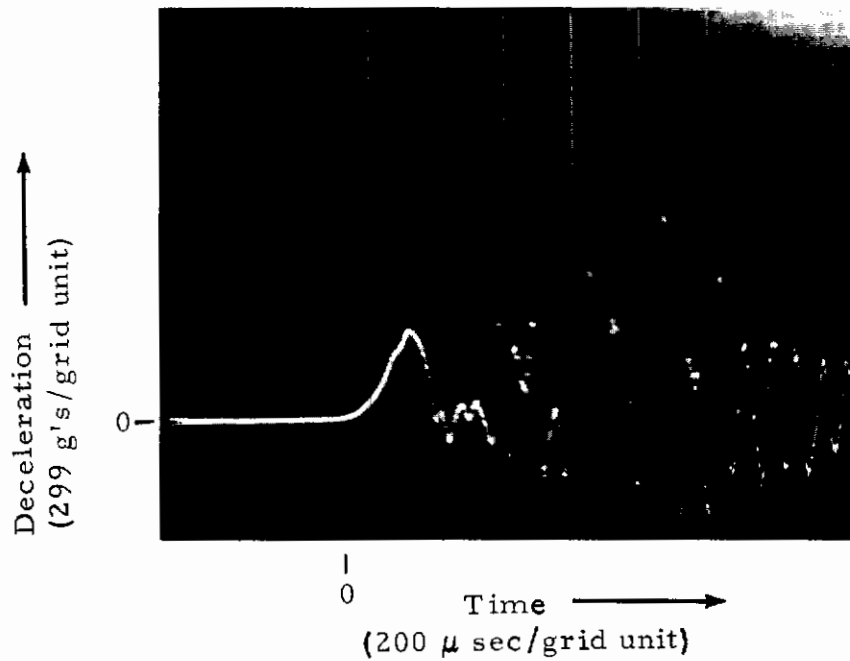


Figure 73. Deceleration Records - Test S-17
($h = .016$ in, $V_0 = 23$ ft/sec)

Contrails



(a) Plate (A)



(b) Plate (B)

Figure 74. Deceleration Records - Test S-19
($h = .008$ in, $V_0 = 33$ ft/sec)

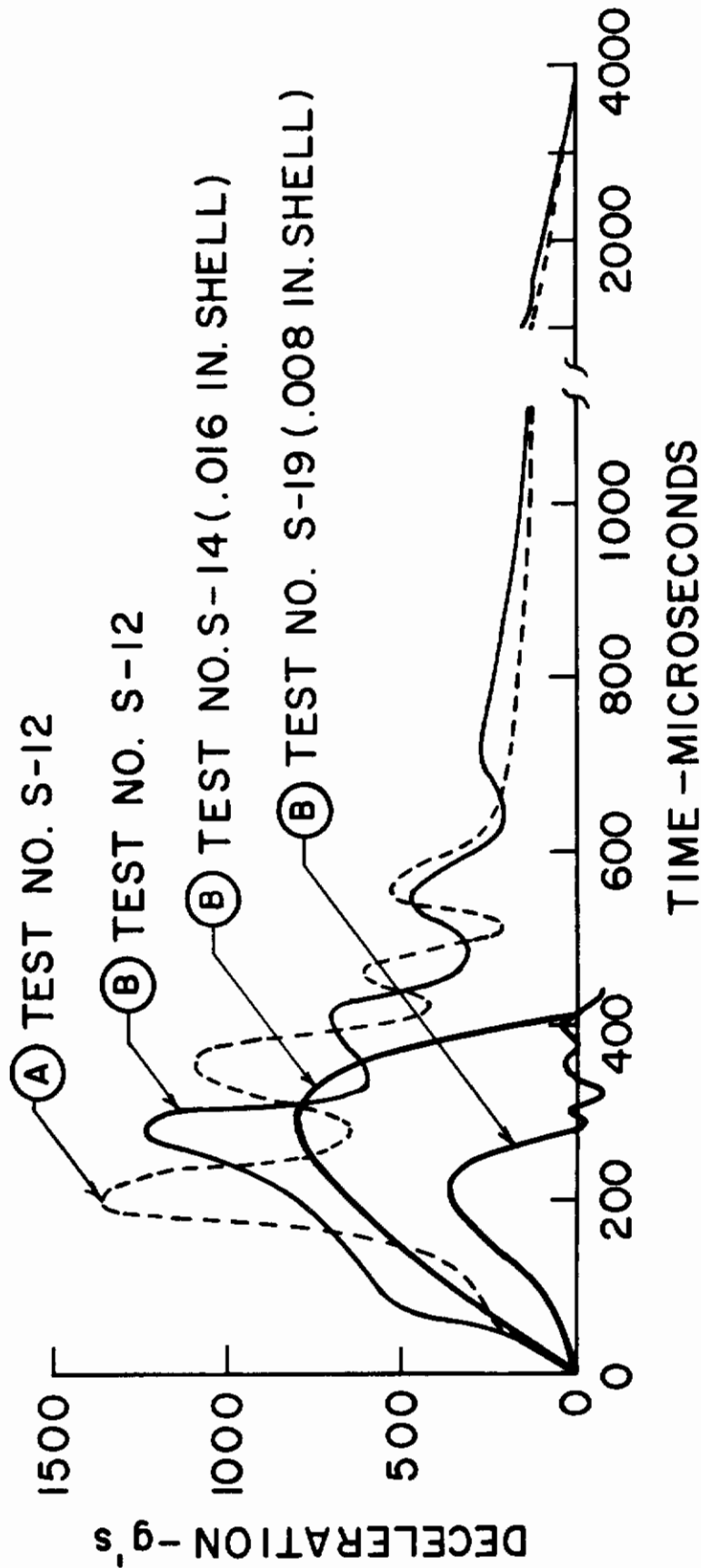


Figure 75. Effect of Shell Buckling on the Deceleration of Plate (B) - Showing a Comparison with the Deceleration of Plates (A) and (B) of the Rigid Body - Vertical Impact into Dry Sand
 $V_0 = 33 \text{ ft/sec}$

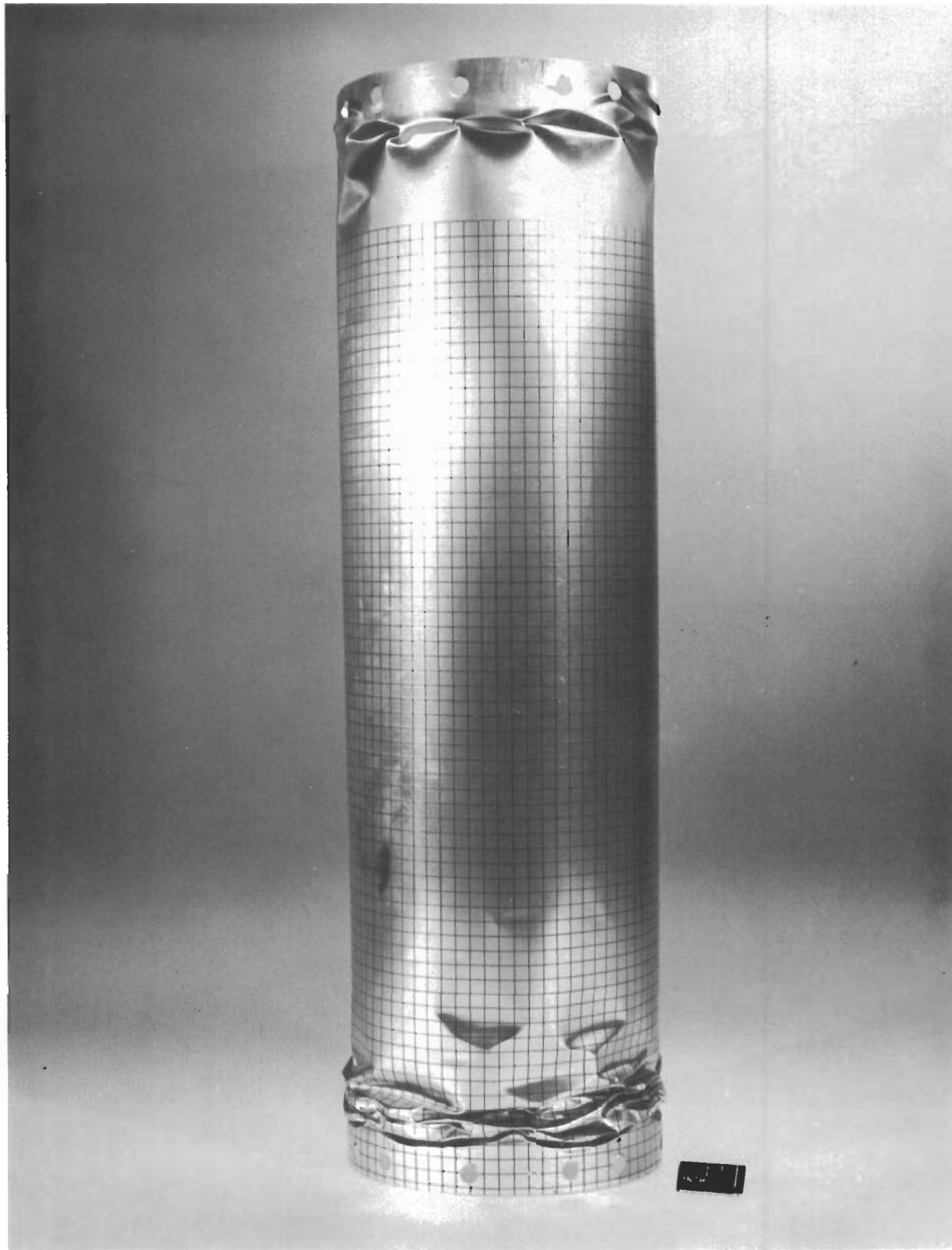


Figure 76. Specimen S-19 After Impact into Dry Sand, $V_o = 33$ ft/sec.
 $h = .008$ in, Impacted End Down

Contrails

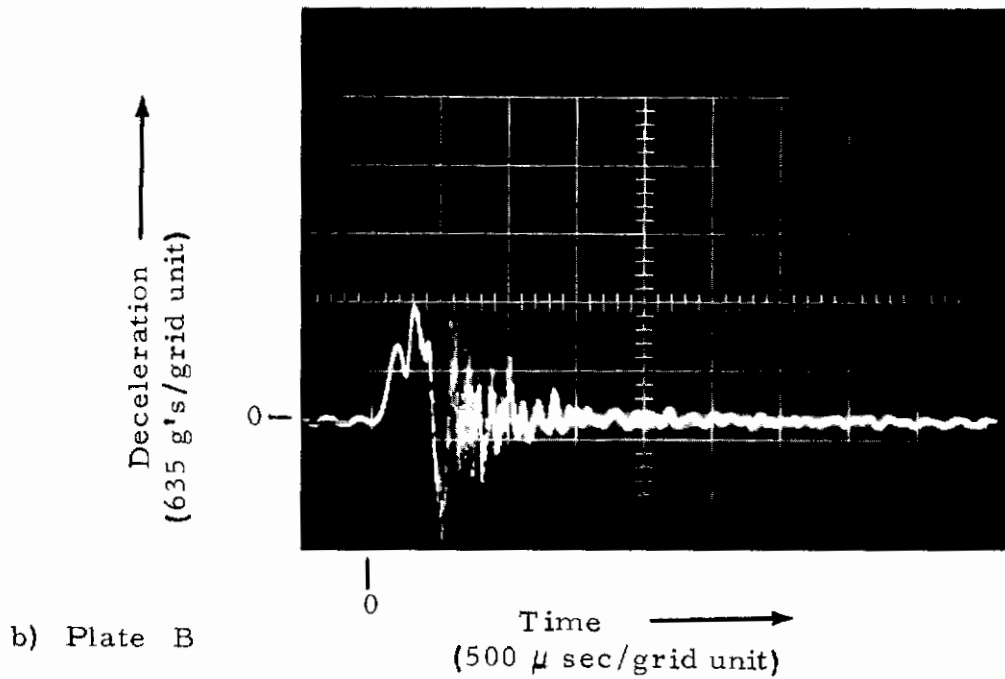
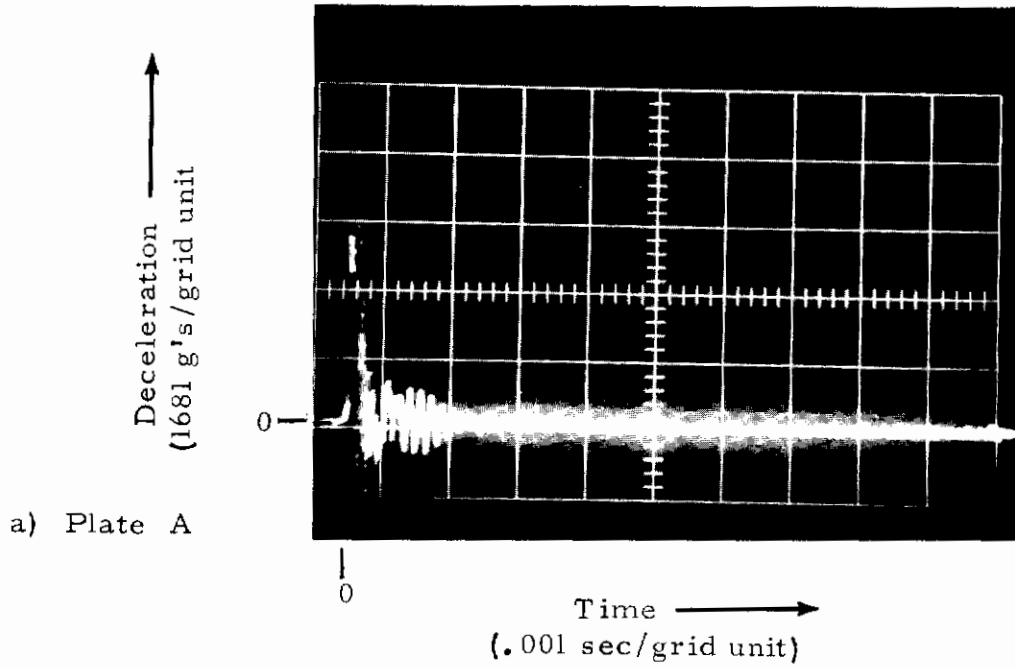


Figure 77. Deceleration Records - Test S-14
($h = .016$ in, $V_0 = 33$ ft/sec)

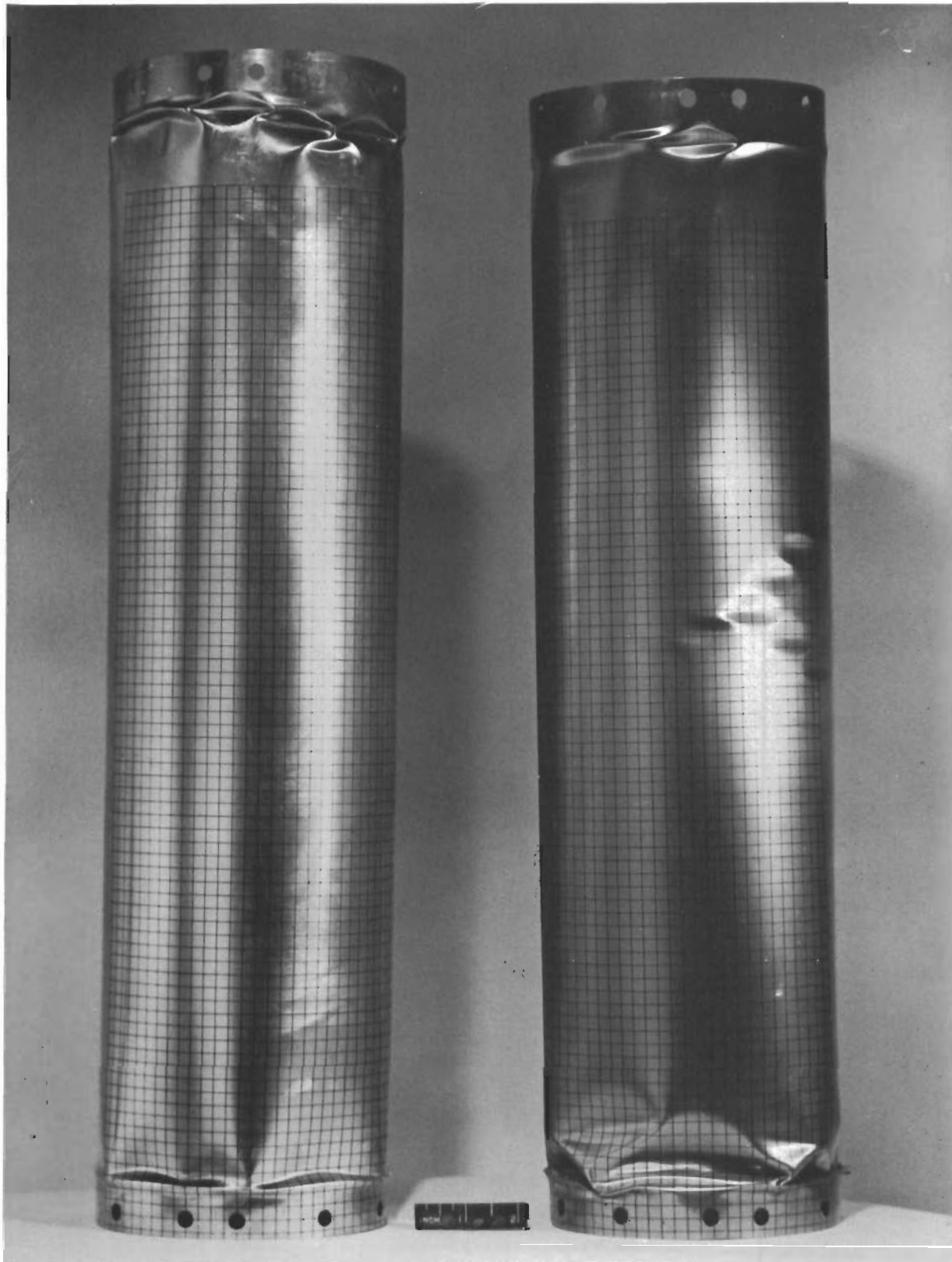
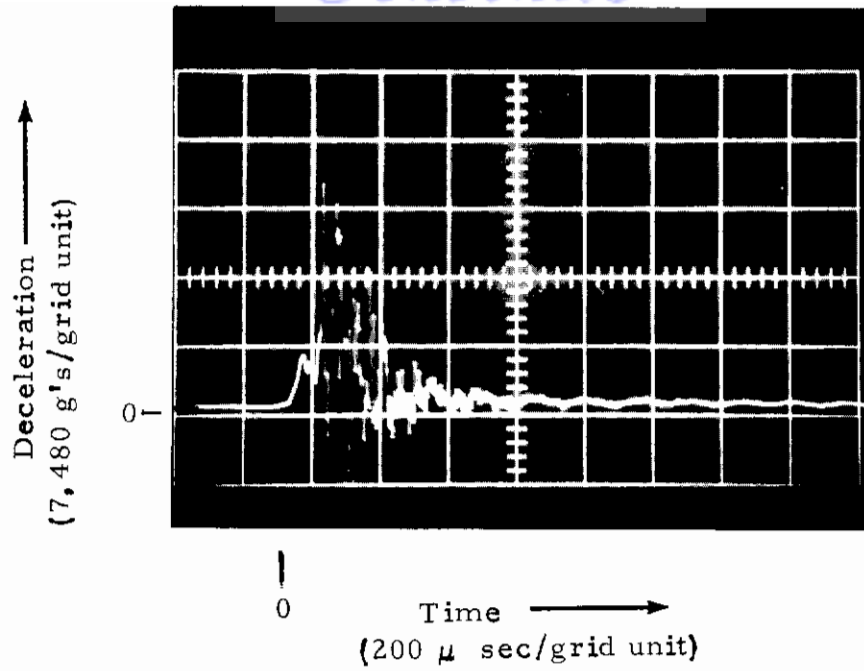
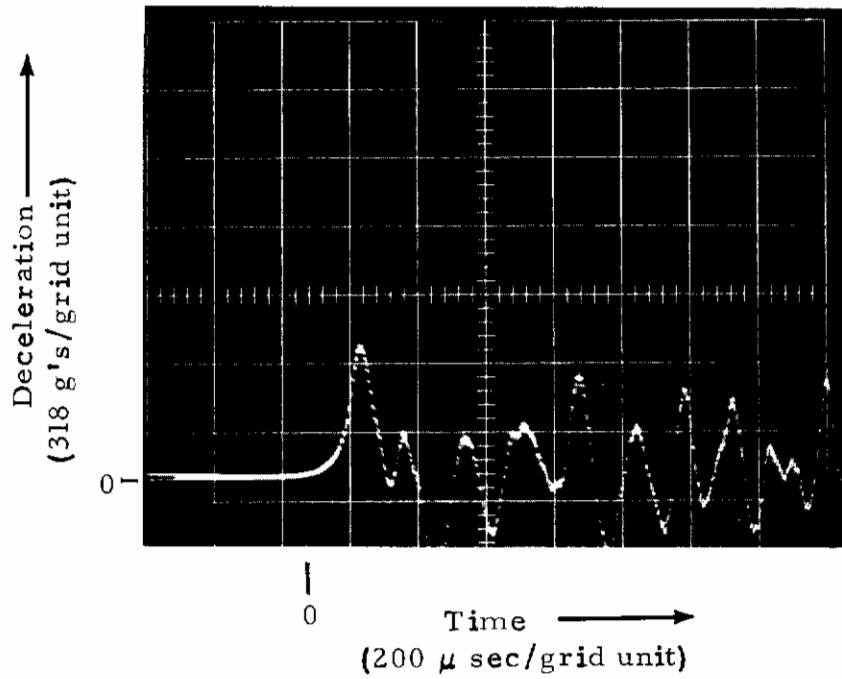


Figure 78. Specimens S-14 (Left) and S-13 (Right) After Impact into Dry Sand, Left- $V_0 = 33$ ft/sec, Right- $V_0 = 43$ ft/sec, $h = .016$ in.

Contrails



(a) Plate (A)



(b) Plate (B)

Figure 79. Deceleration Records - Test No. S-15
($h = .008$ in, $V_0 = 43$ ft/sec)

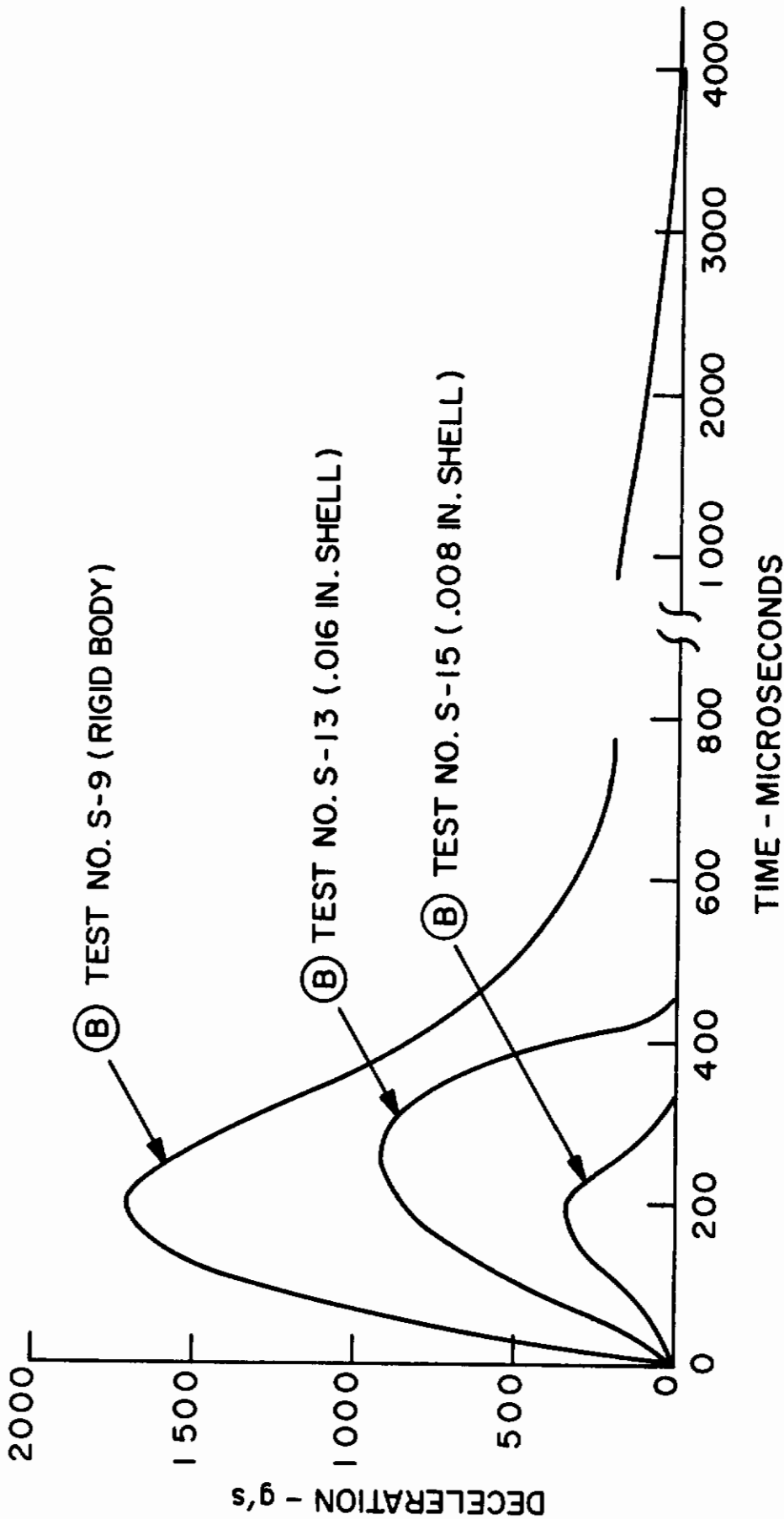


Figure 80. Effect of Shell Buckling on the Deceleration of Plate (B) Showing a Comparison with the Deceleration of Plate (B) of the Rigid Body - Vertical Impact into Sand, $V_0 = 43 \text{ ft/sec}$

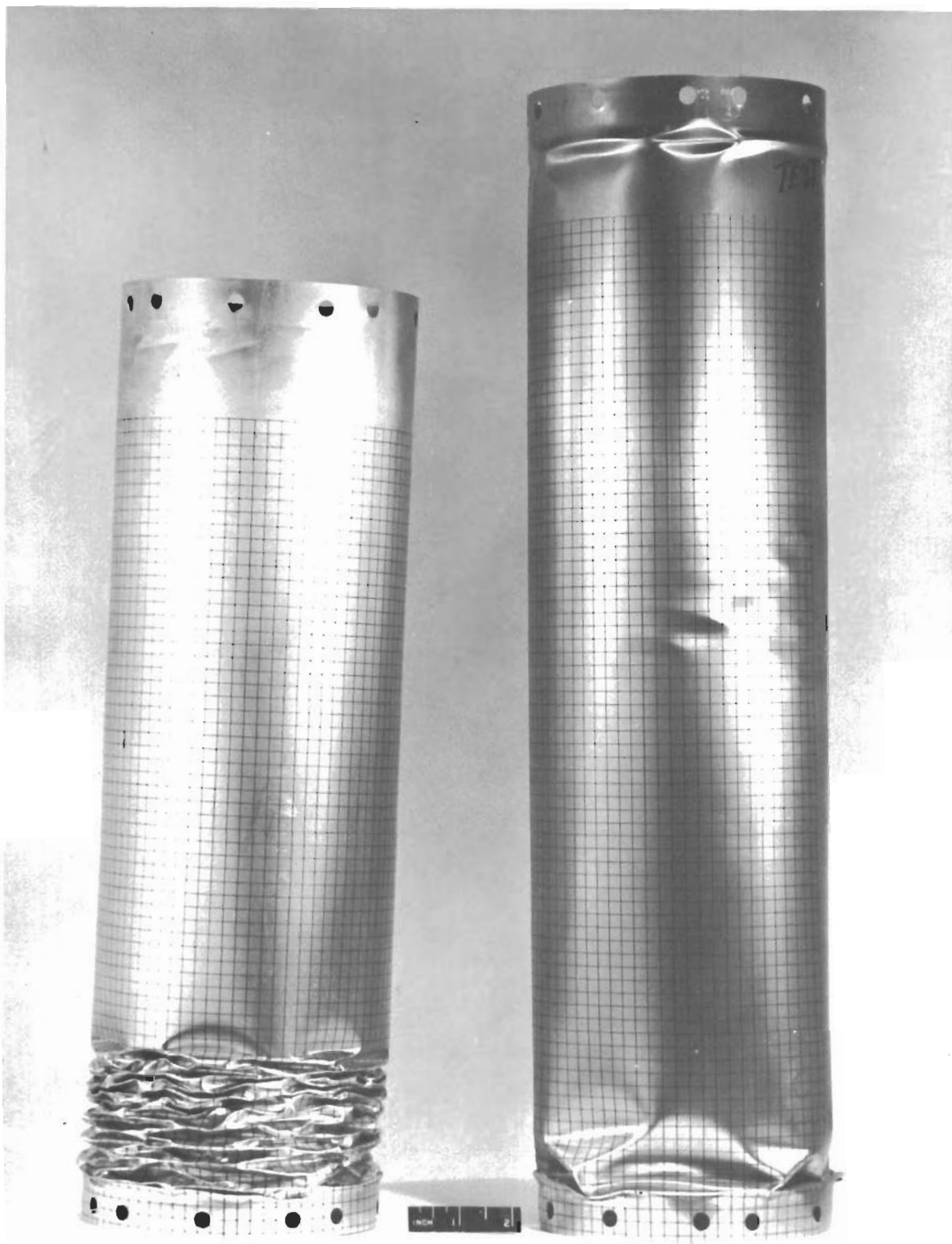


Figure 81. Specimens S-15 (Left, $h = .008$ in) and S-13 (Right, $h = .016$ in) After Impact into Dry Sand, $V_0 = 43$ ft/sec.

Contrails

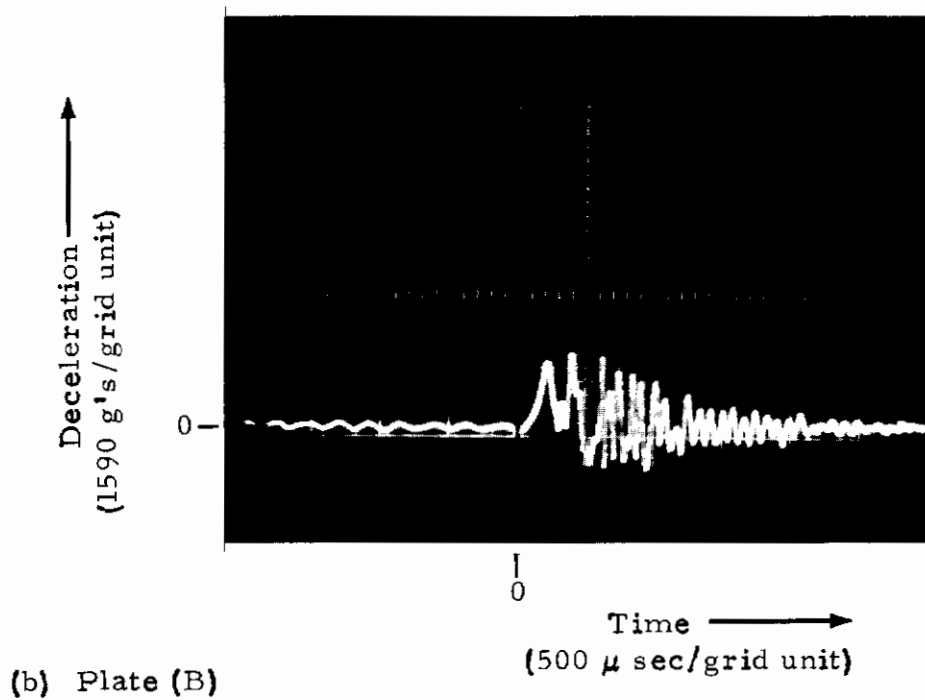
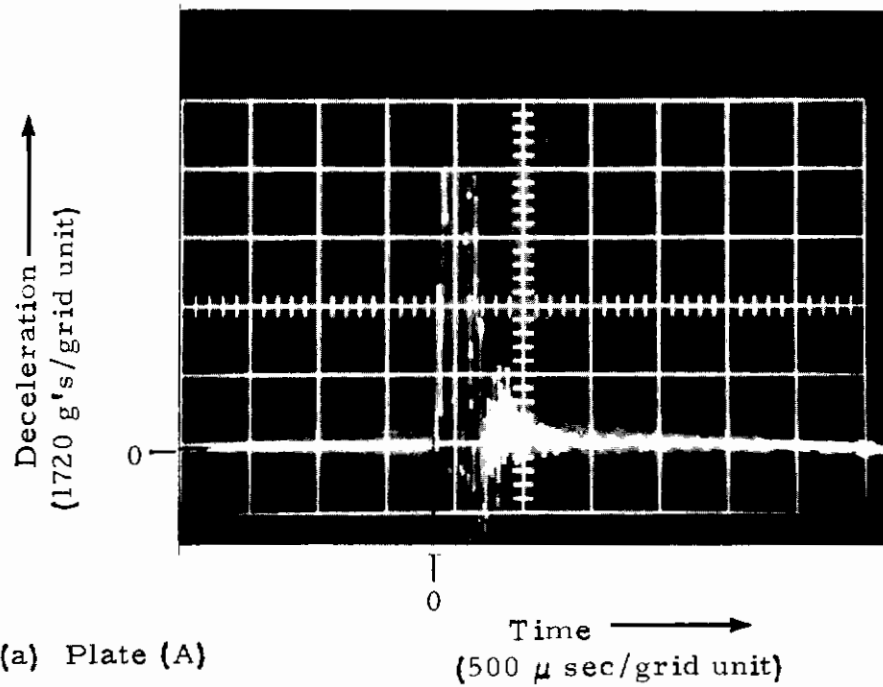


Figure 82. Deceleration Records-Test No. S-13
($h = .016$ in, $V_0 = 43$ ft/sec)

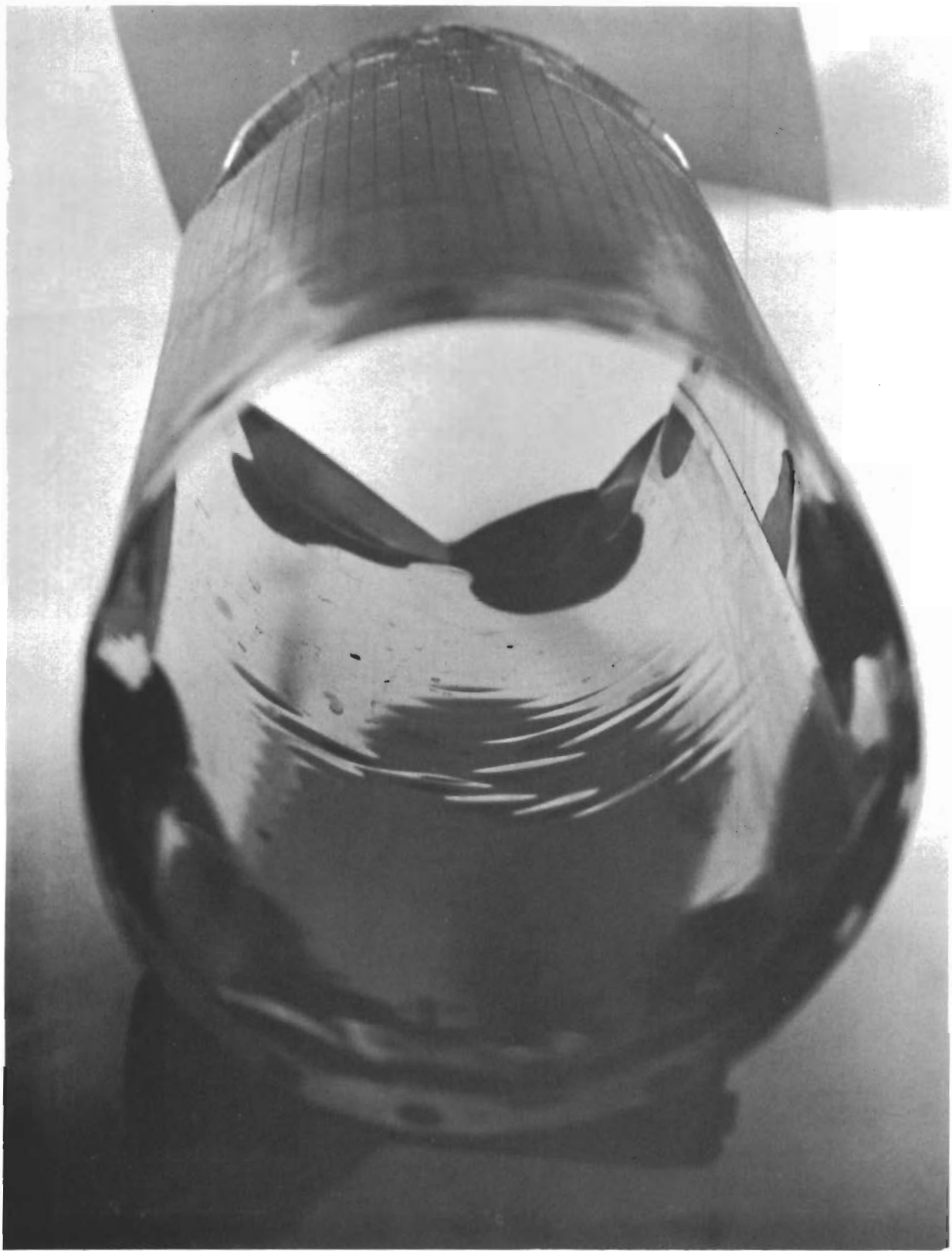


Figure 83. Inside View of Specimen S-13 Showing Permanent Small Amplitude Ring Buckles over a Portion of its Circumference

Contrails

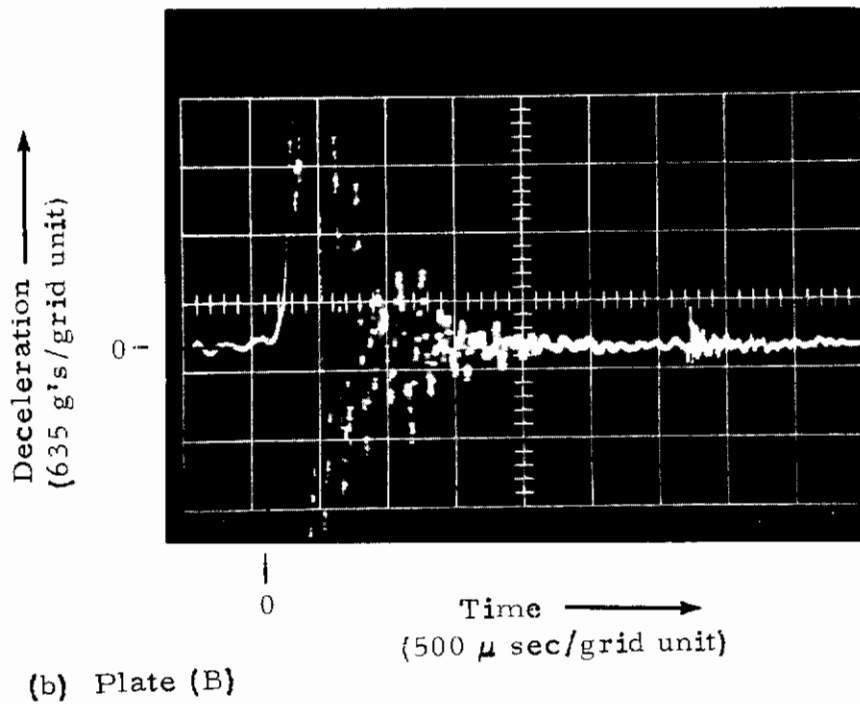
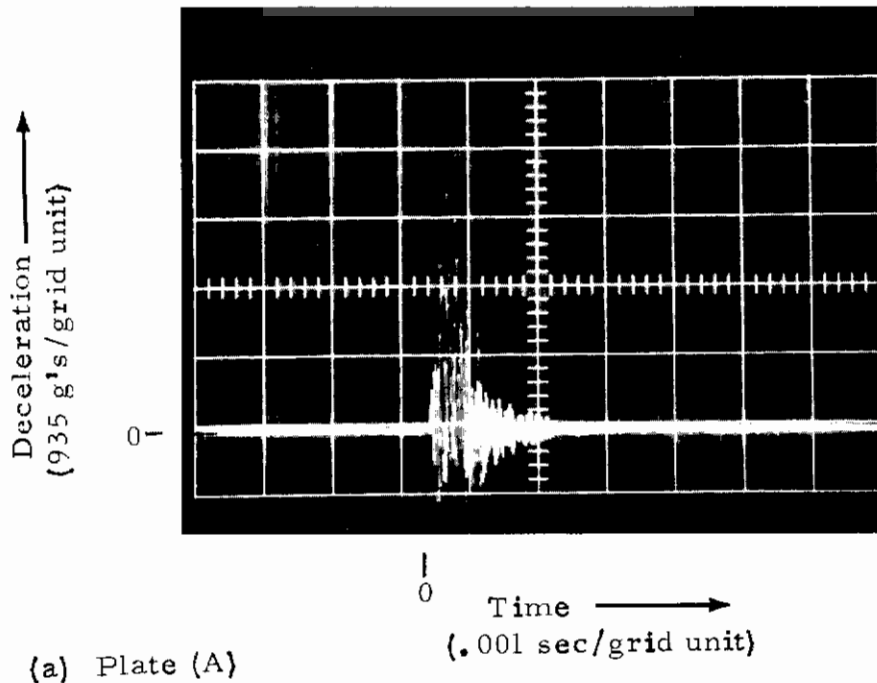


Figure 84. Deceleration Records - Test No. W-2A for the Rigid Body - Impact into Water, $V_0 = 43$ ft/sec

Contrails

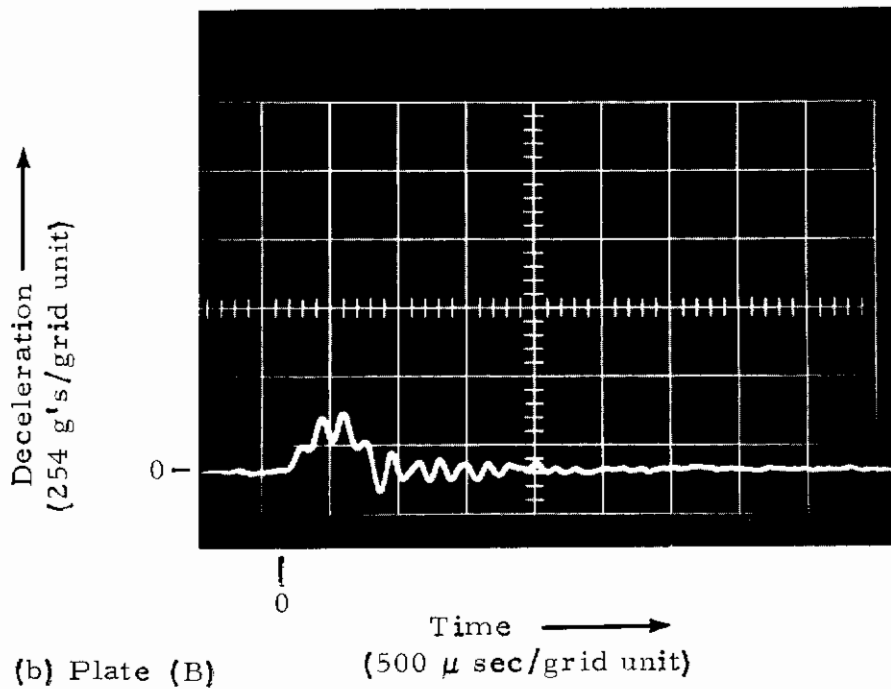
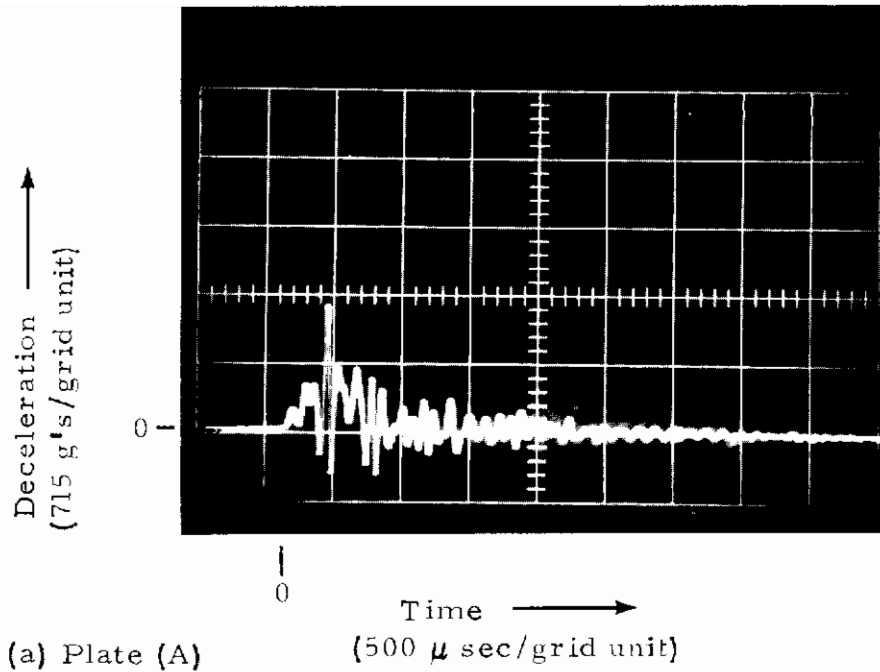


Figure 85. Deceleration Records - Test No. W-7
($h = .008$ in, $V_0 = 43$ ft/sec)

Contrails

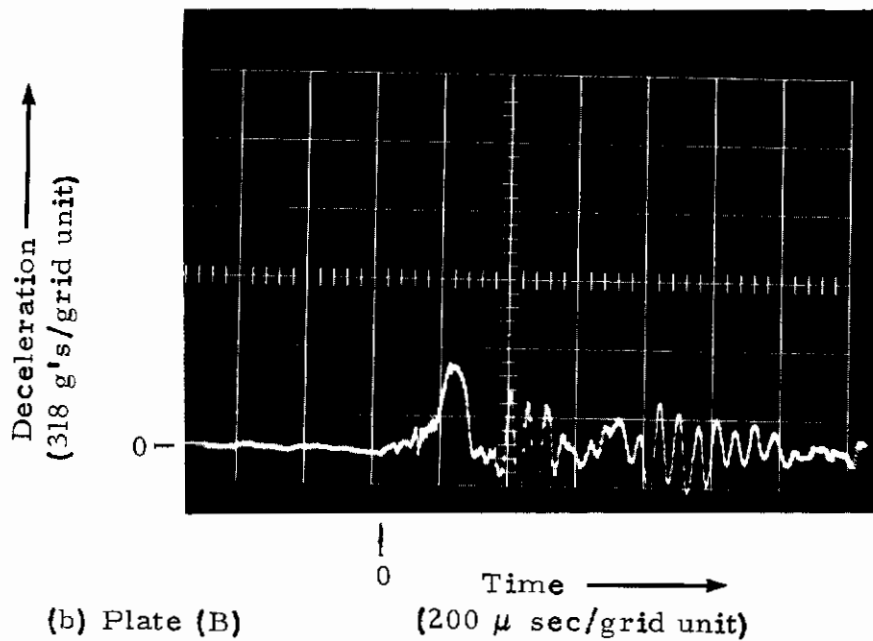
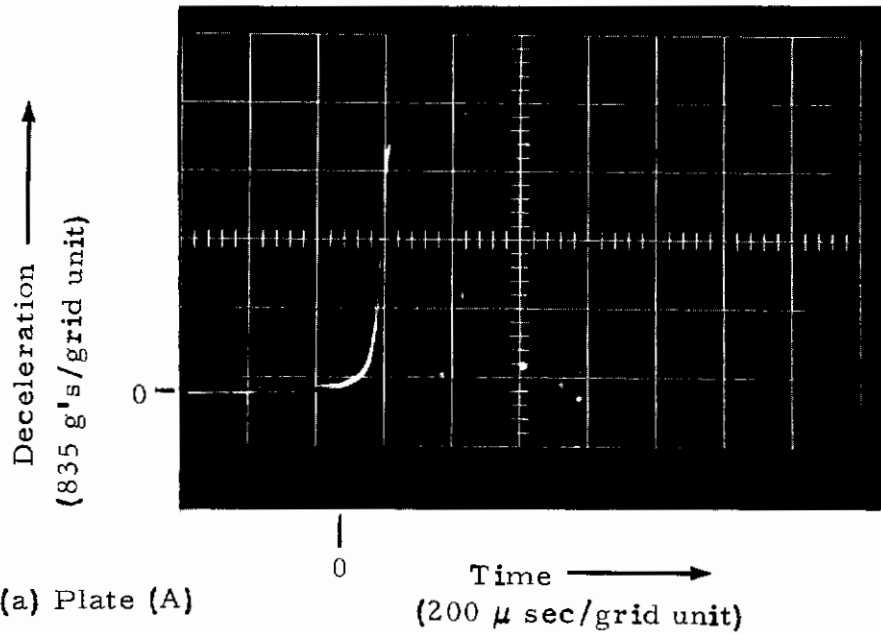


Figure 86. Deceleration Records - Test No. W-8
($h = .008$ in, $V_0 = 43$ ft/sec)

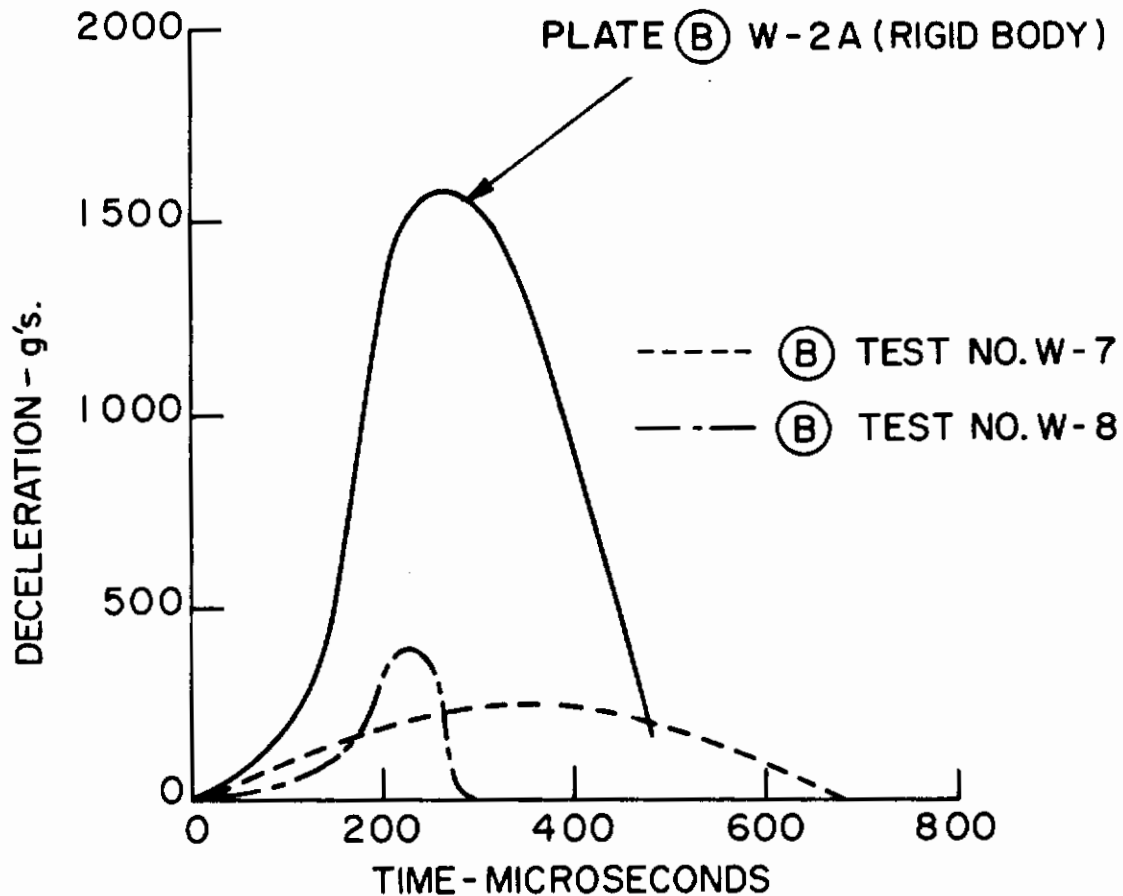


Figure 87. Effect of Shell Buckling on Deceleration of Plate (B), Showing a Comparison with the Deceleration of Plate (B) of Rigid Body - Vertical Impact into Water, $V_0 = 43$ ft/sec, $h = .008$ in

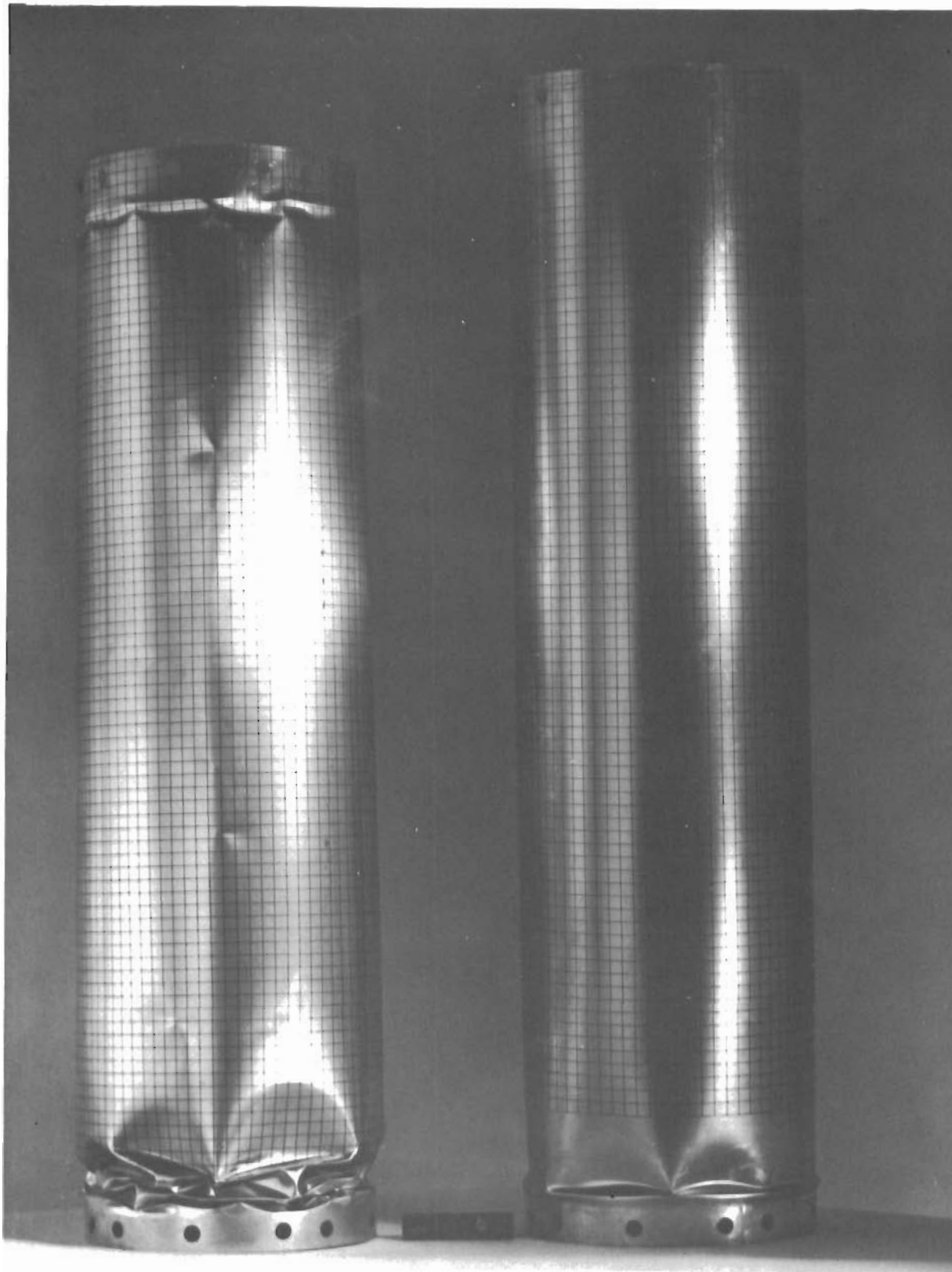


Figure 88. Specimens W-7 (Left, $h = .008$ in) and W-11 (Right, $h = .016$ in) After Impact into Water, $V_0 = 43$ ft/sec.

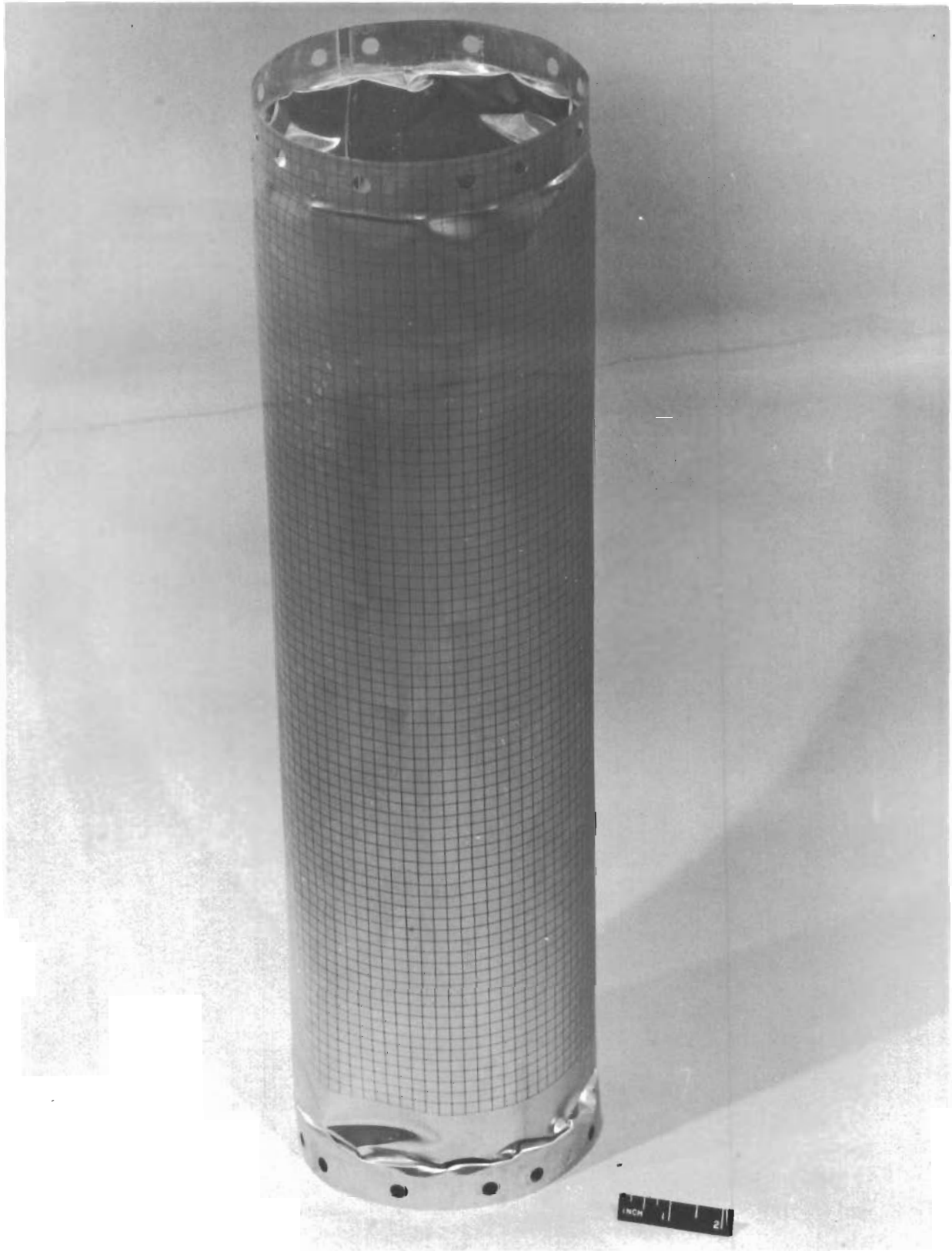


Figure 89. Specimen W-8 (.008 in) After Impact into Water, $V_0 = 43$ ft/sec.

Contrails

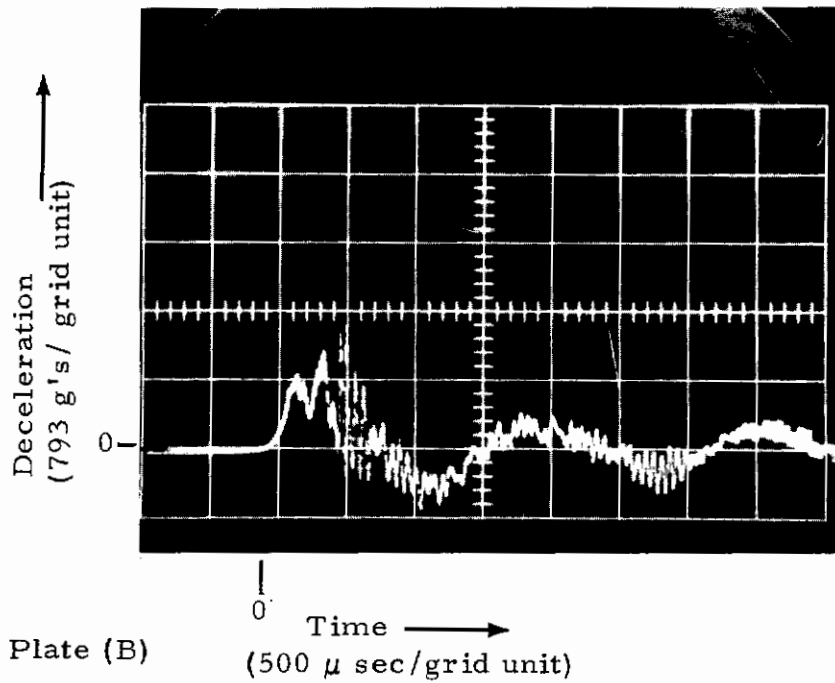
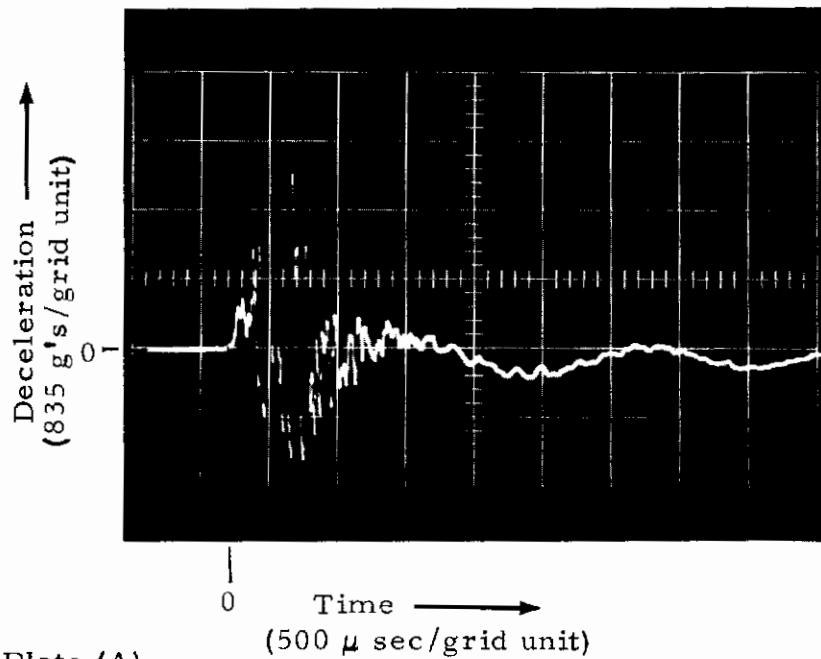
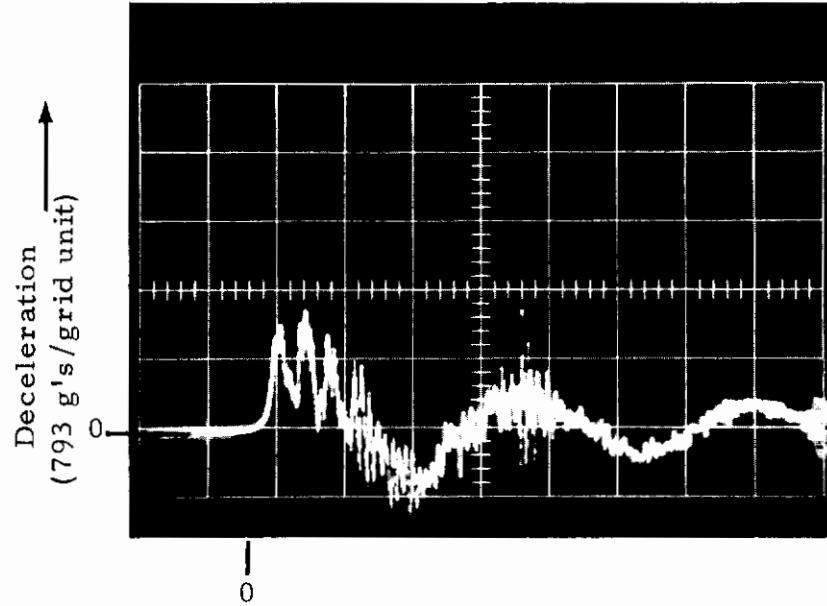
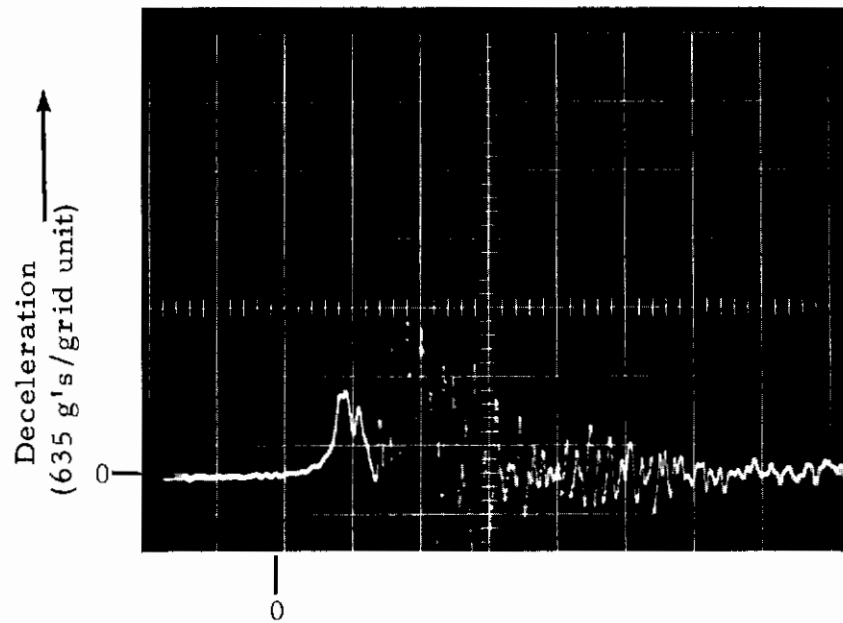


Figure 90. Deceleration Records - Test No. W-9
($h = .016$ in, $V_0 = 43$ ft/sec)

Contrails



(a) Plate (B), W-10
Time (500 μ sec/grid unit)



(b) Plate (B), W-11
Time (500 μ sec/grid unit)

Figure 91. Deceleration Records - Tests Nos. W-10 and W-11 ($h = .016$ in, $V_0 = 43$ ft/sec)

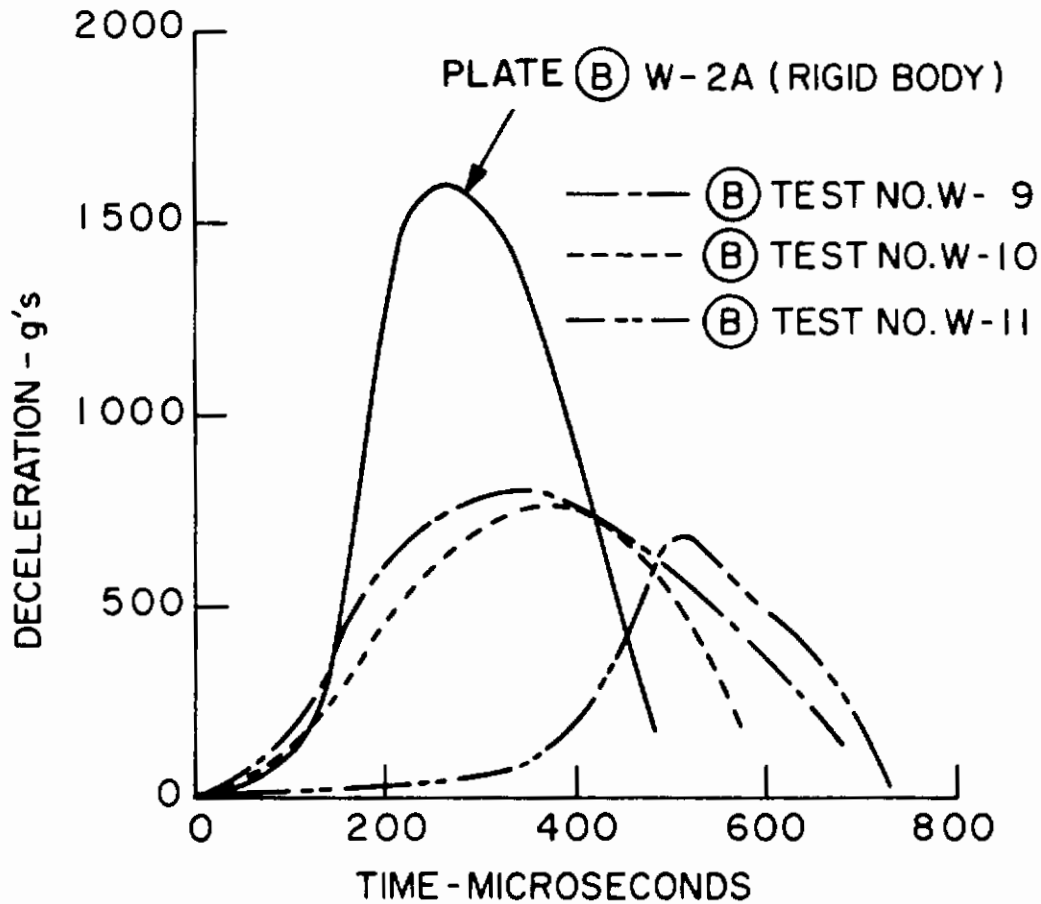


Figure 92. Effect of Shell Buckling on Deceleration on Plate (B), Showing a Comparison with Deceleration of Plate (B) of Rigid Body-Vertical Impact into Water, $V_0 = 43$ ft/sec, $h = .016$ in

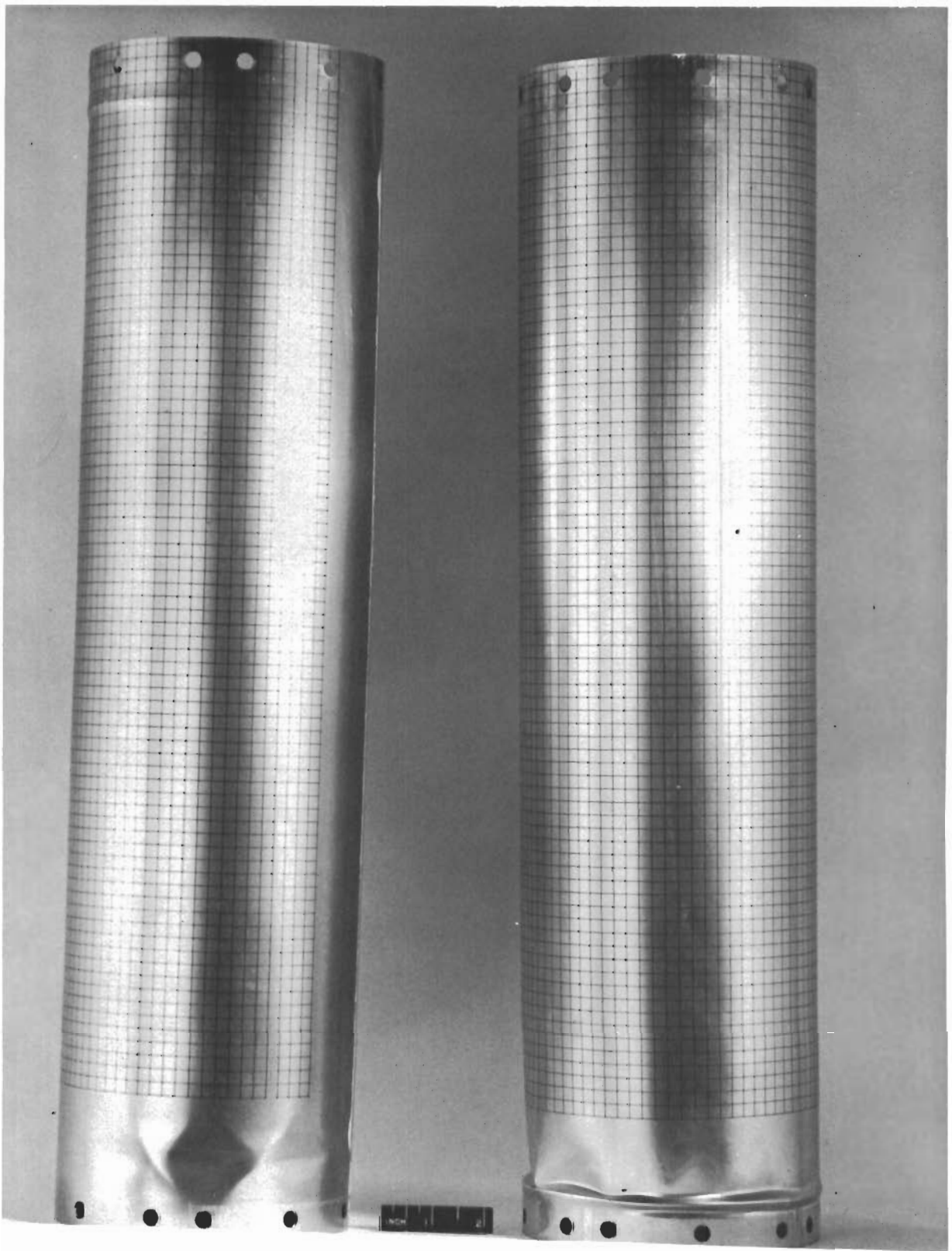
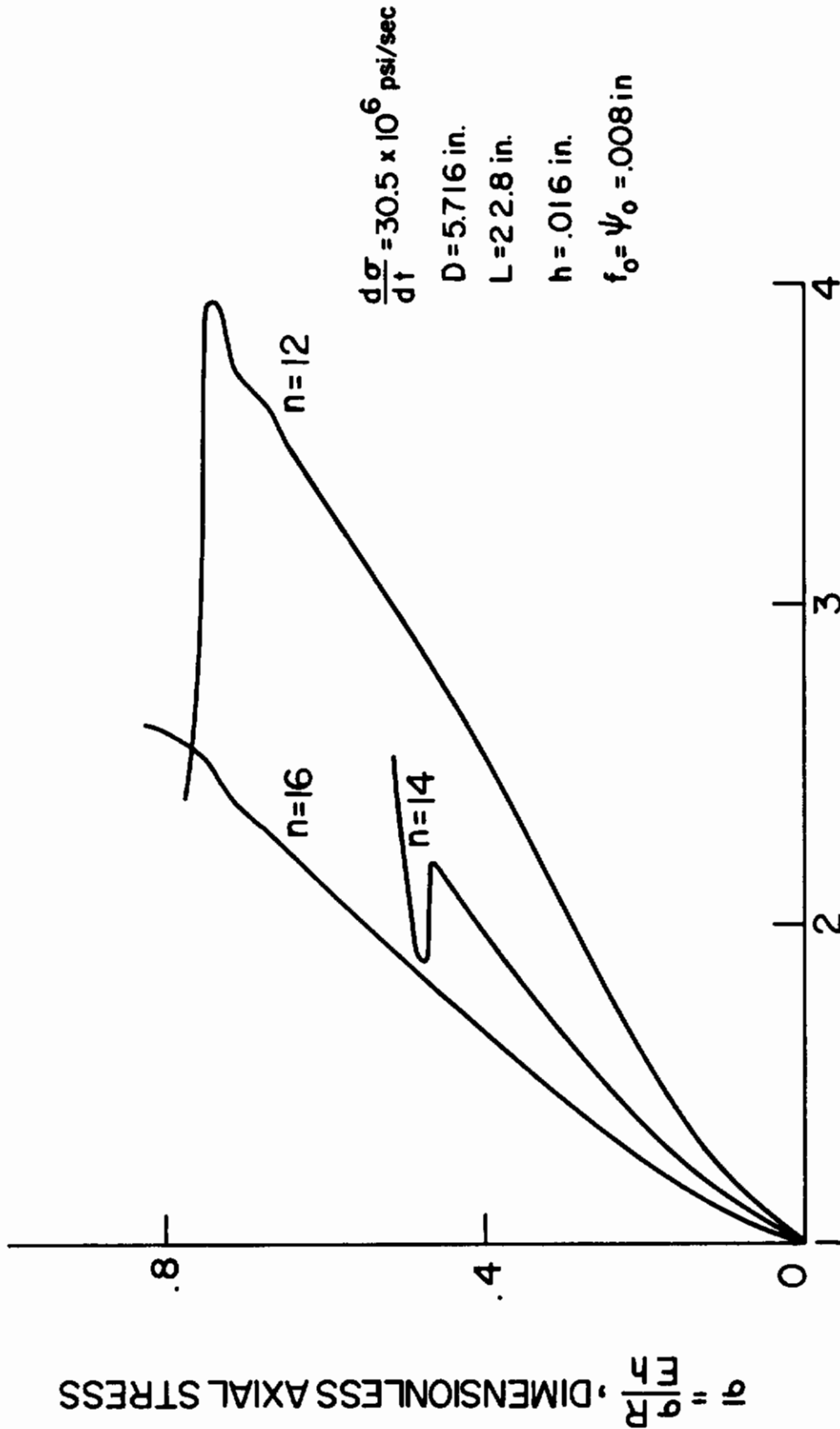
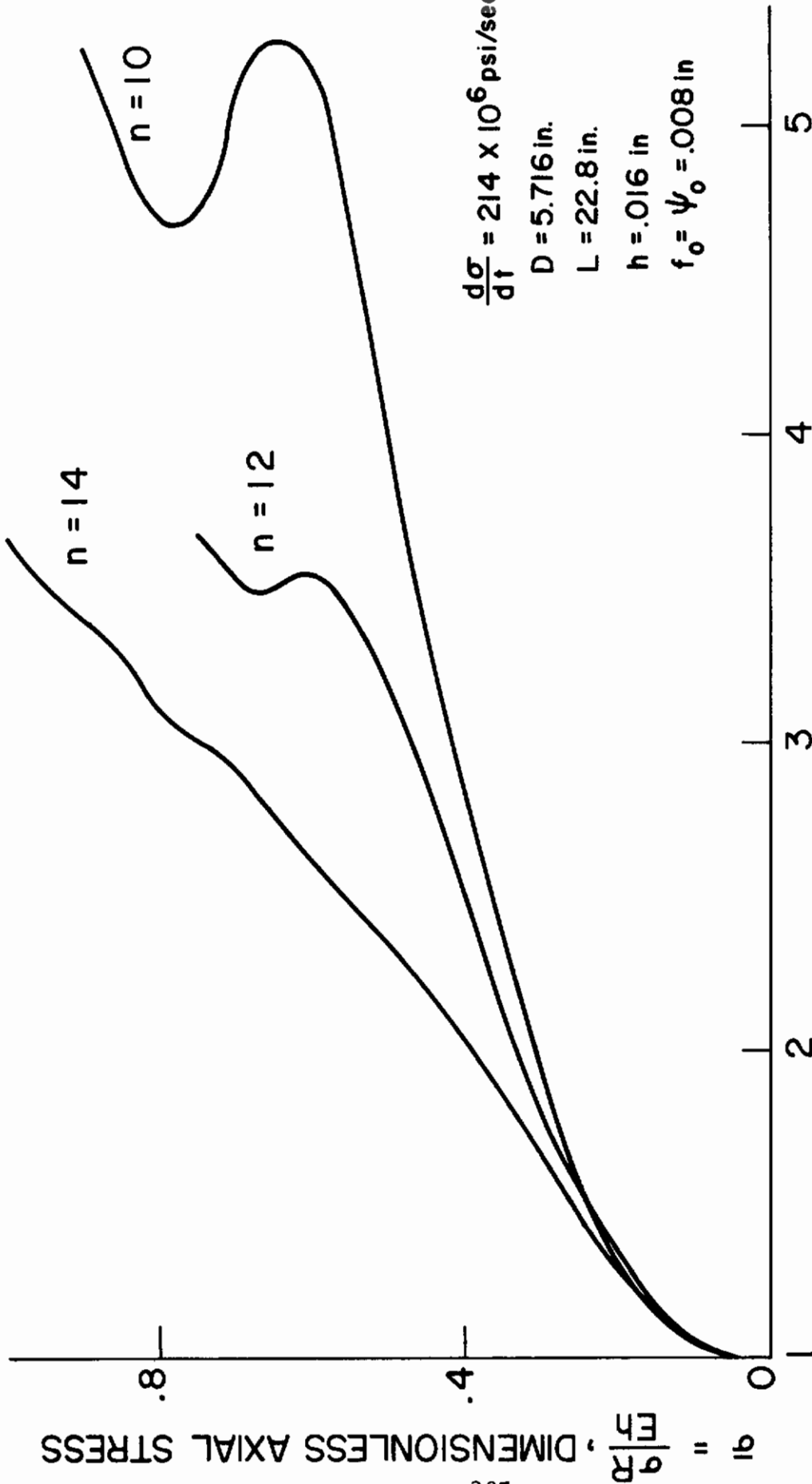


Figure 93. Specimens W-9 (left) and W-11 (right) After Impact into Water, $V_o = 43$ ft/sec, $h_o = .016$ in



$$\zeta = \frac{f_1 + \psi_1}{h}, \text{ DIMENSIONLESS LATERAL DEFLECTION}$$

Figure 94. Dimensionless Axial Stress vs. Dimensionless Lateral Deflection for a Circular Cylindrical Shell Subject to an Axial Force which Varies Linearly with Time.



$$\zeta = \frac{f_1 + \psi_1}{h}, \text{ DIMENSIONLESS LATERAL DEFLECTION}$$

Figure 95. Dimensionless Axial Stress vs. Dimensionless Lateral Deflection for a Circular Cylindrical Shell Subject to an Axial Force which Varies Linearly with Time.

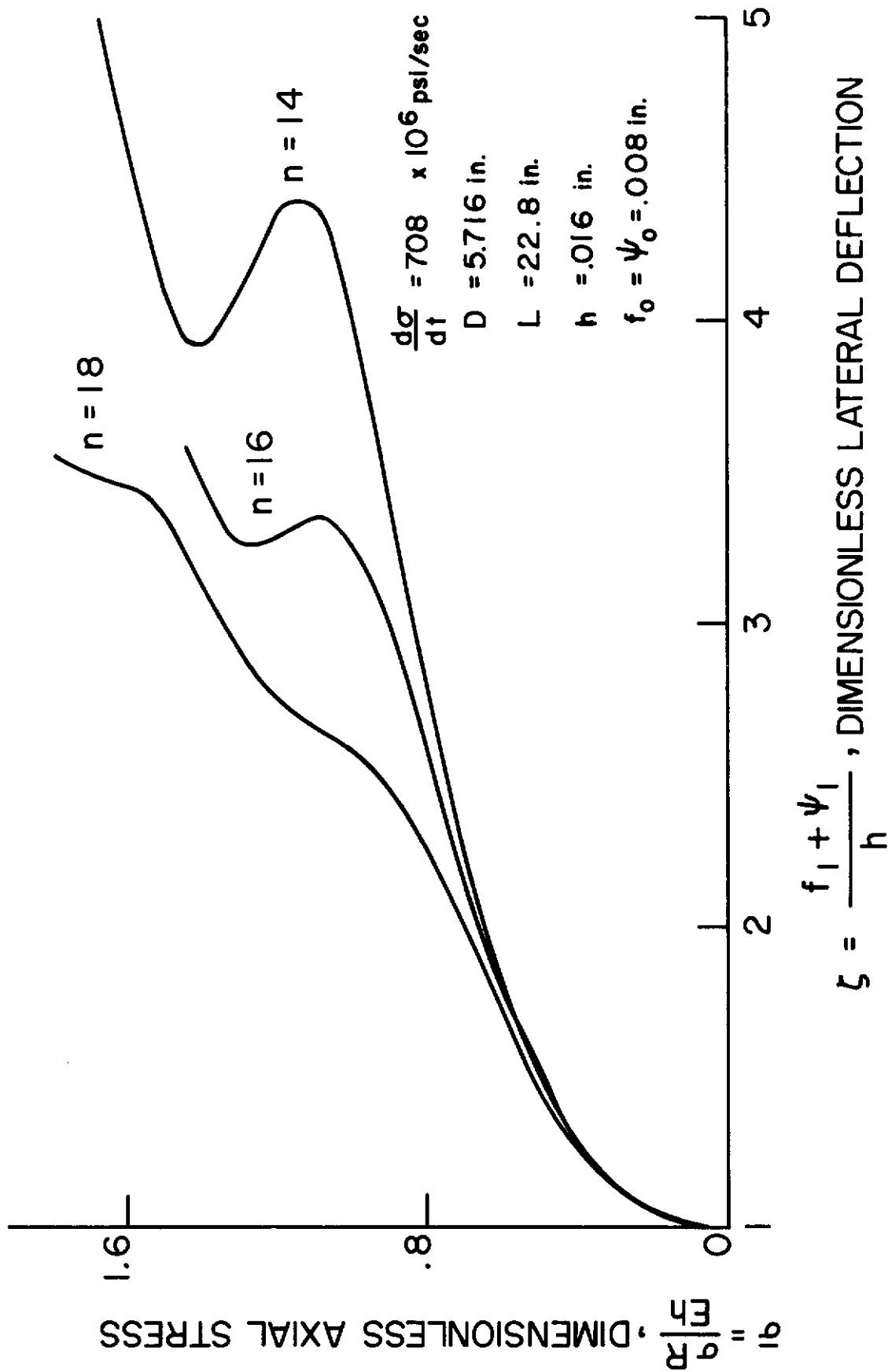
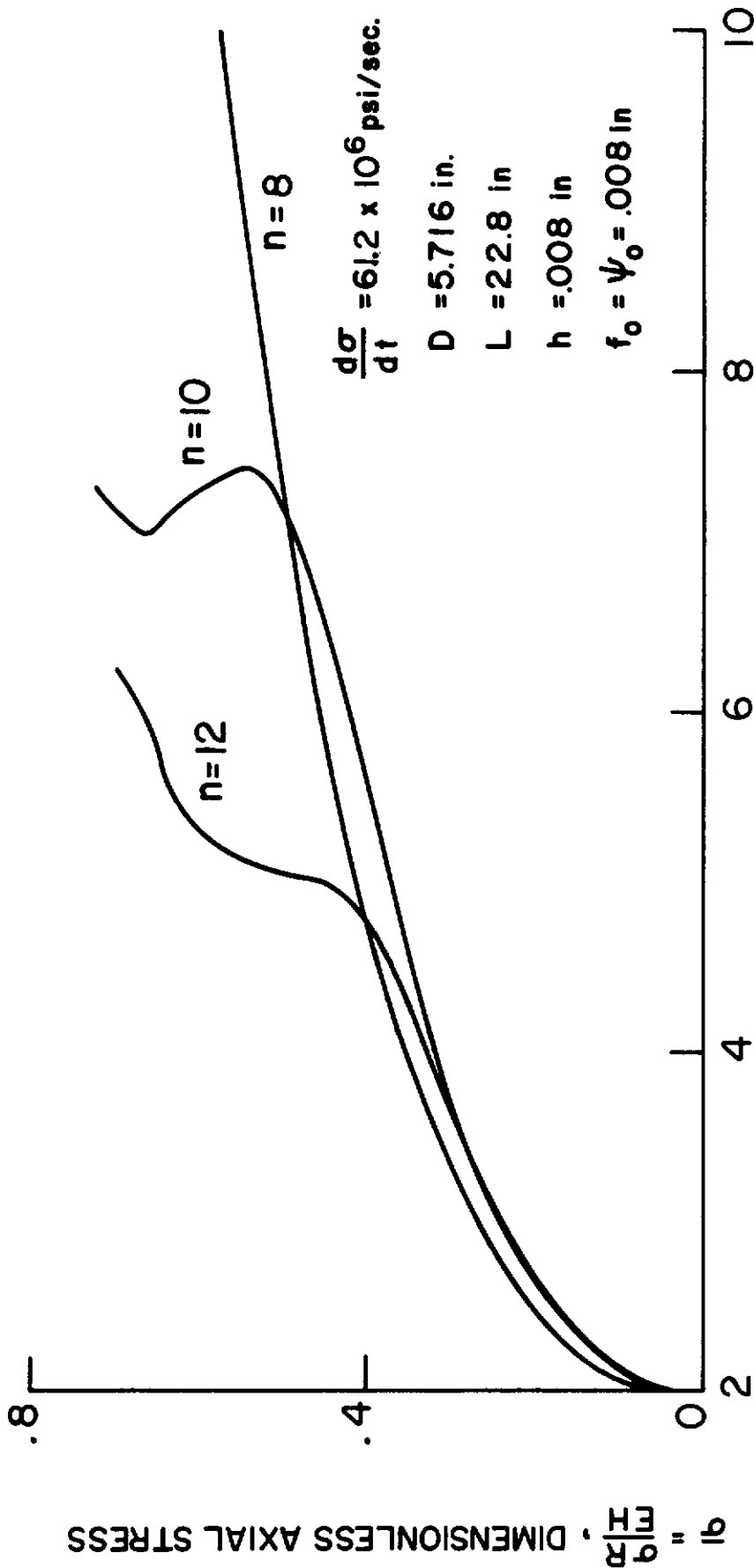
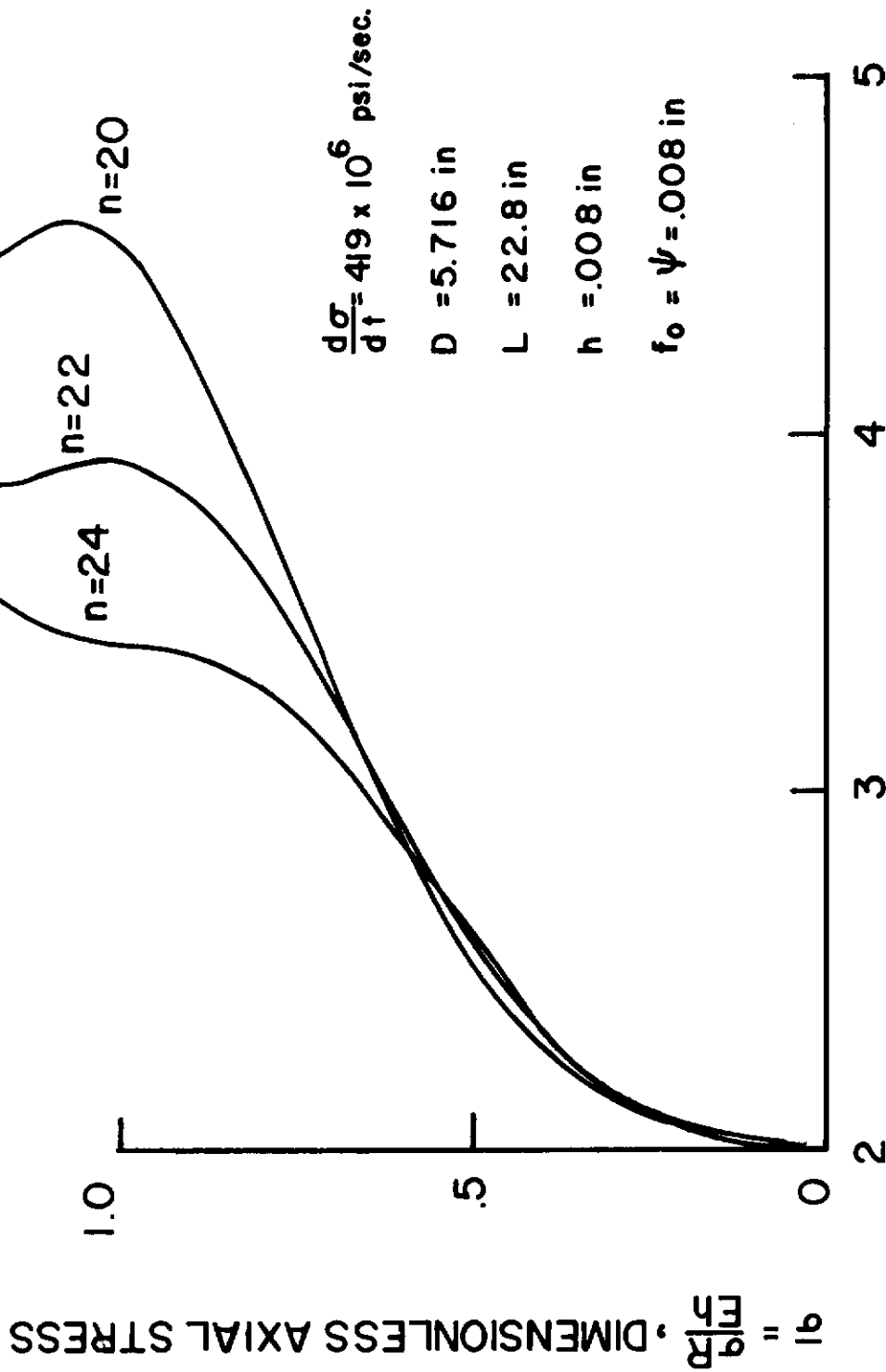


Figure 96. Dimensionless Axial Stress vs. Dimensionless Lateral Deflection for a Circular Cylindrical Shell Subject to an Axial Force which Varies Linearly with Time.



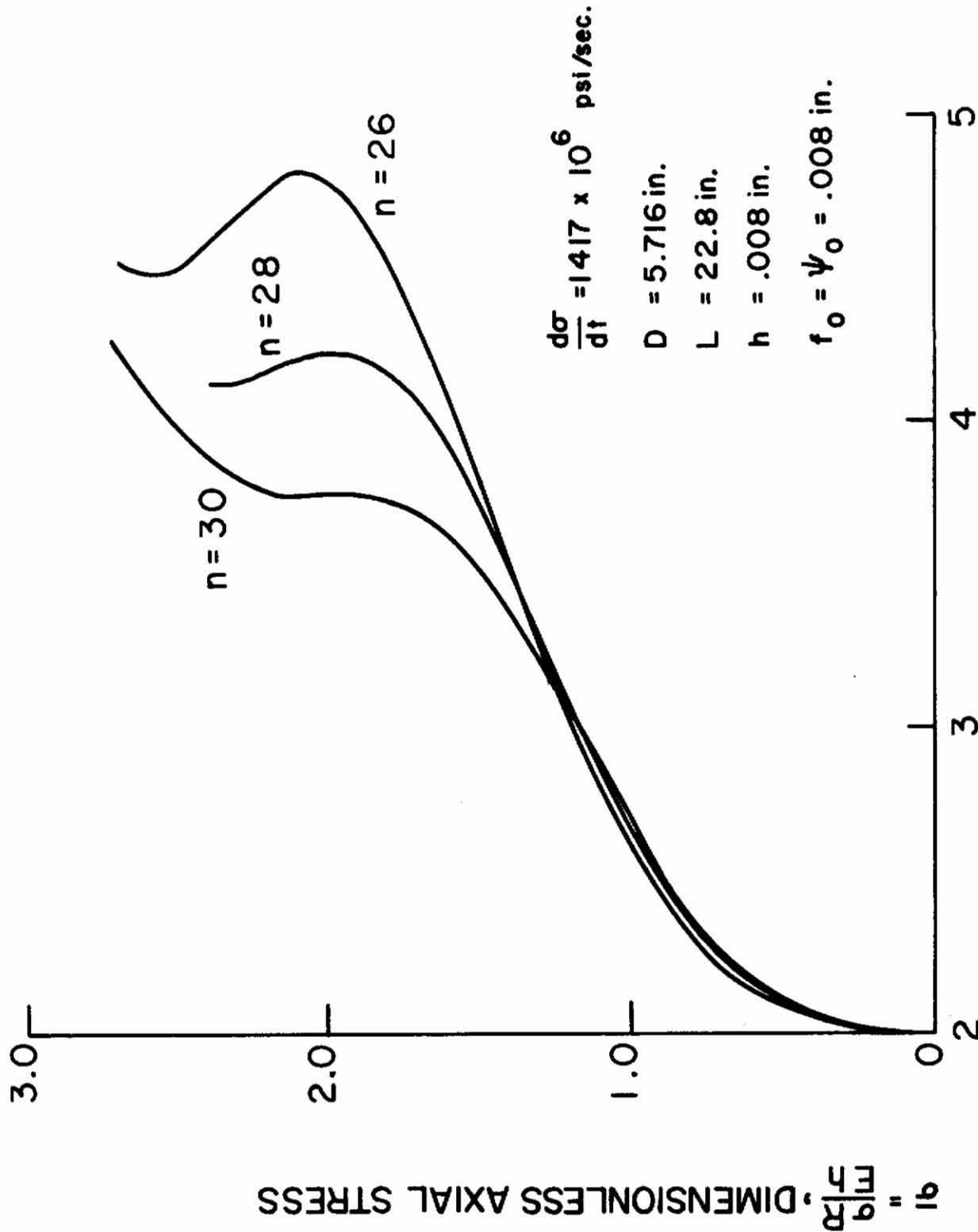
$$\zeta = \frac{f_1 + \psi_1}{h}, \text{ DIMENSIONLESS LATERAL DEFLECTION}$$

Figure 97. Dimensionless Axial Stress vs. Dimensionless Lateral Deflection for a Circular Cylindrical Shell Subject to an Axial Force which Varies Linearly with Time.



$$\zeta = \frac{f_1 + \psi_1}{h}, \text{ DIMENSIONLESS LATERAL DEFLECTION}$$

Figure 98. Dimensionless Axial Stress vs. Dimensionless Lateral Deflection for a Circular Cylindrical Shell Subject to an Axial Force which Varies Linearly with Time.



$$\zeta = \frac{f_1 + \psi_1}{h}, \text{ DIMENSIONLESS LATERAL DEFLECTION}$$

Figure 99. Dimensionless Axial Stress vs. Dimensionless Lateral Deflection for a Circular Cylindrical Shell Subject to an Axial Force which Varies Linearly with Time.

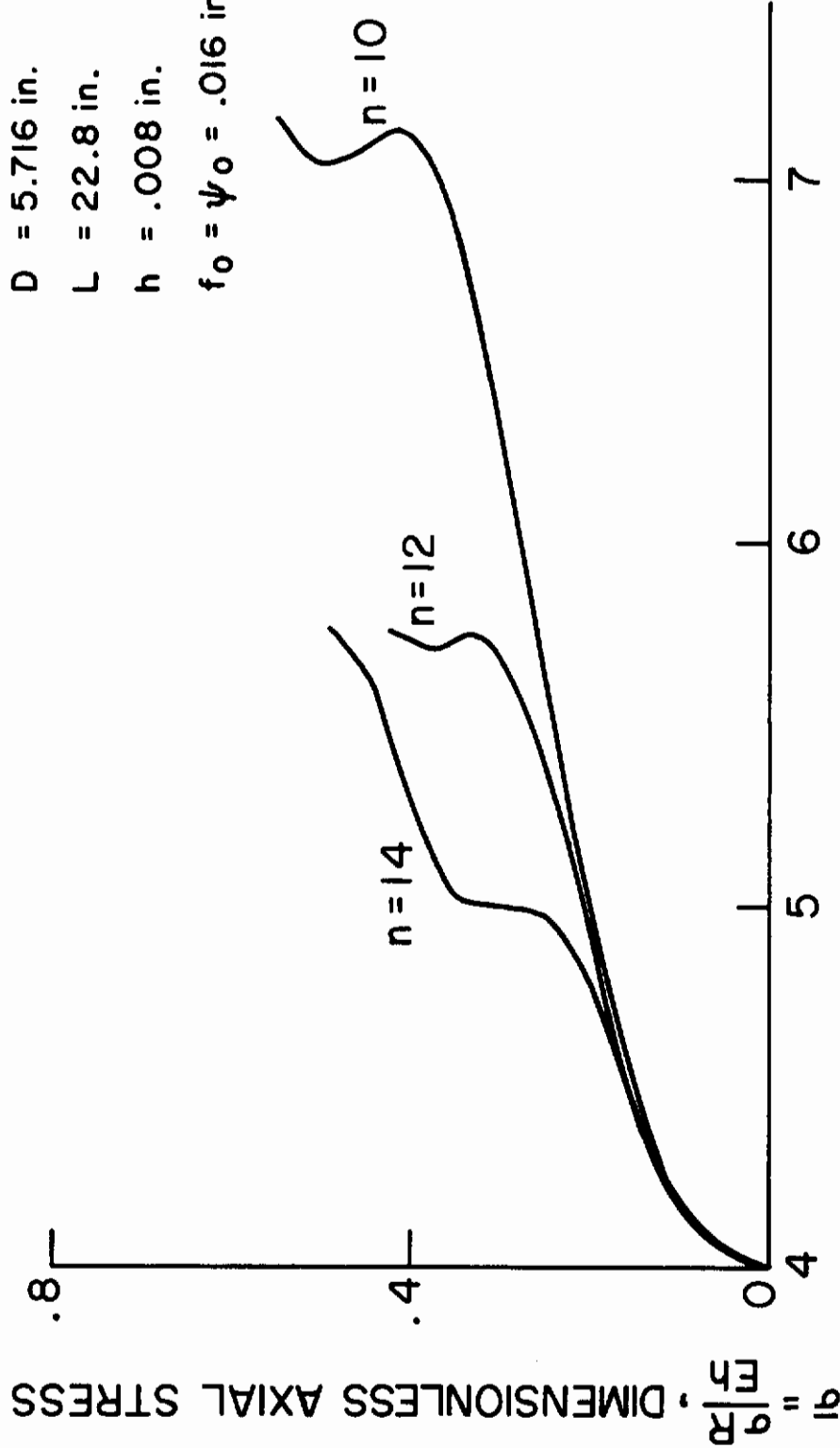
$$\frac{d\sigma}{dt} = 61.2 \times 10^6 \text{ psi / sec.}$$

$$D = 5.716 \text{ in.}$$

$$L = 22.8 \text{ in.}$$

$$h = .008 \text{ in.}$$

$$f_0 = \psi_0 = .016 \text{ in.}$$



$$\zeta = \frac{f_1 + \psi_1}{h}, \text{ DIMENSIONLESS LATERAL DEFLECTION}$$

Figure 100. Dimensionless Axial Stress vs. Dimensionless Lateral Deflection for a Circular Cylindrical Shell Subject to an Axial Force which Varies Linearly with Time.

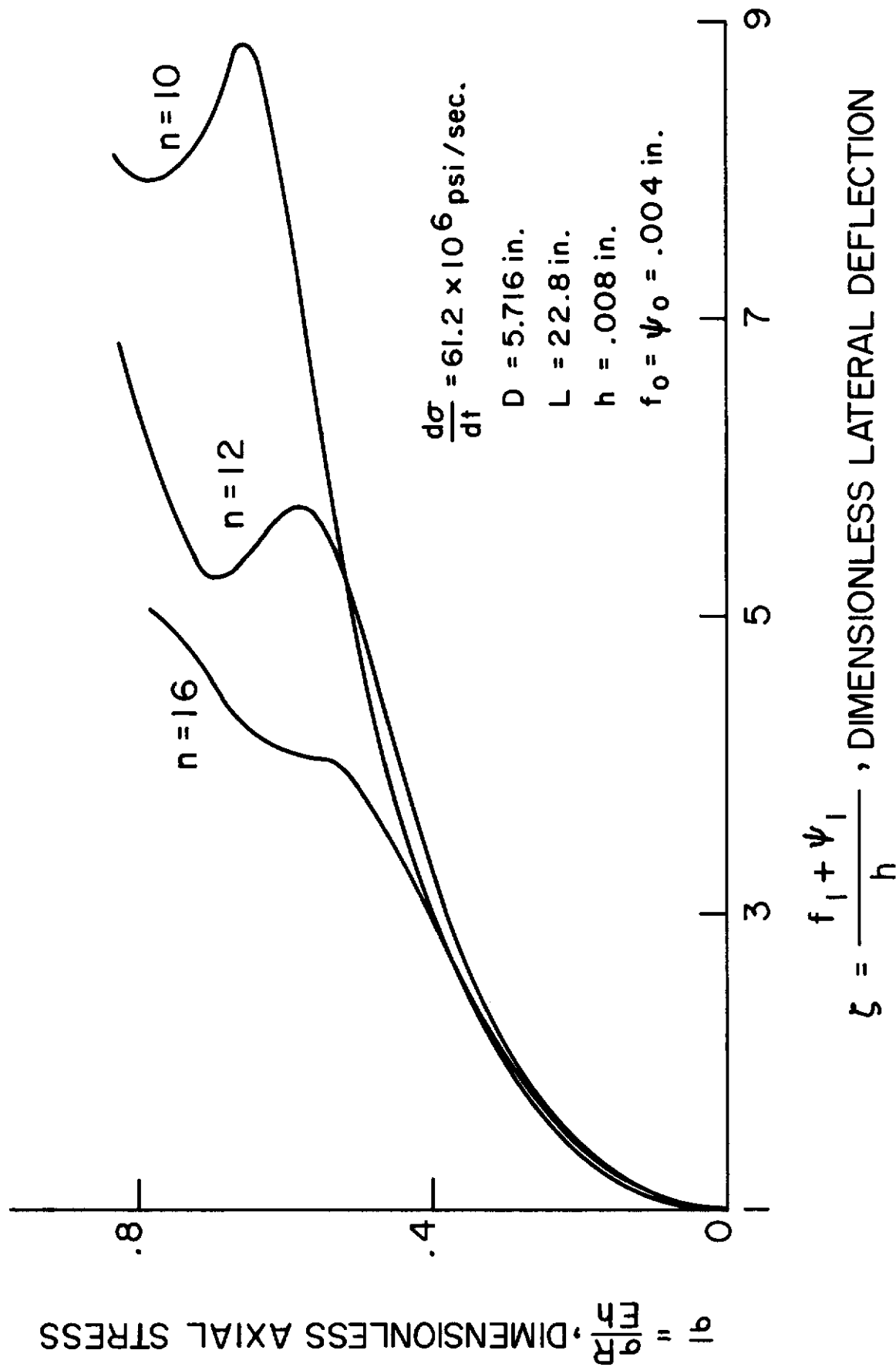
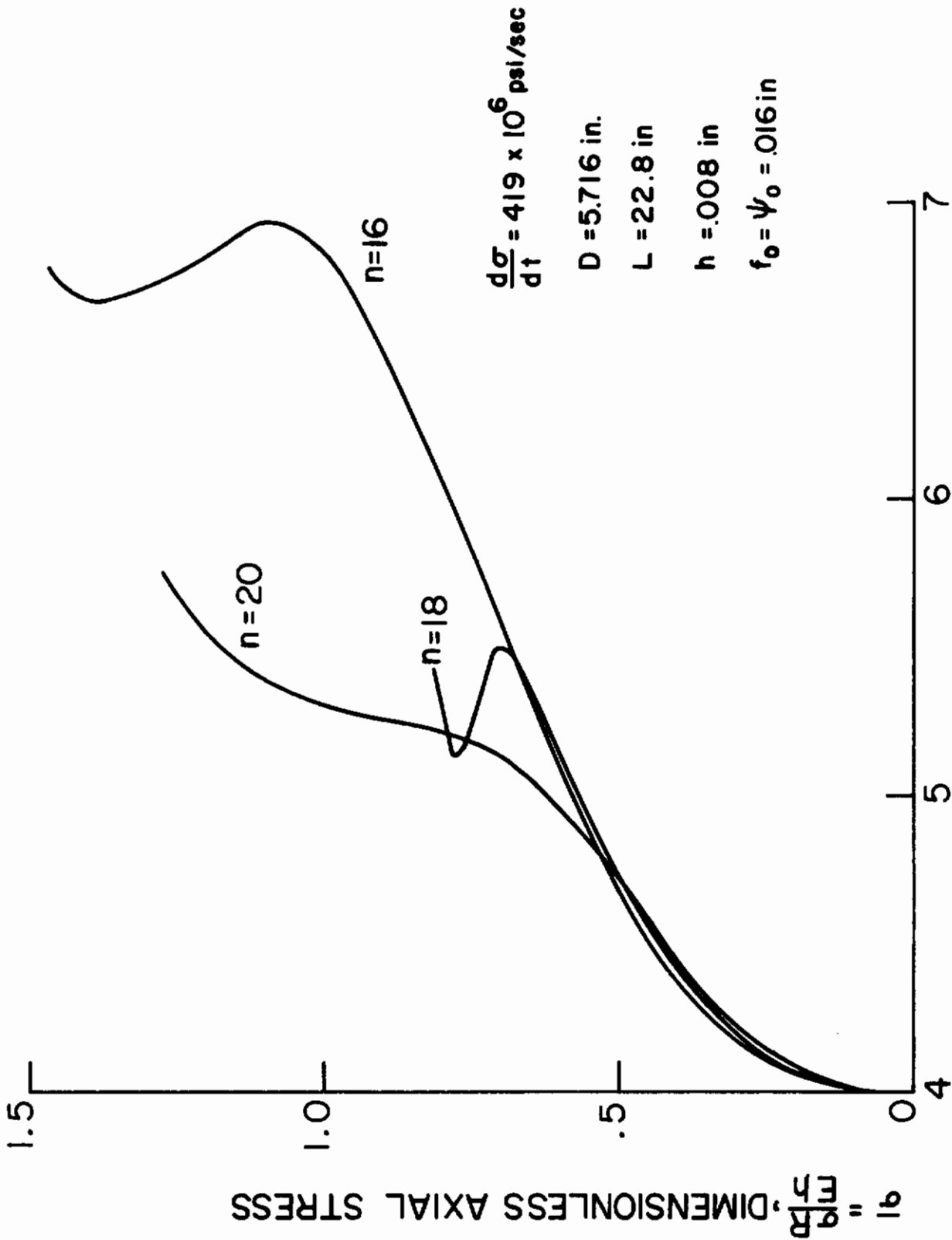
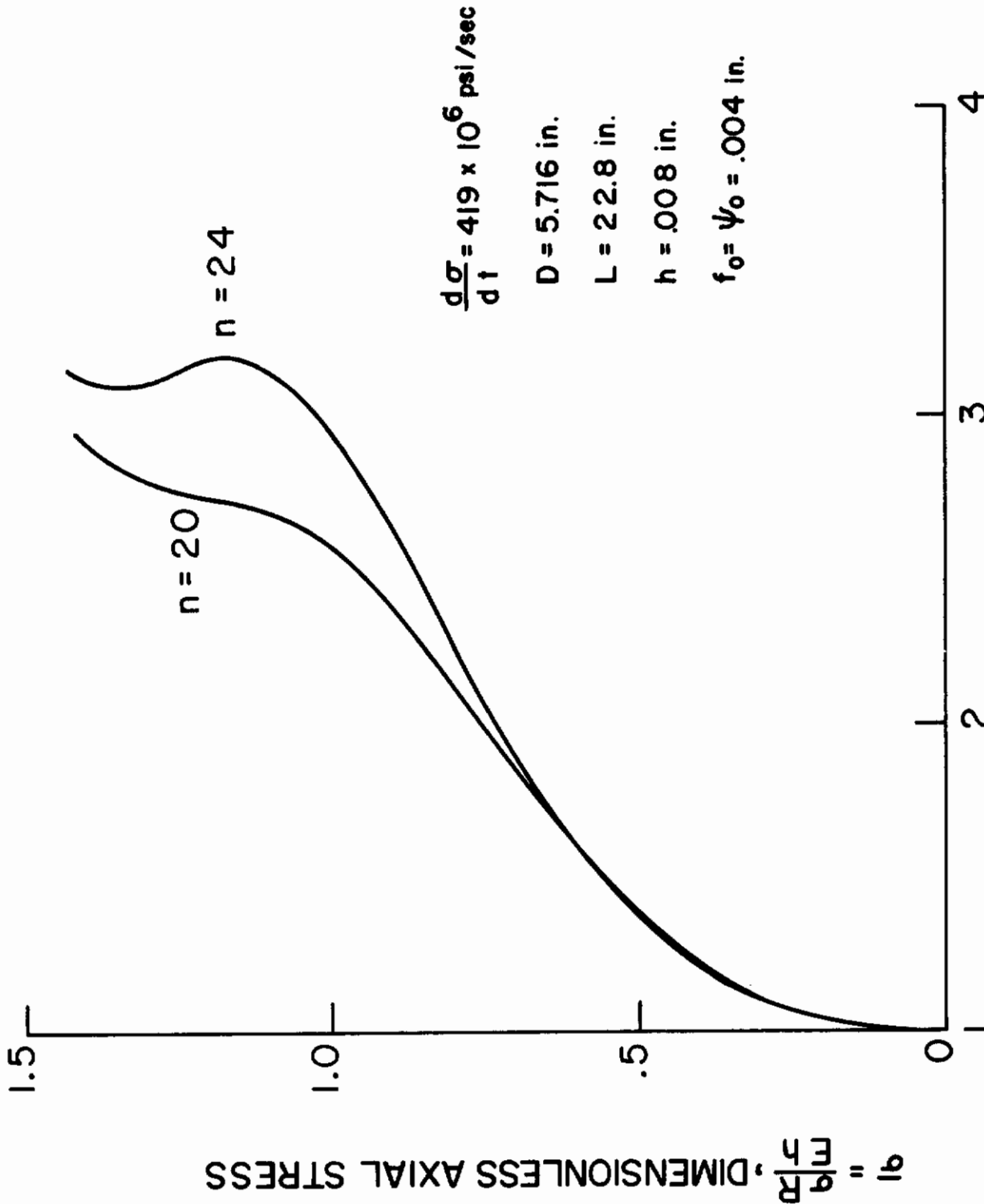


Figure 101. Dimensionless Axial Stress vs. Dimensionless Lateral Deflection for a Circular Cylindrical Shell Subject to an Axial Force which Varies Linearly with Time.



$$\zeta = \frac{f_1 + \psi_1}{h}, \text{ DIMENSIONLESS LATERAL DEFLECTION}$$

Figure 102. Dimensionless Axial Stress vs. Dimensionless Lateral Deflection for a Circular Cylindrical Shell Subject to an Axial Force which Varies Linearly with Time.



$$\zeta = \frac{f_1 + \psi_1}{h}, \text{ DIMENSIONLESS LATERAL DEFLECTION}$$

Figure 103. Dimensionless Axial Stress vs. Dimensionless Lateral Deflection for a Circular Cylindrical Shell Subject to an Axial Force which Varies Linearly with Time.

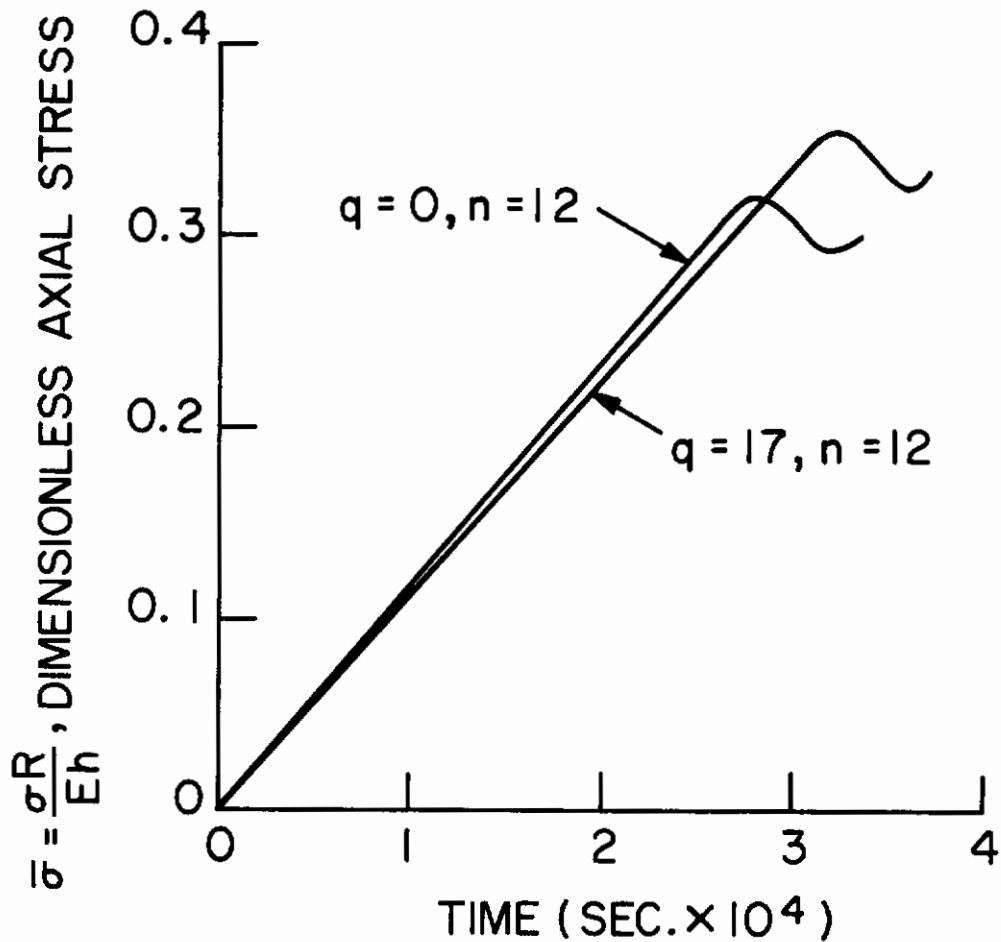


Figure 104. Effect of Internal Pressurization on the Buckling Stress of a Circular Cylindrical Shell Subject to a Constant Velocity of End Shortening ($V_0 = 11.5$ ft/sec., $h = .016$ in, Al.)

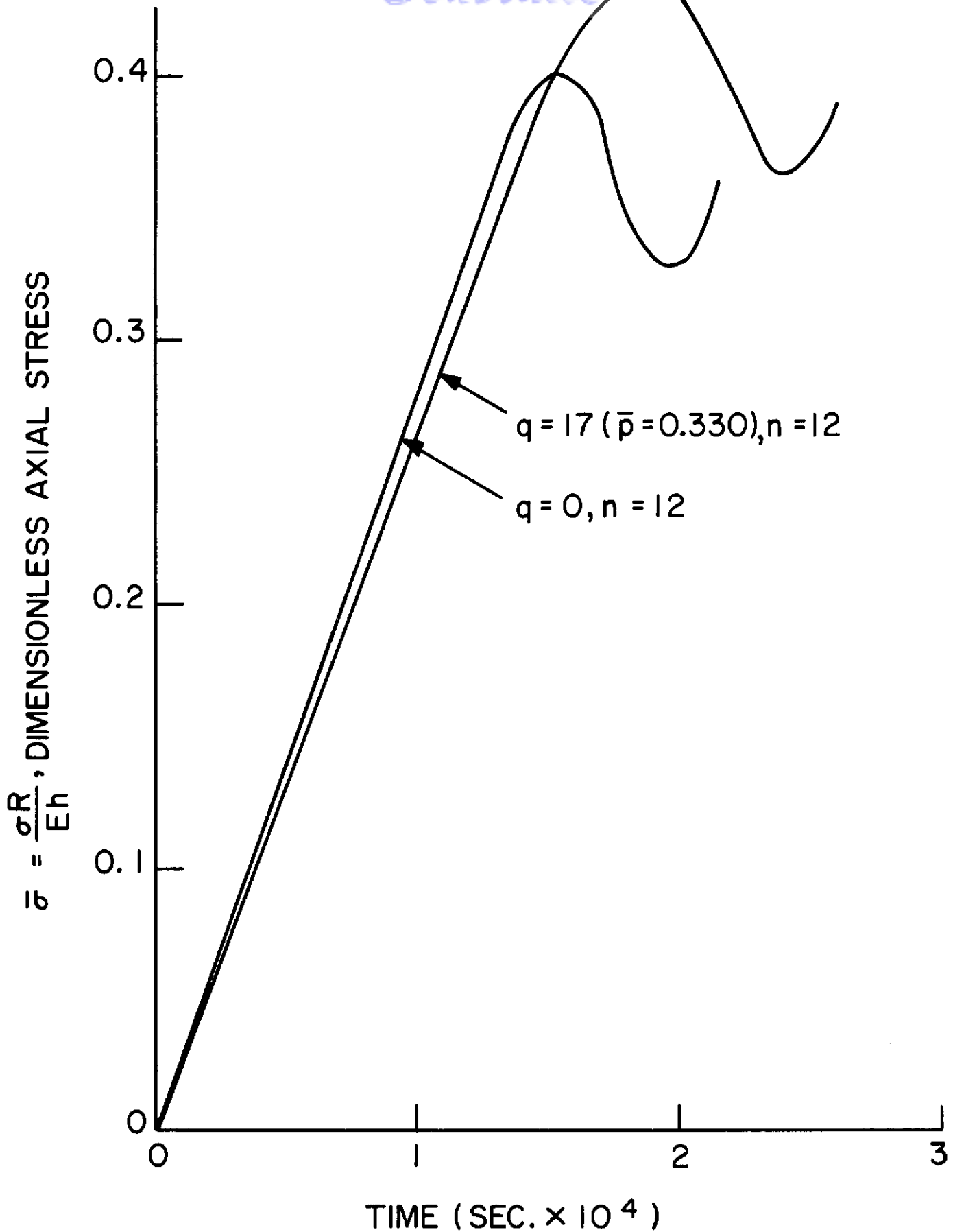


Figure 105. Effect of Internal Pressurization on the Buckling Stress of a Circular Cylindrical Shell Subject to a Constant Velocity of End Shortening ($V_0 = 23$ ft/sec, $h = .016$ in, Al.)

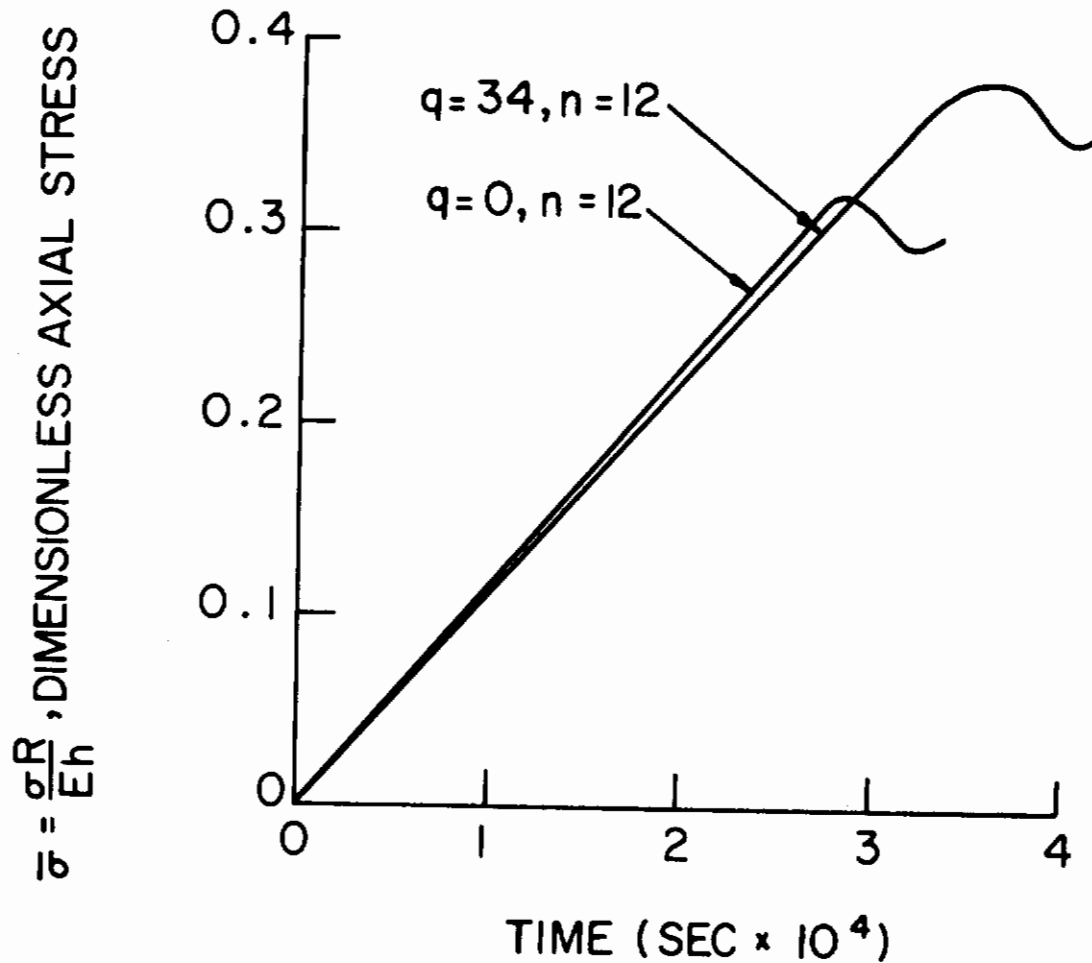


Figure 106. Effect of Internal Pressurization on the Buckling Stress of a Circular Cylindrical Shell Subject to a Constant Velocity of End Shortening ($V_0 = 11.5$ ft/sec, $h = .016$ in, Al.)

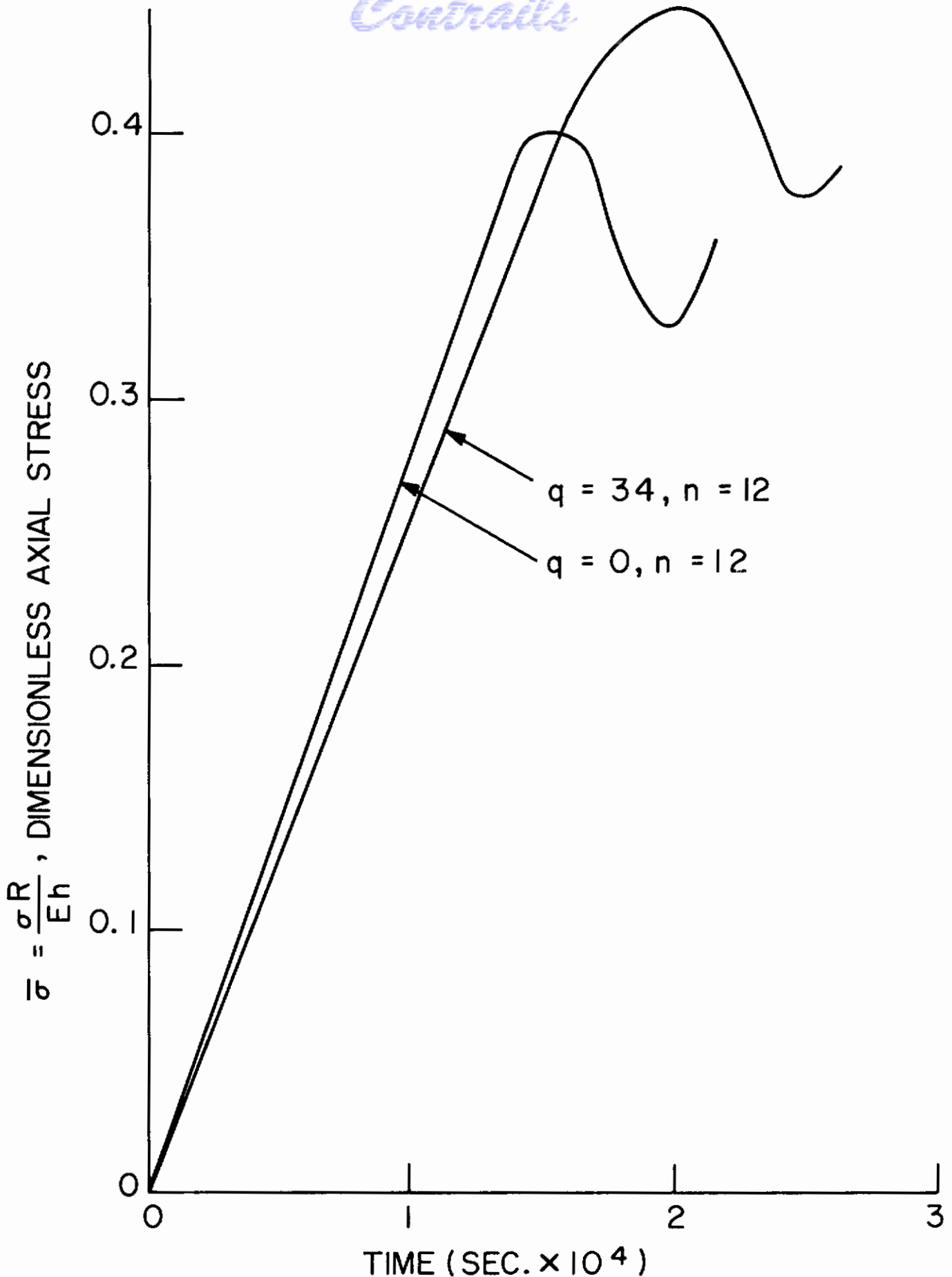


Figure 107. Effect of Internal Pressurization on the Buckling Stress of a Circular Cylindrical Shell Subject to a Constant Velocity of End Shortening ($V_0 = 23$ ft/sec., $h = .016$ in, Al.)

Contrails

Security Classification

DOCUMENT CONTROL DATA - R&D		
<i>(Security classification of title, body of abstract and indexing annotation must be entered when the overall report is classified)</i>		
1. ORIGINATING ACTIVITY (Corporate author)		2a. REPORT SECURITY CLASSIFICATION
Space Sciences Laboratory, Valley Forge Space Technology Center, King of Prussia, Penna.		Unclassified
		2b. GROUP
3. REPORT TITLE		
Dynamic Buckling of Shell Structures Subject to Longitudinal Impact		
4. DESCRIPTIVE NOTES (Type of report and inclusive dates)		
Technical Documentary Report No. FDL-TDR-64-65 December 1964		
5. AUTHOR(S) (Last name, first name, initial)		
Coppa, Anthony P.		
6. REPORT DATE	7a. TOTAL NO. OF PAGES	7b. NO. OF REFS
December 1964	228	36
8a. CONTRACT OR GRANT NO.	9a. ORIGINATOR'S REPORT NUMBER(S)	
AF 33(657)-10220	FDL-TDR-64-65	
b. PROJECT NO.	9b. OTHER REPORT NO(S) (Any other numbers that may be assigned this report)	
1467		
c. Task 146703		
d.		
10. AVAILABILITY/LIMITATION NOTICES		
Inside Front Cover		
11. SUPPLEMENTARY NOTES	12. SPONSORING MILITARY ACTIVITY	
	A. F. Flight Dynamics Lab., Research & Tech. Div., A. F. Systems Command, Wright-Patterson Air Force Base, Ohio	
13. ABSTRACT		
<p>Experimental and theoretical studies of the buckling and collapse of circular cylindrical and conical shells under longitudinal impact are described. Various conditions of loading were investigated such as impact with rigid, fluid, and granular media, and such effects as initial geometrical imperfections, edge support, and loading asymmetry were included. In addition, the effect of axial impact at velocities up to 391 ft/sec on the buckling of thin cylindrical shells was studied experimentally. Finally, three problems, relating to the experiments were studied theoretically: (1) the dynamic buckling of a circular cylindrical shell subject to an axial loading which varies linearly with time, using the nonlinear theory, (2) dynamic buckling of a circular cylindrical shell subject to a constant velocity end displacement, including the effects of plasticity and incorporating extremely large deflections, and (3) the inextensional shortening and collapse modes of conical shells for the complete range of end shortening.</p> <p>Results are presented which show reasonably good comparison between experiment and theory for Problems (1) and (3) and further for the case of internally pressurized circular cylindrical shells under axial impact (this latter result stems from the previous program). In addition, extensional ("ring") collapse waves were obtained in a thin cylindrical shell impacted axially at a velocity of 392 ft/sec. This is believed to be the first time such a mode has been observed in a thin, unpressurized shell.</p>		

14.	KEY WORDS	LINK A		LINK B		LINK C	
		ROLE	WT	ROLE	WT	ROLE	WT
	<p style="font-size: 1.2em; margin: 0;">Dynamic Buckling Buckling Geometry</p>						

INSTRUCTIONS

1. ORIGINATING ACTIVITY: Enter the name and address of the contractor, subcontractor, grantee, Department of Defense activity or other organization (*corporate author*) issuing the report.

2a. REPORT SECURITY CLASSIFICATION: Enter the overall security classification of the report. Indicate whether "Restricted Data" is included. Marking is to be in accordance with appropriate security regulations.

2b. GROUP: Automatic downgrading is specified in DoD Directive S200.10 and Armed Forces Industrial Manual. Enter the group number. Also, when applicable, show that optional markings have been used for Group 3 and Group 4 as authorized.

3. REPORT TITLE: Enter the complete report title in all capital letters. Titles in all cases should be unclassified. If a meaningful title cannot be selected without classification, show title classification in all capitals in parenthesis immediately following the title.

4. DESCRIPTIVE NOTES: If appropriate, enter the type of report, e.g., interim, progress, summary, annual, or final. Give the inclusive dates when a specific reporting period is covered.

5. AUTHOR(S): Enter the name(s) of author(s) as shown on or in the report. Enter last name, first name, middle initial. If military, show rank and branch of service. The name of the principal author is an absolute minimum requirement.

6. REPORT DATE: Enter the date of the report as day, month, year, or month, year. If more than one date appears on the report, use date of publication.

7a. TOTAL NUMBER OF PAGES: The total page count should follow normal pagination procedures, i.e., enter the number of pages containing information.

7b. NUMBER OF REFERENCES: Enter the total number of references cited in the report.

8a. CONTRACT OR GRANT NUMBER: If appropriate, enter the applicable number of the contract or grant under which the report was written.

8b, 8c, & 8d. PROJECT NUMBER: Enter the appropriate military department identification, such as project number, subproject number, system numbers, task number, etc.

9a. ORIGINATOR'S REPORT NUMBER(S): Enter the official report number by which the document will be identified and controlled by the originating activity. This number must be unique to this report.

9b. OTHER REPORT NUMBER(S): If the report has been assigned any other report numbers (*either by the originator or by the sponsor*), also enter this number(s).

10. AVAILABILITY/LIMITATION NOTICES: Enter any limitations on further dissemination of the report, other than those imposed by security classification, using standard statements such as:

- (1) "Qualified requesters may obtain copies of this report from DDC."
- (2) "Foreign announcement and dissemination of this report by DDC is not authorized."
- (3) "U. S. Government agencies may obtain copies of this report directly from DDC. Other qualified DDC users shall request through _____."
- (4) "U. S. military agencies may obtain copies of this report directly from DDC. Other qualified users shall request through _____."
- (5) "All distribution of this report is controlled. Qualified DDC users shall request through _____."

If the report has been furnished to the Office of Technical Services, Department of Commerce, for sale to the public, indicate this fact and enter the price, if known.

11. SUPPLEMENTARY NOTES: Use for additional explanatory notes.

12. SPONSORING MILITARY ACTIVITY: Enter the name of the departmental project office or laboratory sponsoring (*paying for*) the research and development. Include address.

13. ABSTRACT: Enter an abstract giving a brief and factual summary of the document indicative of the report, even though it may also appear elsewhere in the body of the technical report. If additional space is required, a continuation sheet shall be attached.

It is highly desirable that the abstract of classified reports be unclassified. Each paragraph of the abstract shall end with an indication of the military security classification of the information in the paragraph, represented as (TS), (S), (C), or (U).

There is no limitation on the length of the abstract. However, the suggested length is from 150 to 225 words.

14. KEY WORDS: Key words are technically meaningful terms or short phrases that characterize a report and may be used as index entries for cataloging the report. Key words must be selected so that no security classification is required. Identifiers, such as equipment model designation, trade name, military project code name, geographic location, may be used as key words but will be followed by an indication of technical context. The assignment of links, rules, and weights is optional.